

Dipartimento di / Department of  
Biotecnologie e Bioscienze

Dottorato di Ricerca in / PhD program Tecnologie Convergenti per i Sistemi  
Biomolecolari (TeCSBi) Ciclo / Cycle XXXIII

## **TITOLO TESI / THESIS TITLE**

Computational Approaches for bio-materials characterization and biomaterial-  
cell interactions

Cognome / Surname Fontana Nome / Name Federico

Matricola / Registration number 795883

Tutore / Tutor: Prof. Francesco Nicotra

Cotutore / Co-tutor: Dott. Laura Russo

Supervisor: Dott. Fabrizio Gelain

Coordinatore / Coordinator: Prof. Paola Branduardi

**ANNO ACCADEMICO / ACADEMIC YEAR** 2019/2020

University of Milano-Bicocca  
Department of Biotechnology and Biosciences

Ph.D. Course in Converging Technologies for Biomolecular Systems  
XXXIII cycle



Computational Approaches for biomaterials characterization and  
biomaterial-cell interactions

Federico Fontana  
Matr. 795883

Academic Year 2019-2020



# Contents

Glossary	9
Abstract	11
<b>1 Introduction</b>	<b>13</b>
1.1 <b>Molecular Self-Assembly: from Nature to regenerative medicine</b> . . .	14
Peptide-based Biomaterials for Tissue Engineering Applications . . . .	14
1.2 <b>Modeling Strategies for Supra-molecular Bio-materials</b> . . . . .	17
1.2.1 Elucidating structural organization of SAPs . . . . .	17
1.2.2 Steered molecular dynamics simulations of SAPs . . . . .	20
1.2.3 NMR and ssNMR characterization of SAPs . . . . .	21
1.3 <b>A new paradigm for SAPs hydrogels development</b> . . . . .	23
1.4 <b>Computational and experimental methods used in this thesis</b> . . . .	26
1.4.1 <b>Minimization</b> . . . . .	26
Steepest Descents Method . . . . .	26
1.4.2 <b>Molecular Dynamics</b> . . . . .	27
Thermodynamic Ensembles . . . . .	27
1.4.3 <b>From NMR to ssNMR: a brief compendium</b> . . . . .	28
<b>NMR investigation of SAPs aggregates: magic angle spinning</b> <b>(MAS) ssNMR</b> . . . . .	28
<b>Cross Polarization</b> . . . . .	29
<b>2 Morphoscanner</b>	<b>31</b>
2.1 <b>Abstract</b> . . . . .	32
2.2 <b>Introduction</b> . . . . .	33
2.3 <b>Material and Methods</b> . . . . .	34
2.3.1 MD of BMHP1-Derived SAPs . . . . .	34
2.3.2 Choosing the Secondary Structure Parameters in CG-MD Simulations of BMHP1-Derived SAPs . . . . .	35

2.3.3	CG-MD Simulations of 100-mer Systems of BMHP1-Derived SAPs . . . . .	35
2.3.4	CG-MD Simulations of 100-mer Systems of $(LDLK)_3$ and $(LDLD)_3 + (LKLK)_3$ . . . . .	36
2.3.5	Strand-Peptide Alignment Analysis via Morphoscanner . . . . .	36
2.3.6	$\beta$ -Sheet Reconstruction via Morphoscanner . . . . .	38
2.4	<b>Results</b> . . . . .	39
2.4.1	Morphoscanner . . . . .	39
2.4.2	Morphoscanner Validation . . . . .	40
2.4.3	Modeling of Assembling Systems: BMHP1-Derived SAPs, CAPs and $(LDLK)_3$ . . . . .	44
2.4.4	Using Morphoscanner for the Analysis of Self-Assembled Peptidic Aggregates . . . . .	47
2.4.5	Peptide Oligomer Identification . . . . .	53
2.4.6	Tracking Oligomers Arrangement Dynamics and $\beta$ -Structures Organization . . . . .	53
2.5	<b>Conclusions</b> . . . . .	59
3	<b>Coarse-grained molecular dynamics of branched SAPs</b>	<b>61</b>
3.1	<b>Abstract</b> . . . . .	62
3.2	<b>Introduction</b> . . . . .	63
3.3	<b>Material and Methods</b> . . . . .	64
3.4	<b>Results</b> . . . . .	67
3.4.1	CG-MD simulations of pure mixtures of branched peptides . . . . .	67
3.4.2	CG-MD simulation of mixtures of branched and linear peptides . . . . .	75
3.5	<b>Conclusions</b> . . . . .	80
4	<b>Nano-Mechanics of SAPs structures</b>	<b>81</b>
4.1	<b>Abstract</b> . . . . .	82
4.2	<b>Introduction</b> . . . . .	83
4.3	<b>Material and Methods</b> . . . . .	84
4.3.1	Hydrogel preparation and ssNMR characterization at natural abundance . . . . .	84
4.3.2	CG-MD simulations of $(LDLK)_3$ and FAQ- $LDLK_3$ peptides . . . . .	84
4.3.3	UA-MD simulations of FAQ peptides . . . . .	85

4.3.4	UA-Steered molecular dynamics simulations of ( <i>LDLK</i> ) <sub>3</sub> and FAQ-( <i>LDLK</i> ) <sub>3</sub> peptides . . . . .	87
4.3.5	CG-Steered molecular dynamics simulations of ( <i>LDLK</i> ) <sub>3</sub> and FAQ-( <i>LDLK</i> ) <sub>3</sub> peptides . . . . .	88
4.3.6	Analysis of SMD simulations . . . . .	89
4.3.7	Morphoscanner Analysis . . . . .	90
4.4	<b>Results and discussion</b> . . . . .	91
4.4.1	Self-Assembling of ( <i>LDLK</i> ) <sub>3</sub> Fibril Seeds . . . . .	91
4.4.2	ONE-POT CG-MD of ( <i>LDLK</i> ) <sub>3</sub> Fibril . . . . .	93
4.4.3	Assessment of FAQ Self-Assembling Propensity . . . . .	93
4.4.4	Self-Assembling of FAQ-( <i>LDLK</i> ) <sub>3</sub> Fibril Seeds . . . . .	94
4.4.5	Steered Molecular Dynamics Simulations of Fibril Seeds . . . . .	94
	Failure conformations of ( <i>LDLK</i> ) <sub>3</sub> Fibril Seeds . . . . .	96
	Failure conformations of FAQ-( <i>LDLK</i> ) <sub>3</sub> Fibril Seeds . . . . .	101
	Failure conformations of SAPs Fibrils . . . . .	102
4.5	<b>Conclusions</b> . . . . .	108
<b>5</b>	<b>Unveiling Interactions between SAPs and Neural Membranes</b>	<b>109</b>
5.1	<b>Introduction</b> . . . . .	110
5.2	<b>Material and Methods</b> . . . . .	112
5.2.1	Bilayer Composition . . . . .	112
5.2.2	CG-MD Simulations of Neural Membranes . . . . .	112
5.2.3	Interactions among Neural Membrane and ( <i>LDLK</i> ) <sub>3</sub> monomers . . . . .	112
5.2.4	Embedding Aquaporin 4 in Neural Membrane . . . . .	113
5.2.5	CG-MD simulations of Aquaporin 4 Embedded in Neural Membranes . . . . .	114
5.2.6	CG-MD Simulations of ( <i>LDLK</i> ) <sub>3</sub> SAPs Fibril . . . . .	114
5.2.7	CG-MD simulations of minimal model of NSCs with ( <i>LDLK</i> ) <sub>3</sub> fibril . . . . .	115
5.2.8	CG-MD simulation of minimal model of ANSCs with ( <i>LDLK</i> ) <sub>3</sub> monomers . . . . .	115
5.2.9	Analysis . . . . .	115
	Density Fluctuations maps . . . . .	117
	Lipids Motion Patterns . . . . .	117
5.3	<b>Results</b> . . . . .	118
5.3.1	Identification of lipid domains in Neural Membranes . . . . .	118
5.3.2	Interactions among Neural Membranes and ( <i>LDLK</i> ) <sub>3</sub> . . . . .	118
5.3.3	Neural Membrane Riorganization with Embedded AQP4 . . . . .	118
5.3.4	Neural Membrane SAPs Fibril Interactions . . . . .	121

	Long-range Interactions between SAPs Fibril and Neural Membrane . . . . .	121
	Short-range Interactions between SAPs Fibril and Neural Membrane . . . . .	123
5.4	<b>Conclusions</b> . . . . .	125
<b>6</b>	<b>CG Modeling of Glycosylated SAPs</b>	<b>131</b>
6.1	<b>Introduction</b> . . . . .	132
6.2	<b>Material and Methods</b> . . . . .	133
6.2.1	CG-MD simulations of BMHP1 . . . . .	133
6.2.2	CG-MD simulations of O-Maltosylated BMHP1 . . . . .	133
6.2.3	CG-MD simulations of $(LDLK)_3$ -BMHP1 SAPs . . . . .	133
6.2.4	GLycosylation of $(LDLK)_3$ -BMHP1 SAPs . . . . .	134
6.2.5	Analysis . . . . .	135
6.3	<b>Results</b> . . . . .	136
6.3.1	Self-Assembling of BMHP1 and Maltosylated BMHP1 SAPs . . . . .	136
6.3.2	Self-Assembling of differently glycosylated $(LDLK)_3$ -BMHP1 SAPs . . . . .	136
6.4	<b>Conclusions</b> . . . . .	142
<b>7</b>	<b>Conclusions and future perspectives</b>	<b>143</b>
<b>I</b>	<b>Appendices</b>	<b>149</b>
<b>8</b>	<b>Morphoscanner: Additional Tables and Figures</b>	<b>151</b>
8.1	Coarsening of Biotin: from Gromos53a6 to MARTINI . . . . .	152
8.2	Biotin partitioning coefficient . . . . .	155
8.3	Secondary structure parameters from conformational sampling of UA-MD simulations . . . . .	157
8.4	CG-MD simulations setup . . . . .	158
8.5	Shift Values of BMHP1-derived SAPs and $(LDLK)_3$ SAPs . . . . .	159
8.6	UA-MD simulations of 8-mer systems . . . . .	161
	<b>Morphoscanner: the python module</b>	<b>165</b>
	<b>Analysis of CG-MD simulations with Morphoscanner: additional figures</b>	<b>169</b>
<b>9</b>	<b>Branched SAPs: Additional Tables and Figures</b>	<b>175</b>

---

<b>10 Nano-Mechanics of SAPs structures: Additional Tables and Figures</b>	<b>177</b>
10.1 GoMARTINI mapping of $(LDLK)_3$ and FAQ- $(LDLK)_3$ SAPs . . . . .	178
10.2 Failure classification of SAPs seeds and fibrils . . . . .	181
10.3 Computational performance on GPU Geforce GTX 1080 . . . . .	183
<b>Nanomechanics of SAPs structure: Morphoscanner Analysis</b>	<b>185</b>
<b>11 SAPs-Neural Membrane Interactions: Additional Tables and Figures</b>	<b>195</b>
<b>12 CG Modeling of Glycosylated SAPs: Additional Tables and Figures</b>	<b>199</b>
<b>List of Publications</b>	<b>235</b>
<b>Curriculum Vitae</b>	<b>237</b>
<b>Acknowledgements</b>	<b>239</b>





# Glossary

**AA-MD** (All Atom Molecular Dynamics): MD approach where each atom, constituting molecular systems, is considered as single interaction site.

**AFM** (Atomic Force Microscopy): scanning probe microscopy techniques used for force measurement, manipulation and imaging of soft matter at the nanoscale level.

**CAPs** (Complementary co-assembling peptides): bi-phase SAPs systems, which consist of two complementary charged peptide sequences.

**CG-MD** (Coarse-Grained Molecular Dynamics): MD approach where groups of atoms are considered as single interaction sites.

**CryoTEM** (Cryogenic Transmission Electron Microscopy): microscopy technique in which a beam of electrons is transmitted through a sample, which is at temperature of  $\approx 77$  K, to form an image.

**DFT** (Density Functional Theory): computational approach for the investigation of electronic structures of atoms and molecules, based upon the resolution of an equivalent of the Schrodinger equation.

**ECM** (Extra-cellular matrix): complex three-dimensional network of intertwined and entangled nano-bio-structures, such as collagen fibrils, glycoprotein and other macromolecules. ECM plays a pivotal role in the maintenance of cell physiology by providing physical and biochemical cues.

**MD** (Molecular Dynamics): a computational approach that allows to study the movement of atoms and molecules, which are approximated as systems of interacting particles, according to the formalism of molecular mechanics.

**NMR** (Nuclear Magnetic Resonance): a spectroscopy technique that employs the magnetic spin of atom nuclei, to retrieve information about their chemical environments.

**NSCs** (Neural Stem Cells): self-renewing, multi-potent cells capable of generating all neural lineages such as neurons, astrocytes and oligodendrocytes.

**PAs** (Peptide Amphiphiles): self-assembling peptides which structures resemble those of phospholipids, with the head made of hydrophilic amino-acids and a long alkyl tail.

**PNA** (Peptide Nucleic Acid): synthetic oligonucleotide, where the sugar-phosphate backbone have been replaced by N-(2-aminoethyl)-glycine bounded through peptide bonds.

**PTMs** (Post-translational modifications): reversible or irreversible chemical modifications of proteins, occurring after translation.

**RADA-like-SAPs** : class of self-assembling peptides, developed starting from the structural basis of RADA peptides, which spontaneously assemble into highly ordered cross- $\beta$  structures. RADA self-assembly, in water, is mainly driven by hydrophobic interactions among Alanine (Ala, A) residues, while electrostatic interactions among Arginine(Arg, R) and Aspartic Acid (Asp, D) residues are screened from the counter-ions in surrounding aqueous environment.

**SAPs** (Self-assembling peptides): Short amino-acid sequences that spontaneously self-assemble into different supramolecular structures, depending on the environmental conditions.

**SMD** (Steered Molecular Dynamics): MD setup where an external force is applied to one or more interaction sites, while another group can be fixed.

**ssNMR** (solid-state Nuclear Magnetic Resonance): NMR spectroscopy approach suitable to study biomolecular systems that are largely immobile on the NMR time scale.

**TE** (Tissue Engineering): ensemble of therapeutics approaches aiming to repair disease or damaged tissues with the use of cell-biomaterials constructs.

**XRD** (X-ray Diffraction): experimental technique that allows to determine the atomic structure of a crystal, through the study of its diffraction patterns of high-energy electromagnetic radiation (X-rays, wavelength of  $\approx 1-100$  ).

# Abstract

Biomaterials for tissue engineering applications have to comply with several requirements, such as safety, biocompatibility and appropriate mechanical features. The development process of these biomaterials encompasses several scientific approaches, ranging from *in-silico* to *in-vivo*. The *in-silico* optimization of biomaterials features is attracting even larger attention. Indeed, the improvement of this approach will allow to reduce additional costs in the biomaterials development process, due to unnecessary experimental characterizations.

According to this point-of-view, in this thesis is presented a molecular dynamics approach for biomaterial characterization. More in details, self-assembling peptides (SAPs) hydrogels scaffolds have been investigated at the nano-scale and micro-scale, in order to elucidate their intrinsic structure-property-function relationships.

The atomistic and coarse-grained molecular dynamics (CG-MD) have been used for the elucidation of self-assembling pathways of peptide-based scaffolds.

Due to the lack of crucial structural information in CG-MD simulations, the innovative software suite, dubbed Morphoscanner, has been employed for the elucidation of conformational aggregation patterns of SAPs. Then, the mechanical properties and failure mechanisms of SAPs nanostructures have been investigated through the steered MD simulations.

These evidences led the development of a CG-MD approach aiming to elucidate the complex interplay between cell membranes and SAPs nano-fibrils. In particular, MARTINI CG-MD simulations have been used for understanding the effects of SAPS nano-fibril on dynamics of lipid domains in neural membranes.

Such achievements open up new dimensions in the field of biomateriomics, allowing to understand and eventually orchestrate the complex phenomena which affect the mechanical properties and biocompatibility of SAPs biomaterials for tissue engineering applications.



## Chapter 1

# Introduction

## 1.1 MOLECULAR SELF-ASSEMBLY: FROM NATURE TO REGENERATIVE MEDICINE

During the last three decades, molecular self-assembling attracted increasing attention for several reasons. First, human beings have always been fascinated by the emergence of order from chaos, such occurs at several scales in Nature.[1] Second, since the dawn of molecular related disciplines, such as biochemistry and molecular biology, it is widely accepted that the complexity of Life emerges from self-assembly propensities of bio-molecules and their hierarchical self-organization.[1] Third, the domestication of bio-molecular self-assembly allowed scientists and engineers to design the so-called "bottom-up" approach for making innovative bio-materials.[1][2][3].

Briefly, molecular self-assembly processes can be grouped into two classes: static and dynamics. Static self-assembly involves systems that are close to a local or global equilibrium and do not dissipate energy, instead dynamics self-assembly occurs when the formation of ordered structures requires dissipation of energy.[1][4][5]

Few examples of static molecular self-assembly, tailored by Nature, are the lipid membrane formation, the nucleic acid hybridization, the DNA-histones association, and the combination of RNA and ribosomal proteins to form a functional ribosome.[6][7][8] Other examples of static self-assembly, employed in manufacturing, are the formation of ordered microparticles from block copolymers or the formation of nano-fibers from self-assembling peptides.[2][9] Instead, few examples of dynamic molecular self-assembly are the formation of cytoskeleton in eucaryotic cells, the interaction among actin and myosin fibrils in muscular cells.[10][11]

Static biomolecular self-assembly has been mainly exploited for the fabrication of soft materials for tissue engineering and regenerative medicine applications.[12][13] In addition, self-assembling biomaterials have been also used for studying mechanisms ruling abiogenesis and Alzheimer's disease.[1][14][15][16] Self-assembling DNA and self-assembling peptides (SAPs) are the most promising building blocks for biomaterials due to their favorable biocompatibility, tailorability, biomimetic properties and easy tunability of their properties.[17][18][19][20][21]

### Peptide-based Biomaterials for Tissue Engineering Applications

Tissue engineering (TE) applications aim to lead tissues in pathological conditions towards their own physiological states. Healthy tissues are characterized by particular interactions between cells and the extracellular environment. These interactions are finely regulated by the architecture of the extracellular matrix (ECM), which consists of differently glycosylated intertwined fibrillar proteins.[22][23]

SAPs are increasingly attracting attention for applications in TE, due to their ability to spontaneously organize into fibrillar structures and then resemble the main structural and mechanical features of healthy ECM. More in details, SAPs are capable of forming a porous network, displaying specific cell-binding sites, also named functional motifs.[2][17][19][21]

Inspired and motivated by protein assembly in biological systems, various SAP sequences have been studied, leading to the discovery of different assembled molecular structures such as nanofibers, nanorods, nanotubes, nanovesicle and nanoparticles. The aggregation state of SAPs is heavily affected by the sequence and is usually triggered by environmental conditions, such as temperature variations, pH shifts or surrounding ion concentrations. Large efforts have been conducted for improving SAPs features, to avoid harmful effects of triggering stimuli, such as pH shifts or temperature variations, over biocompatibility.

According to this view, three main classes of SAPs have been adopted for tissue engineering applications, i.e. RADA-like-SAPs, complementary co-assembling peptides (CAPs) and peptide amphiphiles (PAs).[2][24][25]

RADA-like-SAPs have been developed, starting from the sequence identified in Zuotin, which consists of hydrophobic alanine and positively charged lysine or negatively charged glutamic acid residues (EAK16).[26] RADA-like-SAPs are peptides that contain alternating charged hydrophilic and hydrophobic residues. Different variants of RADA-like-SAPs have been designed and studied, such as Ac-(*RADA*)<sub>3</sub>-CONH<sub>2</sub>, Ac-(*KLDD*)<sub>3</sub>-CONH<sub>2</sub> and Ac-(*RADADADA*)<sub>2</sub>-CONH<sub>2</sub>. The modular features of this class of SAPs promotes the formation of ordered cross-beta structures. Indeed, interactions among hydrophobic residues drive peptide assembly into nanofibers with charged amino acid side chains exposed to the aqueous environment. RADA-like-SAPs, eventually functionalized, have been largely used in tissue engineering for different purposes, such as hydrogel scaffolds to foster ingrowth of regenerating tissues or as hemostat solutions. [17][18][20]

CAPs are made of positive Ac-(*LKLLK*)<sub>3</sub>-CONH<sub>2</sub> and negative Ac-(*LDLD*)<sub>3</sub>-CONH<sub>2</sub> (eventually functionalized as Ac-KLPGWSG-(*LDLD*)<sub>3</sub>-CONH<sub>2</sub>) modules. The self-repulsion of each module prevents uncontrolled spontaneous self-assembly, while electrostatic interactions between positively and negatively charged peptides drive their co-assembly and lead to nanofibrillar architecture formation. At the meso-scale, both SAPs and CAPs nanofibers are organized into a 3D structure, which retains water and forms a porous hydrogel.[24]

PAs molecular structures resemble those of phospholipids in cell membranes, comprising hydrophobic alkyl tails and hydrophilic heads. In functionalized PAs, peptide moiety is usually formed by three sections: (i) a hydrophobic sequence capable of forming  $\beta$ -sheet structures; (ii) an hydrophilic, eventually charged, section; (iii) a bioactive epitope, also named functional motif.[25][27]



In these SAPs, hydrophobic peptide sequence consists of non-polar amino acid residues (G, A, V, L, I, P, F), while hydrophilic heads consist of positively charged (H, K, R) or negatively charged (D, E) residues. PA self-assembly is driven by the hydrophobic interactions of the alkyl tails, hydrogen bonding and electrostatic repulsion among charged amino acids.[25]

PAs in water self-assemble into nanofibers or nanorods as a result of hydrophobic interactions. Due to the fact PAs are highly sensitive to solution environment, they can self-assemble into alternative structures depending on solvation conditions.

Other SAPs are able to assemble into tubular structures as a consequence of  $\pi$ - $\pi$  interactions among aromatic side chain of amino-acid residues, such as diphenylalanine SAPs.[28] Instead, cyclic peptides self-assemble into hollow  $\beta$ -sheet rich cylinders by stacking on top of each other through stable hydrogen bonds.[29][30]

As already stated, in the sequence of SAPs, it is possible to incorporate functional motifs or other bioactive moieties for altering the biomimetic properties of SAPs or improving control over hierarchical organizations. Functional motifs are short peptides linked to N- or to C- terminus of the original SAPs and can be spaced with few glycine, which are necessary to ensure flexibility and the correct exposure to different target. Also, functional motifs should not alter self-assembling propensity of the original SAPs.[21]

According to the evidences from proteomics and glycomics of ECM, glycosylation is a fundamental post-translation modifications (PTMs) which affect protein stability, folding and cellular localization. Glycoproteins are also involved in cellular recognition and modulation of immune response. Then, the modification of SAPs with carbohydrates represent an intriguing strategy for facilitate control over peptide self-assembly and conferring them additional biomimetic features. Indeed, as demonstrated in the recent work of *Restuccia et al.*, the glycosylation of QQKFQFQFEQQ ("Q11") facilitates hierarchical self-assembly into  $\beta$ -sheet nanofibrils and promotes further lateral association among nanofibrils. In addition, glycosylated Q11 fibril network is more resistant to non-specific cell, bacteria and protein interactions. [31]

Another interesting strategy for improving control over the hierarchical organization of SAPs hydrogels is represented by bioconjugation with DNA, RNA or peptide nucleic acid (PNA). Such strategy, employing the high specificity of nucleic acid hybridization, allows to exert a fine control over the nanostructural organization of the bioconjugated SAPs hydrogels.[32][33][34]

Chemical cross-linking represents another intriguing strategy for improving the control over architectural and mechanical features of SAPs hydrogels. Such approach found applications for the developing of self-standing bioprosthesis for neural tissue engineering.

Indeed, SAPs hydrogels crosslinked with genipin, a natural extract from *gardenia jasminoides*, are suitable for tissue engineering applications due to improved mechanical stability making these materials suitable for electrospinning.[35] The electrospun channel has been shown to have good biocompatibility and promote cell differentiation thanks to their structural and mechanical similarities with ECM. Due to the fact genipin cross-linking is suitable only for lysine-rich SAPs hydrogel, alternative cross-linking methods can be taken into considerations. Few examples are represented by glutaraldehyde[36], that reacts with amine groups, or sulfo-SMCC, that reacts with sulfhydryl and amine groups.[37] However, the application in the clinic of chemical cross-linked SAPs will require additional improvements in reaction yielding and topological control of resulting scaffolds.

## 1.2 MODELING STRATEGIES FOR SUPRA-MOLECULAR BIO-MATERIALS

### 1.2.1 Elucidating structural organization of SAPs

Molecular self-assembly arises from the interplay of non-covalent interactions, such as hydrogen bonding, metal coordination, hydrophobic forces, van der Waals forces,  $\pi$ - $\pi$  interactions, and electrostatic interactions. Then, the accurate modeling of these interactions represent a limiting factor for predicting stability of supramolecular complexes.

Quantum mechanics (QM) approaches have been largely adopted for the accurate description of both covalent than non-covalent interactions in molecular systems. Among QM methods, density functional theory (DFT) attracted increasing attention in supra-molecular biomaterials modeling. Indeed, DFT have been used for predicting and calculating electronic structures of DNA and amino acid base pairs.[38] Further applications consisted in the elucidation of adsorption mechanism of biomolecules on surfaces made of different materials, such as graphene, metal oxides or hydroxyapatite.[39][40][41][42][43] Due to the increasing incidence of Alzheimer's diseases in the modern society, DFT approaches have been also used for the investigation of binding mechanisms of several ligands in amyloid- $\beta$  structures.[44][45][46][47] Emerging SAPs supra-molecular structures resemble the organization of amyloid fibril; this similarity encouraged the application of DFT approaches for the prediction of structural and vibrational properties of SAPs aggregates [48][49].

Due to the high computational demands, DFT calculations, and more in general QM approaches, can't be used for the study of systems which sizes are relevant for experimental characterization. The computational investigation of biomaterials at the nano- and micro-scale can be performed using molecular dynamics (MD) approach.

MD approaches consist in the resolution of Newton's equations of motion for a system of interacting particles, according to the molecular mechanics (MM) formalism. In molecular

mechanics, the validity of Born-Oppeneimer approximation allow to calculate the potential energy of a system as function of nuclear position, ignoring the electrons motions, using force fields. Then, MM and MD approaches found large applications in the field of biomaterial science.

As shown in Eq. 1.1, the functional form of potential energy in molecular mechanics can be split into two parts:

$$E = E_C + E_{NC} \quad (1.1)$$

The first part of Eq. 1.1 refers to the contributions of the covalent bond and angle deformations as highlighted in 1.2. The first item describe the interactions between two bonded atom as harmonic function. The second item refers to the bending of valence angles among three atoms. The third item is a torsional potential describing rotations around the bonds in function of the angle. The fourth item restricts the geometry of molecules by means of limitation of torsion of improper dihedral angles.

$$E_C = \sum_B k_b(b - b_0)^2 + \sum_A k_\theta(\theta - \theta_0) + \sum_{DH} k_\phi(1 + \cos(n\phi - \phi_0)) + \sum_{IM} k_\psi(\psi - \psi_0) \quad (1.2)$$

The second part in Eq. 1.1, relates to the contributions of the non-covalent interactions, as shown in Eq. 1.3.

All-atom (AA) force fields are largely used in the investigation of supramolecular systems, due to the high accuracy in the description of exact conformation of molecular building blocks. Indeed, AA-MD allow to monitor H-bonding as well as aromatic and charge-charge interactions by representing them using Coulomb and Lennard-Jones potential, as shown in 1.3.

$$E_{NC} = \sum_{Nb(i,j)} 4\epsilon_{ij} \left( \left( \frac{\sigma}{r_{ij}} \right)^{12} - \left( \frac{\sigma}{r_{ij}} \right)^6 \right) + \sum_{Nb(i,j)} \frac{q_i q_j}{\epsilon_D r_{ij}} \quad (1.3)$$

The first item in 1.3 describes the Van der Waals forces as Lennard-Jones potential. The last item represents the electrostatic forces modeled as Coulomb potential. The definition of a force field requires the estimation of the parameters, such as  $K_b$ ,  $K_\theta$ , and  $\sigma_{ij}$  and the definition of the atom types, which define the local properties in the neighborhood of each atom. Atom type is a parameter that usually describes the atomic number, the hybridisation state and the local environment surrounding a certain atom. In other words, the atom type defines how an atom affects the properties of the surrounding environment. In particular, the interactions among atom types, of two covalent bonded atoms, defines the limitations of covalent bonds and angles. In CG force-fields, such as MARTINI, it is not possible to define the atom types. Indeed, more atoms are represented as a single CG bead. So, the

equivalent concept interaction site is always adopted.[50] Such parameters can be optimized through QM calculations, as above mentioned, and also with a variety of experimental data.

AMBER, CHARMM and OPLS are the well-known and most used AA force-field for the simulation of self-assembling biomolecular systems. However, comparative studies showed clear inconsistencies between these force fields in predicting self-assembling tendencies of peptides and other molecules. Another limitation of atomistic force-field is represented by the limit in time and length scales that can be achieved.[51]

Such limitations can be overcome in several ways, also taking into account evidences from experimental characterization of self-assembling biomaterials.

Restrained atomistic MD simulations can be used to gain insights into self-assembly pathways of biomolecular systems. Such approach require structural details from several experimental sources such as X-ray diffraction (XRD) or nuclear magnetic resonance (NMR). Restrained MD, firstly applied for protein structural refinement, have been also used for elucidation of characterization of self-assembling peptide systems.[52][53] Indeed, restrained MD simulations, integrating data derived from NMR nuclear Overhauser enhancements (NOE), allowed to elucidate conformation transitions of substance P or antimicrobial peptides in bi-phase membrane mimics.[54][55] Recently, restrained atomistic MD simulations have been employed for the elucidation of assembly pathways of SAPs hydrogels, retrieving structural parameters from ssNMR and cryo-TEM analysis of such hydrogels.[56][57]

Coarse-grained molecular MD simulations (CG-MD) have proven to be suitable for the investigation of systems of biological importance. More in general, CG molecular models played a pivotal role in the simulations of soft matter systems. In almost all CG models, the pair potentials are computationally efficient but don't always accurately describe all systems properties. Potentials can be derived in order to reproduce microscopic properties from fine-grained simulations (bottom-up approach) or macroscopic-thermodynamic quantities (top-down approach).[58] However, both approach can be combined together in order to develop coarse-grained potentials. The validation of a new CG model requires the definition of the ability of properties prediction at the thermodynamics state point used during its development (representability) and at different state points (transferability).

Among the several CG force-fields, MARTINI found large applications in the field of supra-molecular chemistry due to his good properties of representability and transferability.[50][58][59] Indeed, MARTINI have been used for the simulations of several bio-molecular classes, such as DNA, proteins, lipids and carbohydrates.[60][61] MARTINI molecular dynamics (MD) simulations have been largely used to elucidate the self-assembly pathways and structuring propensities of several peptide sequences at the nanoscale and mesoscale level. In the last years, MARTINI MD simulations were also used for the elucidation of emerging fibrillar network of bioconjugated SAPs, which have been used for tissue engineering

applications.[34][62][63]

The ultimate challenge in the field of biomaterials modeling is represented by cross-linked SAPs hydrogels.[37][35] The cross-linking reactions involve the formation of chemical bonds, which was possible to address with QM approaches, until a few years ago. In the recent years, different multi-scale modeling approaches have been established, mainly based upon QM/MM approaches.[64][65] To cope with limited computational resources, more complicated hybrid approaches have been developed, such as the hybrid QM/MM/CG MARTINI setup.[66] Due to the complicated technical issues to be addressed, this method has found very limited application such as in multi-scale modelling of enzymes.

Reactive CG-MD simulations represents a valid alternative for modeling cross-linking reactions in biomaterials. This approach is suitable for modeling systems that have the same reaction occurring multiple times, such as cross-linked SAPs hydrogels.[67] However, due to its recent introduction, this method has not already been tested for large systems simulations.

### 1.2.2 Steered molecular dynamics simulations of SAPs

Tissue engineering applications of innovative SAPs hydrogels are closely tight to their mechanical properties. Indeed, adequate mechanical features promote ingrowth of regenerating tissues around implanted hydrogel scaffold. According to a materiomimetic point-of-view, mechanical properties depends on the structural properties of hydrogel at the nano- and micro-scales.[68][69]

Steered MD (SMD) simulations represent a valid approach for the investigation of mechanical properties of biomacromolecular structures, such as axial and torsional rigidity, mimicking the AFM or optical tweezers experiments. As single-molecule technique, atomistic SMD have been used to elucidate the role of hydrogen bonding and charge interactions on bending stiffness of ER/K alpha-helix peptides.[70] SMD simulations allowed to clarify also mechanical properties of peptide aggregates such as A $\beta$  1-42 amyloid fibrils or coiled coil structural motifs.[71]

SMD simulations were also used for the estimation of the interaction strength of peptides in monolayers or aggregates. As shown in fig. 1.1, SMD have been used to estimate thermodynamic stability of the surfactant like peptides (SLPs, a particular class of PAs) fibril and oligomer models in aqueous solution, determined through ssNMR characterization and MARTINI CG-MD simulations, respectively. In these pulling simulations, an external mechanical force is applied to one SLP which is then dragged from an aggregate core. With this approach, the potential of mean force (PMF) profile has been derived, which is a good representation of the dissociation energy from the fibril ( $\Delta G_f$ ) or oligomer ( $\Delta G_o$ ). These

results show that it takes  $\approx 3$  fold more energy to pull one SLP out from the fibril structure than from the oligomer structure. This means that fibril structures are much more stable configurations than the oligomer. Since the magnitude of the dissociation energy is an indicator for the thermodynamic stability of the supramolecular assemblies, these results suggested that an increasing number of charges in the head-group caused more perturbations to the more ordered fibril structures than to the less ordered oligomer. The structural strain caused by increased electrostatic repulsion forces would be more detrimental for brittle rigid structures (fibrils) than for flexible structures (oligomers).[72]

Such results extended the conclusions of the work of Yu and Schatz, which used SMD to force transition between the bound, corresponding to a micelle cylinder fiber, and free state of 90 PAs in aqueous solution. They found that PAs assembly pathway is mainly dominated by conformational disorder-to-order transition, including forming secondary structures along with tail-head core-shell alignment and condensation that leads to total exclusion of water from the core.[73]

Atomistic SMD simulations suffer of the same limitation of classical MD simulations. CG-SMD simulations have been used to investigate mechanical properties of even larger aggregates. MARTINI SMD simulations have been used for the elucidation of protein-ligand mechanisms, i.e. docking simulations.[74] Instead, the MARTINI SMD approach found limited application for mechanical investigations of supra-molecular assemblies, because it does not allow conformational transitions that are quite common in the biological systems instead. The recently developed GoMARTINI overcome the main limitation of the MARTINI approach, allowing to track conformational transitions.[75] GoMARTINI SMD has proven to be suitable for elucidation of mechanical features of SAPs aggregates, such as fibril structures. Indeed, as shown in Chapter 4, GoMARTINI SMD simulations of SAPs fibrils provide comparable results to atomistic SMD simulations.

### 1.2.3 NMR and ssNMR characterization of SAPs

As already stated, reliable atomistic MD and CG-MD simulations of SAPs hydrogels require structural restraints from NMR experiments.

NMR is a spectroscopy technique which employees the magnetic properties of nuclei that contain an odd number of protons and an odd number of neutrons. Indeed, nuclei that contain an even number of protons and an even number of neutrons, such as  $^{12}\text{C}$ ,  $^{16}\text{O}$  and  $^{32}\text{S}$  are NMR inactive. Instead, isotopes which contain an odd number of protons or neutrons, such as  $^1\text{H}$ ,  $^2\text{H}$ ,  $^{13}\text{C}$ ,  $^{15}\text{N}$  and  $^{31}\text{P}$ , are commonly used in biological NMR.

NMR is widely used in studying molecular structures, dynamics and molecular interactions at atomic level. In the case of proteins, solution-state NMR can be employed to study

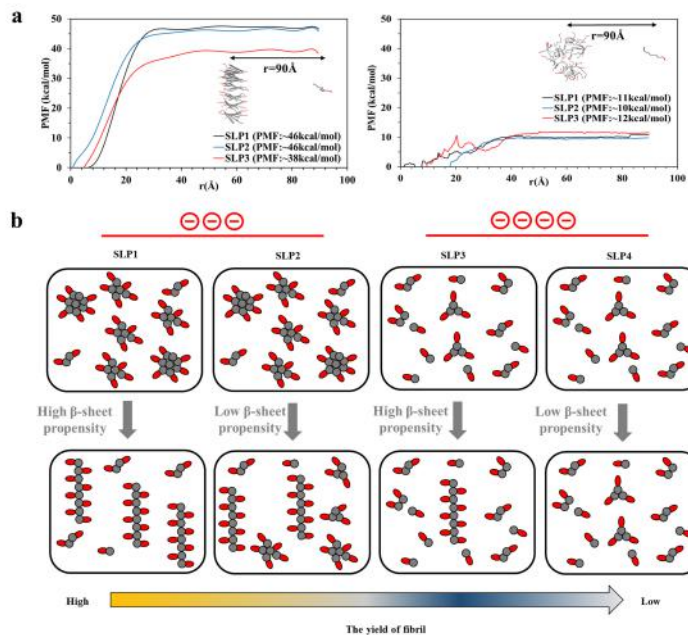


FIGURE 1.1: **Control over the fibrillization yield by varying the oligomeric nucleation propensities of surfactant-like peptides.** a) Potential of mean force (PMF) profiles of fibril (left) and oligomer (right) models along the reaction coordinate  $r$  derived from Steered MD (SMD) simulations provides information on the thermodynamic stability of fibril and oligomer structures. Increasing the number of charges of the head-groups reduced structural stability of the fibrils however, not in the oligomers. A representative SMD trajectory, during which a SLP monomer is dragged from the core of oligomer and fibril model for 90 along  $r$ , is shown under each graph. b) Graphical representation of the proposed mechanism leading to the different yields of nanofibers between SLP 1-4. The size distribution of the oligomeric intermediates is controlled by the number of head-group charges, which the less charged SLPs form bigger sized oligomer (2 on the left) and the more charged SLPs form smaller sized oligomers (2 on the right). Between the SLPs with the same charges, the fibrillization propensity is modulated by the  $\beta$ -sheet propensities of the tail group, with the SLP of higher  $\beta$ -sheet propensities giving higher yields of fibrils i.e. SLP1>2 and SLP3>4.

*Adapted from Lau et al. [72]*

relative small proteins (up to 35 kDa) that undergo rapid Brownian motion in solution. Recent advances in tailored isotope labeling schemes allow extending solution-state NMR to unveil side chains conformations of certain residues in large bio-molecular complexes.

Until few years ago, solution-state NMR played a pivotal role in determination of secondary structure and conformation of monomeric SAPs, both in organic than in aqueous media.[53][76] Nowadays, solution-state NMR is also employed for the characterization of surface of SAPs hydrogels and proteinaceous matrices.[77]

Neoglycosylation represents a well-established functionalization approach for increasing biocompatibility of pre-assembled collagen matrices. The neoglycosylation reaction mainly involves amine group of lysine residues. The quantification of the residual lysine amino groups is usually performed through  $^1\text{H}$  NMR spectroscopy. [78] In the recent work of *Wallace et al.* has been demonstrated the application of solution-state NMR spectroscopy to measure the surface chemical properties of the nanofibers of hydrogels formed from N-functionalised SAPs.[77]

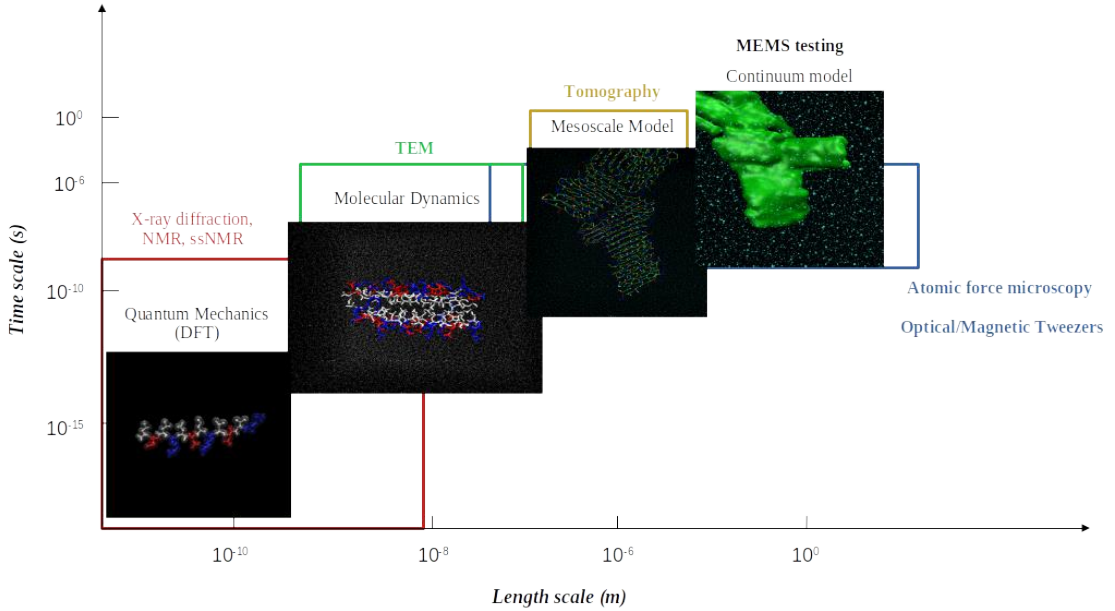
Solid-state NMR (ssNMR) is a suitable method to study large bio-molecular systems that are largely immobile on the NMR time scale. Indeed, ssNMR has been largely employed for elucidating structural and dynamics features of complex proteinaceous aggregates, such as amyloid and self-assembling peptides fibrils. In addition, ssNMR have been used to study protein complex in lipid bilayers, protein-nucleosome interactions and dynamic protein assemblies.[79] [80]

As shown in recent work of *Jekhmene et al.* and in Chapter 4,  $^{13}\text{C}$ -detected dipolar cross-polarization ssNMR is suitable for characterization of SAPs hydrogels, without synthetic isotope enrichment.[57] More in details, ssNMR evidences have been used for the secondary structure assignment in MD simulations, which provided precious insights, and comparable with larger scale investigation (such as AFM) about supra-molecular organization of SAPs.[57]

### 1.3 A NEW PARADIGM FOR SAPS HYDROGELS DEVELOPMENT

SAPs hydrogels are one of the most promising classes of biomaterials for tissue engineering applications. Nowadays, the development of even more performing SAPs is an open challenge. Indeed, SAPs hydrogels have to satisfy several requirements: 1) Molecular architectures and nano-structuring features; 2) Mesoscale topological arrangement; 3) Mechanical properties.[21] All these requirements contribute to bio-compatibility and bio-mimetic features of resulting hydrogel. Almost all of these stuffs can be addressed according to an *in-silico* approach, eventually validated through dedicated experimental characterization.





**FIGURE 1.2: Biomaterial Multiscale Modeling** The deep understanding of hierarchical organization of biomaterials requires an arsenal of computational and experimental techniques. Computational approaches, supported and validated by experimental evidences, can be used to transverse throughout a wide range of length and time scales. More in details, results of quantum mechanical calculation can be used to validate atomistic (or coarse-grained) molecular dynamics simulations. Eventually, results of atomistic (or coarse-grained) simulations can be used to develop constitutive equation of biomaterials. Experimental techniques, such as X-ray diffraction and nuclear magnetic resonance provide atomic-scale information about the 3D structure of constituents of biomaterials. These information can be used to validate molecular dynamics simulations. Instead, atomic force microscopy (AFM) and optical/magnetic tweezers extrapolate information about mechanical properties of single molecules or supramolecular aggregates, enabling direct comparison of experiment and simulation.

The most complete and accurate frameworks for biomaterials characterization is shown in fig. 1.2. Such approach have been widely used for the elucidation of the hierarchical organization and mechanical properties of naturally derived materials such as collagen or spider-silk.[81][82][83] The success of this approach relies on the combination of multidisciplinary theories, multiscale simulation methods (e.g. molecular dynamics and finite element analysis) and multiscale experiments (e.g. X-ray diffraction, NMR, AFM). This new paradigm

of material research lays on the evidence that the structural and mechanical complexity of self-assembling biomaterials reflects the hierarchical organization of biomacromolecules. The chemical nature of the molecular interactions, as well as the structural arrangement of the biomolecular building blocks, across many hierarchical scales, heavily affects the mechanical behavior of biological materials. At the micro- and nano-scale, differently from crystalline materials, which show mechanisms such as dislocation spreading or crack extension, biological materials feature molecular unfolding or sliding, when undergo to mechanical stress. At larger length scales, where the interactions with cells become more evident, more complicated mechanisms contribute to biomaterials mechanics behaviour.

**The scope of the current thesis** concerns the development of a computational framework, analogously to that shown in fig. 1.2, for the development and characterization of innovative SAPs hydrogels.

In Chapter 2, a general approach based on MARTINI CG-MD simulations for multi-scale modeling of SAPs is presented. Here, CG-MD simulations have been used to elucidate self-assembly pathways of a two classes of peptides: (i) the BMHP1-derived SAPs and (ii) complementary co-assembling peptides (CAPs). To highlights differences in supra-molecular organizations of diverse SAPs, an innovative tool, dubbed Morphoscanner (now also available as python module) has been developed.

In chapter 3, MARTINI CG-MD simulations have been used to evaluate structural features of the innovative branched SAPs, especially when mixed with traditional linear SAPs. Another time, Morphoscanner helped to highlight  $\beta$ -structuring propensities of the diverse mixed SAPs systems.

In chapter 4, GoMARTINI CG-SMD simulations have been used for the multi-scale mechanical characterization of SAPs aggregates. Thanks to Morphoscanner, it has been possible to classify failure mechanisms of SAPs aggregates, even taking into account the contribution of functional motifs.

In chapter 5, MARTINI CG-MD simulations were used to investigate interactions among neural stem cells and SAPs fibrils, which were built taking into account the evidences from Chapter 2 and 4. These results completed the characterization of SAPs presented in previous chapters, depicting the biocompatibility as an emerging property of cell-biomaterial systems, that can be measured according to the chemical-physical properties of such systems.

Finally, in chapter 6, starting from the evidences of 2, 4 and 5, an innovative class of Glycosylated SAPs have been developed *in-silico*.

## 1.4 COMPUTATIONAL AND EXPERIMENTAL METHODS USED IN THIS THESIS

### 1.4.1 Minimization

Molecular static self-assembly involves systems that are close to the global minimum conformation. Then, the identification of this conformation, through numerical methods, plays a pivotal role in the molecular modelling of self-assembling systems.

Commonly, the potential energy of a multi-molecular systems, calculated through molecular-mechanics approaches, is a complicated multidimensional function of the atomic coordinates (sometimes dubbed *hypersurface*) The minimum conformations correspond to the stable states of the system. Any movement away from a minimum gives an unstable conformation. There are several methods for the identification of system conformations, characterized by the lowest potential energy.

The minimization approaches allow to identify the vector  $\vec{x} = [x_1, x_2, x_3, \dots, x_n]$ , corresponding to the atomic coordinates, for which the function potential energy, denoted with  $f$ , has the minimum value.

Minimization algorithms are classified as derivative or non-derivative. The first class of minimization algorithms employs first or second-order derivative, while the latter class do not use derivatives. Furthermore, the derivative minimization algorithms can be classified as first order, which use the first order derivative, as well as second order, which use both first and second order derivatives. The most frequently used first order minimization methods are the method of *steepest descents* and the *conjugate gradient* method. Instead, the second order minimization methods are the method of *Newton-Raphson* and *Quasi-Newton* method.

In the next paragraph will be elucidate the *steepest descents* method.

#### Steepest Descents Method

The *Steepest descents method* changes the system coordinates following the direction parallel to the functional gradient of potential energy. With a system that consists of  $3N$  coordinates this direction is represented by a vector  $\vec{s}_k$ , as reported in the equation 1.4, wher  $G_k$  indicates the gradient operator of the potential energy function.

$$s_k = -\frac{g_k}{|g_k|} \quad (1.4)$$

The minimum location can be performed using a **line search** or **arbitrary step** approach.

The purpose of the **line search** approach is to locate a minimum along a line through the multidimensional space, where the potential energy function is defined. Such iterative approach requires the satisfaction of the condition in the equation 1.5, which means that the search proceeds according to consecutive orthogonal directions.

$$g_k * g_{k-1} = 0 \quad (1.5)$$

However, **line search** approach may itself be computationally demanding. In order to cope with limited computational resources, it will be better to consider a step of arbitrary length along the vector  $\vec{s}_k$ . This defines the **arbitrary step** approach.

### 1.4.2 Molecular Dynamics

As already stated in section 1.2.1, molecular dynamics (MD) consists of an iterative approach that allows to calculate the velocity and position of atoms, according to the mechanical mechanics formalism. MD represents a deterministic method, that allows to calculate any future state of a system starting from its current state. MD calculates the system evolution within time, generating its representative configurations, which allow predictions of thermodynamics and structural properties. Such realistic predictions through MD approaches are tightly connected to the choice of adequate integration interval, dubbed *time-step*. Indeed, the wrong choice of integration interval may lead to unrealistic physical predictions. By fixing **periodic boundary conditions** it is possible to perform MD simulations with a small number of particles, in such a way that particles experience forces as they were in a continuous medium.

#### Thermodynamic Ensembles

MD simulations are usually performed under constant conditions, fixed through the definition of a **thermodynamic ensemble**. The choice of a **thermodynamic ensemble** depends on the experimental features which should be investigated.

**Thermodynamic ensembles** are defined by a small set of parameters, such as temperature (**T**), pressure (**P**), volume (**V**), energy (**E**) and the number of particles (**N**). Different ensembles are common:

- The **Microcanonical ensemble (NVE)** is characterized by a fixed number of atoms (**N**), a fixed volume (**V**), and a fixed energy (**E**). These conditions define an isolated system.

- The **Canonical ensemble (NVT)** is characterized by a fixed number of atoms (N), a fixed volume (V), and a fixed temperature (T). This ensemble usually find application in the equilibration phase, that precedes the production run of MD simulations.
- The **Isobaric-Isothermal ensemble (NPT)** is characterized by a fixed number of atoms (N), a fixed pressure (P), and a fixed temperature (T). This ensemble is largely adopted for reproducing the experimental conditions of the laboratory reactions.
- Instead, the **Grand canonical ensemble ( $\mu$ VT)** is characterized by a fixed chemical potential ( $\mu$ ), a fixed volume (V) and temperature (T).

### 1.4.3 From NMR to ssNMR: a brief compendium

As already stated, NMR employees the magnetic properties of nuclei that contain and odd number of protons and an odd number of protons. NMR is used to study relative small proteins (up to 35 kDa), which undergo to rapid Brownian motion in solution. The fast atoms tumbling averages out anisotropic NMR effects and provides high-resolution NMR spectra.

However, large part of the systems investigated by biomaterials scientist are largely immobile on NMR time scale. The ssNMR approaches help overcome this limitation. Indeed, ssNMR finds wide applications in the investigations of protein aggregates such as amyloid or SAP fibrils.

#### **NMR investigation of SAPs aggregates: magic angle spinning (MAS) ssNMR**

Large supramolecular aggregates, such as SAPs fibrils, are characterized by slow molecular tumbling that hampers an adequate NMR spectral resolution. More in details, orientation dependent interactions, including chemical shift anisotropy (CSA) and magnetic dipole-dipole interactions, are not averaged out, thereby resulting in anisotropic line shapes.

CSA interaction, are dependent on the orientation of the molecules in the static magnetic field, applied to the sample of interest. This causes CSA lines broadening, which is also caused by asymmetry of the electronic distribution around the nuclei.

Dipole-dipole interactions, also known as dipolar coupling, emerge as a consequence of the close localization of two homonuclear or heteronuclear spins. Then, the two spins are affected by their mutual magnetic fields, which effective intensities depends upon the relative spin positions.

The magic angle spinning (MAS) is commonly used for improving spectral resolution. The MAS approach consists in rotating the sample at an angle of  $54.74^\circ$  with respect to the

static magnetic field. Using high-speed MAS rotors, the  $^{13}\text{C}$ - $^{13}\text{C}$  and the  $^{13}\text{C}$ - $^1\text{H}$  dipolar couplings are usually averaged out. Adopting this approach, detection in ssNMR is mostly performed on  $^{13}\text{C}$  nuclei. In addition,  $^1\text{H}$ -spins is applied during evolution and detection to improve spectral resolution, despite averaging out  $^1\text{H}$ - $^1\text{H}$  coupling is quite hard, without improvement of hardware setup.

### Cross Polarization

The low signal sensitivity in ssNMR is related to the detection of  $^{13}\text{C}$ , which have a low gyromagnetic ratio. The ssNMR analysis of SAP hydrogel scaffolds was extensively performed through cross-polarization (CP) experiments. [57] (See also Chapter 4). In CP experiments, magnetization is transferred from abundant spins (mostly  $^1\text{H}$ ) via heteronuclear dipolar couplings to the spins  $S$  that are close in space, i.e.  $^{13}\text{C}$ . Then, the magnetization of  $^{13}\text{C}$  is increased of  $\approx 4$  times, according to the eq. 1.6.

$$H_D^{IS} = \frac{\mu_0 \gamma_1 \gamma_2 \hbar^2}{16\pi^3 r^3} (3 \cos^2 \theta - 1) I_{1Z} I_{2Z} \quad (1.6)$$

In eq. 1.6,  $\gamma$  is the gyromagnetic ratio,  $\theta$  is the angle between the sample and the magnetic field,  $\hbar$  is Planck constant,  $I_z$  are the spin components parallel to the direction of the magnetic field applied on the sample. In the CP experiments ( $^{13}\text{C}$ - $^1\text{H}$  coupling) used in this thesis, the ratio of  $\gamma_1/\gamma_2$  is equal to 4.



## Chapter 2

# Morphoscanner

*Adapted from* Gloria Anna Ada Saracino\*, **Federico Fontana\***, Shehrazade Jekhmane, Joao Medeiros Silva, Markus Weingarh, Fabrizio Gelain. "*Elucidating Self-Assembling Peptide Aggregation via Morphoscanner: A New Tool for Protein-Peptide Structural Characterization*", In: ***Advanced Science*, Volume 5, page 1800471 (2018)**

*\*The authors equally contributed to the manuscript*



## 2.1 ABSTRACT

Self-assembling and molecular folding are ubiquitous in Nature: they drive the organization of systems ranging from living creatures to DNA molecules. Elucidating the complex dynamics underlying these phenomena is of crucial importance. However, a tool for the analysis of the various phenomena involved in protein/peptide aggregation is still missing. Here, an innovative software is developed and validated for the identification and visualization of  $\beta$ -structuring and  $\beta$ -sheet formation in both simulated systems and crystal structures of proteins and peptides. The novel software suite, dubbed Morphoscanner, is designed to identify and intuitively represent  $\beta$ -structuring and  $\beta$ -sheet formation during molecular dynamics trajectories, paying attention to temporary strand-strand alignment, sub-oligomer formation and evolution of local order.

Self-assembling peptides (SAPs) constitute a promising class of biomaterials and an interesting model to study the spontaneous assembly of molecular systems *in vitro*. With the help of coarse-grained molecular dynamics the self-assembling of diverse SAPs is simulated into molten aggregates. When applied to these systems, Morphoscanner highlights different  $\beta$ -structuring schemes and kinetics related to SAP sequences.

It is demonstrated that Morphoscanner is a novel versatile tool designed to probe the aggregation dynamics of self-assembling systems, adaptable to the analysis of differently coarsened simulations of a variety of biomolecules.

## 2.2 INTRODUCTION

The spontaneous organization of initially chaotic biological systems has helped scientists to explore the origins of Life on Earth.[14][15][16][1] Indeed, it is widely accepted that the self-assembling propensity of DNA, RNA, proteins, and peptides is one of the main molecular mechanisms that may have sparked Life as we know it. The so called “bottom-up” approach to design self-assembling materials, is directly inspired by this fascinating phenomenon.[1][84][85]

Self-assembling materials are also used as models to study molecular mechanisms that cause abiogenesis and Alzheimer’s disease.[14][15][16][1] Moreover, self-assembling peptides, inspired by the properties of biomolecules, have been developed for applications in diverse nanoscience sectors such as electronics, material science, and regenerative medicine.[13][12] The identification of stable domains that act as novel structuring motifs is critical for the development of self-assembling biomaterials.[84][85][12] Furthermore self-assembling peptides (SAPs) are promising building blocks for tissue engineering due to their favorable biocompatibility, tailorability and biomimetic properties.[86][87][88][89]

In the last decade our efforts have been focused on the development of SAP hydrogels for nervous regeneration and we designed different classes of SAPs such as functionalized SAPs [90], complementary co-assembling peptides (CAPs) and BMHP1-derived SAPs.[24][19] These peptides, featuring a promising pro-regenerative potential in neural tissue engineering applications, form differently  $\beta$ -structured filaments depending on their sequences and, in the case of BMHP1-derived SAPs, depending on the presence of biotin at the N-terminus.[19][91] Others demonstrated that, before assembling into nanoscaled filaments, SAPs initially self-aggregate into oligomeric molten globules that are shaped by hydrophobic interactions.[92][93][94] Within such molten globules peptides can adopt conformations of packing similar to paracrystalline and ordered nuclei. According to the protein nucleation mechanism this organization is due to the interplay between the forced spatial confinement of peptides and optimized (in terms of potential energy) nonbonded interactions.[95] Smith and colleagues demonstrated that amyloid cross- $\beta$ -structures of the peptide A $\beta$ (16–22) can assemble through a dynamic conformational phylogeny. In their work isotope-edited infrared spectra allowed to quantify the relative distribution of paracrystalline intermediates formed from intermolecular molten globules in which nucleation occurred previously.[92]

Furthermore, molecular dynamics simulations are a powerful tool to study peptide self-assembly, and showed that molten peptide oligomers could act as incubators for  $\beta$ -structuring.[96][97][98][99][100][101][102][103] Nonetheless, at the molecular level it is still unclear how oligomer-to-fibril transition emerges. Indeed, currently available tools to analyze molecular dynamics do not allow to track key events of the self-assembling process such

as the evolution of secondary structure patterns over time.

Coarse-grained molecular dynamics (CG-MD), enabling the simulation of larger systems on longer simulation times, showed great potential for high throughput screenings of the self-assembling propensity of biomolecules. In addition, CG-MD simulations allowed to estimate self-assembling propensity of different peptide sequences for a wide latitude of potential applications.[104][105][106][107] Nonetheless, analytical tools for the quantitative tracking of secondary structure patterns (such as  $\beta$ -structures) over MD trajectories are still lacking. This is an important limitation, given that knowledge of the time-dependent formation of secondary structures is crucial for a deeper understanding of the self-assembling phenomenon. In order to recognize  $\beta$ -structuring domains, we developed a topological pattern recognition software based on the multilayer graph theory, named Morphoscanner, and we validated it on diverse protein structures. Here, we applied Morphoscanner to MARTINI CG-MD simulations of peptide systems featuring spatial dimensions that are typical of molten particles.[92][93] Simulations have been designed to mimic the experimental conditions that trigger peptides to self-assemble into nanostructured hydrogels.

Thanks to the high adaptability of our software-suite to different sequences and system sizes, we could demonstrate that SAPs exhibit sequence-dependent intra-oligomer organization in agreement with previously described self-assembly models.[90][24][19][91][92][93]

## 2.3 MATERIAL AND METHODS

### 2.3.1 MD of BMHP1-Derived SAPs

The sequences of the simulated BMHP1-derived SAPs are listed in Fig. 8.6. Peptide monomers have the C-terminus amidated and the N-terminus biotinylated (or acetylated). Lysine residues are in the protonated state. Extended conformations of monomers were built with Pymol software by imposing all-trans geometry on the backbone dihedrals. Molecular dynamics were run using version 4.5.5 of the GROMACS simulation package and the GROMOS53a6 force field: systems comprised eight monomers each as reported previously and explicit aqueous solvent.[91] Coarse-grained molecular dynamics simulations have been conducted on octameric or 100-meric systems using MARTINI force field version 2.2. The choice of secondary structure parameters for 100-meric systems was made by comparing UA-MD and CG-MD simulations of 8-meric systems of BMHP1-derived SAPs.

### 2.3.2 Choosing the Secondary Structure Parameters in CG-MD Simulations of BMHP1-Derived SAPs

To select the most appropriate secondary structure parameters for 100-mer system simulations, UA and CG simulations of 8-mer systems were compared. Gyration radius, nematic order parameter, and the aggregation curves were used to assess the agreement between UA and CG molecular models.[91] Starting configurations of the systems modeled in UA and CG simulations consisted of extended (E) or UA sampled (SAM) monomers comprising the octameric systems.

Three different choices of SS parameters were proposed in CG-MD simulations: fully extended, coil or UA-sampled secondary structures (see Tables 8.1, 8.2 and 8.3). The SAM secondary structures parameters are monitored on UA-MD simulations by means of the DSSP algorithm as reported in the previous work.[91]

CG-MD simulations (using the above mentioned sets of SS parameters) and UA-MD simulations were then compared. CG-MD simulations of UA-sampled conformers with fully extended SS parameters resulted in gyration radii, nematic order parameters, and aggregation orders in higher agreement with the UA simulations, as shown in Figures 8.9, 8.10, 8.11.

### 2.3.3 CG-MD Simulations of 100-mer Systems of BMHP1-Derived SAPs

The boxes containing unsolvated peptides were built using the PACKMOL software.[108] UA-sampled monomer conformations were inserted in random orientations and positions, so that the atoms belonging to different peptides were at least at 0.1 nm away from each other.[108] Boxes, filled with MARTINI CG water beads, were chosen so as to mimic the 3% (w/v) concentration of SAPs typically used in empirical tests. As mentioned in section 2.4.3 fully extended SS parameters were adopted (see Figure 8.6). Ions (Na and Cl) were added to neutralize the systems up to 0.015 M concentration of NaCl, in order to reproduce salt concentration of diluted PBS (1x) solution. The production phase was conducted using constant temperature, pressure, and number of molecules (i.e., the NPT ensemble). Temperature, pressure, constraints, cut-off value, periodic boundary conditions, and integration-step settings were identical to 8-mer systems simulations. Three random distributions of peptides and ions were generated and simulated for 500 ns. One of the replicas as per each SAP sequence was extended up to 2000 or 4500 ns.

### 2.3.4 CG-MD Simulations of 100-mer Systems of $(LDLK)_3$ and $(LDLD)_3 + (LKLK)_3$

A similar approach was adopted for simulations of  $(LDLK)_3$  and CAPs. All-trans configuration of the  $(LDLK)_3$ ,  $(LDLD)_3$ , and  $(LKLK)_3$  were generated by Pymol (<http://www.pymol.org/>). The C- and N-termini of peptide monomers were amidated and acetylated, respectively. At neutral pH, lysine and aspartic acid side chains, because of their weak basic and acidic nature, can be considered fully protonated and deprotonated, respectively. Peptide were distributed (using PACKMOL) in explicit water cubic boxes. Prior to production, systems underwent an equilibration phase (a 3000-steps minimization using steepest descent method). The production phase was conducted in NPT ensemble in order to reproduce experimental conditions used in previous works.[19][109]

### 2.3.5 Strand-Peptide Alignment Analysis via Morphoscanner

Despite the structural differences observed in crystallography,  $\beta$ -sheets can be described as a regular 2D lattice graph stabilized by covalent bonds (along the direction of the backbone chains) and by hydrogen-bonds (among the backbone chains). We introduced the definition of  $\beta$ -contact to define the “edges” along H-bonds direction (2.1):

$$\beta_{contact} = \delta(r_{ij} - r_0) \quad (2.1)$$

where  $\delta$  is the Dirac measure,  $r_{ij}$  is the distance between backbone atom-group (grain) center-of-masses  $i$  and  $j$ ,  $r_0$  represents the distance between two  $\beta$ -strands in cross- $\beta$  structures (range between 4.7 and 5.3 Å)

The numerical representation of  $\beta$ -contacts network is provided by the BB matrix, whose elements are described in Equation 2.2:

$$BB_{ij} = \beta_{contact}(i, j) \quad (2.2)$$

The description of the interactions between two strands or peptides is provided by the Strand Backbone Contact matrix: a square matrix whose dimensions correspond to the number of strand/peptide backbone grains.

A set of matrices, named shift matrices, was developed to be used as references for the identification of the mutual arrangements described by the strand backbone contact matrix. Shift matrices describe the different arrangements between pairs of peptides. In

detail, parallel and antiparallel shift arrangements are described using the following matrix notation:

$$P_{ij}^+ = \delta_{i+k,j} \quad (2.3)$$

$$P_{ij}^- = \delta_{i-k,j} \quad (2.4)$$

$$A_{ij}^+ = \delta_{n-i+k,j} \quad (2.5)$$

$$A_{ij}^- = \delta_{n-i-k,j} \quad (2.6)$$

In the previous formulas  $\delta_{ij}$  identify the Kronecker delta,  $n$  is the number of peptide backbone grains,  $i, j$  are the indexes of peptide backbone grains (varying within  $n$ ), and  $k$  is the shift value. This set of matrices describing the peptide interaction library can be represented using the following compact notation:

$$L = L_{ijz} \quad (2.7)$$

where  $z$  is the index of shift matrices in the library.

To calculate the maximum similarity of shift matrices with peptide backbone matrix, the normalized cross-correlation function (NCC) was used[110]

$$NCC(p, q, z) = \frac{\sum_{i=0}^{RES-1} \sum_{j=0}^{RES-1} BB(i+p*RES)(j+q*RES)*L(i,j,z)}{\sqrt{\sum_{i=0}^{RES-1} \sum_{j=0}^{RES-1} BB(i+p*RES)(j+q*RES)} \sqrt{\sum_{i=0}^{RES-1} \sum_{j=0}^{RES-1} L(i,j,z)}} \quad (2.8)$$

$Z$  is the index of the shift matrix  $L_{ijz}$  that maximize the value of NCC function.  $P$  and  $q$  denote the area of the BB matrix corresponding to the peptide backbone contact matrix.

Each element of the strand potential  $\beta$ -interaction matrix, describing mutual alignment between couples of strands, is defined as follows:

$$P_{pq} = Z \quad (2.9)$$

### 2.3.6 $\beta$ -Sheet Reconstruction via Morphoscanner

Flat and twisted  $\beta$ -sheet structures are detected by Morphoscanner by using the backbone contact and the strand interaction matrices, i.e., handling the peptidic system as 2D-lattice graph. In detail, the algorithm identifies a triplet of strands making a  $\beta$ -structure. It calculates the area of the system backbone contact matrix, corresponding to the interaction between the first pair of strands, and reduces this area to a row vector, as shown below

$$v_r = \left( \sum_{i=0}^n (A(i, 1)), \sum_{i=0}^n (A(i, 2)), \dots, \sum_{i=0}^n (A(i, n)) \right) \quad (2.10)$$

Morphoscanner identifies the area corresponding to the other pair of strands, giving another column vector

$$v_c = \left( \sum_{j=0}^n (A(1, j)), \sum_{j=0}^n (A(2, j)), \dots, \sum_{j=0}^n (A(n, j)) \right) \quad (2.11)$$

Finally, the projection of  $v_r$  on  $v_c$  is calculated as a dot product

$$v_p = v_r * v_c \quad (2.12)$$

The number of consecutive residues defining a structuring  $\beta$ -sheet along the covalent bonds direction is calculated as the maximum number of elements included between two non-null elements. In this way,  $\beta$ -sheet structures are identified as curved rectangular 2D-lattices whose dimensions are defined by strands and by the number of backbone grains.

## 2.4 RESULTS

### 2.4.1 Morphoscanner

Network analysis and graph theory have found many applications in the study of protein structures and dynamics. Many studies focused on the development of algorithms for recognition or prediction of secondary structures such as  $\alpha$ -helix and  $\beta$ -sheet arrangements. Due to of the large number of information to be taken into account (e.g., solvent accessibility, contact potentials, residue types), however, the main application of the currently available algorithms consists in the analysis of single Protein Data Bank (PDB) structures.[111][112][113][114] Indeed, many software packages cannot be applied to analyze molecular dynamics (MD) trajectories. Furthermore, currently available MD analysis tools for secondary structure analysis do not include a software adaptable to different coarsening levels of the simulated systems.[115][116][117] To identify  $\beta$ -sheet arrangements and to study their relative alignments in MD simulations we developed the Morphoscanner tool. The classical flat  $\beta$ -sheet arrangement was first described by Pauling and Corey as a rectangular flat shape. However, crystallographic studies showed that  $\beta$ -sheets tend to fold into saddle-shaped surfaces as result of the interplay of individual peptide twisting and inter-chain hydrogen bonding. While the recognition of the hydrogen bond pattern is important for the identification of  $\beta$ -structures, hydrogen bonds (H-bonds) are sometimes not explicitly modeled in MD models. To identify both flat and twisted arrangements compatible with  $\beta$ -sheets, Morphoscanner represents the peptide system as a 2D-lattice graph defined on two axes[116][118]: one runs parallel to the backbone direction, the other one goes parallel to the H-bonds direction. The edges along backbone direction represent covalent bonds. Instead, each edge along H-bonds direction represents a  $\beta$ -contact if the center-of-masses of two backbone group-of-atoms belonging to different peptides are closer than 4.7–5.3 Å, which is the typical inter  $\beta$ -strand distance in  $\beta$ -sheet structures.[119] The  $\beta$ -contacts network has been numerically represented trough a matrix (dubbed BB matrix) which is used to dynamically rationalize the global and local amount of the “in & out-of-register” mutual disposition of strands in the system.[120] For this purpose, the BB matrix has been coarsened from residue-to-residue to strand-to-strand interaction level, thereby yielding a strand potential  $\beta$ -interaction matrix named P matrix. Such “potential  $\beta$ -interaction” is used to underline that the topological organizations identified by Morphoscanner are compatible with  $\beta$ -structures. For sake of brevity “ $\beta$ -interactions” will be used along the text instead of “potential  $\beta$ -interactions.” The calculation of  $\beta$ -interactions was achieved through a pattern-matching algorithm comparing the BB matrix with a set of shift matrices describing all possible mutual alignment between two strands.[121] Indeed, each shift matrix describes a single mutual alignment of two adjacent strands in function of the k parameter



called shift value indicating their respective degree of sliding. For sake of clarity the possible parallel and antiparallel alignments (with positive or negative shifts) of the tested peptides are represented in 8.7 and 8.8. The dynamic reconstruction of topologies compatible with  $\beta$ -structuring has been faced with a dynamic multilayer network approach.[122] The interaction network formed by all residues in the system is investigated using the  $\beta$ -contacts (BB matrix) and  $\beta$ -interactions (P matrix), then the potential  $\beta$ -structures are identified through the following heuristic: 1) a triplet of consecutively adjacent strands is identified in the P matrix, 2) and that same triplet has to satisfy in the BB matrix the minimum conditions for the number and distribution of inter-strands H-bonds. In brief, in a triplet of strands, the same portion of one strand must form a minimum of three  $\beta$ -contacts with each of two neighboring strands. The iteration of such continuity criteria allows to identify both stable and evolving  $\beta$ -sheets.

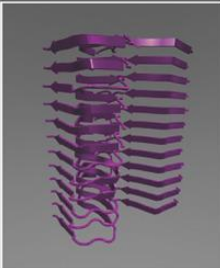
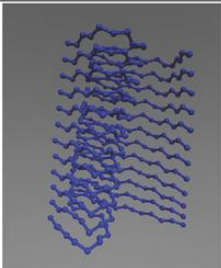
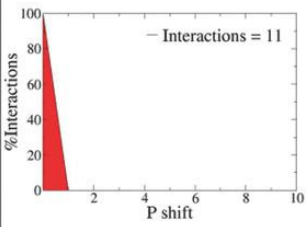

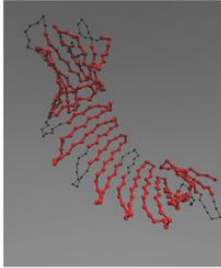
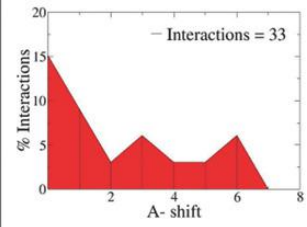
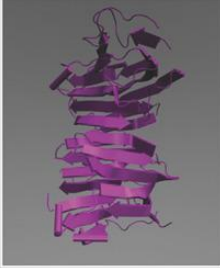
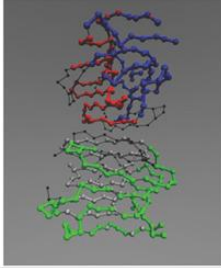
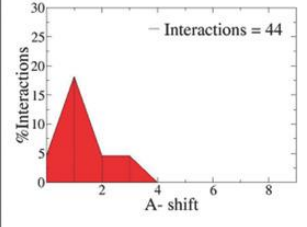
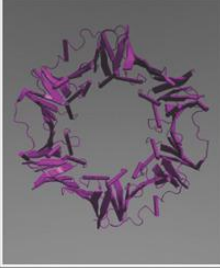
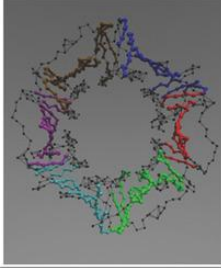
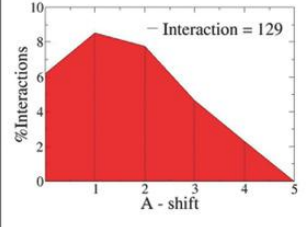
## 2.4.2 Morhoscanner Validation

The primary input for Morphoscanner is a series of contact map derived from PDB structures or molecular dynamics trajectories. Morphoscanner requires the following information: the number of strands (S) and the number of amino-acid residues per strands (strand length, SL) in which the protein sequence should be divided. Morphoscanner returns different outputs and calculates the  $\beta$ -strand percentage (%Ms) as follows:

$$\%Ms = \frac{\text{Number of } \beta\text{-strands}}{\text{Number of strands}} * 100 \quad (2.13)$$

Also, we introduced an intuitive graphical representation called “shift profile” in order to highlight the preferential arrangement of strands. To validate Morphoscanner we analyzed some protein structures as reported in Figure 2.1. As our main focus was to characterize coarse-grained systems of SAPs, protein structures from PDB were CG-mapped according to the MARTINI model and subsequently analyzed using Morphoscanner (given the intrinsic versatility of Morphoscanner, this procedure could have been performed on other levels of structural coarsening). Thanks to web server STRIDE, the secondary structures assignment for each PDB structure could be readily computed. The STRIDE output files were evaluated through an in-house developed “R script” which works similarly to Morphoscanner. The above cited script returns the  $\beta$ -strand percentage (%S\*), similarly to the Morphoscanner output

$$\%S^* = \frac{\text{Number of } \beta\text{-strands}}{\text{Number of strands}} * 100 \quad (2.14)$$

PDB_ID	VMD	Morphoscanner	% $\beta$ -structure	Predominant $\beta$ -sheet profile
2mxu 42-Residue Beta Amyloid Fibril			%S* = 100 %Ms = 100	
2fkg Engineered OspA			%S* = 85 %Ms = 77	
1d2s (BA) Laminin G-like domain			%S* = 88 %Ms = 91	
3bep (BA) <i>E. Coli</i> beta clamp			%S* = 56 %Ms = 56	

**FIGURE 2.1: Morphoscanner validation on different protein structures.** A series of PDB structures were analyzed with STRIDE-based R script and Morphoscanner. In the first column, the reference PDB structures are represented as cartoon using VMD. In the second column, CG structures are visualized highlighting  $\beta$ -sheets identified through Morphoscanner.  $\beta$ -strand percentages calculated via R script (%S\*) and Morphoscanner (%MS) are shown in the third column. In addition, shift profiles were used to quantify strand displacement in each structure. In the last column we depicted just the predominant shift profile. P = parallel alignment; A+ = antiparallel alignment with positive shift; A- = antiparallel alignment with negative shift. The analyses of 2mxu (SL = 32, S = 12) were in agreement and showed that strands were parallel aligned. In 2fkg (SL = 9, S = 35) strands were preferentially antiparallel aligned. The same conclusions were reached for 1d2s (SL = 10, S = 34) and 3bep (SL = 6, S = 122) analysis.

The comparison between %S\* and %Ms was used to determine if Morphoscanner successfully identified  $\beta$ -sheet structures.

Amyloid plaques are a defining characteristic of Alzheimer's disease. The A $\beta$  (1-42) fibrils is the initial and predominant constituent of amyloid plaques. We investigated the A $\beta$  (1-42) amyloid fibrils (2mxu) structure. To analyze this structure, SL and S were set to values of 32 and 12, respectively. The ssNMR analyses of A $\beta$  (1-42) amyloid fibrils revealed parallel  $\beta$ -strands arrangement.[123] The Morphoscanner analyses were fully in agreement with the abovementioned structural investigations, and they were confirmed by a STRIDE analysis of PDB structures (%S\* = 100, %Ms = 100), as shown in Figure 2.1. Indeed, all the potential  $\beta$ -sheet structures showed a preferential parallel in-register alignment.

We further tested Morphoscanner on an engineered Boriella OspA structure (2fkg), a  $\beta$ -sheet rich self-assembly mimicry. Its structure consists of  $\beta$ -hairpin repeats connected by turn motifs.[124] To analyze the 2fkg structures, SL and S were set to 9 and 35, respectively. The analyses through STRIDE and Morphoscanner provided similar results (%S\* = 85, %Ms = 77). In agreement with structural analysis performed by Makabe et al., Morphoscanner identified an antiparallel out-of-register  $\beta$ -strands organization (see Figure 2.1; Figure 2.2). In addition,  $\beta$ -sheet profiles revealed a different progressive strand displacement accountable by twisting and bending between different strands.

Morphoscanner was also tested on different biological assemblies that have pivotal roles in diverse metabolic pathways. Laminin are high-molecular weight proteins of the extra-cellular matrix and constitute the biologically active part of the basal lamina, influencing cell differentiation, migration, and adhesion. These proteins consist of different subunits comprising the lamin-g-like module (see 1d2s in Fig. 2.1) which mediates the binding

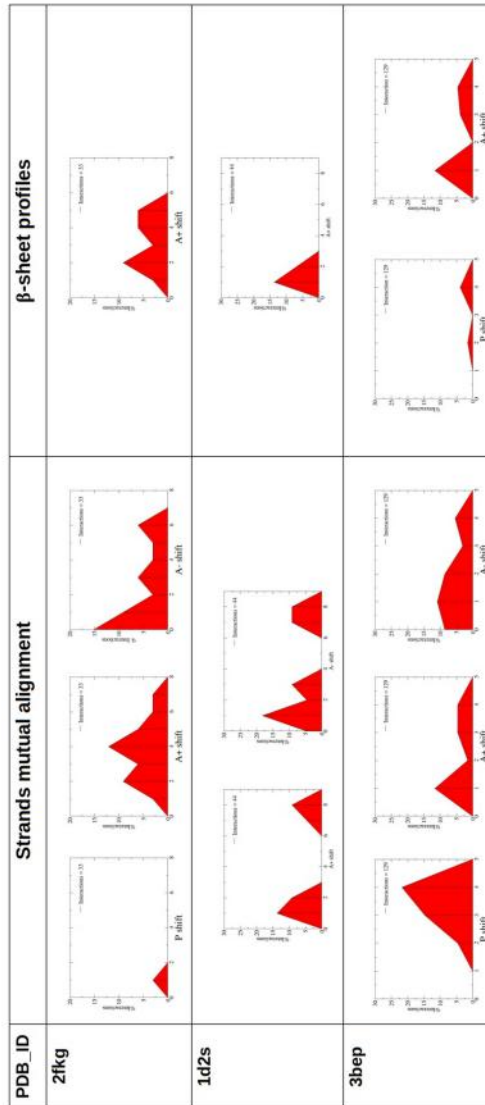


FIGURE 2.2: **Shift profiles of the proteins** shown in 2.1 Different PDB structures, subsequently CG-mapped, were analysed through Morphoscanner. Shift profiles indicated anti-parallel alignments of strands for 2fkg. This folding was reflected in  $\beta$ -sheet structures: indeed,  $\beta$ -strands featured mainly A+ anti-parallel alignments. In 1d2s mainly anti-parallel out-of-register strands and  $\beta$ -sheets were seen. The organization of 3bep was more complex: indeed, most strands followed a parallel alignment, while  $\beta$ -strands were preferentially anti-parallel aligned out-of-register by one-residue.

to different molecules such as heparin and the cell surface receptor alpha-dystroglycan (alpha-DG).[125] To perform the analysis of the 1d2s structure, SL and S were set to 10 and 34, respectively. The Morphoscanner and STRIDE analyses reported the same results (%S\* = 88, %MS = 91). In addition, as demonstrated by crystallographic analyses, Morphoscanner revealed a preferential antiparallel alignment among potential  $\beta$ -strands (see Figure 2.2).

*Escherichia coli*  $\beta$ -clamp is a subunit of the DNA polymerase III holoenzyme which consists of two identical subunits, made of 366 residues each.[126] To obtain a periodic division of 3bep structure, SL and S were set to 6 and 122, respectively. Morphoscanner identified the antiparallel  $\beta$ -sheet structures, as shown in Figure 2.1; Figure 2.2, which could be perfectly superimposed to  $\beta$ -sheet representation obtained by VMD. This was also demonstrated by comparison between Morphoscanner and STRIDE statistics (%S\* = 56, %Ms = 56), as shown in Figure 2.1.

### 2.4.3 Modeling of Assembling Systems: BMHP1-Derived SAPs, CAPs and (*LDLK*)<sub>3</sub>

Looking for a broad SAP analysis, CG-MD simulations were used to study the self-assembling propensity of seven punctually mutated BMHP1-derived SAPs, the almost neutral (*LDLK*)<sub>3</sub> SAP and the two complementary charged (*LDLD*)<sub>3</sub> + (*LKLK*)<sub>3</sub>, CAPs (see 8.6).[91][127][24] Systems comprised a total of identical 100 peptides for BMHP1-derived SAPs and (*LDLK*)<sub>3</sub>, and 50 plus 50 oppositely charged peptides in case of mixed CAPs.

In this work molecular interactions in CG-MD simulations were modeled by the MARTINI force field that has recently showed promising potential for the high-throughput screenings of SAPs.[50][59][58] In MARTINI, four heavy atoms are usually represented by one CG bead, while a lower ratio is used for atoms involved in rings (See Fig. 2.3). Bonded interactions are described with bond, angle and dihedral energy functions, while non-bonded interactions are described through Lennard-Jones and Coulomb functions. Given that some of the BMHP1-derived SAPs include N-terminal Biotin-tag, which was not yet available for the MARTINI force-field, we parametrized the biotin tag as follows: structural and interaction parameters were extrapolated from previous UA simulations and validated through octanol/water partition coefficient (logP) calculations. Experimental and calculated logP values did not show significant differences (See Sections 8.1 and 8.2).[91][50][59]

Notably, in MARTINI the secondary structure of molecules is fixed throughout the simulation, therefore the choice of the secondary structure (SS) parameters is crucial for the reliability of the modeled system. A fully extended secondary structure was adopted for

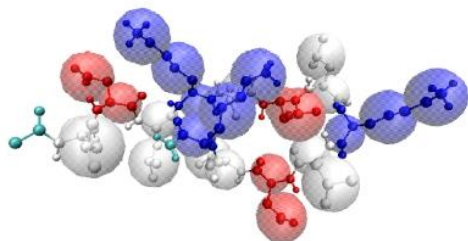
both  $(LDLK)_3$  and CAPs because of 1) the presence of equally spaced identical or opposite charges along the same short peptides and 2) their typical  $\beta$ -sheet signature in circular dichroism spectra (See Fig. 2.3).[\[24\]](#)[\[127\]](#)

In case of BMHP1-derived SAPs, in line with previously published works, the chosen secondary structure assignment was initially derived by comparing united atom (UA) and CG simulations of octameric systems.[\[90\]](#)[\[19\]](#)[\[91\]](#)[\[128\]](#) In CG simulations of octamers, three different secondary structure sets (all extended, all coil or sampled conformational distribution of monomers in UA simulations) were combined with two starting structures distributions: all extended and sampled configurations of monomers in UA. After comparing gyration radius, aggregation order, and alignment degree (see the Section 2.3.2 for details and Figures 8.9, 8.10, 8.11) of UA and CG simulations of octamers, we chose fully extended secondary structures and sampled structural configurations for the subsequent CG simulations of BMHP1-derived peptides 100-mer systems.[\[59\]](#)

## MARTINI mapping and conformations of $(LDLK)_3$

A)

**Sampled Conformation**



A<sub>I</sub>) Secondary structure parameters:

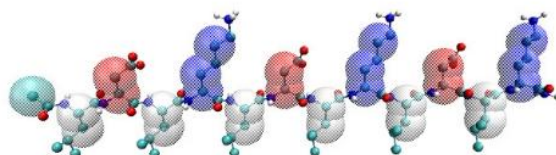
**CCTTTCTTTCCC**

A<sub>II</sub>) Backbone type assignment:

**P5-P5-Nda-Nda-Nda-P5-Nda-Nda-Nda-P5-P5-P5**

B)

**Fully-extended conformation**



B<sub>I</sub>) Secondary structure parameters:

**EEEEEEEEEEEE**

B<sub>II</sub>) Backbone type assignment:

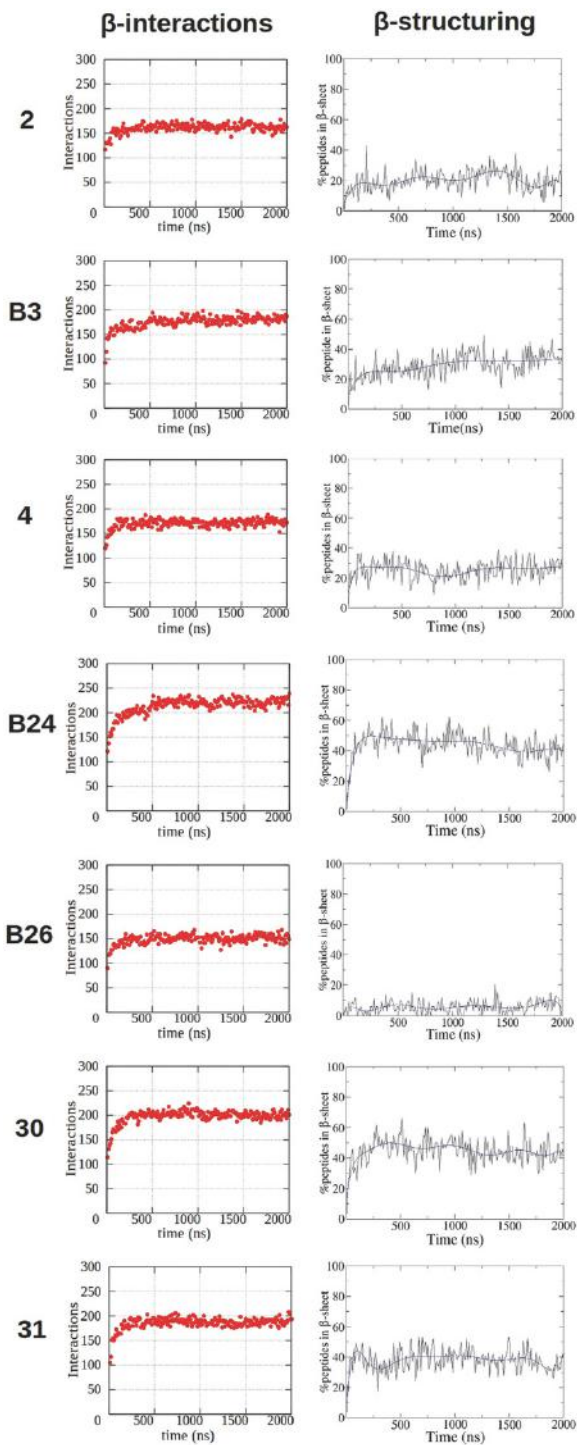
**Nda-Nda-Nda-Nda-Nda-Nda-Nda-Nda-Nda-Nda-Nda-Nda-Nda-Nda-Nda**

FIGURE 2.3: **Coarse-grained model of  $(LDLK)_3$  peptide.** MARTINI CG-mapped model of  $(LDLK)_3$  monomers, superimposed on the atomistic models. Each CG bead represents four heavy atoms (C,N,O,S) and the related hydrogen. The assignment of secondary structure parameters limits the accessible conformation of peptides. The final conformation of peptide monomers can be classified as **Sampled** or **Fully-extended**, as shown in *A* and *B* respectively. As shown in *A<sub>I</sub>* and *A<sub>II</sub>*, the assignment of coil secondary structure parameters (*C*) implies polar backbone type (*P5*, MARTINI bead type), not capable of forming hydrogen bonds. Instead, as shown in *B<sub>I</sub>* and *B<sub>II</sub>*, the assignment of extended secondary structure parameters (*E* or *T*) implies backbone atom type which mimic the formation of hydrogen bonds (*Nda*, MARTINI bead type).

#### 2.4.4 Using Morphoscanner for the Analysis of Self-Assembled Peptidic Aggregates

In MARTINI CG-MD simulations, the fixed SS parameters allow to discriminate between various secondary structures, however, they do not allow to detect any secondary structure transitions. Notwithstanding this limitation, it is possible to evaluate the movement of secondary structure elements in the simulated systems.[50][59] Morphoscanner was used for the analyses of the CG-MD simulations of SAPs in 8.6 with extended secondary structure parameters. S and SL parameters were set equal to the number of peptides and of backbone grains per peptide, respectively. The organization of the simulated systems over time was schematized into a count of both total the  $\beta$ -interactions in the system and the percentage of peptides taking part in potential  $\beta$ -sheets formation (Figures 2.4 and 2.5).





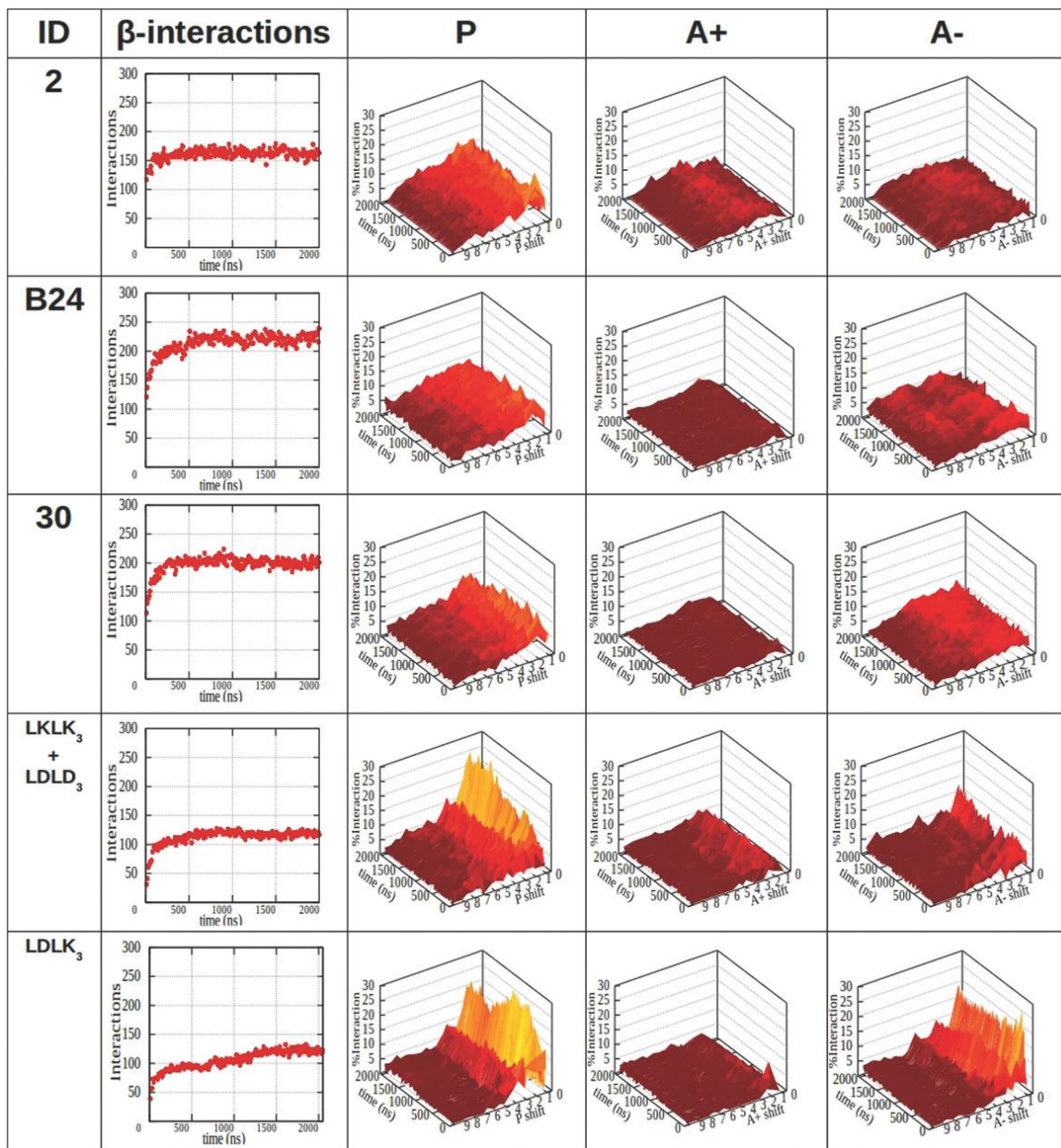
**FIGURE 2.4:  $\beta$ -interactions and  $\beta$ -structuring of SAPs in CG-MD simulations with extended SS parameters.** The onset of  $\beta$ -interactions does not warrant the formation of  $\beta$ -sheet structures. This is clearly evident from the comparison among peptides 2,4 and B26. The above-mentioned SAPs reached the same number of  $\beta$ -interactions, but B26 had the lowest degree of  $\beta$ -structuring propensity, followed by 2 and 4. Such features are attributable to their sequences and, in particular, to N-terminal functionalization.

We used a shift profile representation over time (Figures 2.4 and 2.5) to track peptides preferential arrangement during self-assembling. Lastly, the shift profile approach was adopted to monitor peptides arrangement within  $\beta$ -sheets structures (Figure 8.12).

The total number of  $\beta$ -interactions in BMHP1-derived SAPs, CAPs, and  $(LDLK)_3$  was 150 to 240. B24 showed the highest number  $\beta$ -interactions, while the lowest numbers were found in CAPs and  $(LDLK)_3$  (Figure 2.5; Figure 8.12), caused by different peptides arrangement within oligomers. CAPs and  $(LDLK)_3$  assembled into bilayered structures made of peptides packed side-by-side. Instead peptide B24, similarly to other BMHP1-derived SAPs, assembled in ovoid oligomers where interactions among neighboring peptides were favored. BMHP1-derived SAPs preferentially aligned in parallel out-of-register of one residue ( $\approx 10$ -15% of total  $\beta$ -interactions).

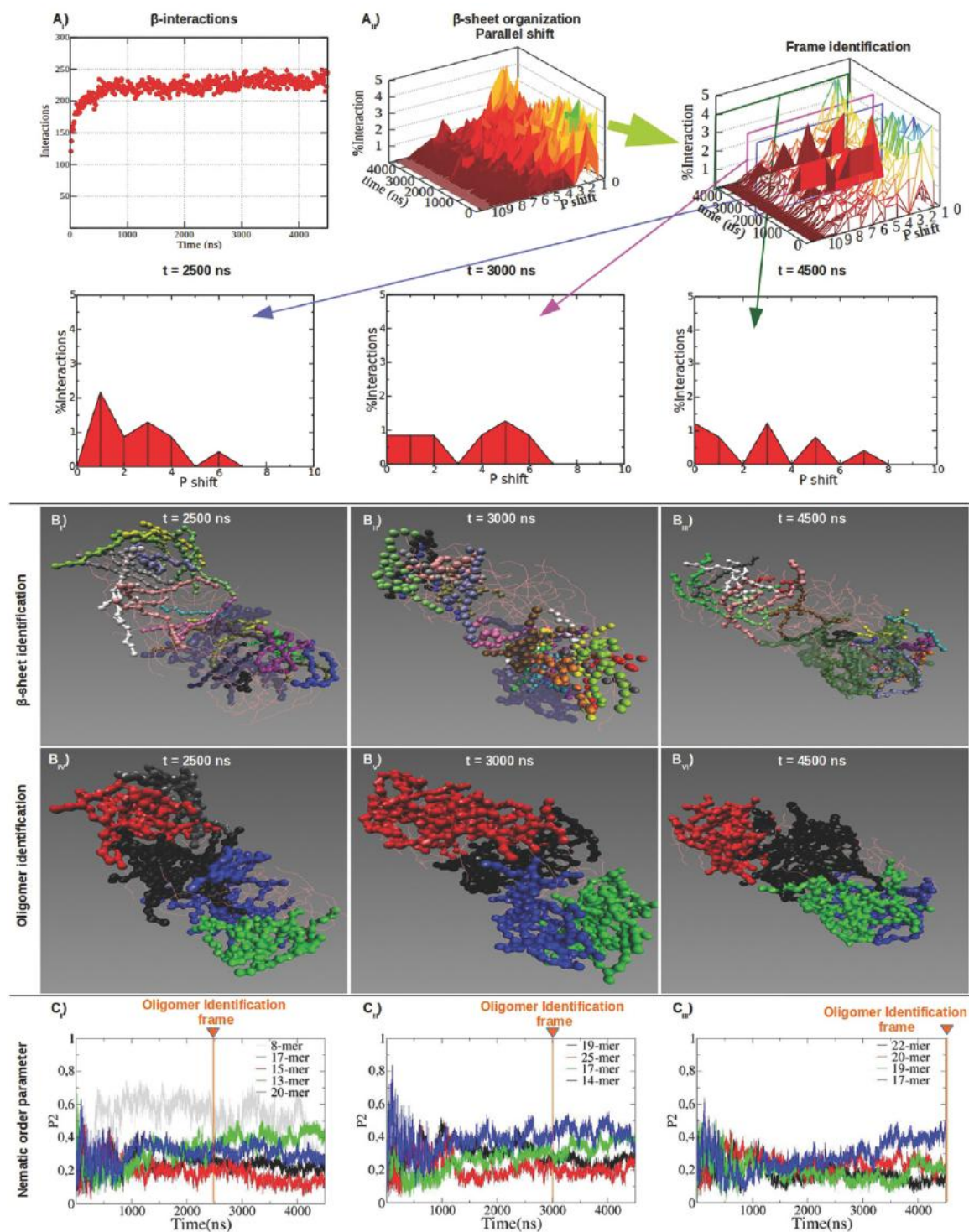
CAPs and  $(LDLK)_3$  were preferentially shifted by one residue in P ( $\approx 10\%$ ) and in A-alignments ( $\approx 25\%$ ). As shown in 2.5 and Figure 8.12, all the potential  $\beta$ -interactions in aggregates formed by CAPs took part in  $\beta$ -sheet structures. Indeed, all peptides contributed to  $\beta$ -sheet formation in all simulations within 50 ns (data not shown).

BMHP1-derived peptides generally showed a variable  $\beta$ -structuring propensity related to the punctual mutations in their sequences (see 8.6). SAP 2, made of the BMHP1 motif and a triplet of Gly, did not show a good *beta*-structuring propensity. Only 10% of the total simulated SAP 2 peptides took part in  $\beta$ -sheets formation (Figure 2.2) and they preferentially aligned in parallel out-of-register by 1 residue (Figure 2.6; Figures 8.13 and 8.14). The introduction of Trp at the N-terminus improved the  $\beta$ -structuring propensity of SAP 4, with 25% of peptides involved in  $\beta$ -structuring (8.12). Biotinylation increased the  $\beta$ -sheet structuring propensity in B3: indeed 30% of peptides were involved in  $\beta$ -sheets structures (Figure 2.4). B24 showed the highest propensity to  $\beta$ -sheet structuring.



**FIGURE 2.5: Analysis of mutual alignment of peptides featuring diverse self-assembling propensities.** Peptides mutual alignment shift profiles of SAP 2, B24, and 30 which were simulated with extended secondary structure parameters (see 8.6). P refers to parallel alignment, A+ to antiparallel alignment with positive shift, A- to antiparallel alignment with negative shift. BMHP1-derived SAPs preferentially shifted by one residue in P alignment, but (LDLK)<sub>3</sub> and CAPs showed much stronger alignment in both P and A- alignments at one residue shift. This feature was likely due to the electrostatic interactions among their complementary charged side-chains. On the other hand, the mutation of Pro and Ser with Ala increased the number of  $\beta$ -interactions in B24 and 30 assemblies if compared to SAP 2 (see 8.6). Biotinylation also slightly improved  $\beta$ -sheet structuration propensity in B24 in respect to 30. Notably, CAPs and (LDLK)<sub>3</sub> showed less  $\beta$ -interactions than BMHP1-derived SAPs. This was due to the different shapes of supramolecular aggregates; (LDLK)<sub>3</sub> and CAPS formed bilayered  $\beta$ -sheet-rich aggregates. BMHP1-derived SAPs formed ovoid aggregates where peptide strands could simultaneously interact with multiple surrounding peptides.

Indeed, 50% of B24 peptides fell within  $\beta$ -sheets (Figure 2.4), and the large part of pairs of  $\beta$ -strands were preferentially aligned in parallel out-of-register with neighboring pairs by one and two residues as shown in Figure 2.1 and Figure 8.14. These increments were ascribable to both the N-terminal biotinylation and the substitution of Pro and Ser with Ala. The substitution of Btn with Trp decreased the formation of stable  $\beta$ -sheet structures in peptide 30 in comparison with B24 (Figure 2.4): even if they showed similar preferential alignments (Figure 2.5; Figure 8.14) just 40% of peptides were involved in  $\beta$ -sheet structures. In the case of peptide 31 the first Ser of the BMHP1 motif was mutated with Ala, but apparently, when compared to SAP 30, did not alter the  $\beta$ -structuring propensity of the system (Figure 2.4). The introduction of biotin at the N-terminal position did not improve  $\beta$ -structuring propensity in B26 (2.4): only 10% of peptides were part of  $\beta$ -sheets. As shown in Figures 8.13 and 8.14, B26 peptides were preferentially aligned in parallel out-of-register by one residue and nine residues, likely because of preferential pairings between Lys backbone and Biotin amide groups.[129][130]





**FIGURE 2.6: Structural characterization of B24 molten particles at different timeframes.** B24 showed good  $\beta$ -sheet propensity ( $A_I$ ) characterized by parallel out-of-register  $\beta$ -strands ( $A_{II}$ ). Parallel  $\beta$ -sheets shift profiles became wider between 2500 and 4500 ns: this was matched by changes in  $\beta$ -sheet topology ( $B_{I,II,III}$ ) and influenced the identification of oligomers ( $B_{IV,V,VI}$ ). P2 was calculated for the identified oligomers ( $C_{I,II,III}$ ). Same colors between  $B_{IV,V,VI}$  and  $C_{I,II,III}$  point at the same oligomers identified at the selected timeframes. P2 values of the identified oligomers were calculated for all timeframes. The identified oligomers ranged from 8-mer to 25-mer aggregates. Interestingly, oligomers ( $B_{IV,V,VI}$ ) featuring higher order (or P2 values in  $C_{I,II,III}$ ) showed a large presence of  $\beta$ -sheets ( $B_{I,II,III}$ ).

### 2.4.5 Peptide Oligomer Identification

To more efficiently describe the onset and subsequent arrangement of “seeds of self-assembling” within the molten globules we combined our recently introduced methodology with classical analyses, such as radius of gyration and nematic order parameter.[116] However, in big system simulations locally ordered aggregates may not be described by cumulative parameters of the overall system: therefore, it was necessary to track the oligomers formed during the self-assembling process. Indeed, others proposed a nucleation-dependent polymerization model to describe fibril formation from monomeric peptides to heterogeneous nuclei (or peptide micelles) and finally mature fibrils.[131][94][132] Oligomer identification required the implementation of a “nearest neighbor algorithm” on binary entries obtained by thresholding distances among peptide center-of-masses. Threshold distance was set at 1.1 nm as in XRD spectra it represents the typical equatorial distance of cross- $\beta$  structures.[132] In the so-obtained contact matrix 1 value points at a distance falling within the chosen range, thus giving a “forest” of ones.[133] The algorithm first explores each subtree representing neighboring center-of-masses, then backtracks and provides the peptides constituting each oligomer.[134]

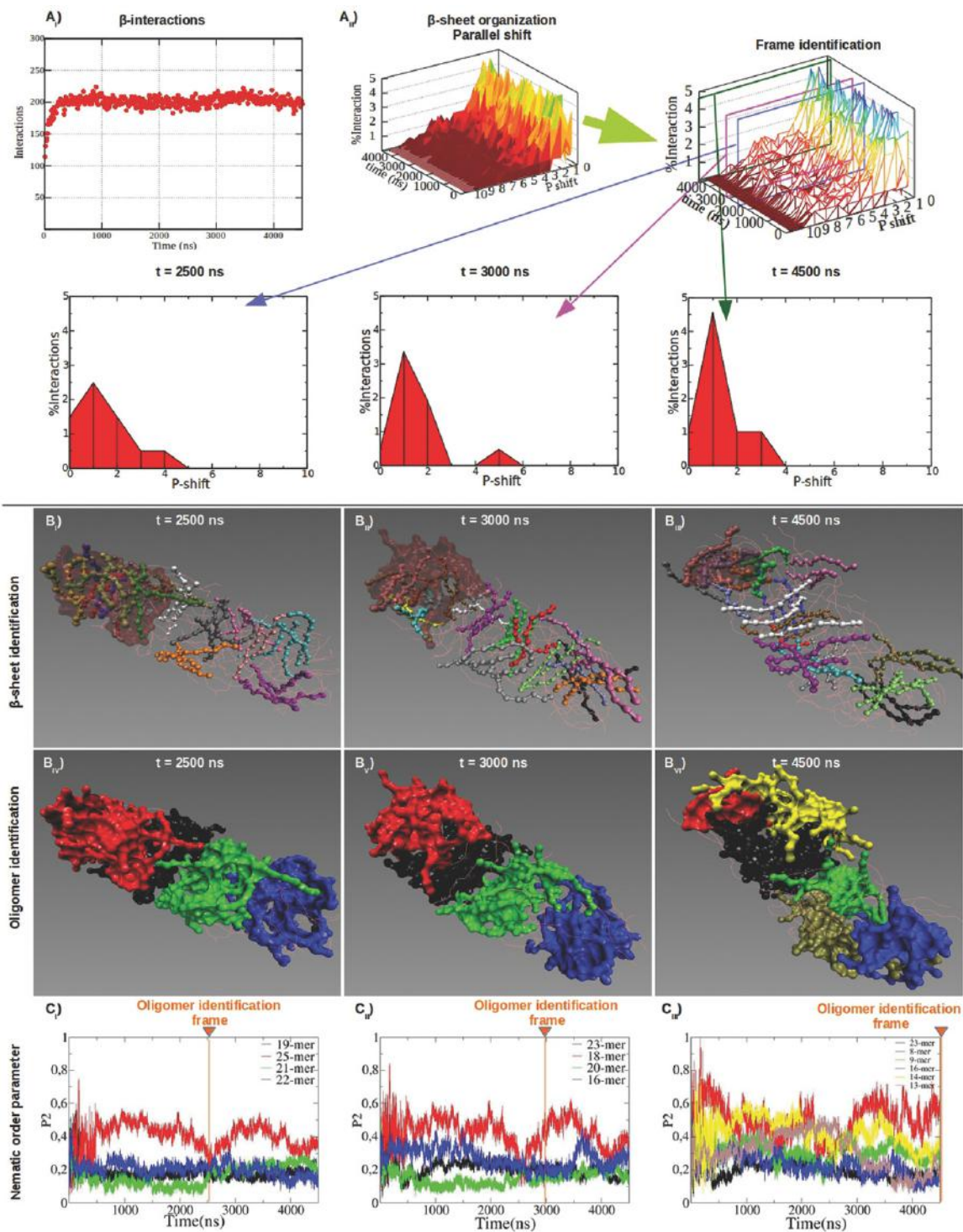
### 2.4.6 Tracking Oligomers Arrangement Dynamics and $\beta$ -Structures Organization

The combined use of the Morphoscanner and of the oligomer identifier algorithm allowed to detect oligomeric species with different local structural features. Then, we obtained a more detailed analysis of the  $\beta$ -structuring propensity of the simulated systems. As previously mentioned peptide B24 displayed good  $\beta$ -structuring propensity (Figure 2.4) and the total amount of  $\beta$ -interactions stabilized after 500 ns. However, Figure 2.6 $A_{II}$  shows that  $\beta$ -sheets changed their internal organization (see also Figure 8.15); at 2500 ns  $\beta$ -strands were

preferentially aligned in parallel out-of-register by one residue, but this was not the case at 3000 ns and at 4500 ns. Oligomers showed limited variations in global morphology and mutual disposition (Figure 2.6 $B_{IV,V,VI}$ ) over time. As shown in Figure 2.6C, the nematic order parameter P2 of almost all identified oligomers at different time-points fluctuated below 0.5: this was indicative of a modest (but still developing) peptide arrangement over time.

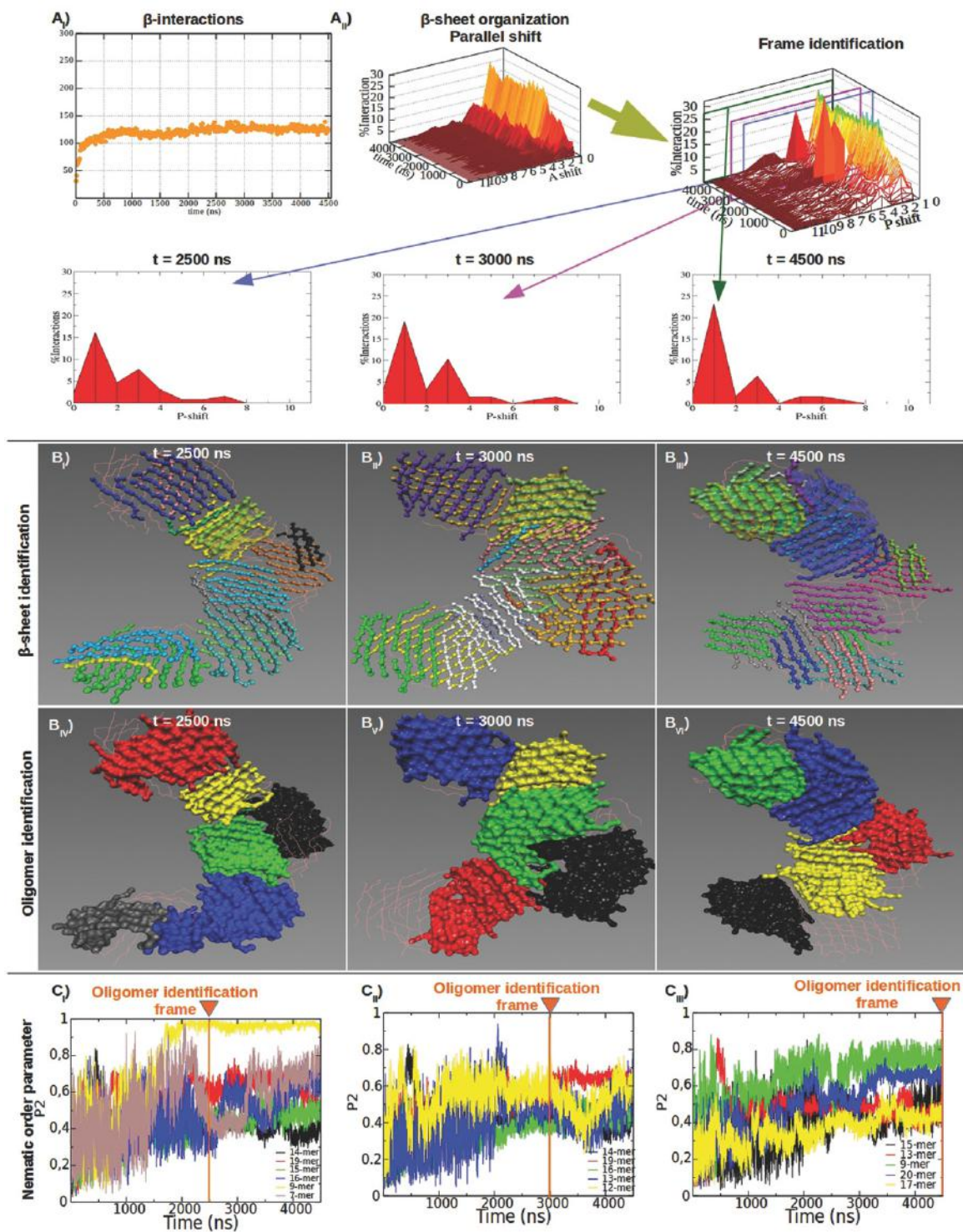
The same analysis workflow was applied to peptide 30. In agreement with previous empirical studies,[19] the mutation of Biotin with Trp in peptide 30 yielded to a more stable  $\beta$ -structuring (Figure 2.7; Figure 8.16) than in B24. Indeed, from the early stage of SAP 30 self-assembling,  $\beta$ -strands were preferentially aligned in parallel out-of-register by one residue (Figure 2.7A; Figure 8.16). In addition, more similar oligomers of peptide 30 were identified at different time-points (Figure 2.7 $B_{IV,V,VI}$ ) and their calculated order was mostly higher than in B24 (Figure 2.7C).

CAPs, thanks to their alternated opposite charged side-chains, self-assembled into stable  $\beta$ -sheets (Figure 2.8A), forming a “patchwork” of bilayered aggregates.[24] CAPs formed bilayered oligomers (Figure 2.8 $B_{IV,V,VI}$ ) characterized by a significant presence of  $\beta$ -sheets (Figure 2.8 $B_{I,II,III}$ ) and by an high internal alignment (Figure 2.8C). This behavior was dictated by strong electrostatic interactions among oppositely charged side-chains fostering the formation of well-defined  $\beta$ -structures. Nonetheless, variable oligomer identification and unstable P2 values revealed a still ongoing arrangement of the system given by a persistent “sliding” of the patches composing the two layers. The same tendencies were also observed for  $LDLK_3$  peptides. Indeed, as reported in our previous work, such peptides formed  $\beta$ -structured and highly ordered bilayered aggregates.[21]





**FIGURE 2.7: Structural characterization of 30 molten particles at different timeframes.** SAP 30 had a good  $\beta$ -structuring propensity ( $A_I$ ) and peptides were mutually aligned in parallel out-of-register by one residue within  $\beta$ -sheets ( $A_{II}$ ). Shift profiles of parallel  $\beta$ -sheets became sharper after 2500 ns but did not vary as extensively as in B24. The topology of  $\beta$ -sheets changed slightly ( $B_{I,II,III}$ ): this was reflected in a modest variation of the identified oligomers at different timeframes ( $B_{IV,V,VI}$ ). Same colours between  $B_{IV,V,VI}$  and  $C_{I,II,III}$  point at the same oligomers identified at the selected timeframes. P2 values of the identified oligomers were calculated for all timeframes. More ordered oligomers ( $C_{I,II,III}$ ) were characterized by stronger presence  $\beta$ -sheet structures ( $B_{I,II,III}$ ). The oligomers identified at 4500 ns were more heterogeneous and with higher P2 values ( $C_{I,II,III}$ ): big oligomers identified in previous timeframes were here split in two or more subgroups.



**FIGURE 2.8: Structural characterization of CAPs  $(LDDL)_3 + (LKLK)_3$  molten particles at different timeframes.** CAPs established less  $\beta$ -interactions ( $A_I$ ) than in BMHP1-derived SAPs and  $\beta$ -strands were preferentially aligned in parallel out-of-register by one residue throughout the simulations ( $A_{II}$ ). CAPs formed stable  $\beta$ -sheet structures ( $B_{I,II,III}$ ) mainly matching oligomers distribution ( $B_{IV,V,VI}$ ).  $\beta$ -sheets paired into bilayered aggregates but with different orientations. Same colours between  $B_{IV,V,VI}$  and  $C_{I,II,III}$  point at the same oligomers identified at the selected timeframes. P2 values of the identified oligomers were calculated for all timeframes. The identified oligomers displayed a superior order (values of P2) and a slow but ongoing trend of increments toward more ordered assemblies ( $C_{I,II,III}$ ).

## 2.5 CONCLUSIONS

Morphoscanner, a novel software developed for secondary structure analysis of differently coarsened simulations of proteinaceous structures, combines into a single “suite” the advantages of both MD analysis and secondary structures pattern recognition tools.[113][114][115][116] On previously characterized protein structures Morphoscanner recognized their  $\beta$ -sheet organization and provided new information about their relative orientation and alignment. In Morphoscanner we also included a new high-throughput workflow to investigate different facets of self-assembly: its graphical and quantitative analyses provided new insights of SAP systems evolution over time. It was possible to more efficiently elucidate the self-assembly process of BMHP1-derived peptides,  $(LDLK)_3$ , and CAPs. BMHP1-derived SAPs self-assembled into molten particles mostly composed of peptides aligned in parallel out-of-register, a thermodynamically stable alignment that however may prevent any subsequent evolution toward well-structured nanofibers detected in previous experimental works.[19][92] On the other hand,  $(LDLK)_3$  and CAPs formed patches of anti-parallel  $\beta$ -rich aggregates evolving toward cross- $\beta$  packings, yielding to highly ordered systems compatible (at longer timeframes) with empirical observations.[24][19] Lastly, we developed a software suite useful for the analysis of molecular assembly, easily adaptable to other chemical species and coarsening levels. Indeed it can be potentially applied to the study of biological processes such as DNA, RNA hybridization or abnormal protein assembly.[131][135][136] Thus, the achieved level of characterization may turn useful in nanotechnology but also in biomolecular and astrobiological studies focused on the emerging properties of self-assembling systems.[14][15][16][1]



## Chapter 3

# Coarse-grained molecular dynamics of branched SAPs

*Adapted from* R.Pugliese, **F.Fontana**, A. Marchini, F. Gelain. "*Branched peptides integrate into self-assembled nanostructures and enhance biomechanics of peptidic hydrogels*", In: *Acta Biomaterialia*, Volume 66, Pages 258-271 (2018)

### 3.1 ABSTRACT

Self-assembling peptides (SAPs) have drawn an increasing interest in the tissue engineering community. They display unquestionable biomimetic properties, tailorability and promising biocompatibility. However their use has been hampered by poor mechanical properties making them fragile soft scaffolds.

To increase SAP hydrogel stiffness we introduced a novel strategy based on multiple ramifications of  $(LDLK)_3$ , a well-known linear SAP, connected with one or multiple *lysine knots*. Differently branched SAPs were tested by increasing the number of  $(LDLK)_3$ -like branches and by adding the neuroregenerative functional motif BMHP1 as a single branch. While pure branched peptides did not have appealing self-assembling propensity, when mixed with the corresponding linear SAP they increased the stiffness of the overall hydrogel of multiple times. Notably, optimal results (or peak) were obtained 1) at similar molar ratio (between linear and branched peptides) for all tested sequences and 2) for the branched SAPs featuring the highest number of branches made of  $(LDLK)_3$ . The functional motif BMHP1, as expected, seemed not to contribute to the increase of the storage modulus as efficiently as  $(LDLK)_3$ .

Interestingly, branched SAPs improved the  $\beta$ -sheet self-arrangement of  $(LDLK)_3$  and allowed for the formation of assembled nanofibers. Indeed in coarse-grained molecular dynamics we showed they readily integrate in the assembled aggregates providing "molecular connections" among otherwise weakly paired  $\beta$ -structures. Lastly, branched SAPs did not affect the usual response of human neural stem cells cultured on  $(LDLK)_3$ -like scaffolds *in vitro*. Hence, branched SAPs may be a valuable new tool to enhance mechanical properties of self-assembling peptide biomaterials harmlessly; as neither chemical nor enzymatic cross-linking reactions are involved. As a consequence, branched SAPs may enlarge the field of application of SAPs in tissue engineering and beyond.

### 3.2 INTRODUCTION

Over the last decade, there has been an increasing interest in regenerative medicine as the "ultimate" therapy for damaged tissues or organs. As a consequence, different scaffolds have been developed to either deliver and/or recruit cells.[137][138][139][140] Scaffolds should properly "interact" with seeded cells and host tissues, this means they should be preferably biomimetic and with adequate biomechanical properties coaxing transplanted cell differentiation and engraftment as well as host tissue ingrowth.[141][142][143] Lastly, to minimize adverse host tissue reactions and provide a physical support for the tissues surrounding the implant, scaffold mechanical properties should preferentially match those of native tissues.[141][144][145]

The use of self-assembling peptides (SAPs) has become a leading strategy in regenerative medicine, being tailorable, synthetic, bioabsorbable and highly biocompatible biomaterials. Also, they can display different functional motifs interacting with cells and proteins involved in cell signalling, thus making them biomimetic.[146][18] It is usually said that SAP "mimic" the peptide-based extracellular matrix (ECM). This is why they have been tested as fillers, hemostat solutions, wound healers or injectable scaffolds for the regeneration of dental pulp, cartilage, spinal cord injury, traumatic brain injury and infarcted heart.[147][148][149][150][151][152][153][154][155] SAP biomaterials showed promise as self-adapting scaffolds preventing haemorrhage and decreasing the harmful immune response (in case of acute injuries). SAP scaffolds created microenvironments stimulating endogenous regeneration and were also capable of spatially guide regenerating tissues.[151][153][156][157][158] Moreover, self-assembling multi-domain peptides (MDP), thanks to their ability of mimicking vascular endothelial growth factor (VEGF), promoted angiogenesis and ischemic tissue recovery by modulating the inflammation and neoangiogenesis.[159][160][161] MDP are also an effective vehicle for delivery of bioactive molecules such as IL-4, MCP-1, TGF- $\beta$ 1 and EGF, thus creating a versatile platform for tissue regeneration.[161][162][163] The self-assembling phenomenon is mainly ascribable to weak transient non-covalent interactions among packed peptide molecules: as a consequence, it yields to soft and fragile hydrogels.[21] Summarized, while storage moduli of 50 Pa–1500 Pa of linear SAPs match the stiffness of the brain (300–2000 Pa), tissues like skin (4000 Pa) and articular cartilage (20 MPa) are still beyond reach.[146][20][164][165][166]

This biomechanical limitation should be overcome to more accurately tune their properties and enlarge the number of their possible applications in tissue engineering (TE).

To this purpose, chemical cross-linking of self-assembled structures may be an interesting option but it may also bring other drawbacks like possible toxic side effects of synthetic cross-linkers and chemical reactions hardly reproducible for future clinical applications. Therefore



we introduced new-branched self-assembling peptides to be used as "molecular connectors" within and among self-assembled nanostructures made of linear SAPs. We synthesized three different branched SAPs, featuring an increasing number of self-assembling "branches" made of the well-known linear  $(LDLK)_3$ .<sup>[146][20][167][168][169][170]</sup> Coarse-grained dynamics of branched-and-linear peptide systems demonstrated an intriguing level of integration of branched SAPs within linear SAP-made nanostructures as long as the sequence of branches matches that one of linear SAPs.

### 3.3 MATERIAL AND METHODS

All-trans conformation of linear and branched peptides were generated by PyMol and mapped in accordance with MARTINI model.<sup>[50]</sup> The C- and N-terminal of peptide monomers were amidated and acetylated respectively. At neutral pH, lysine and aspartic acid side chains, because of their weak basic and acidic nature, can be considered fully protonated and deprotonated respectively. The bond parameters for coarse-grained (CG) simulation of  $N\alpha$ ,  $N\epsilon$ -di-Fmoc-Lysine has been calculated as previously reported by Rahimi *et al.*<sup>[171][59]</sup>

Peptides have been randomly distributed in explicit water cubic boxes built by using PACKMOL in order to have the correct spatial distribution of the monomers.<sup>[50]</sup> Atoms belonging to different peptides were placed at minimum distance of 10 Å far from each other (see Table 9.1 for details).

In MARTINI coarse-grained molecular dynamics (CG-MD) simulations it is necessary to define peptide secondary structures, and the abovementioned parameters, to which individual amino acid residues must evolve: we chose peptide extended conformations because of 1) the presence of equally spaced identical charges along the same short peptide chain (or branch) and 2) empiric evidences obtained from FTIR analysis.<sup>[59]</sup>

Molecular dynamics simulations were performed using the version 4.5.5 of GROMACS package.<sup>[172]</sup> Prior to the production phase, the systems underwent an equilibration phase (a 3000-steps minimization using steepest descents method) in order to eliminate high-energy interactions. The production phase was conducted in the NPT ensemble. Solutes and solvent were coupled independently to an external bath ( $T = 300$  K) with a coupling constant ( $\tau_T$ ) of 0.1 ps using v-rescale thermostat.<sup>[173]</sup> Periodic boundary conditions were imposed, and pressure was maintained at 1 bar using the Berendsen coupling.<sup>[174]</sup> The isothermal compressibility was set at  $3 \times 10^4 \text{ bar}^{-1}$  and the coupling constant ( $\tau_P$ ) was 0.1 ps. The constraints on lengths of bonds and angles with the LINCS algorithm.<sup>[175]</sup> All systems were simulated for 1500 ns using an integration time-step of 20 fs, while snapshots of individual trajectories were saved every 100 fs.

Quantification of peptide chains mutual alignment and organization of  $\beta$ -sheets within aggregates have been carried out using previously in-house developed software (2). The software was modified to analyze systems made of both linear and branched peptides. In this case for sake of simplicity we considered peptide branches as independent linear peptides (Fig. 9.1). Thus, the  $N\alpha$ ,  $N\epsilon$ -di-Fmoc-Lysine and glycine residues were not considered during the  $\beta$ -strands orientation analysis within aggregates. Data provided from this analysis has been represented with a new graphical aid named "**shift profile**". Shift profiles are three-dimensional plots with **time** on the  $x$ -axis expressed in nanoseconds, **shift values** on the  $y$ -axis and **the percentage of the total amount of interactions** on the  $z$ -axis. This graphical aid allowed us to quantify the degree of displacement among aligned peptides whose backbone center-of-masses are at distances compatible with inter-peptide H-bonds formation (See Figure 8.8).

The number of contacts among branches or linear peptides, which correspond to the possibility of forming inter-peptide H-bonds between amidic groups, has been calculated. The existence of a contact is positive if the distance between two backbone grains is less than 0.569 nm. In addition, the percentage of branched peptides involved in  $\beta$ -structuring nuclei has been calculated as follows:

$$\%Integration = \frac{NG_{\beta}}{NG_{Tot}} * 100 \quad (3.1)$$

where  $NG_{\beta}$  is the number of backbone grains which establish a contact with other backbone grains of the system and  $NG_{Tot}$  is the total number of backbone grains of branched peptides. This value provides a quantification of the integration of branched peptides in stable  $\beta$ -sheet structures.

To assess the formation of salt-bridges[176][177] and the distribution of side-chains of charged amino acids the radial distribution function was calculated as follows:

$$g_{AB}(r) = \frac{1}{\rho_B} \frac{1}{N_A} \sum_{i=0}^{N_A} \sum_{j=0}^{N_B} \frac{\delta(r_{ij} - r)}{4\pi r^2} \quad (3.2)$$

where  $\rho_B$  is the density of type-B particles averaged over all spheres (radius  $< r_{max}$ ) centered on each type-A particle.  $\delta(r_{ij} - r)$  is the Kronecker delta.  $r_{max}$  is half of the box length.

Analyses were performed by GROMACS bundle tools.

To better characterize the gyration radius and the nematic order parameter of spontaneously formed aggregates during self-assembly we identified peptides belonging to different aggregates via an in-house developed software. We performed spatial clustering on the center of mass of peptides: two peptides belonged to the same aggregate if the distance between their

centers of mass is lower than 1.1 nm, i.e. the equatorial distance between two  $\beta$ -strands in a cross- $\beta$  structure.[178] In this work, the software has been used to assess the integration of branched peptides into different peptide oligomers in order to verify their integration within different cross- $\beta$  structures.

## 3.4 RESULTS

### 3.4.1 CG-MD simulations of pure mixtures of branched peptides

Coarse-grained molecular dynamics (CG-MD) simulations have been used to investigate the mechanism of self-assembly of both pure and mixtures of linear and branched peptides. The simulated systems resembled the peptides concentration used in empiric experiments (1% w/v).

Firstly, we evaluated the aggregation and  $\beta$ -structuring propensity of pure  $(LDLK)_3$ , BMHP1-bis $(LDLK)_3$ , tris $(LDLK)_3$  and epta $(LDLK)_3$  peptides. In this set of simulations (see 9.1 for details) the systems assembled into big clusters comprising all simulated peptides: clusters showed different morphologies depending on the sequence. In the simulations of  $(LDLK)_3$  a progressive recruitment of differently oriented blocks yielded to a final aggregate constituted by a "patchwork" of peptides, where each "patch" showed backbone alignments similar to co-assembling peptides.[24] We analyzed the arrangement of the assembled peptides by taking special care to peptide mutual alignment and  $\beta$ -sheet formation. The shift profile analysis (See 8.8 for details) showed that  $(LDLK)_3$  peptides were preferentially aligned with zero-residue (15%), two-residues (15%), four-residues (10%) antiparallel shift arrangements and with one-residue (20%), three-residues (5%) parallel shift arrangements (Fig. 3.1).

These alignments are compatible with a full involvement of amines and carboxylic groups into electrostatic interactions: the periodic distribution of the charged amino acid side chains of  $(LDLK)_3$  drives the supramolecular organization into stable  $\beta$ -sheet structures displaying a hydrophilic surface and a hydrophobic pocket, as shown in Figure 3.2,  $A_I$ ,  $A_{II}$ .

On the contrary, BMHP1-bis $(LDLK)_3$  showed a poor preferential alignment 3.1  $B$  and salt-bridge formation (data not shown) likely because of an intrinsic lower propensity of BHMP1-branch to self-assemble with  $(LDLK)_3$ -branches. On the contrary, the electrostatic interactions among lysine and aspartic acid side chains of pure tris $(LDLK)_3$  did not drive the self-assembling process in a well-organized structure such as  $(LDLK)_3$  but rather in a T-shape aggregate (Fig. 3.2  $B_I$ ,  $B_{II}$ ).

The shift profiles pointed out that the three identical branches of the peptide were aligned according to zero-residue (5%), two-residues (10%), four-residues (10%) antiparallel shift arrangements and to three-residue (15%) parallel shift arrangements (Fig. 3.3 A).

The lower formation of ordered  $\beta$ -sheet structures of tris $(LDLK)_3$ , in comparison with  $(LDLK)_3$ , can be ascribed to the presence of the Lys-knots that reduced the degrees-of-freedom of the  $(LDLK)_3$ -branches.[136] Similarly, in molecular dynamics simulations of epta $(LDLK)_3$ , where the presence of Lys-knots is greater, a preferential alignment of the  $(LDLK)_3$ -branches into  $\beta$ -sheets was not detected (Fig.3.3  $B$ ) even though lysines and

aspartic acids side-chains were fully involved in the formation of salt-bridges (Fig.3.3  $C_I$ ,  $C_{II}$ ). Final outcome of these dynamics was the formation of an unstructured globular supramolecular structure. The observed "poor structuring" behavior was in accordance with low mechanical properties and shorter nanofibers formation of pure branched-peptides showed by empirical experiments.[109]

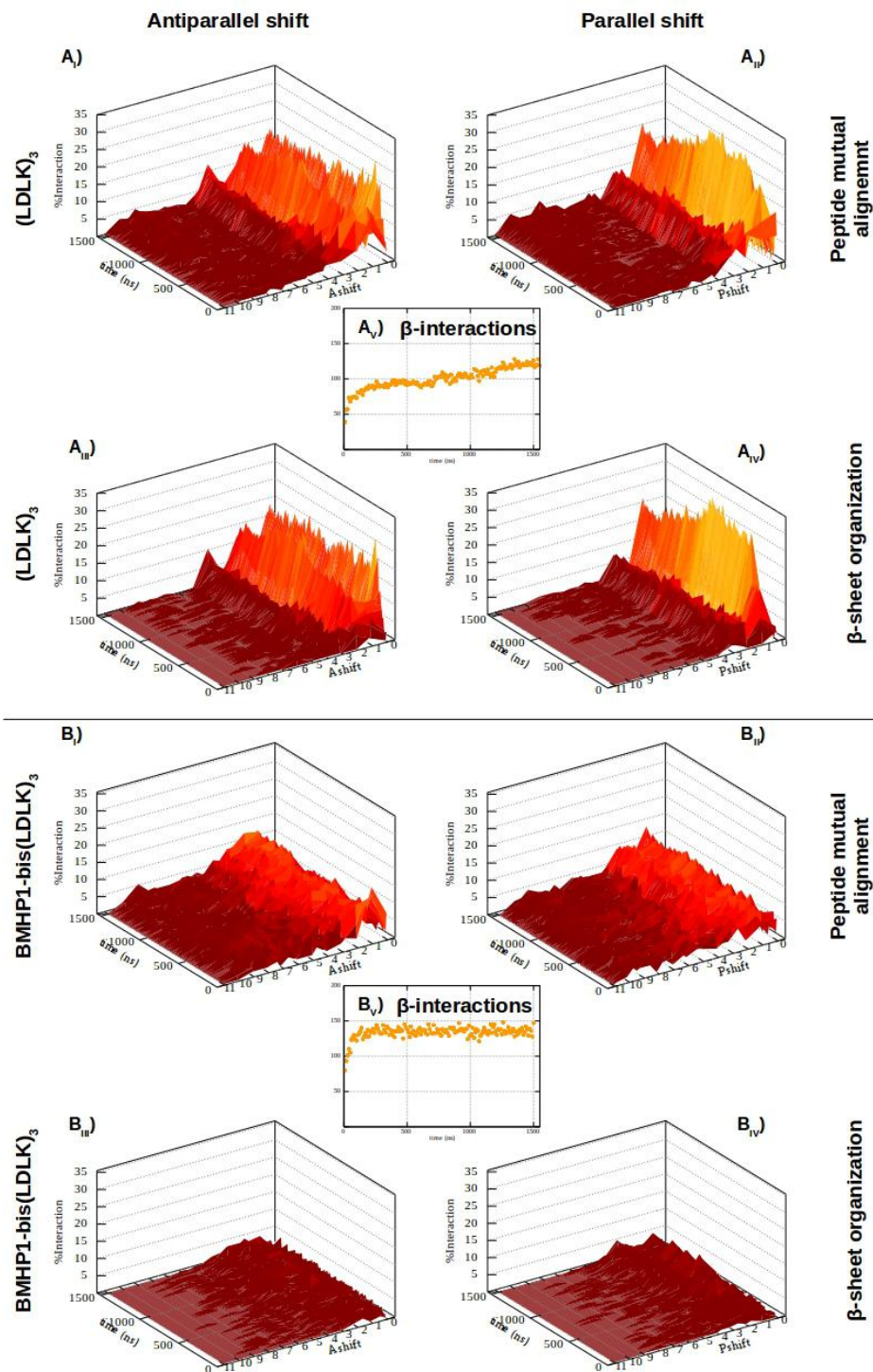


FIGURE 3.1: **Shift profiles of pure  $(LDLK)_3$  and BMHP1-bis $(LDLK)_3$  peptides.**  $(LDLK)_3$  peptide antiparallel ( $A_I$ ) and parallel ( $A_{II}$ ) mutual alignments.  $\beta$ -sheet antiparallel ( $A_{III}$ ) and parallel ( $A_{IV}$ ) arrangements within  $\beta$ -sheet structuring nuclei.  $A_V$ ) Number of interactions among couples of peptides compatible with the formation of  $\beta$ -sheet structures. BMHP1-bis $(LDLK)_3$  branches antiparallel ( $B_I$ ) and parallel ( $B_{II}$ ) mutual alignments.  $\beta$ -sheet antiparallel ( $B_{III}$ ) and parallel ( $B_{IV}$ ) arrangements within  $\beta$ -sheet structuring nuclei.  $B_V$ ) Number of interactions among couples of branches compatible with the formation of  $\beta$ -sheet structures. Modest propensity of BMHP1-bis $(LDLK)_3$  to  $\beta$ -sheets arrangements can be appreciated in respect to  $(LDLK)_3$ .

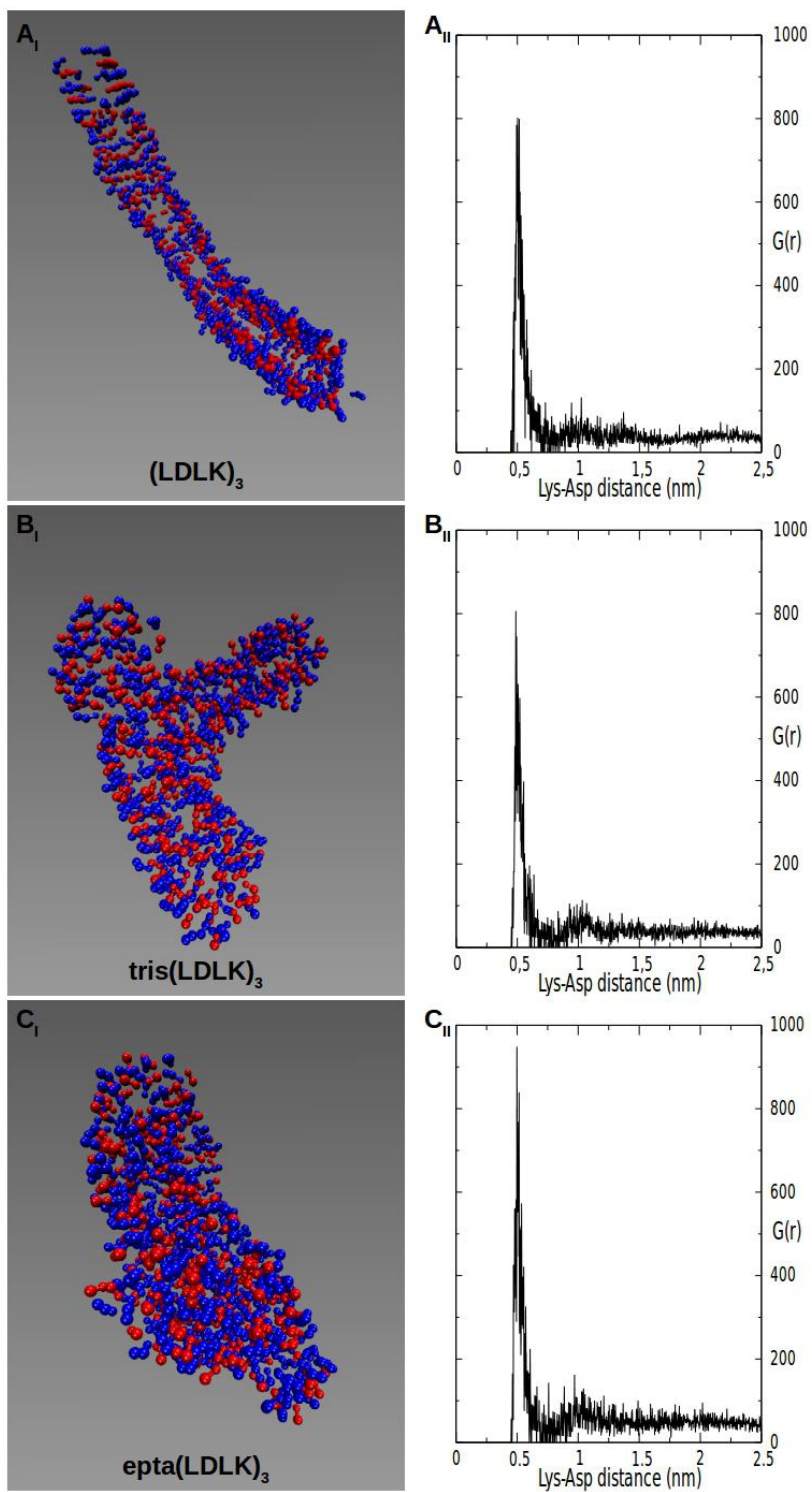
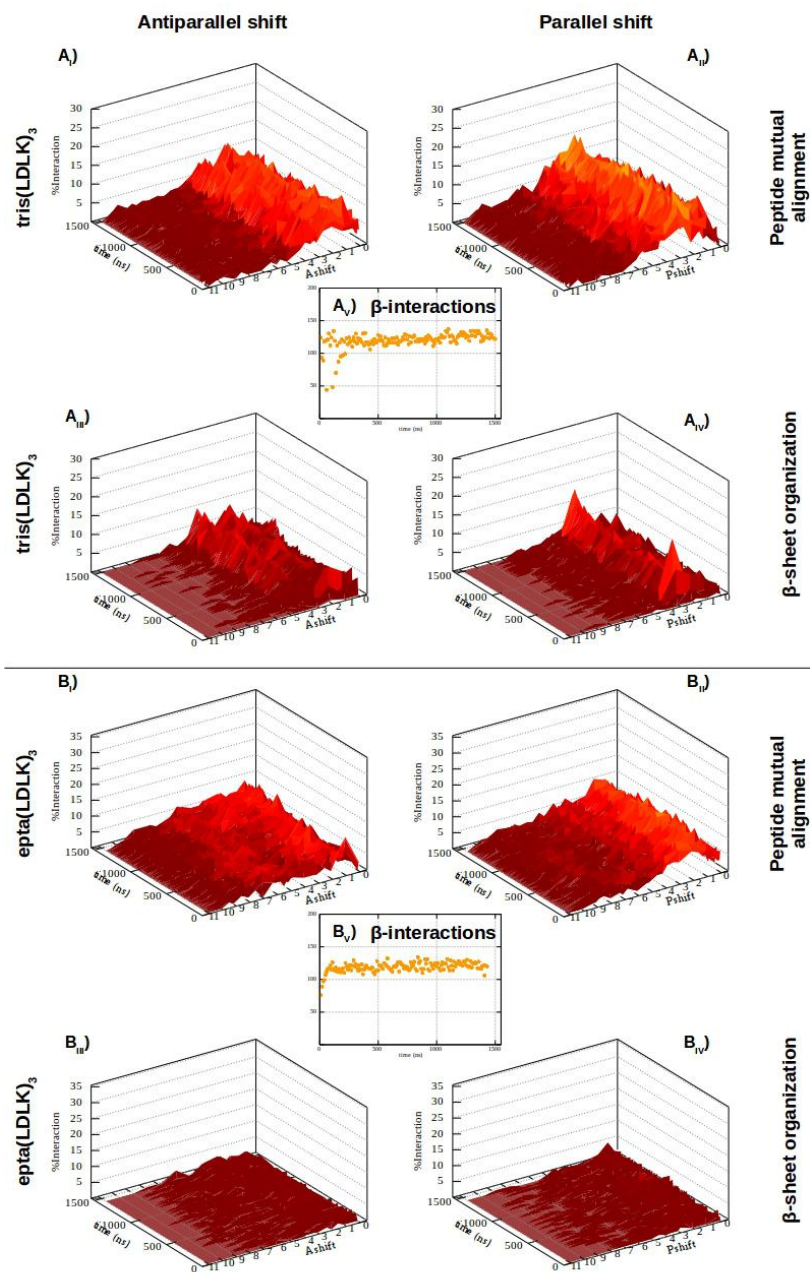




FIGURE 3.2: **Lys and Asp distribution** snapshot at time of 1500 ns of  $(LDLK)_3$  ( $A_I$ ),  $\text{tris}(LDLK)_3$  ( $B_I$ ) and  $\text{epta}(LDLK)_3$  ( $C_I$ ) at 1% (w/v). The distribution of the Lysine and Aspartic acid side-chains is represented in blue and red respectively.  $A_{II}$ - $B_{II}$ - $C_{II}$ ) Radial function distribution function of the distances among Lys and Asp side-chains of pure  $(LDLK)_3$ ,  $\text{tris}(LDLK)_3$  and  $\text{epta}(LDLK)_3$  peptides respectively. In all simulations the peak of radial distribution function at  $d \approx 0.6$  nm demonstrates the involvement of Lys and Asp residues in the formation of salt-bridges.



**FIGURE 3.3: Shift profiles of pure tris(*LDLK*)<sub>3</sub> and epta(*LDLK*)<sub>3</sub> branched SAPs.** tris(*LDLK*)<sub>3</sub> antiparallel (*A<sub>I</sub>*) and parallel (*A<sub>II</sub>*) peptide mutual alignments. (*A<sub>III</sub>*)  $\beta$ -strands antiparallel and parallel (*A<sub>IV</sub>*) arrangement within  $\beta$ -sheet structuring nuclei. *A<sub>V</sub>*) Number of interactions among couples of tris(*LDLK*)<sub>3</sub> branches compatible with the formation of  $\beta$ -sheet structures. epta(*LDLK*)<sub>3</sub> antiparallel (*B<sub>I</sub>*) and parallel (*B<sub>II</sub>*) peptide mutual alignments. Antiparallel (*B<sub>III</sub>*) and parallel (*B<sub>IV</sub>*)  $\beta$ -strands arrangement within  $\beta$ -sheet structuring nuclei of epta(*LDLK*)<sub>3</sub>. (*B<sub>V</sub>*) Number of interactions among couples of epta(*LDLK*)<sub>3</sub> branches compatible with the formation of  $\beta$ -sheet structures. Pure tris(*LDLK*)<sub>3</sub> showed higher self-assembling propensity than epta(*LDLK*)<sub>3</sub> but lower than pure (*LDLK*)<sub>3</sub>.

### 3.4.2 CG-MD simulation of mixtures of branched and linear peptides

A different scenario was obtained with CG-MD simulations of systems made of mixed linear and branched peptides. The investigation of molecular arrangements influencing the biomechanics of the tested hydrogels was a MR value of 131, 157 and 150 for  $(LDLK)_3$ /BMHP1-bis $(LDLK)_3$ ,  $(LDLK)_3$ /tris $(LDLK)_3$  and  $(LDLK)_3$ /epta $(LDLK)_3$  respectively.

Shift profiles of  $(LDLK)_3$ /BMHP1-bis $(LDLK)_3$  were similar to those observed in  $(LDLK)_3$ . The  $(LDLK)_3$  /BMHP1-bis $(LDLK)_3$  preferentially assembled at zero-residue (20%), two-residues (15%), four-residues (5%) antiparallel shift arrangements (Fig.3.4  $A_I$ , Fig. 3.5  $A_I$ ) and at one-residue (25%), three-residues (5%) parallel shift arrangements (Fig. 3.4  $A_{II}$ ,  $A_{III}$ , Fig. 3.5  $A_{II}$ ).

In addition, BMHP1-bis $(LDLK)_3$  showed  $\approx 80\%$  integration into  $\beta$ -sheet structures (Fig. 3.4  $A_{IV}$ ), with its three branches embedded into the same  $\beta$ -sheet (Fig. 3.4  $A_{IV}$  and Fig. 3.6  $A_I$ ,  $A_{II}$ ,  $A_{III}$ ). Instead,  $(LDLK)_3$ /tris $(LDLK)_3$  peptides preferentially aligned at zero-residue (15%), two-residues (15%), four-residues (5%) antiparallel shift (Fig. 3.4  $B_I$ , Fig. 3.5  $B_I$ ) and at one-residue (25%), three-residues (5%) parallel (Fig. 3.4  $B_{II}$ ,  $B_{III}$ , Fig. 3.5  $B_{II}$ ) shift arrangements.

Better than BMHP1-bis $(LDLK)_3$ , likely because of the presence of three  $(LDLK)_3$  branches, tris $(LDLK)_3$  highly incorporated into  $\beta$ -sheet structures with an integration percentage of 90% (Fig. 3.4  $B_{IV}$ ): its three  $(LDLK)_3$ -branches were integrated within the same  $\beta$ -sheet (Fig. 3.6  $B_I$ ,  $B_{II}$ ,  $B_{III}$ ) or at the interface between two ones. Lastly, shift profiles of  $(LDLK)_3$ /epta $(LDLK)_3$  showed that mixtures of branched and linear peptides were thoroughly aligned at zero-residue (20%), two-residues (15%), four-residues (5%) antiparallel shift (Fig. 3.4  $C_I$ , Fig. 3.5  $C_I$ ) and at one-residue (25%), three-residues (5%) parallel shift arrangements (Fig. 3.4  $C_{II}$ ,  $C_{III}$ , Fig. 3.5  $C_{II}$ ). Epta $(LDLK)_3$  too was highly integrated (%Integration = 90) into  $\beta$ -sheet structures (Fig. 3.4  $C_{IV}$ ) with its branches connecting different  $\beta$ -sheet structures (Fig. 3.6  $C_I$ ,  $C_{II}$ ,  $C_{III}$ ). Indeed, unlike what was observed in BMHP1-bis $(LDLK)_3$  (Fig. 3.4  $A_V$ ,  $A_{VI}$ ) and tris $(LDLK)_3$  (Fig. 3.4  $B_V$ ,  $B_{VI}$ ) peptides, epta $(LDLK)_3$  branches could coordinate different oligomers (i.e. colored cross- $\beta$  structures in Fig. 3.4  $C_V$ ,  $C_{VI}$ ).

In summary, CG-MD simulations, in good agreement with the empirical characterization, showed that branched peptides, when sharing the same self-assembling sequence of linear SAPs and featuring chain "flexibility" given by glycines of the "lysine knot", do not affect the linear  $(LDLK)_3$  tendency to assemble into  $\beta$ -sheet structures. They can actually embed into self-assembled cross- $\beta$  structures by covalently connecting otherwise weakly paired  $\beta$ -sheets.

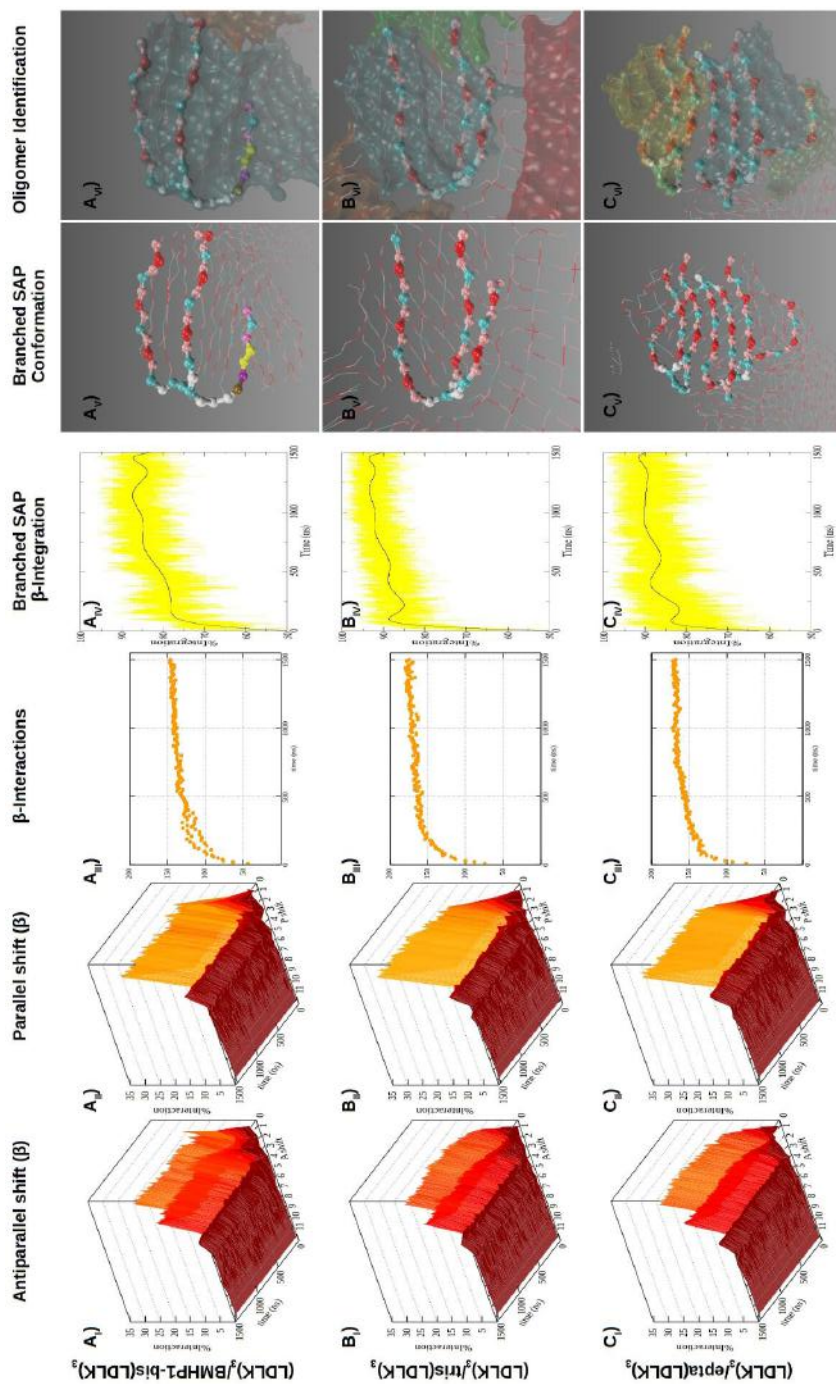


FIGURE 3.4: **CG-MD simulations of branched-SAPs.** In  $(LDLK)_3$ /BMHP1-bis $(LDLK)_3$   $\beta$ -sheets were preferentially aligned at zero-residue, two-residues and four-residues antiparallel shift arrangements ( $A_I$ ) and at one-residue shift parallel arrangement ( $A_{II}$ ). The number of peptide interactions among couples of peptides compatible with the formation of  $\beta$ -sheet structure slowly increased till 1000 ns when it reached a plateau ( $A_{III}$ ). At 1500 ns BMHP1-bis $(LDLK)_3$  showed the lowest (among the tested branched-SAPs) integration in  $\beta$ -sheet structures of linear SAPs ( $A_{IV}$ ), likely due to the lack of complementarity between BMHP1 and  $(LDLK)_3$  peptide side chains. BMHP1-bis $(LDLK)_3$  folded in a  $\epsilon$ -like shape that allowed the self-complementary alignment between the opposite charged side-chains of  $(LDLK)_3$  peptides and  $(LDLK)_3$ -branches ( $A_{V-VI}$ ). The shift profiles of  $(LDLK)_3$ /tris $(LDLK)_3$  ascribable to  $\beta$ -strands antiparallel and parallel arrangements showed similar trends to  $(LDLK)_3$ /BMHP1-bis $(LDLK)_3$  ( $B_{I-II-III-IV}$ ).  $(LDLK)_3$ /tris $(LDLK)_3$  reached better degree of integration in  $\beta$ -sheet structures ( $B_{V-VI}$ ) thanks to the substitution of BMHP1-branch with a  $(LDLK)_3$ -branch. The final  $\epsilon$ -like shape of tris $(LDLK)_3$  allows a good peptide alignment and salt-bridges formation among all  $(LDLK)_3$ -branches and linear peptides. Profile shifts of  $(LDLK)_3$ /epta $(LDLK)_3$  ( $C_{I-II-III-IV}$ ) did not show differences to other branched-SAPs: it also integrated into surrounding  $(LDLK)_3$   $\beta$ -sheet structures ( $C_{IV}$ ). Intriguingly its complex molecular structure allows for the folding of its branches into parallel and antiparallel  $\beta$ -sheets and for their integration into multiple different cross- $\beta$  oligomers of  $(LDLK)_3$  ( $C_{V-VI}$ ).

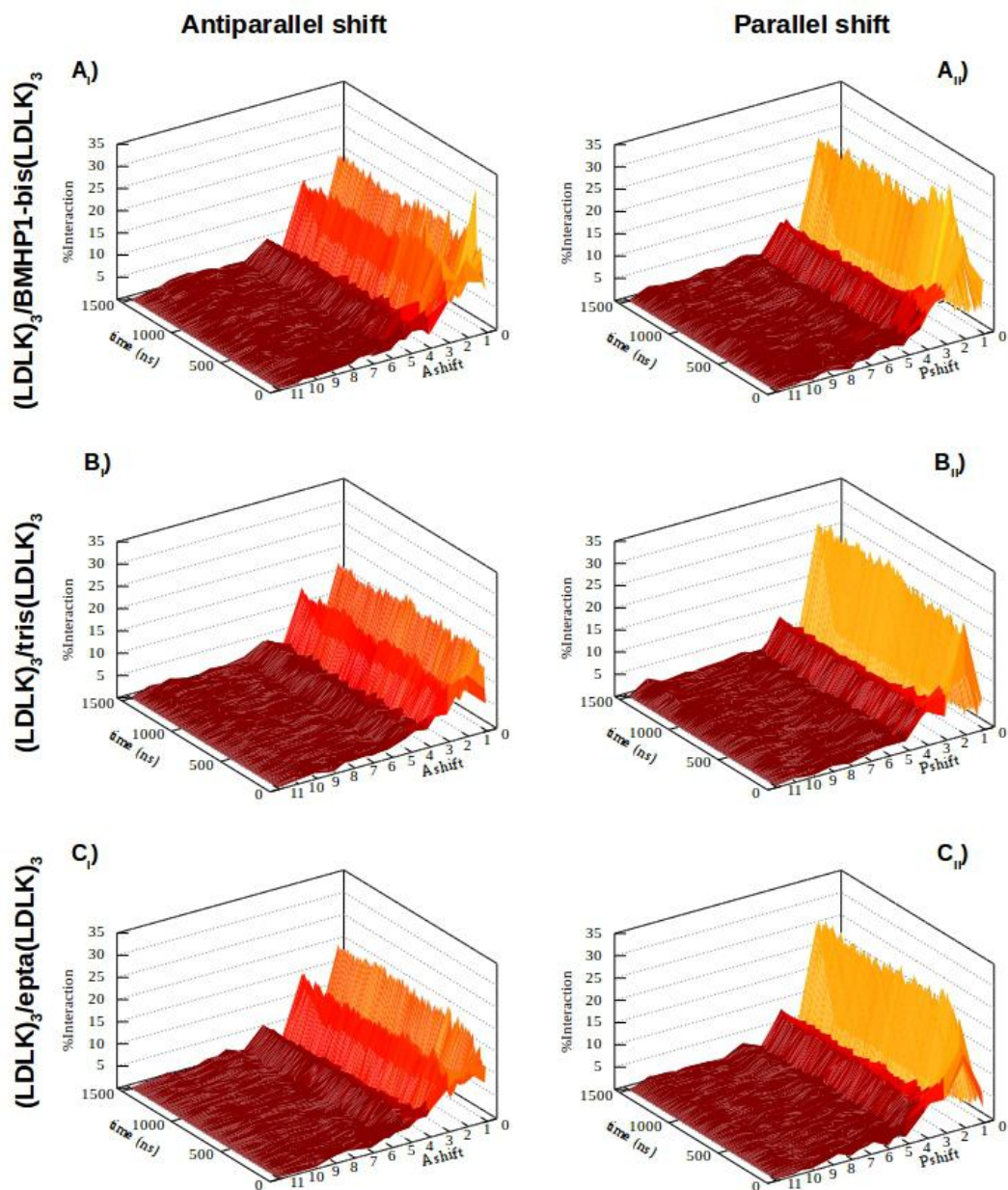


FIGURE 3.5: **Shift profiles of mixed linear and branched peptides.**  $A_{I-II}$ ) Antiparallel and parallel peptide mutual alignments of  $(LDLK)_3/BMHP1-bis(LDLK)_3$  at MR of 131.  $B_{I-II}$ ) Antiparallel and parallel peptide mutual alignments of  $(LDLK)_3/tris(LDLK)_3$  at the MR of 157.  $C_{I-II}$ ) Antiparallel and parallel peptide mutual alignments of  $(LDLK)_3/epta(LDLK)_3$  at the MR of 150. Addition of branched peptides did not affect  $\beta$ -structure formation in  $(LDLK)_3$  systems.



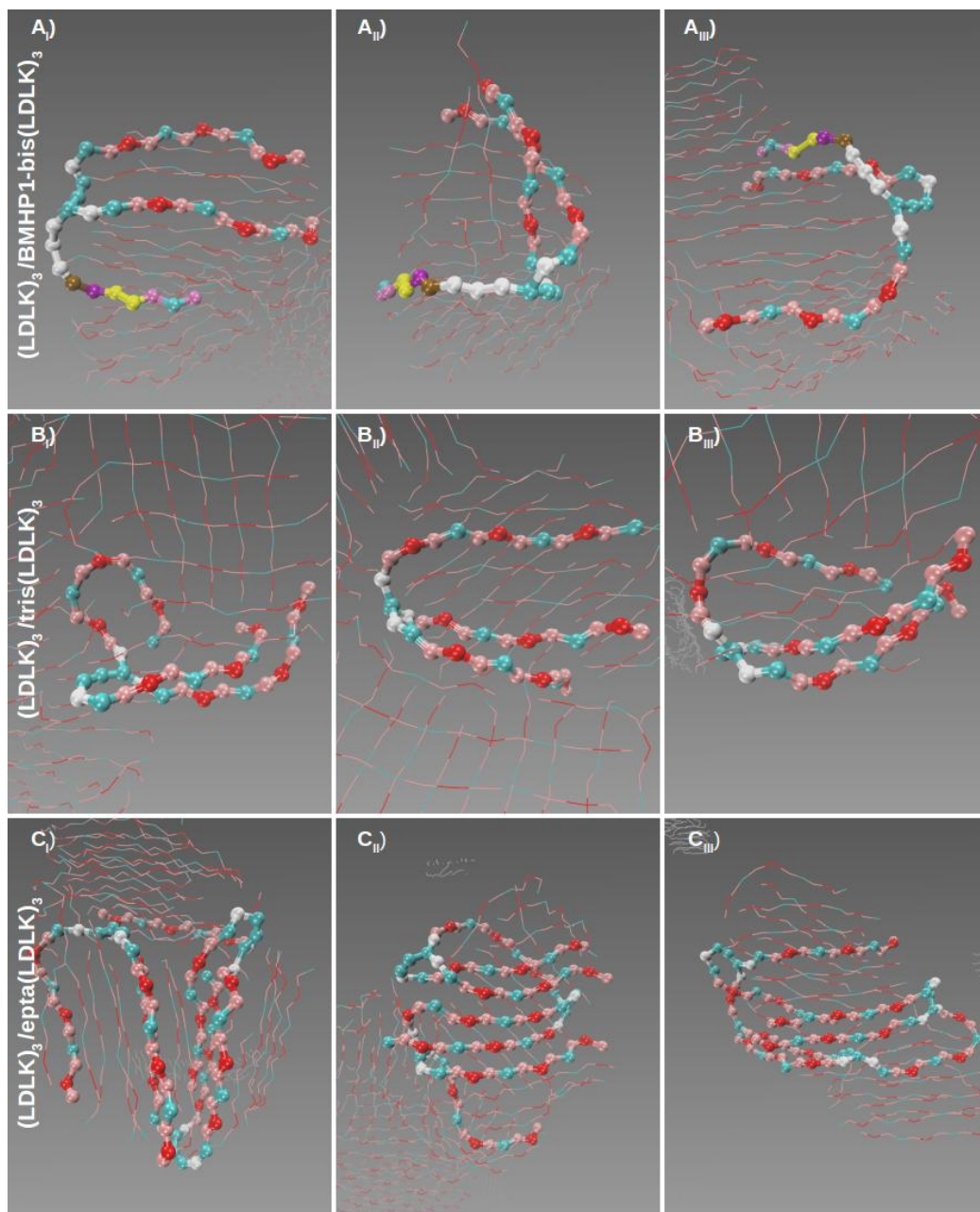


FIGURE 3.6: **Final conformations (at the end of CG-MD simulations) of single molecules of branched-SAPs mixed with linear  $(LDLK)_3$ .**  $A_{I-II-III}$   $(LDLK)_3$ /BMHP1-bis( $LDLK$ ) $_3$  simulation replicates at the molar ratio of 131.  $B_{I-II-III}$   $(LDLK)_3$ /tris( $LDLK$ ) $_3$  at the molar ratio of 157.  $C_{I-II-III}$   $(LDLK)_3$ /epta( $LDLK$ ) $_3$  at the molar ratio of 150. Lysine, Aspartic acid, Glycine and Leucine are in cyan, red, white and pink respectively. Branched SAPs integrated within the self-formed cross- $\beta$  structures of the linear SAP, they also acted as connectors within and amongst different  $\beta$ -layers.



### 3.5 CONCLUSIONS

Improving biomechanics of self-assembling peptide hydrogels is a crucial step forward potentially enlarging their possible applications in regenerative medicine. Branched SAPs were demonstrated to be feasible tools to improve the mechanical properties of self-assembling scaffolds without chemical or enzymatic cross-linking, alternative strategies that may lead toxic side-effects. Branched SAP molecules embed into self-assembled cross- $\beta$  structures and act as molecular knots within and among  $\beta$ -sheets, thus preserving the well-known possibilities for linear SAP functionalization. Indeed, branched SAPs may be added to both standard and previously functionalized SAPs to match the desired mechanical strength and to add multiple heterogeneous functional motifs or tags. Therefore this work increases the potential of SAP scaffold customization for new regenerative therapies.

## Chapter 4

# Nano-Mechanics of SAPs structures

*Adapted from Federico Fontana, Fabrizio Gelain. "Probing mechanical properties and failure mechanisms of fibrils of self-assembling peptides", In: **Nanoscale Advances**, Volume 2, page 190-198 (2020)*

#### 4.1 ABSTRACT

Self-assembling peptides (SAPs) are a promising class of biomaterials amenable to easy molecular design and functionalization. Despite their increasing usage in regenerative medicine, a detailed analysis of their biomechanics at the nanoscale level is still missing. In this work, we propose and validate, in all-atom dynamics, a coarse-grained model to elucidate strain distribution, failure mechanisms and biomechanical effects of functionalization of two SAPs when subjected to both axial stretching and bending forces. We highlight different failure mechanisms for fibril seeds and fibrils, as well as the negligible contribution of the chosen functional motif to the overall system rupture. This approach could lay the basis for the development of “more” coarse-grained models in the long pathway connecting SAP sequences and hydrogel mechanical properties.

## 4.2 INTRODUCTION

Bio-molecular self-assembly has inspired the so-called “bottom-up” approach to design self-assembling biomaterials.[2][1][14][16][15][3] Among them, self-assembling peptides (SAPs) were adopted to investigate crucial issues in different scientific fields, e.g. the investigation of the mechanisms ruling abiogenesis and Alzheimer’s disease in biology, or solar energy harvesting in electronics and regenerative medicine applications in biomaterials science.[14][179][104] Furthermore, SAPs have been exploited for tissue engineering applications thanks to their favorable biocompatibility, tailorability and biomimetic properties.[3][109][146] Indeed, SAPs have been used in neural tissue engineering for the treatment of brain injury and spinal cord injury (SCI)[109][35][146]: i.e. SAPs were tested as hydrogel scaffolds capable of spatially guiding regenerating nervous tissues and creating suitable microenvironments for nerve regeneration. However, additional tissue engineering applications of SAP hydrogels are limited by weak control/prediction of their mechanical properties, given by usually reversible and temporary non-covalent interactions at the molecular and nano-scale levels. Despite the recent remarkable progress in nanomechanics, a straight correlation between SAP nanostructural organization and mechanical features is still missing.[180][181] On one hand, atomistic and coarse-grained (CG) molecular dynamics (MD) simulations have been used, in combination with empirical experiments, to elucidate the self-assembly pathways and structuring propensities of several peptide sequences at the nanoscale level.[181][182][105][97][91] On the other hand, steered molecular dynamics (SMD) simulations have been efficiently adopted to investigate the mechanical properties of biomacromolecular structures such as axial and torsional rigidity.[183][184][185] To cope with limited computational resources, several CG force fields were developed and tested. Among them, the MARTINI force field, initially developed for the investigation of lipid assemblies, was largely used for the investigation of protein and peptide systems, providing interesting insights into structuring phenomena in even larger multi-molecular systems.[50][59][186][187][98] Nonetheless, the MARTINI SMD approach found limited applications, because it does not allow conformational transitions [81][188] that are quite common in the biological system instead. On the other hand, GoMARTINI overcomes the main limitation of the MARTINI approach, allowing us to track conformational transitions.[75] In order to elucidate the structure–mechanics relationship of peptide systems at the nano- and micro-scales, we here propose and validate an innovative fine-to-coarse molecular modeling approach. SAP structuring and mechanical features of the obtained fibrils have been investigated through both atomistic and GoMARTINI-based MD simulations. Atomistic and GoMARTINI-based SMD simulations, analyzed through the recently developed software dubbed Morphoscanner,[189] provided comparable results despite the different computing

times required and provided insights into the length-dependent failure mechanism of SAP fibrils, opening new opportunities in the field of nanomechanics, laying the foundation for the building of reliable mesoscale models.

## 4.3 MATERIAL AND METHODS

### 4.3.1 Hydrogel preparation and ssNMR characterization at natural abundance

In order to elucidate supramolecular organization of peptide hydrogels, ssNMR experiments were performed with solid-phase synthesized peptides. Solid-state NMR (ssNMR) provided atomic-level structural information about hydrogels organization. This allowed to derive secondary structure information at residue-level from the so-called "secondary chemical shifts". The  $(LDLK)_3$  and FAQ- $(LDLK)_3$  hydrogels were prepared by dissolving purified peptide powder at a concentration of 1% (w/v) in distilled water, sonicated for 30 min, and incubated at 4 °C for 24h, a day prior the ssNMR characterization. The rigid fractions of the self-assembling peptides were quantified using one-dimensional (1D), so-called dipolar NMR experiments (i.e. experiments that rely on the presence of dipolar couplings between  $^1\text{H}$  and  $^{13}\text{C}$ ). NMR experiments were performed without synthetic  $^{13}\text{C}$ -isotope enrichment.

All  $^{13}\text{C}$ -detected CP experiments were initially optimised on  $^{13}\text{C}$ -labelled histidine and by using a  $^1\text{H}$  to  $^{13}\text{C}$  CP magnetization transfer-time of 1 ms for all samples: the obtained parameters were used for the hydrogels without further optimisation. The spectra were acquired at 700 MHz magnetic field and 15 kHz magic angle spinning (MAS) and 278 K sample temperature.

### 4.3.2 CG-MD simulations of $(LDLK)_3$ and FAQ- $LDLK_3$ peptides

All-trans configuration of  $(LDLK)_3$  and FAQ- $(LDLK)_3$  peptides were generated by Pymol (<https://pymol.org>) and mapped according to the MARTINI model. The C- and N- terminal of peptide monomers were acetylated and amidate respectively. At neutral pH, arginine, lysine and aspartic acid side chains, because of their weak basic and acidic nature, can be considered fully protonated and deprotonated respectively. Peptides have been randomly distributed in explicit water cubic boxes built by using PACKMOL in order to have the correct spatial distribution of the monomers.[108] Atoms belonging to different peptides were placed at minimum distance of 10 Å far from each other (see fig. 4.2 for details). In MARTINI coarse-grained molecular dynamics (CG-MD) simulations it is necessary to define peptide secondary structures, and the above mentioned parameters, to which individual amino acid residue must evolve.[50] The secondary structures have been assigned as shown

in fig. 4.2, according to the evidences obtained from previous experimental analyses [21] and from ssNMR spectra as shown in Fig. 4.1. (See Section 4.3.1 for ssNMR experiment details) MD simulations were performed using the version 4.5.5 of GROMACS package. Prior to the production phase, the systems underwent to an equilibration phase (a 3000-steps minimization using steepest descents method) in order to eliminate high-energy interactions. The production phase was conducted in the NPT ensemble. Solutes and solvent were coupled independently to an external bath ( $T = 298$  K) with a coupling constant ( $\tau_T$ ) of 1 ps using v-rescale thermostat. Periodic boundary conditions were imposed, and pressure was maintained at 1 bar using the Berendsen coupling.[174] The isothermal compressibility was set at  $3 \times 10^{-4}$  bar $^{-1}$  and the coupling constant ( $\tau_P$ ) was 1 ps. The constraints on lengths and angles of the bonds were applied with the LINCS algorithm. All systems were simulated as indicated in Table S1 using an integration time-step of 20 fs, while snapshots of individual trajectories were saved every 100 fs.

### 4.3.3 UA-MD simulations of FAQ peptides

Due to the lack of accurate structural information about FAQ peptides, the self-assembly process of this SAP class has been investigated by means of more accurate UA-MD simulations. The simulation details of FAQ-derived SAPs are shown in Fig. 4.4. Peptide monomers have the C-terminus amidated and the N-terminus acetylated. Arginine residues are in the protonated state. Extended conformations of monomers were built with Pymol software by imposing all-trans geometry on the backbone dihedrals (<https://pymol.org>).

The monomers in extended conformation have been embedded in a box of explicit water and submitted to three simulations of 50 ns/each with different initial velocity distributions. A distance of 10 Å has been left between the peptide and the box edges to preserve the minimum image convention. On the obtained conformational sampling, a cluster analysis has been performed by means of the gromos algorithm of Daura.[190] Taking into account each frame of the MD trajectory, the clusters of structures were identified through RMSD among each pair of structures.[190] The structures with the highest number of neighbours was taken as center of each cluster, i.e. centrotypes. The centrotypes of the first cluster were used to prepare systems containing eight monomers: each system was composed by centrotypes picked up in relative amount needed to achieve 70–80% representation degree of the monomeric sampling. The initial configurations of the multi-peptide systems were prepared by insertion of the selected centrotypes in random orientations and positions in cubic boxes filled by explicit water and so that atoms belonging to different peptides were at least 10 Å away from each other.[108]

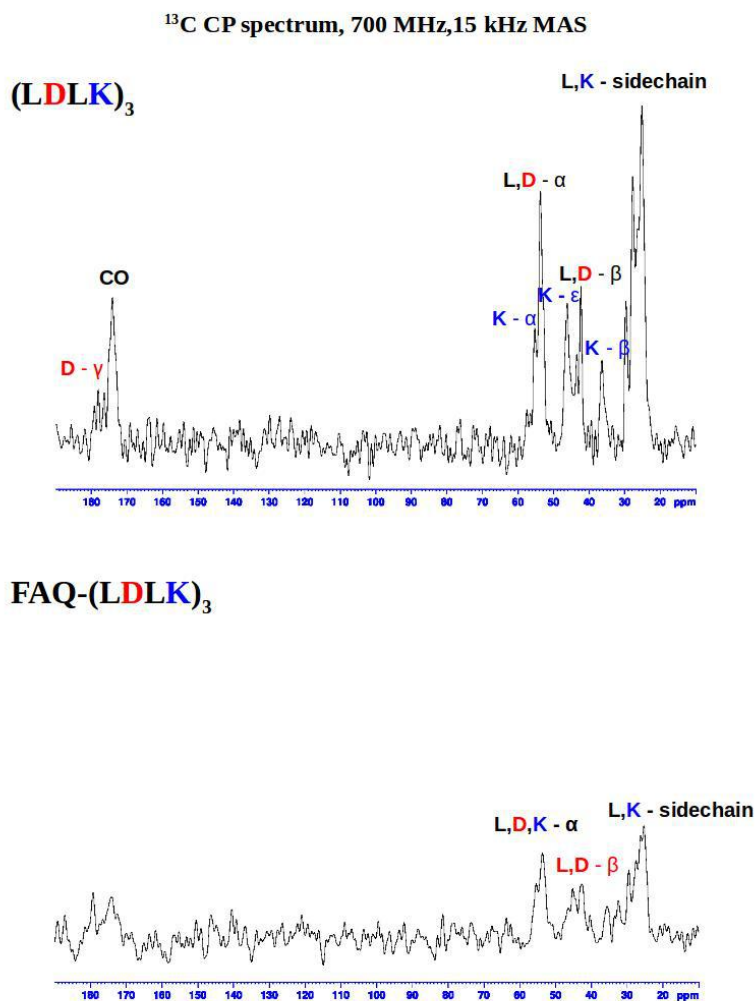


FIGURE 4.1:  $^{13}\text{C}$ -detected dipolar cross-polarization ssNMR spectra: characterization of the immobile fraction of the hydrogels. The ssNMR spectra showed that  $(LDLK)_3$  SAPs were fully assembled, completely rigid, and  $\beta$ -structured. Indeed, the chemical shifts corresponding to  $\beta$ -strand conformation were easily identified. Instead, the FAQ- $(LDLK)_3$  SAPs showed a lower rigidity at the nanoscale level. However, the chemical shift pointed out that  $(LDLK)_3$  moieties assembled in rigid and  $\beta$ -structured aggregates. Such information has been used to assign secondary structure parameters in GoMARTINI simulations. See Section 4.3.1 for details about hydrogels preparation and ssNMR characterization.

Molecular dynamics were run using version 4.5.5 of the GROMACS simulation package and the GROMOS53a6 force field. Prior to the production phase, the systems underwent an equilibration phase consisting in the following steps: steepest descent minimization first in vacuum then in water and ions, a brief simulation in NVT ensemble with 2 fs time-step, position restrained peptides and the temperature fixed at 298 K. The production phase was conducted in the NPT ensemble. Solutes and solvent were coupled independently to an external bath ( $T = 298$  K) with a coupling constant ( $\tau_T$ ) of 0.1 ps using v-rescale thermostat. Periodic boundary conditions were imposed, and pressure was maintained at 1 bar using the Berendsen coupling.[174] The isothermal compressibility was set at  $4.5 \cdot 10^{-5}$  bar<sup>-1</sup> and the coupling constant ( $\tau_P$ ) was 0.1 ps. The constraints on lengths and angles of the bonds were applied with the LINCS algorithm. All systems were simulated as indicated in Fig. 4.4 using an integration time-step of 2 fs, while snapshots of individual trajectories were saved every 10 fs.

#### 4.3.4 UA-Steered molecular dynamics simulations of $(LDLK)_3$ and FAQ- $(LDLK)_3$ peptides

The initial conformations of the systems have been obtained through back-mapping procedure of the resulting structures from CG-MD simulations (See Fig. 4.3, Fig. 10.8, Fig. 10.9, Fig. 10.14, Fig. 10.16). At the neutral pH, lysine and arginine and aspartic acid side chains, because of their weak basic and acidic nature, can be considered fully protonated and deprotonated respectively. Steered molecular dynamics simulations were run using the version 2016.3 of the GROMACS simulation package, using two GTX 1080 GPUs. Two set of UA-SMD, named axial stretching and bending, have been conducted using the Gromos53a6 force-field. Prior to the production phase, the systems underwent to an equilibration phase consisting in the following steps: steepest descent minimization first in vacuum then in water and ions, a brief simulation in NVT ensemble with a 2 fs time-step, position restrained peptides and the temperature fixed at 298 K. Then a 200 ps long simulation in NVE ensemble, with position restrained peptides has been conducted in order to optimize the charge side-chains orientations.

The production phase was conducted in the NVE ensemble, in order to conserve internal energy and momentum of the supra-molecular systems. This approach allowed to correlate the changes in supra-molecular architectures with their mechanical properties. Indeed, in the microcanonical ensemble the internal energy is fixed at  $E$  and the first law of thermodynamics can be written as follows:

$$\Delta E = \Delta Q + \Delta W \quad (4.1)$$



$\Delta W$  represents the work done on the molecular system and can be described by the following expression:

$$\Delta W = \Sigma X_i dx_i \quad (4.2)$$

This quantity depends on the presence of external forces  $X_i$  and has huge consequences on the statistical mechanical definition of entropy:

$$S = k \ln \Omega = S(E, x_i) \quad (4.3)$$

This expression for the entropy can be inverted to give E as function of S:

$$S(E, x_i) \iff E(S, x_i) \quad (4.4)$$

Then, the inter-dependency relation among constraints and configurations of the system can be derived as follows:

$$\left(\frac{\delta S}{\delta x_j}\right)_{E, x_i \neq x_j} \quad (4.5)$$

According to the above equation, the adoption of NVE ensemble for SMD allowed to monitor the configurations of the peptide systems at constant energy by varying constraints. In axial stretching scenario, one end of the fibril (seed) structure has been fixed by constraining the motion of C $\alpha$ -atoms at the bottom strand of the sheets. The other end of the fibril was deformed by axial loading. Instead, in bending scenario the unrestrained end was deformed by lateral loading. The boundary conditions consisted of fixing C $\alpha$ -atoms on the top and bottom strands with a SMD spring constant equal to 1000 kJ\* $\text{mol}^{-1} \text{nm}^2$  and a displacement rate of 0.01 nm/ps. Each system was simulated in explicit water box and submitted to five production runs differing for the initial velocity distribution, as shown in fig. 4.6.

The constraints on lengths and angles of the bonds were applied with the LINCS algorithm. All systems were simulated as indicated in fig. 4.6 using an integration time-step of 2 fs, while the snapshots and the measures of force/displacement of individual trajectories were saved every 10 fs.

### 4.3.5 CG-Steered molecular dynamics simulations of (LDLK)<sub>3</sub> and FAQ-(LDLK)<sub>3</sub> peptides

The initial conformations of the systems have been obtained through back-mapping procedure of the resulting structures from CG-MD simulations (See Fig. 4.3, Fig. 10.8, Fig. 10.9,

Fig. 10.14, Fig. 10.16). CG-SMD simulations were run using the version 2016.3 of the GRO-MACS simulation package, using two GTX 1080 GPUs. Two set of CG-SMD, analogues to UA-SMD simulations, have been conducted using the GoMARTINI force-field.[75] In GoMARTINI CG-MD simulations, it has been necessary to define peptide secondary structures through Lennard-Jones interactions based on the contact map of native fibril (seed). The Lennard-Jones potential is defined as follows:

$$U_{LJ} = 4\epsilon_{ij}[(\frac{\sigma}{r})^{12} - (\frac{\sigma}{r})^6] \quad (4.6)$$

In GoMARTINI model,  $\epsilon_{ij}$  is usually set to a larger value than in MARTINI force-field and represents the strength of the hydrogen bonds and other contribution such as ionic bridges. Indeed, the parameter  $\epsilon_{ij}$  is expressed in unit of  $\epsilon = 6.276 \text{ KJ/mol}^{-1}$ . Then, the parameter  $\lambda$  in the native contact energy,  $\epsilon_{ij} = \lambda\epsilon$ , is a tunable parameter of the GoMARTINI model, whose optimum value can be found to match quantitatively the GoMARTINI and UA model.[75] To reproduce the tendencies observed in UA-SMD, the value of  $\lambda$  was set to 0.5. Prior to the production phase, the systems underwent to an equilibration phase consisting in the following steps: steepest descent minimization first in vacuum then in water and ions, a brief simulation in NVT ensemble with 0.002 ps time-step, position restrained peptides and the temperature fixed at 298 K. Then a 200 ps long simulation in NVE ensemble, with position restrained peptides has been conducted in order to optimize the charge side-chains orientations.

The production phase was conducted in the NVE ensemble. In axial stretching scenario, one end of the fibril (seed) structure has been fixed by constraining the motion of backbone grains at the bottom strand of the sheets. The other end of the fibril was deformed by axial loading. Instead, in bending scenario the unrestrained end was deformed by lateral loading. The boundary conditions consisted of fixing backbone grains on the top and bottom strands with an SMD spring constant equal to  $1000 \text{ kJ}^*\text{mol}^{-1} \text{ nm}^2$  and a displacement rate of 0.01 nm/ps. Each system was simulated in explicit water box and submitted to five different simulations, as shown in fig. 4.7. The constraints on lengths and angles of the bonds were applied with the LINCS algorithm. All systems were simulated as indicated in fig. 4.7 using an integration time-step of 2 fs, while the snapshots and the measures of force/displacement of individual trajectories were saved every 10 fs.

#### 4.3.6 Analysis of SMD simulations

The cross-sectional area of each fibril (or seed) has been approximated to a rectangle, whose sides are defined by two segments; the first segment joining the center of mass of two  $\beta$ -strands, the second segment joining the N- and C- terminus of peptides belonging to one

end of the fibrils.

The stress-strain curves were obtained by converting the force-displacement curves. Stress values were derived by dividing the force values for the cross-sectional area, according to the following formula:

$$\sigma(t) = F(t)/A_c \quad (4.7)$$

Where  $F(t)$  indicates the value of the force obtained from SMD,  $A_c$  indicates the measure of the cross-sectional area.

The engineering strain curves were obtained from the displacement curves through the following formula:

$$\epsilon(t) = \frac{L(t) - L(0)}{L(0)} \quad (4.8)$$

Where  $L(t)$  indicates the measure of the displacement at a given time-step,  $L(0)$  indicates the starting length of the structures. Young's modulus and Shear modulus have been derived by measuring the slope of the stress-strain curves. The distribution of strains within fibrils (or seeds) has been calculated through the formula of shear contribution ratio:

$$s(L) = \frac{1Eh^2}{4GL^2} \quad (4.9)$$

If  $s(L) \geq 1$ , non-covalent interactions (i.e. hydrogen bonds) are being shared (pulled orthogonal to the bonding direction)

If  $s(L) \leq 1$ , non-covalent interactions (i.e. hydrogen bonds) are stretched in tension (pulled in the bonding direction)

### 4.3.7 Morphoscanner Analysis

As reported in chapter 2 the input parameters of Morphoscanner were set equal to the number of peptides (S) and of backbone grains (or  $C\alpha$  atoms in the UA model) (SL). Then, S was set equal to 8 for the analysis of fibril seed simulations (Fig.4.3, 4.8), whereas S was set equal to 100 for the analysis of fibril simulations (Fig. 4.10, 4.11). Instead, SL was set equal to 10, 12 and 22 for the analysis of FAQ,  $(LDLK)_3$  and FAQ- $(LDLK)_3$  MD simulations respectively. The organization of the systems over time was schematized into a count of the total  $\beta$ -interactions in the systems.  $\beta$ -interactions were set to 1 when distance between backbone atom-groups (grains) or  $C\alpha$  atoms fall between 4.7 and 5.3 Å. In addition, the shift profiles were used to track peptides preferential arrangement during self-assembling.

Sequence ID	Sequence	Box size (nm)	CG ions beads (NA+/CL-)	CG Water beads	N° of peptides + N° of seed (8-mer)	N° of sim x time (ns)
(LDLK) <sub>3</sub>	<b>LDLKL</b> <i>DLKL</i> <b>DLK</b>	12.39	0/0	15829	8	3 x 250
(LDLK) <sub>3</sub>	<b>LDLKL</b> <i>DLKL</i> <b>DLK</b>	28.99	0/0	189597	20 + 10	1 x 20000
FAQ-(LDLK) <sub>3</sub>	<i>FAQRVPPGGGL</i> <b>DLKL</b> <i>DLKL</i> <b>DLK</b>	12.40	0/8	15822	8	3 x 250

FIGURE 4.2: **CG-MD simulations setup.** (*LDLK*)<sub>3</sub> and FAQ-(*LDLK*)<sub>3</sub> SAPs aggregation propensity was evaluated through CG-MD simulations. Secondary structure (SS) parameters have been assigned according to experimental evidences; the residues with extended SS have been highlighted in bold, whereas the residues with coil SS have been highlighted in italic. The 8-mers (fibril seeds) were modeled adopting the standard MARTINI approach. The 100-mer systems was modeled adopting ONE-POT CG-MD approach; the fibril seeds were modeled according to GoMARTINI mapping, meanwhile the monomers were mapped as used in standard MARTINI approach.

## 4.4 RESULTS AND DISCUSSION

### 4.4.1 Self-Assembling of (*LDLK*)<sub>3</sub> Fibril Seeds

The self-assembling and  $\beta$ -structuring propensity of (*LDLK*)<sub>3</sub> SAPs were investigated using MARTINI CG-MD simulations and Morphoscanner (See 4.2 and Fig.4.3). [187][189] As shown in Fig. 4.3a, (*LDLK*)<sub>3</sub> octameric systems (i.e. fibril seeds), assembled preferentially into the double-layered  $\beta$ -sheet structure within 150 ns, and their  $\beta$ -sheet organization were depicted in peptide mutual alignment (PMA) graphs, describing antiparallel alignments. However, (*LDLK*)<sub>3</sub> peptides were also aligned in parallel out-of-register of one-residue resulting in a less ordered double-layered  $\beta$ -sheet structure (Fig. 10.8 and 10.9). Indeed, in-register parallel alignment implied repulsive interactions among identically charged side chains resulting in slow self-assembly kinetics and lower  $\beta$ -structuring propensity.

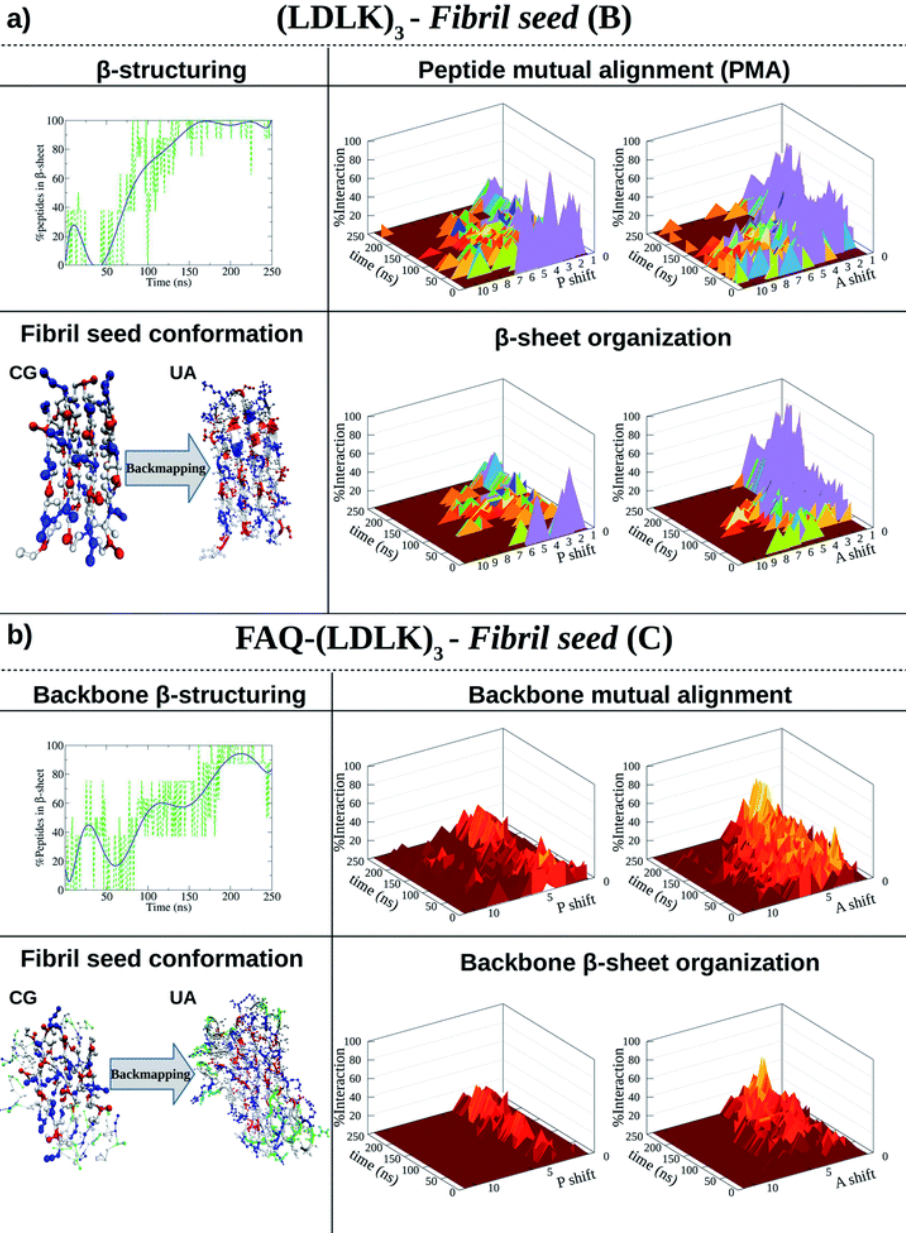


FIGURE 4.3: **Shift profiles and  $\beta$ -structuring propensity of  $(LDLK)_3$ -derived SAPs.** P refers to parallel alignment and A refers to anti-parallel alignment. The resulting structures from CG-MD were back-mapped and then used as starting conformations for SMD simulations. (a) In 150 ns,  $(LDLK)_3$  SAPs aggregate into stable double-layered  $\beta$ -sheet structures (Morphoscanner analysis, see Chapter 10), yielding strong anti-parallel alignments. Such a tendency was likely due to the electrostatic interactions among oppositely charged side chains of lysine and aspartic acid residues. (b) Alignment analysis of FAQ- $(LDLK)_3$  backbones showed weaker alignments in both A and P, mirrored by lower  $\beta$ -sheet organization. This feature was likely due to the presence of the FAQ functional motif at N-termini, which may have interfered with  $\beta$ -sheet formation among self-assembling backbones.

#### 4.4.2 ONE-POT CG-MD of $(LDLK)_3$ Fibril

To investigate the native supramolecular organization of  $(LDLK)_3$  fibrils (100-mer), a 20  $\mu$ s-long one-pot CG-MD simulation has been performed according to the data reported in 4.2. Each fibril seed (8-mer), obtained through the CG-MD simulation (Fig. 4.3a), was mapped according to the GoMARTINI model, whereas monomers were mapped according to the standard MARTINI model.[98][75] GoMARTINI partially exceeded the main drawback of the MARTINI model allowing us to monitor secondary structure transitions. Indeed, the GoMARTINI model has proven to be suitable for the investigation of peptide/protein folding and unfolding processes.[75] As shown in Fig. 10.10, in a one-pot CG-MD simulation, the formation of oligomers has been driven by the presence of preformed fibril seeds, resulting in fast self-assembly kinetics, where monomers incorporated into the fibril seed surfaces instead of aggregating into globular clusters.

PMA within fibril seeds influenced the overall peptide alignment within fibrils. Indeed, SAPs within fibrils were also preferentially antiparallel aligned (Fig. 4.3a and 10.10). Such a high degree of order was reflected in a strong  $\beta$ -sheet organization and testified by the growing trend of the nematic order parameter, beyond the threshold value of 0.5 (Fig. 10.10). These tendencies were ascribable to the presence of alternating oppositely charged side chains of Lys and Asp, leading to the formation of stable double-layered  $\beta$ -sheet structures.

#### 4.4.3 Assessment of FAQ Self-Assembling Propensity

$(LDLK)_3$  SAPs were functionalized by linking the FAQ sequence at the N-terminus because of its relevance for nerve regeneration.[146] FAQ functional motif (alone) self-assembling propensity was evaluated through UA-MD simulations (see 4.4). Morphoscanner analysis

Sequence ID	Sequence	Box size (nm)	UA ions (NA+/CL-)	UA Water molecules	N° of peptides	N° of sim x time (ns)
FAQ	FAQRVPPGGG	4.0	0/1	2124	1	3 x 50
FAQ	FAQRVPPGGG	12.39	0/8	8126	8	3 x 250

FIGURE 4.4: **UA-MD simulations setup.** FAQ functional motif self-assembling propensity was evaluated through united-atom molecular dynamics (UA-MD) simulations. Each system was represented according to Gromos53a6 force-field mapping. The monomer simulations have been performed in smaller boxes than 8-mer simulations. Indeed, in UA-MD simulations of monomers, the box sizes have been chosen to respect the minimum image convention. Instead, in UA-MD simulations of 8-mer, the box sizes have been imposed to reproduce the concentration of the self-assembling peptides (i.e. 1% w/v), usually adopted in rheological characterization of SAPs hydrogels.[21][189] The peptide conformations, obtained from monomer simulations, have been used to prepare the starting configuration of 8-mer systems.

revealed good aggregation but weak  $\beta$ -structuring propensity of FAQ motifs (see Figures 4.5, 10.11, 10.12): the formation of well-ordered double-layered  $\beta$ -sheet structures was likely hampered by the presence of Pro residues.

#### 4.4.4 Self-Assembling of FAQ-(LDLK)<sub>3</sub> Fibril Seeds

This tendency affected FAQ-(LDLK)<sub>3</sub> self-assembly and  $\beta$ -structuring scenario. Indeed, the backbone moieties of the functionalized peptide showed weaker anti-parallel alignment, whereas functional motifs did not assemble into ordered structures (Fig. 4.3b and 10.13). However, FAQ functional motif aggregation features interfere with the formation of well-ordered aggregates. In one case, FAQ functionalization led to slower aggregation kinetics and to lower  $\beta$ -structuring propensity (Fig. 10.14 and 10.15).

In another simulation, FAQ functionalization altered the formation of the double-layered  $\beta$ -sheet structure leading to an orthogonal orientation of the  $\beta$ -sheets (Fig. 10.16 and 10.17)

#### 4.4.5 Steered Molecular Dynamics Simulations of Fibril Seeds

The above-mentioned structures were backmapped, and then two sets of steered molecular dynamics (SMD) simulations, named axial stretching and bending, have been conducted using Gromos53a6 and GoMARTINI force-fields (see 4.6 and 4.7).[191][70][68][69]

In the axial stretching scenario, a constant force has been applied at one end of the fibril seed while the other end remained fixed. Instead, in the bending scenario, a constant lateral force has been applied to the unrestrained end of the fibril seed. These set-ups aimed to

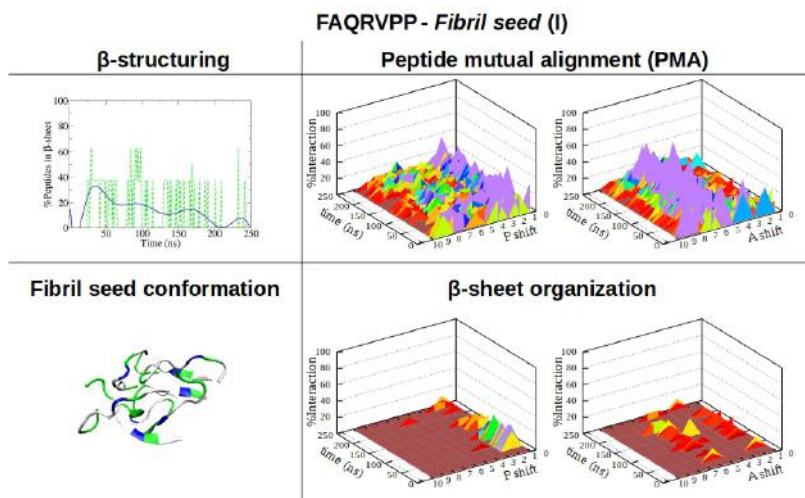


FIGURE 4.5: Shift profiles and  $\beta$ -structuring propensity of FAQ SAPs, 1st replica. FAQ peptides didn't show any preferential mutual alignment. This tendency is also reflected in  $\beta$ -sheet organization. Such features were due to the " $\beta$ -breaker" effect of Pro residues.

Sequence ID	Sequence	Box size (nm)	Simulation Classification	N <sup>o</sup> of peptides	N <sup>o</sup> of sim x Time (ps) x N <sup>o</sup> of seed
(LDLK) <sub>8</sub>	LDLKLDLKLDLK	12.4 x 12.4 x 12.4	Axial Stretching	8	5 x 300 x 3
(LDLK) <sub>8</sub>	LDLKLDLKLDLK	12.4 x 12.4 x 12.4	Bending	8	5 x 300 x 3
(LDLK) <sub>96</sub>	LDLKLDLKLDLK	56.1 x 10 x 8	Axial Stretching	96	5 x 1000 x 1
(LDLK) <sub>96</sub>	LDLKLDLKLDLK	28 x 30 x 8	Bending	96	5 x 1000 x 1
FAQ-(LDLK) <sub>8</sub>	FAQRVPPGGGLDLKLDLKLDLK	17 x 8 x 8	Axial Stretching	8	5 x 600 x 3
FAQ-(LDLK) <sub>8</sub>	FAQRVPPGGGLDLKLDLKLDLK	8 x 17 x 8	Bending	8	5 x 1000 x 3
FAQ-(LDLK) <sub>96</sub>	FAQRVPPGGGLDLKLDLKLDLK	90 x 10 x 8	Axial Stretching	96	5 x 1000 x 1
FAQ-(LDLK) <sub>96</sub>	FAQRVPPGGGLDLKLDLKLDLK	45 x 45 x 8	Bending	96	5 x 2000 x 1

FIGURE 4.6: UA-SMD simulations setup. The fibril seeds obtained through CG-MD simulations have been used as starting configurations of UA-SMD simulations. Each system was simulated in explicit water box and submitted to five simulations differing for the initial velocity distribution.

mimic the biological assays used in single-molecule experiments to assess the mechanical properties (or the persistence length) of bio-filaments. SMD simulations have been used to obtain additional nanoscale details hardly available



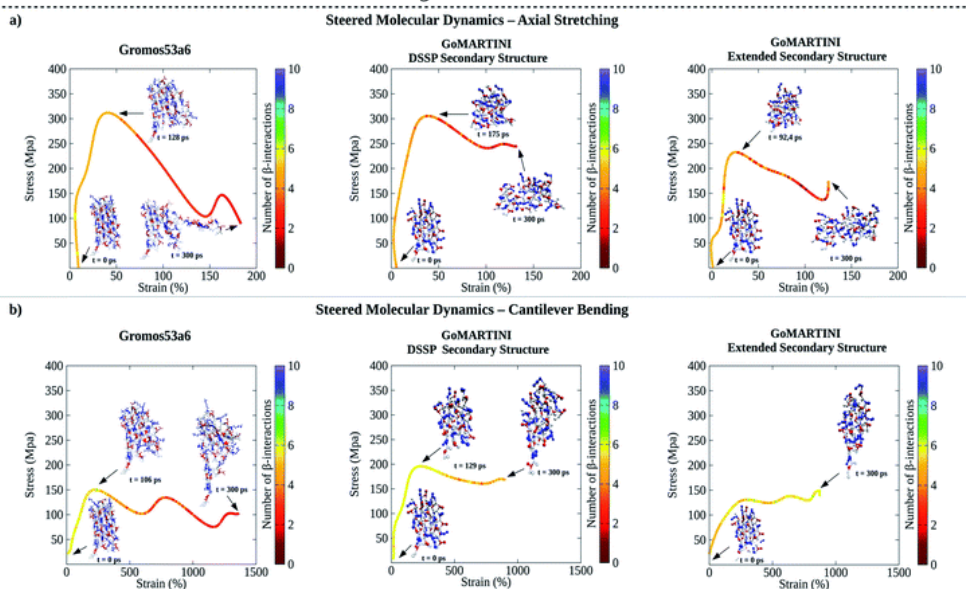
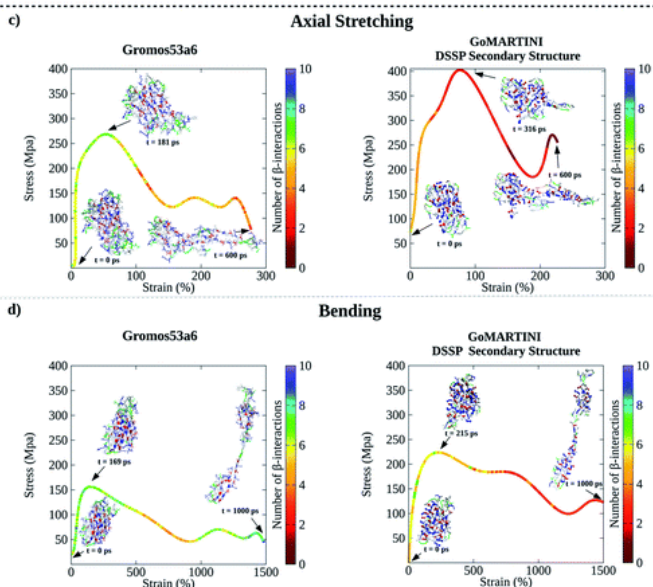
Sequence ID	Sequence	Box size (nm)	Simulation Classification	N° of peptides	N° of sim x Time (ps) x N° of seed
(LDLK) <sub>3</sub>	<b>LDLKLDLKLDLK</b>	12.4 x 12.4 x 12.4	Axial Stretching	8	5 x 300 x 3
(LDLK) <sub>3</sub>	<b>LDLKLDLKLDLK</b>	12.4 x 12.4 x 12.4	Bending	8	5 x 300 x 3
(LDLK) <sub>3</sub>	<i>LDLKLDLKLDLK</i>	12.4 x 12.4 x 12.4	Axial Stretching	8	5 x 300 x 3
(LDLK) <sub>3</sub>	<i>LDLKLDLKLDLK</i>	12.4 x 12.4 x 12.4	Bending	8	5 x 300 x 3
(LDLK) <sub>3</sub>	<b>LDLKLDLKLDLK</b>	56.1 x 10 x 8	Axial Stretching	96	5 x 1000 x 1
(LDLK) <sub>3</sub>	<b>LDLKLDLKLDLK</b>	28 x 30 x 8	Bending	96	5 x 1000 x 1
(LDLK) <sub>3</sub>	<i>LDLKLDLKLDLK</i>	56.1 x 10 x 8	Axial Stretching	96	5 x 1000 x 1
(LDLK) <sub>3</sub>	<i>LDLKLDLKLDLK</i>	28 x 30 x 8	Bending	96	5 x 1000 x 1
FAQ-(LDLK) <sub>3</sub>	<b>FAQRVPPGGGLDLKLDLKLDLK</b>	17 x 8 x 8	Axial Stretching	8	5 x 600 x 3
FAQ-(LDLK) <sub>3</sub>	<b>FAQRVPPGGGLDLKLDLKLDLK</b>	8 x 17 x 8	Bending	8	5 x 1000 x 3
FAQ-(LDLK) <sub>3</sub>	<i>FAQRVPPGGGLDLKLDLKLDLK</i>	90 x 10 x 8	Axial Stretching	96	5 x 1000 x 1
FAQ-(LDLK) <sub>3</sub>	<i>FAQRVPPGGGLDLKLDLKLDLK</i>	45 x 45 x 8	Bending	96	5 x 2000 x 1

FIGURE 4.7: CG-SMD simulations setup.  $(LDLK)_3$  and FAQ- $(LDLK)_3$  fibril (seed) mechanical features were evaluated through GoMARTINI SMD simulations. Secondary structure (SS) parameters have been assigned through DSSP algorithm or imposed as fully extended according to experimental evidences; the residues with extended SS have been highlighted in bold, whereas the residues with coil SS have been highlighted in italic.

from single-molecule spectroscopy experiments, (e.g. non-covalent interaction interplay occurring within protein folding transitions).[69] Indeed, such experiments have been used to (1) compare and validate the GoMARTINI approach against the Gromos53a6 one (see 10.1, 10.2 and 10.3)[75] and (2) to classify the bending failure mechanisms of peptide seeds and fibrils related to hydrogen bond and non-covalent interaction deformations (see 10.4 and 10.5).[69][192]

### Failure conformations of $(LDLK)_3$ Fibril Seeds

As shown in Fig. 4.8a, UA-SMD and CG-SMD axial stretching simulations identified different failure conformations of the  $(LDLK)_3$  fibril seed. Indeed, in UA-SMD the failure took place at the maximum stress of 323 MPa ( $\epsilon = 52\%$ ), whereas in GoMARTINI it happened at 310 MPa ( $\epsilon = 28\%$ ) and 236 MPa ( $\epsilon = 36\%$ ) for SS parameters assigned through DSSP or as all-extended respectively (see also 10.1 and 10.2).

**(LDLK)<sub>3</sub> - Fibril seed (B)****FAQ-(LDLK)<sub>3</sub> - Fibril seed (C)**

**FIGURE 4.8: Computational nanomechanics characterization of SAP fibril seeds.** The number of  $\beta$ -interactions refers to the number of  $\beta$ -contacts among  $(LDLK)_3$  moieties identified through Morphoscanner. (a) UA-SMD maximum stress of axial stretching was equal to 323 MPa ( $\epsilon = 52\%$ ;  $t = 128$  ps; no of  $\beta$ -interactions = 6). GoMARTINI maximum stress was influenced by SS assignment: in the case of DSSP SS assignment, the maximum stress was equal to 310 MPa ( $\epsilon = 28\%$ ;  $t = 175$  ps; no of  $\beta$ -interactions = 6), whereas with extended SS parameters, it was equal to 236 MPa ( $\epsilon = 36\%$ ;  $t = 92$  ps; no of  $\beta$ -interactions = 6). (b) UA-SMD axial bending maximum stress was equal to 163 MPa ( $\epsilon = 250\%$ ;  $t = 106$  ps; no of  $\beta$ -interactions = 6). Again, maximum stress in GoMARTINI was heavily affected by SS parameters: i.e. it was 200 MPa ( $\epsilon = 250\%$ ) and 150 MPa ( $\epsilon = 1000\%$ ) for respectively DSSP-assigned and extended SS parameters. (c) UA-SMD axial stretching test highlighted the failure conformation and stress value for FAQ- $(LDLK)_3$  at 281 MPa ( $\epsilon = 50\%$ ). Such a conformation was similar to the one identified through GoMARTINI ( $\sigma = 400$  MPa;  $\epsilon = 75\%$ ). In the case of FAQ- $(LDLK)_3$ , DSSP assigned the extended SS parameters to the  $(LDLK)_3$  self-assembling backbone, whereas it assigned random coil SS parameters to residues comprising the functional motif. (d) UA-SMD axial bending maximum stress was equal to 160 MPa ( $\epsilon = 50\%$ ). Instead, GoMARTINI maximum stress was 247 MPa ( $\epsilon = 220\%$ ).

Despite these differences, failure conformations were characterized by the same number of  $\beta$ -interactions (i.e. 6), suggesting similar failure mechanisms. However, it became clear that MARTINI bead-type assignment significantly influenced the elastic moduli of  $(LDLK)_3$  seeds in GoMARTINI. Indeed, the assignment of backbone and side-chain beads corresponding to coiled secondary structures (SS) overestimated the overall elastic modulus values detected with extended SS parameters, (10.1 and Fig. 4.9a).[59]

Similarly, in bending tests, aimed at estimating the shear moduli (Fig. 4.8b and 4.9c†), Morphoscanner analysis at failure revealed comparable  $\beta$ -sheet arrangements of the fibril seeds, while failure stresses in UA-SMD and GoMARTINI simulations were 163 MPa ( $\epsilon = 250\%$ ) and 200 MPa/150 MPa ( $\epsilon = 250\%$  and SS parameters assigned via DSSP/  $\epsilon = 1000\%$  and all-extended SS parameters) (see 10.1 and 10.2). Different  $\epsilon$  values observed in GoMARTINI simulations were attributable to the level of interactions (pointing at the Lennard-Jones potential well depth) among MARTINI grains. In more detail, the DSSP algorithm assigned random coil SS parameters to  $(LDLK)_3$  backbone grains, resulting in polar backbone grains. Instead, when extended SS parameters were assigned, the backbone grains were modeled as non-polar. The interactions among polar grains are stronger than the interactions among non-polar grains.[50] This implied a general increase of fibril stiffness for  $(LDLK)_3$  when GoMARTINI mapping via DSSP yielded SS parameters set to random coil conformation.

By comparing the average elastic modulus and shear modulus of each fibril seed we extracted

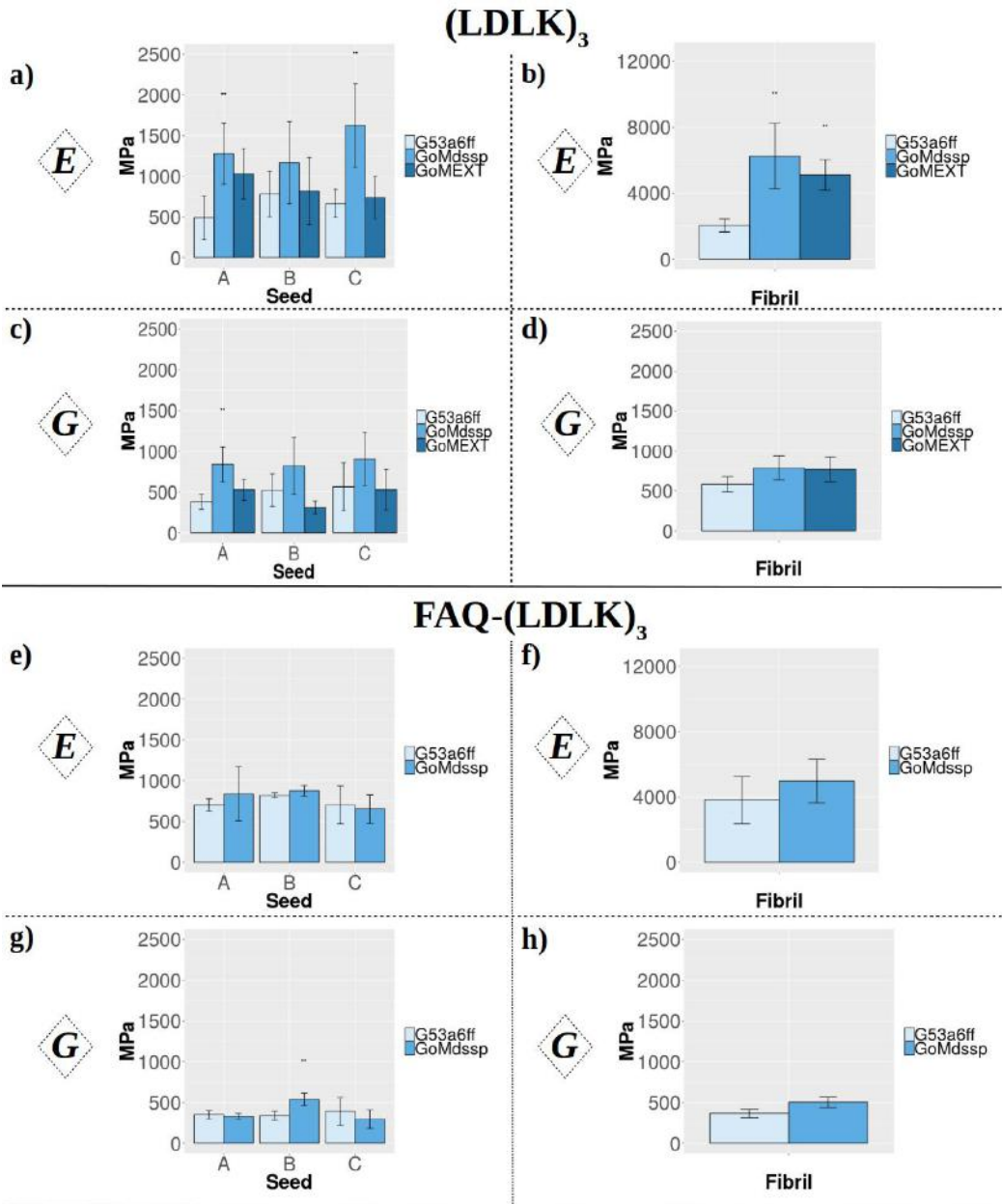


FIGURE 4.9: **Statistical analysis of Young's and Shear Moduli.** G53a6ff refers to the UA-SMD approach. GoMdssp refers to the CG-SMD approach with SS parameters assigned as shown in figures 10.1 and 10.3 GoMEXT refers to CG-SMD approach with SS parameters assigned as shown in Fig. 10.2. E refers to the Young's Modulus and G to the shear modulus. The GoMdssp approach provided similar results to G53a6ff approach.

the shear contribution ratio, a value pointing at the strain distribution within the fibril seeds (see 10.4).[\[69\]](#) In both UA-SMD and GoMARTINI SMD, the shear contribution ratio described similar bending failure mechanisms within  $(LDLK)_3$  fibril seeds. Indeed, as shown in 10.4, the  $(LDLK)_3$  bending failure was predominantly dominated by shear stresses, where non-covalent interactions stretched orthogonally to their directions. Moreover, the axial stretching depicted in UA-SMD stress–strain curves showed multiple peaks owing to a slip-stick motion taking place only when interacting surfaces in  $\beta$ -sheet nanocrystals (adjacent  $\beta$ -strands) are rigidly stabilized and act cooperatively. Such a feature was less evident in GoMARTINI-SMD stress–strain curves, probably due to the smoother energy function describing the interactions among grains in the MARTINI model.[\[50\]\[59\]\[75\]\[68\]](#)

### Failure conformations of FAQ-(LDLK)<sub>3</sub> Fibril Seeds

The failure conformations of FAQ-(LDLK)<sub>3</sub> fibril seeds showed also small differences between the adopted modeling approaches (see 10.3), with axial stretching failure conformations at maximum stresses of 281 MPa ( $\epsilon = 50\%$ ) and 400 MPa ( $\epsilon = 75\%$ ) in UA-SMD and CG-SMD simulations respectively (Fig. 4.8c). In addition, bending stress values were 160 MPa ( $\epsilon = 50\%$ ) and 247 MPa ( $\epsilon = 220\%$ ) in UA-SMD and CG-SMD simulations respectively (Fig. 4.8d). These values were similar to those observed in the simulations of (LDLK)<sub>3</sub> seeds. Such evidence, due to the similar SS parameter assignments, suggested that the presence of the functional motif slightly affected the failure mechanism of SAP fibril seeds.

This observation was corroborated by Morphoscanner analysis and by shear contribution ratio calculation, identifying similar bending failure mechanisms (10.5) for both FAQ – (LDLK)<sub>3</sub> and (LDLK)<sub>3</sub>, mainly led by shear stresses.

### Failure conformations of SAPs Fibrils

To elucidate the failure mechanisms of SAP fibrils, two fibril models, resembling the geometry of amyloid fibrils,[180][193] were built taking into account the outcome analysis of one-pot CG-MD (Fig. 10.10) and tested through the SMD approach (see Figures 4.6 and 4.7). The initial structure of the  $(LDLK)_3$  fibril was imposed by patching multiple fibril seeds sharing the molecular conformation shown in Fig. 4.3a. Also, in the case of  $FAQ - (LDLK)_3$ , UA-MD simulations pointed out that FAQ functionalization weakly affects the  $(LDLK)_3$  moieties' alignment (Figures 4.5, 10.11 and 10.12). Then, keeping in mind the results from one-pot CG-MD (Fig. 10.10) of  $(LDLK)_3$ , we postulated that, also for  $FAQ - (LDLK)_3$ , alignment within fibrils resembled that observed in fibril seeds (Fig. 4.3b).

$(LDLK)_3$  fibril conformations at failure, as shown for fibril seeds, were heavily affected by SS assignment (see 10.1 and 10.2). Indeed, CG-SMD axial stretching simulations overestimated the average Young's modulus ( $E$ ) (Fig. 4.9b) found in UA-SMD (Fig. 4.10a-c), whereas CG-SMD bending simulations provided comparable shear modulus ( $G$ ) values (Fig.4.9d) to those detected from UA-SMD (Fig. 4.10d-f). By comparing the average elastic and shear moduli of the  $(LDLK)_3$  fibril, the bending failure mechanism was predominantly dominated by the deformation of non-covalent interactions along the fibril direction (Fig. 10.4).

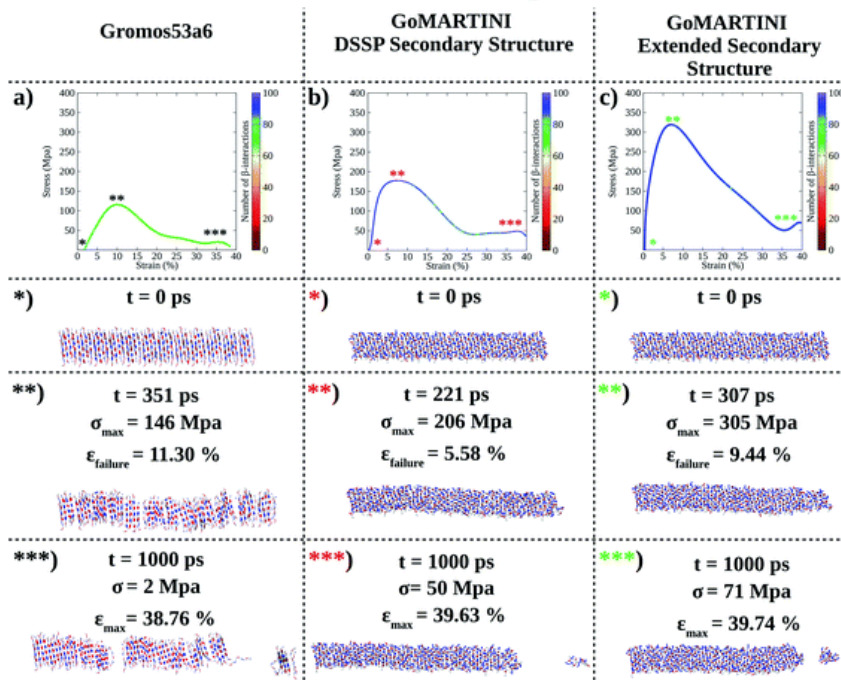
The same tendencies have been also observed in the  $FAQ - (LDLK)_3$  fibril (Fig. 4.11a-d, Fig. 4.9f, h and Fig. 10.5).

The evidence from the atomistic model demonstrated that the strain distribution characterizing the bending failure mechanism of SAP nano-filaments is length-dependent and mainly influenced by the geometrical properties of peptide aggregates.[109][182][105][69] Despite the influence of CG bead types on elastic and shear moduli, similar evidence was also confirmed in the CG model. The fibril bending failure was dominated by the deformation of non-covalent interactions along the fibril direction (see Figures 10.4 and 10.5).

Interestingly, the FAQRVPP functional motif did not contribute significantly to the Young and shear moduli of the fibril seeds: this was the case for both UA-SMD and CG-SMD (Fig. 4.9a, e, c and g). Consequently, in  $FAQ - (LDLK)_3$  fibrils as well, the strain distribution was predominantly influenced by the length of peptide assemblies (Fig. 4.9b, d, f and h). Indeed, as shown in figures 10.4 and 10.5, in the investigated fibril seeds, the shear contribution ratio pointed out that shear deformations were predominant in bending deformations, whereas in fibril systems, the shear deformations contributed less than 15% over the total bending deformations. Such evidence clearly shows that the shear strain distribution is less homogeneous in fibrils than in fibril seeds, causing the propagation of several structural defects in fibrils (see Figures 4.8, 4.10 and 4.11). Finally, fibril failure mechanisms have not been affected by stacking fibril seeds next to each other (Fig. 4.12).



## Axial Stretching



## Bending

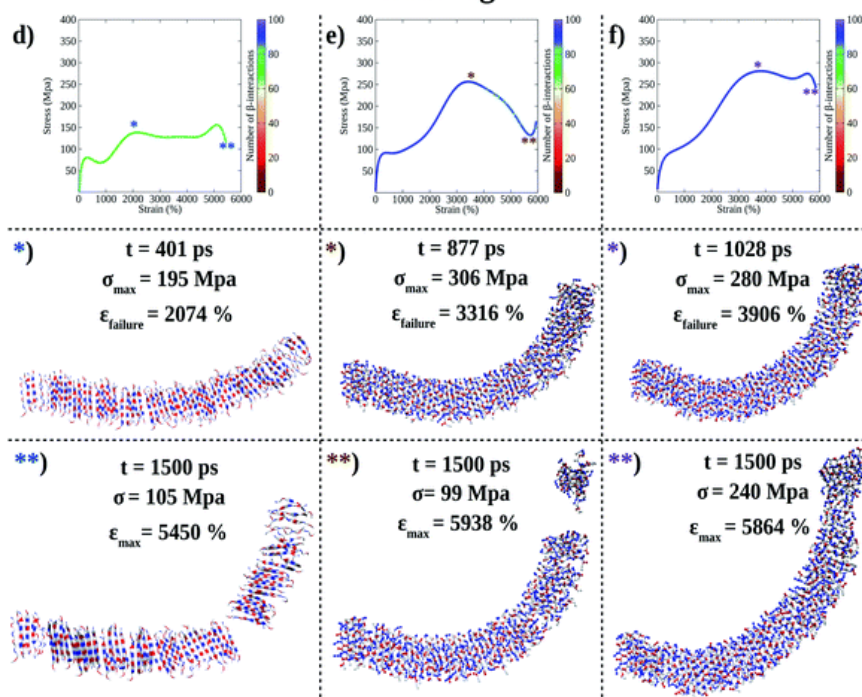
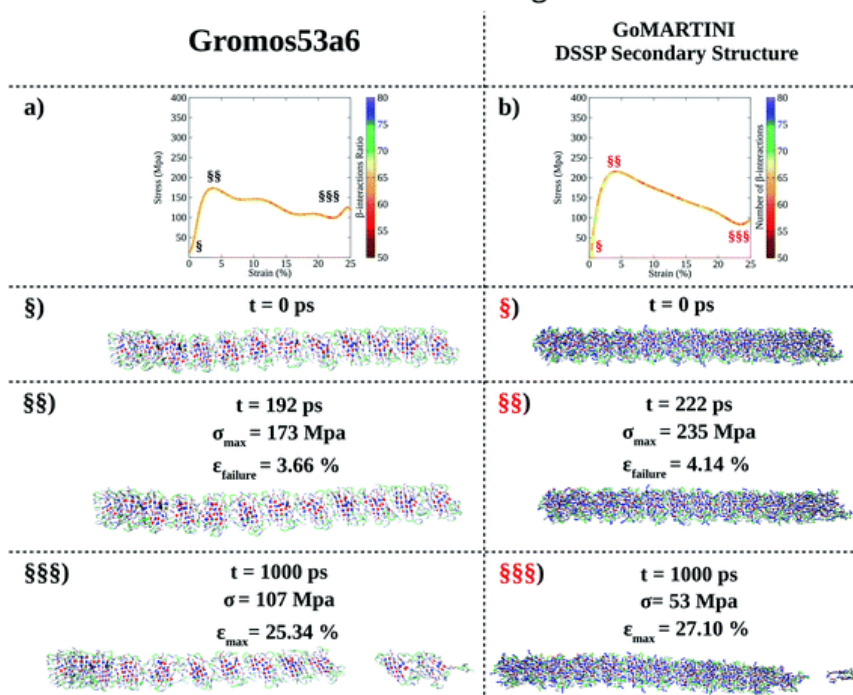




FIGURE 4.10: **Computational nanomechanics characterization of the  $(LDLK)_3$  fibril.** The number of  $\beta$ -interactions refers to the number of  $\beta$ -contacts detected among  $(LDLK)_3$  backbones. (a) UA-SMD axial stretching failure stress was 146 MPa. In GoMARTINI, the maximum stress was influenced by SS parameter assignments: (b) in the case of DSSP-derived SS parameters, the maximum stress was equal to 206 MPa, (c) whereas with extended SS parameters, it was 305 MPa. (d) UA-SMD axial bending failure stress was equal to 195 MPa. As expected, in GoMARTINI, the maximum stress was again heavily affected by SS assignment: (e) with DSSP it was equal to 306 MPa, (f) while with extended SS parameters it was 280 MPa. In the detected failure conformations in UA-SMD simulations, fibrils display multiple rupture points; this may be due to the enhanced stability of  $\beta$ -sheet structures when modeled with the Gromos force field. This was also demonstrated through Morphoscanner analysis (see Chapter 10 for details), which identified the same number of  $\beta$ -interactions throughout UA-SMD simulations. This feature was not reflected in GO-SMD simulations. Indeed, Morphoscanner identified small variations in the number of  $\beta$ -interactions.

## Axial Stretching



## Bending

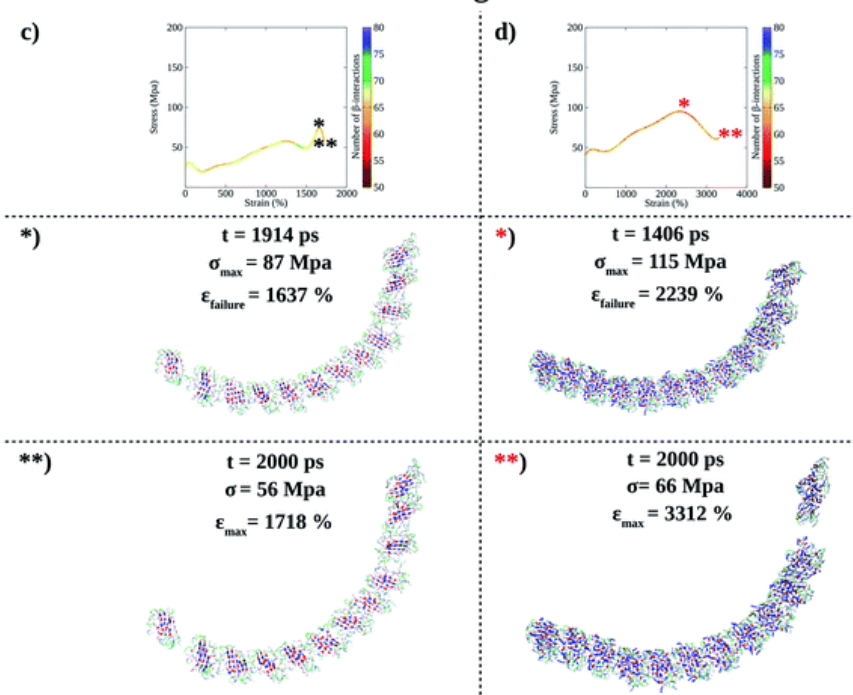


FIGURE 4.11: **Computational nanomechanics characterization of the FAQ-(LDLK)<sub>3</sub> fibril.** The number of  $\beta$ -interactions refers to the  $\beta$ -contacts among (LDLK)<sub>3</sub> backbones detected with Morphoscanner (see Chapter 10 for details). (a) UA-SMD axial stretching maximum stress was 192 MPa. (b) GoMARTINI maximum stress was equal to 235 MPa. (c) UA-SMD axial bending maximum stress was 87 MPa. (d) Instead, GoMARTINI maximum stress was equal to 115 MPa. As shown for (LDLK)<sub>3</sub> fibrils, Morphoscanner identified a constant number of  $\beta$ -interactions in UA-SMD simulations, whereas it identified little variation in CG-SMD simulations: this can be ascribable to the more fragile rupture observed in UA-SMD simulations.

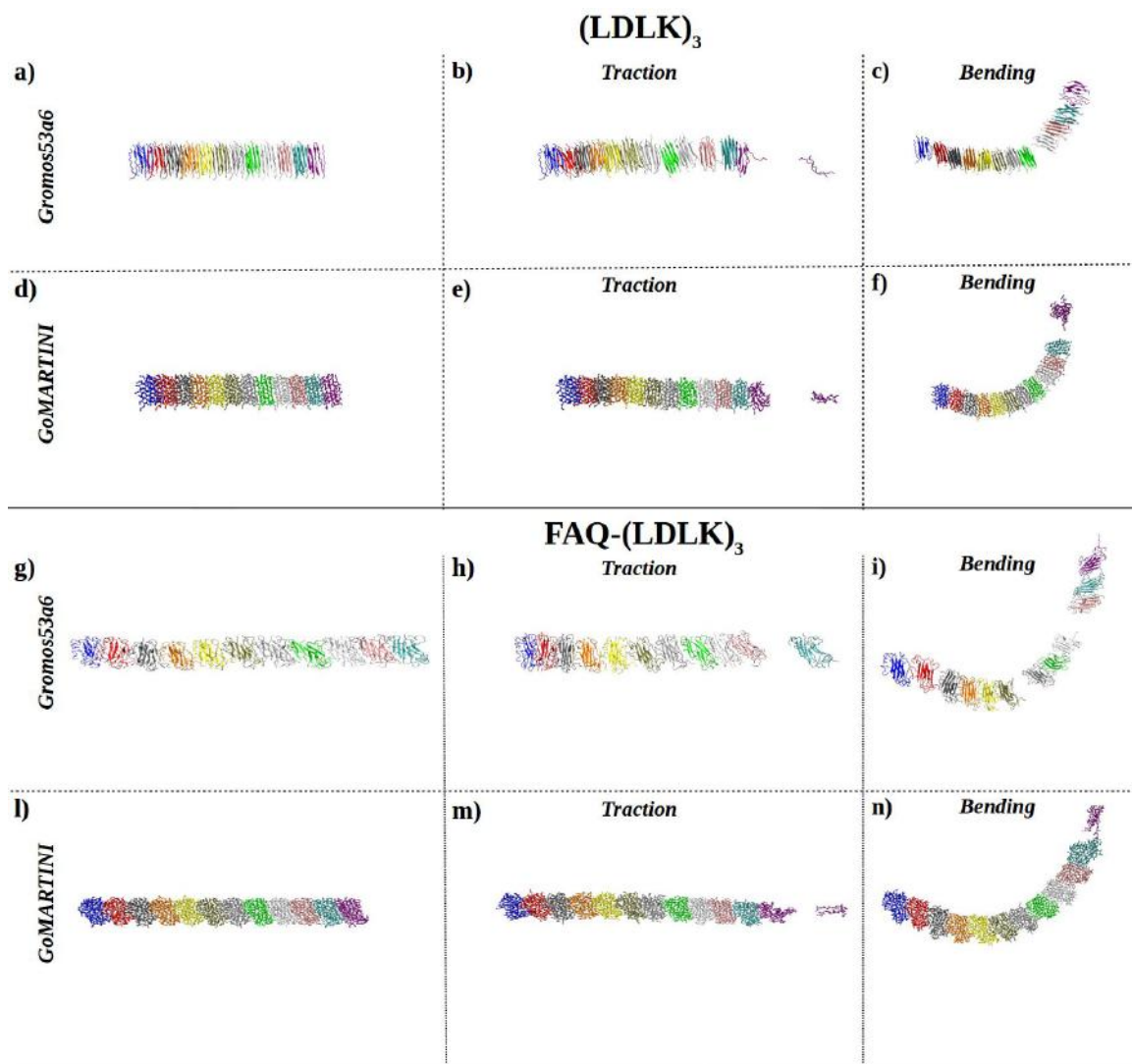


FIGURE 4.12: **Graphical representation of failure mechanism of SAPs fibrils.** Gromos53a6 refers to the UA-SMD approach, whereas GoMARTINI refers to the CG-SMD setup. The  $(LDLK)_3$  and  $FAQ-(LDLK)_3$  fibril structures have been built by stacking fibril seed structures, which are highlighted by different colors. In UA-SMD (b) and CG-SMD axial stretching simulations (e) the  $(LDLK)_3$  fibrils shown similar failure mechanisms, which involved the displacement of two  $\beta$ -strands belonging to the un-restrained end of the models (as depicted in a and d). By analyzing bending UA-SMD (a) and CG-SMD (f) simulation of  $(LDLK)_3$  fibrils, it has been possible to observe little differences in the failure mechanisms. Indeed, the failure rupture points don't correspond to fibril seed contact-point. The same conclusion can be addressed also for  $FAQ-(LDLK)_3$  fibrils, by visual inspection of failure structures reported in h), i), m) and n).

## 4.5 CONCLUSIONS

In the present study, SMD simulations have been used to investigate the mechanical features of  $(LDLK)_3$  and  $FAQ - (LDLK)_3$  SAPs. The evidence from SMD simulations pointed out that the shear modulus of fibrils is higher in  $(LDLK)_3$  than in  $FAQ - (LDLK)_3$  (Fig. 4.9d–h): such results well correlate with previous rheological data of  $FAQ - (LDLK)_3$  and  $(LDLK)_3$  hydrogels, featuring a higher shear modulus for  $(LDLK)_3$  than for  $FAQ - (LDLK)_3$  hydrogels.[21][109]

In addition, the comparison of the elastic and shear moduli of fibrils demonstrated that bending failure modes depended on the length of the fibrils, while it was less influenced by the presence of the FAQ functional motif. Indeed, fibril seeds' bending failure mechanism was mainly ruled by shear deformation of non-covalent bonds (e.g. H-bonds), whereas fibrils' failure mechanism was led by tensional stretching of non-covalent bonds resulting in multiple failure points.

In summary, the GoMARTINI force-field, provided that the assignment of CG-bead types is crucial for trustworthy results, is suitable for the investigation of key mechanical features of peptidic nanostructures. GoMARTINI-SMD simulations provided comparable results to those obtained through UA-SMD.[75] It has also been observed that using the GoMARTINI force-field allows for the reduction of computational costs, accelerating the production phase by about 10 times ( 10.6 and 10.7).[194] This evidence corroborates the strategy of using GoMARTINI-SMD for the investigation of larger SAP systems and other biomaterials.

## Chapter 5

# Unveiling Interactions between SAPs and Neural Membranes

## 5.1 INTRODUCTION

Neural membranes are complex assemblies of lipids, proteins that separate intra-cellular from the extra-cellular environment and are also involved in neural preservation and functioning. Indeed, neural membranes are the main sites associated with signal transduction and triggering of action potentials. The different sets of lipids can mediate neuronal communications by specific interactions with proteins and through bilayer-protein interactions.[195][196] In addition, non-uniform lipid mixing and lipid segregation can modulate membrane properties, heavily influencing conductance, aggregation and trafficking.[197] [198][199] Then, the investigation of interactions among neural membrane and SAPs will be useful for the comprehension of the improvement of neural tissue engineering applications.

Neural tissue engineering is aiming to revolutionize the future of medicine. During the last two decades, several approaches, based on the use of biocompatible hydrogels, have been tested as potential medical treatments for several pathological conditions (spinal cord injury, traumatic brain injury and degenerative diseases). Self-assembling peptides (SAPs) hydrogels represent one of the most promising candidate for tissue engineering applications.[17][18][19][20] More encouraging results can be obtained when SAPs hydrogels are seeded with adult neural stem cells (NSCs).[200][201] In order to deepening the understanding of SAPs hydrogels effects on NSCs proliferation and differentiation, it is necessary to investigate interactions among neural membrane and hydrogels, at the molecular level.

Coarse-grained molecular dynamics (CG-MD) simulations have been proven to be suitable for the modeling of membrane of several organism and organelles.[202][203] MARTINI CG-modeling has been largely used for the investigation of mechanical deformations and interactions of lipid and plasma membranes. In addition, CG-MD simulations have proven to be suitable for the elucidation of "lipid domains" fluctuations depending on the environmental conditions.[202][204][205]

Despite the growing interest in this approach, few studies about neural membranes are available.[206] Further, MARTINI force-field and its variant GoMARTINI have been largely used for the structural and mechanical characterization of SAPs systems.[75][189] (See also Chapter 4) In this work, an innovative CG frameworks, for the investigation of interactions among SAPs and neural membrane, is presented.

A series of even more complex models of neural membrane have been simulated in presence of (*LDLK*)<sub>3</sub> SAPs. More in details, the neural membrane was modeled using the MARTINI force-field, then lipid densities and motion patterns were analyzed in order to understand the dynamics of "lipid domains". In order to reproduce a minimal model of NSCs membrane, and taking into account the effect of ions concentrations on lipid dynamics, the Aquaporin 4 has

been embedded within the neural membrane. Indeed, Aquaporin 4 is the most expressed protein water channel in NSCs.[207][208][209] Lastly, a system constituted by two neural membranes, separating two environments which differ in ion contents, has been modeled in order to resemble the feature of a NSC. Such approach allowed to elucidate effects of  $(LDLK)_3$  SAP fibrils on lipid domains dynamics, shedding a new light on the *in-silico* investigation of mechanisms ruling biocompatibility of innovative materials for neural tissue engineering applications.



## 5.2 MATERIAL AND METHODS

### 5.2.1 Bilayer Composition

The Neuronal Membrane composition was derived and optimized from *Ingólfsson et al.*[206] An overview of the neural membrane is given in Fig. 5.1. The starting bilayer structures has been built using *insane*, adding a total of 1335 lipids molecules.[210] The neural membrane is mainly constituted by Phosphatidylcoline (PC), Phosphatidylethanolamine (PE), Sphingomyelin (SM), Phosphatidylserine (PS), Glycolipid, Cerebrosides, Phosphatidylinositol (PI), Phosphatidylinositol phosphates (PIPs), Ceramides, Diacylglycerols and Cholesterol (CHOL). As shown in Fig 5.1, the neural membrane mainly consists of unsaturated lipids and cholesterol in both leaflets. The main differences among the two leaflets are: 1) The presence of Glycolipid only in the outer leaflet; 2) The presence of PIPs and PS only in the inner leaflet; 3) The higher concentration of SM in the outer leaflet than in the inner one. In table 11.1 are listed the specific lipids types used and their counts in the inner/outer leaflets.

### 5.2.2 CG-MD Simulations of Neural Membranes

Simulations were performed using the GROMACS simulation package version 4.6.5, with the standard Martini version 2.2 simulation settings.[59] After initial energy minimization (1000 steps), a short equilibration phase of 1 ns was applied. The production phase, as well as the equilibration phase, was performed with a time-step of 20 fs, at temperature of 310 K set using velocity-rescaling thermostat, with a time constant of 1ps (2ps for equilibration phase).[173] A semi-isotropic pressure of 1 bar was maintained with parrinello-rahman barostat, with a compressibility of  $3 \cdot 10^{-4} \text{ bar}^{-1}$  and a relaxation time constant of 12 ps. Production runs of 1  $\mu\text{s}$  were performed without position restraints on lipid beads, with a time-step of 10 fs.

### 5.2.3 Interactions among Neural Membrane and $(LDLK)_3$ monomers

Lipids domains organization is transient and depending on the environmental conditions. As previously demonstrated by other groups, the interactions of plasma membrane with protein structures heavily affects membrane properties.[196][211] In order to elucidate the effect of  $(LDLK)_3$  monomers on lipids domains organization, a MARTINI CG-MD simulation, in similar conditions as in section 5.2.2, has been performed. The main difference consists in the addition of 13  $(LDLK)_3$  monomers, in order to reproduce the hydrogel forming concentration of 1% w/v, analogously to the simulations performed in Chapter 2.

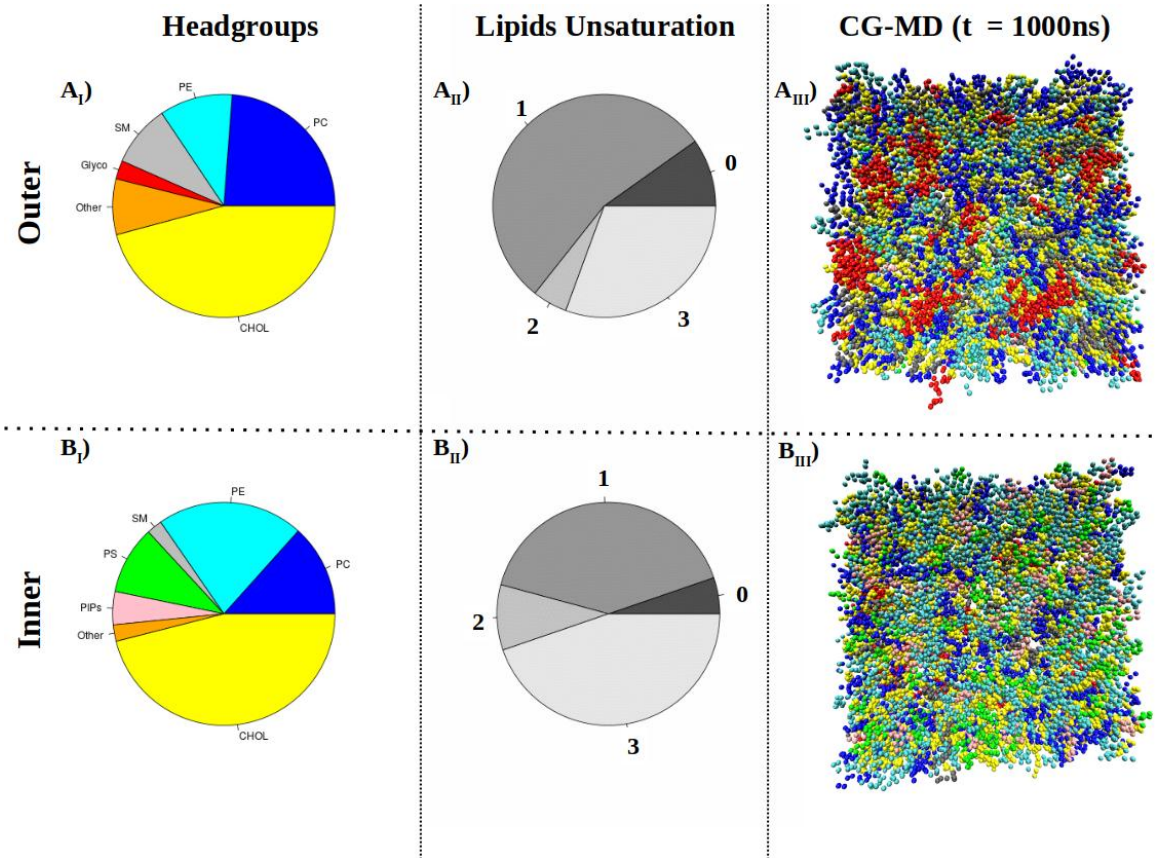


FIGURE 5.1: **Neural Membrane lipid distributions.**  $A_I)$  and  $B_I)$  pie charts of the overall distribution of the main lipids head-groups in the outer and inner leaflet, respectively, after  $1\mu s$  of CG-MD simulations.  $A_{II})$  and  $B_{II})$  pie charts show the overall distribution of unsaturated lipids analogously to  $A_I)$  and  $B_I)$ , respectively. The lipids in the snapshots of outer ( $A_{III})$  and inner ( $B_{III})$  leaflets are colored as follows: PC, *blue*; PE, *cyan*; SM, *gray*; PS, *green*; glycolipids (Glyco), *red*; PIPs, *pink*; Other, *orange*; cholesterol(CHOL), *yellow*.

#### 5.2.4 Embedding Aquaporin 4 in Neural Membrane

The NSCs membrane contains hundred of different proteins and lipids. Aquaporin 4 (AQP4) is the mainly expressed water channel protein in mammalian NSCs membrane, and play a pivotal role in NSCs differentiation. AQP4 is also involved in brain water balance, astroglial cell migration and in the neural signal transduction. [207][208][209] In addition, AQP4

overexpression in brain tissues is associated with pathological conditions such as spongiform encephalopathy, neuromyelitis optica, multiple sclerosis and Alzheimer's disease.[209] Then, in order to build a more complex model of NSCs membrane, CG model of AQP4 has been embedded within neural membrane (See Section 5.2.1 for details). The starting structure of Aquaporin 4 (PDB ID: 3GD8), after removal of all the non-protein molecules, was converted in a CG MARTINI model. In order to stabilize secondary structure arrangements, an elastic network was applied on atom pairs within a cutoff of 0.9 nm. The elastic network has been applied on each monomer of the tetramer.[212] One copy of CG protein was placed in a simulation box of 19 x 19 nm, and lipids, in a composition corresponding to the neural membrane model developed by Ingölfsson and colleagues (See Section 5.2.1 for details), were added using *insane*, for a total of ca. 1200 lipids molecules in each membrane. Water molecules, counterions and 150 mM NaCl were added in order to reproduce the physiological conditions.

### 5.2.5 CG-MD simulations of Aquaporin 4 Embedded in Neural Membranes

Prior the production phase, Aquaporin 4 (AQP4) embedded in neural membrane systems underwent to an initial energy minimization of 1000 steps. Then, the systems underwent to an equilibration run of 100 ps, with a time-step of 2 fs. A further equilibration run of 1000 ps with a time-step of 10 fs was performed in the presence of position restraints on all the protein beads, with a force constant of 100 kJ mol<sup>-1</sup> nm<sup>-2</sup>. The production phase, as well as the equilibration runs, were performed by applying a constant temperature of 310 K using velocity-rescaling, with a time constant of 1 ps (2ps for equilibration phase). The pressure conditions are the same used in 5.2.2. Production runs of 1  $\mu$ s were performed without position restraints on lipid beads, with a time-step of 10 fs.

### 5.2.6 CG-MD Simulations of (LDLK)<sub>3</sub> SAPs Fibril

A (LDLK)<sub>3</sub> fibril model has been built according to the evidence obtained in section 4.4.2. More in details, the SAPs fibril has been built resembling the geometry of an amyloid fibril as shown in section 4.8. Then, the fibril model underwent to an initial energy minimization of 1000 steps. Prior the buiding of the minimal model of NSCs, as illustrated in 5.2.7, the systems underwent to an equilibration run of 100 ps, with a time-step of 2 fs, followed by another equilibration run of 100 ps, with a time-step of 10 fs.

### 5.2.7 CG-MD simulations of minimal model of NSCs with $(LDLK)_3$ fibril

In order to investigate the interactions among SAPs fibril and NSCs, two systems have been built as shown in Fig.5.2. Both systems resemble the chemical-physical features of neural membranes, which are not involved in the "active" propagation of action potentials. Indeed, membranes (for composition see Table 11.1) embed an AQP4 each one, and are placed at a distance of  $\approx 30$  nm away each other. Then, the membranes separate two regions, which are characterized by different ion concentrations, as shown in Table 11.2. Such ion concentrations establish a membrane potential of  $\approx -70$  mV. Then, in the first system, a  $(LDLK)_3$  fibril (See 5.2.6 for additional details) has been placed at a distance of  $\approx 30$  nm from membrane (I). Instead, in the second system, a  $(LDLK)_3$  fibril has been placed close to the neural membrane (I) (See fig. 5.2). Both systems underwent to the same molecular dynamics protocol previously illustrated in 5.2.5, differing only in production run durations. Indeed, **System I** underwent to a production run of 1500 ns, with a time-step of 10 fs, in order to investigate long-range interactions with neural membranes. Instead, **System II** underwent to a production run of 750 ns, in order to investigate the short-range interactions with neural membranes. The length of production runs have been settled after several attempts to cope with limited computational resources and provide adequate description of mechanisms that lead to the interactions among peptide fibrils and neural membranes.

### 5.2.8 CG-MD simulation of minimal model of ANSCs with $(LDLK)_3$ monomers

In order to elucidate the interactions among SAPs monomers and NSCs, a system have been built following a similar approach to that illustrated in Section 5.2.7. In this case, 73  $(LDLK)_3$  monomers have been added in the extra-cellular environment, instead of a pre-build fibril. The system underwent to a production run of 1000 ns, with a time-step of 10 fs.

### 5.2.9 Analysis

For the analyses, as shown in Fig. 5.1 and table 11.1, lipids were categorized according to head group. For the tails, lipids were divided into three main classes, as shown in the recent works of *Ingolfsson et al* and *Corradi et al*[202][206][196]: fully-saturated(FS), poly-unsaturated (PU) and cholesterol (CHOL). The FS lipid class consists of DPSM, DPG1, PNG1, DPG3, PNG3, DPGS, DPCE, POP1, POP2 and POP3 (see table 11.1). Whereas, the PU lipid class consists of DPPC, POPC, DOPC, POPE, PFPC, POPS, PAPC, PUPC,

## SAPs Fibril-Neural Membrane CG-MD

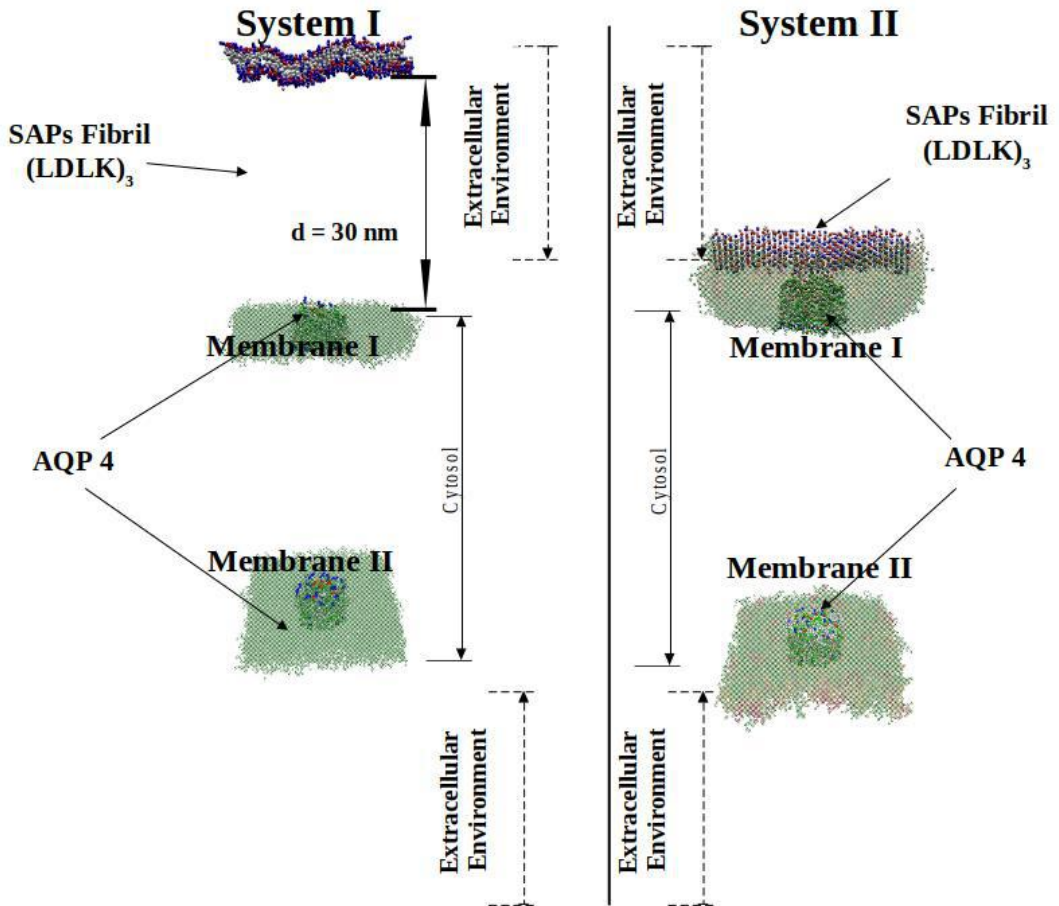


FIGURE 5.2: **CG-MD minimal model of NSCs.** In order to investigate interactions among SAPs fibril and NSCs, two minimal models have been built. Briefly, the geometry of the systems resemble the organization of neural cells. Indeed, two membranes (with Aquaporin 4 embedded) separate two environments: 1) Intracellular environment or *cytosol*; 2) Extracellular environment. These environments differ for ion contents, as shown in table 11.2. In starting configuration of **System I**, a (LDLK)<sub>3</sub> SAPs fibril has been placed at a distance of  $\approx 30$  nm from **Membrane I**. Instead, in starting configuration of **System II** the SAPs fibril has been placed in contact with **Membrane I**.

PIPI, PAPI, PUPI, OIPC, OUPC, PUPE, PAPE (see table 11.1). All the analysis, unless otherwise specified, were performed on the last 500 ns of each simulation system.

### Density Fluctuations maps

Number density maps of lipids in the xy plane were computed using the *g\_densmap* tool in Gromacs and averaged on the last 100 ns of each simulation systems, unless otherwise specified. Then, average density ( $\rho_{ave}$ ) value is calculated at the starting frame of the analysis interval (e.g. frame at 900 ns if the simulation ends at 1000 ns). In order to taking in account enrichment/depletion with respect to a homogeneous mixture, the Density Fluctuations Maps were calculated according to the following equation:

$$\rho_{new} = \left( \frac{\rho_{[i,j]}}{\rho_{ave}} \right) * 100 \quad (5.1)$$

In equation 5.1,  $\rho_{[i,j]}$  correspond to every point in the density map to be reweighted. The new score has the property to be positive for  $\rho_{i,j}$  values larger than  $\rho_{ave}$  and negative value for values smaller than  $\rho_{ave}$ .

### Lipids Motion Patterns

Streamlines are curves tangent to the motion vectors, that describes trajectory of a particle in a stationary vector field at a given time. Formally, given a 2D time-dependent vector field  $v(x, t) = (v_x, v_y)$ , a streamline  $S$  is a parametric curve  $S(\tau)$  defined at time  $t$  and starting from a point  $p$ .  $S(\tau)$  is given by the equation 5.2, with the boundary condition defined as 5.3.

$$\frac{dS}{d\tau} = v(S(\tau), t) \quad (5.2)$$

$$S(0) = p \quad (5.3)$$

Any sample point of the streamline is given by:

$$S(l) = S(0) + \int_0^l v(S(\tau), t) d\tau \quad (5.4)$$

with the curvilinear coordinate  $l \in [-l_1, l_2]$  and  $l_1, l_2 \geq 0$ . In order to track lipid diffusion in CG-MD simulations, the motions have been represented visualizing streamlines. The motions of FS and PU lipids, have been analyzed by tracking PO4 beads. Instead, the motions of CHOL, have been analyzed by tracking ROH beads.

## 5.3 RESULTS

### 5.3.1 Identification of lipid domains in Neural Membranes

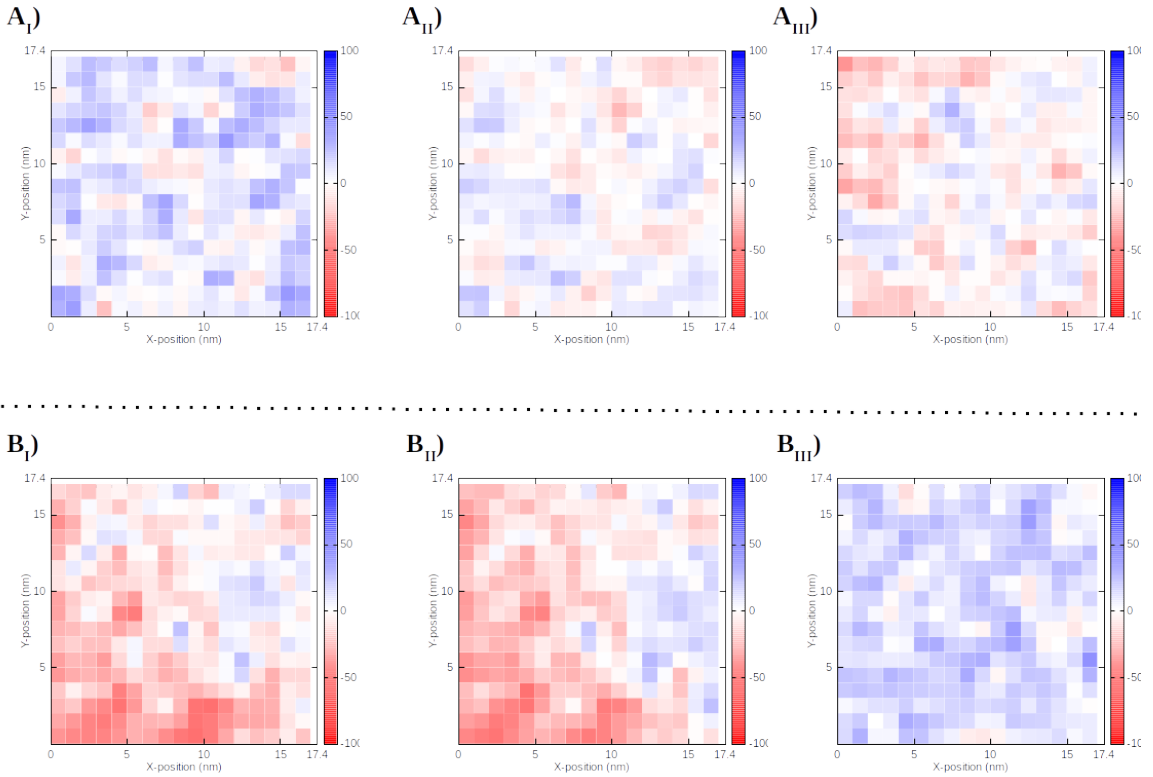
As previously stated, neural membrane are complex assemblies of lipids and proteins. Similarly to other type of membranes, it is possible to identify differences in composition between the two leaflets and in lipids localization. Such features are usually referred as "lipid domains", whose dynamics and sizes fluctuate depending on the environmental conditions. CG-MD simulations of single neural membrane (See section 5.2.2 for details), revealed different "lipid domains". Outer membrane consists of PC, PE, SM, glycolipids and cholesterol, while inner membrane doesn't contain glycolipids but is mainly made of PIPS and PS (See fig. 5.1*A<sub>I</sub>*, *B<sub>I</sub>*). Then, outer leaflet mainly consists of saturated lipids and monounsaturated lipids (See fig. 5.1*A<sub>II</sub>* and table 11.1). Instead inner leaflet is mainly characterized by the presence of poly-unsaturated lipids (See fig. 5.1*A<sub>II</sub>* and table 11.1). The differences in lipid mixtures heavily affect the formation and stabilization of lipid domains. Indeed, in the last 100ns of CG-MD simulation, CHOL and FS lipids co-localize in outer leaflet (fig. 5.3 *A<sub>I</sub>*, *A<sub>II</sub>*), while PU lipids are mainly concentrated in the inner leaflet (fig. 5.3 *B<sub>III</sub>*).

### 5.3.2 Interactions among Neural Membranes and (*LDLK*)<sub>3</sub>

As shown in fig. 5.4, lipid domains and motion patterns were heavily affected by the interactions with self-complementary SAPs (*LDLK*)<sub>3</sub>. Indeed, in the last 100 ns of CG-MD simulation (See section 5.2.3 for details), the overall CHOL concentration increased in the outer leaflet (fig. 5.4 *A<sub>I</sub>*) while decreased in the inner leaflet (fig. 5.4 *B<sub>I</sub>*). This changes in CHOL distributions are attributable to the deposition of (*LDLK*)<sub>3</sub> monomers on the outer leaflet (fig. 5.4, *C<sub>I</sub>*). Indeed, CHOL in outer leaflet co-localize with (*LDLK*)<sub>3</sub> SAPs, while CHOL motion patterns in inner leaflet were not altered (See fig. 5.3 and fig. 5.4 *B<sub>I</sub>*, *D<sub>I</sub>* for comparison). Further, FS lipids motion patterns were altered by the presence of SAPs monomers (fig. 5.4 *C<sub>II</sub>*), resulting in altered densities patterns, in outer leaflet (fig. 5.4 *A<sub>II</sub>*). On the contrary PU lipids densities patterns were unaltered and it is not possible to define a precise motion pattern (fig. 5.3 *A<sub>III</sub>*, *B<sub>III</sub>*, fig 5.4 *A<sub>III</sub>*, *B<sub>III</sub>*, *C<sub>III</sub>* and *D<sub>III</sub>*).

### 5.3.3 Neural Membrane Riorganization with Embedded AQP4

In order to simulate more complex membrane systems, aquaporin 4 has been embedded within neural membrane, as described in section 5.2.4. A 1  $\mu$ s long CG-MD simulations have been performed in order to highlight membrane protein fingerprint, analogously to the



**FIGURE 5.3: Lipid domains in Neural Membrane.** CG-MD simulations (See 5.2.2 for technical details) of single neural membrane reveal different distributions of PU, FS lipids and CHOL between the two leaflets. More in details, CHOL and FS lipids densities in the outer leaflet increase through the last 100 ns of CG-MD simulations ( $A_I$ ,  $A_{II}$ ), whereas decrease in the inner leaflet ( $B_I$ ,  $B_{II}$ ). Instead, PU lipids follow a reversed tendencies ( $A_{III}$ ,  $B_{III}$ ). Such patterns identify the so-called "lipid domains".

work of *Corradi et al.* (See section 5.2.5 for details). By analysing the densities map of lipids, grouped into the three above mentioned classes and calculated over the last 100 ns of simulation, a clear depiction of AQP4 fingerprint emerged: 1) CHOL and FS lipids are mainly concentrated in the inner leaflet (See fig.5.5  $A_I$ ,  $A_{II}$ ,  $B_I$  and  $B_{II}$ ) and CHOL is characterized by an higher degree of mobility than FS lipids, as highlighted in streamlines visualization in fig. 5.5  $C_I$ ,  $C_{II}$ ,  $D_I$  and  $D_{II}$ ; 2) PU lipids are characterized by great



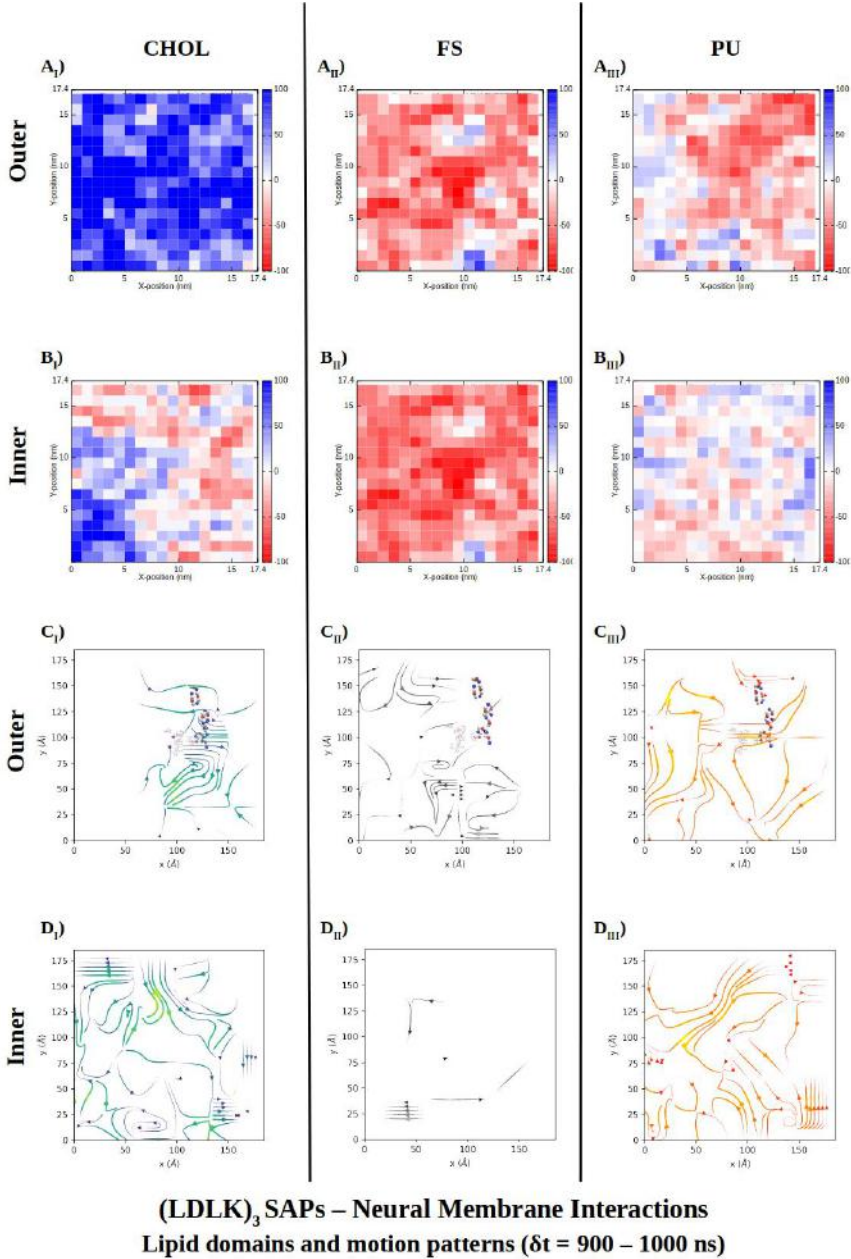


FIGURE 5.4: **Interaction patterns among neural membranes and  $(LDLK)_3$  SAPs monomers.** The interactions of  $(LDLK)_3$  monomers with neural membranes define precise interaction patterns. Indeed, CHOL density increases  $A_I$  while its mobility decreases  $C_I$ , in the outer leaflets (See fig. 5.3 for comparison). Instead, on the inner leaflet, CHOL shows a reversed tendencies ( $B_I$  and  $C_I$ ). In addition, FS lipids colocalize with  $(LDLK)_3$  monomers ( $A_{II}$ ,  $B_{II}$ ,  $C_{II}$  and  $D_{II}$ ). Instead, PU lipids show a similar tendency to that observed in 5.3

mobility in both leaflets (fig. 5.5  $C_{III}$  and  $D_{III}$ ) resulting in densities patterns similar to those identified by *Corradi et al* for Aquaporin 1 (fig. 5.5  $A_{III}$ ,  $B_{III}$ ).[196][204]

### 5.3.4 Neural Membrane SAPs Fibril Interactions

In neural tissue engineering applications, neural stem cells are usually seeded or encapsulated into SAPs scaffold. Scanning electron microscopy characterization revealed that neural stem cells are entrapped into a mesh of intertwined SAPs nano-fibrils. For understanding the interactions among SAPs nano-fibrils and neural stem cells, two minimal CG models have been developed.

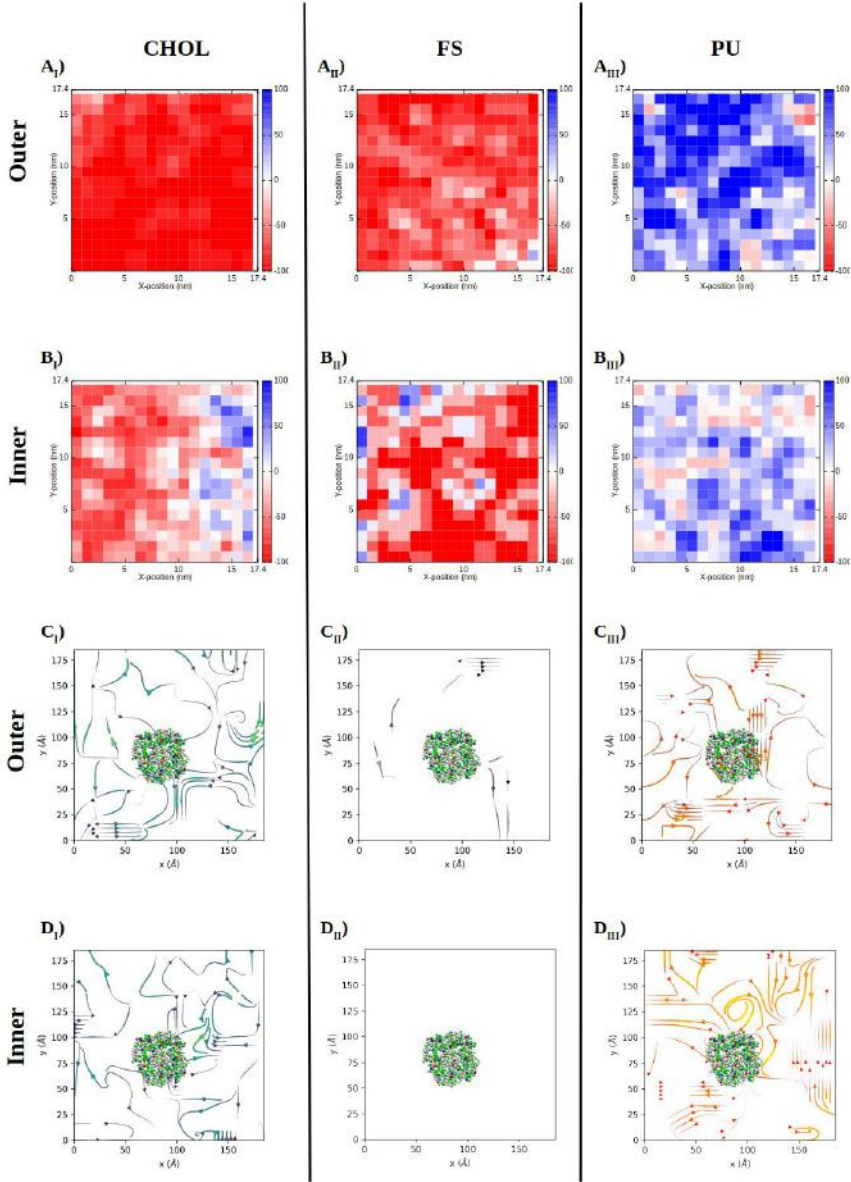
Starting from the experimental and computational evidences (See Chapter 2 and Sections 4.4.2 and 4.8), the  $(LDLK)_3$  fibril model has been built (For technical details see Section 5.2.6). Then, two CG minimal models, resembling the features of NSCs, were built as shown in section 5.2.7. The first model has been used to elucidate the effect of long-range interactions on lipid domains and motion patterns. Instead, the second configuration allowed to elucidate the SAPs fibril deposition mechanism on neural membranes and the subsequent effects of short-range interactions on lipid dynamics.

#### Long-range Interactions between SAPs Fibril and Neural Membrane

The starting configuration of the first CG minimal model is shown in fig. 5.2. After the equilibration phase, the  $(LDLK)_3$  fibril was 30 nm away from the **Membrane I**. As shown in 5.6, in the first 1200 ns of CG-MD simulation,  $(LDLK)_3$  SAPs fibril moved towards the neural membrane (**Membrane I**). Then, in the following 300 ns, SAPs fibril moved away from **Membrane I** and reached a stationary distance of about 11 nm. The minimum distance ( $\approx 6$  nm) has been reached at the time of 1200 ns. Diffusion movement of  $(LDLK)_3$  fibrils was associated with roto-translations.

For sake of clarity, the geometry of  $(LDLK)_3$  fibril allows to define three faces, depending on the view, as shown in fig. 11.1. The faces are also different in terms of chemical properties. Indeed, the **side face** (fig. 11.1 A) is highly hydrophobic due to the exposition of the "leucine zipper" to the solvent. Then, the **side face** represents an eligible site for docking of hydrophobic molecular entities. Instead, the **top-bottom face**, easily identifiable by rotation of fibril around its own axis, is highly hydrophilic due to the exposition of charged side chains of lysine and aspartic acid. The third face, identifiable by rotation around equatorial axis, is usually not exposed to the solvent and it is hydrophobic. Such features affected the evolution of the system.

As shown in fig. 5.6A, at time of 0 ns, the  $(LDLK)_3$  fibril was oriented with charged **top-bottom face** pointing to the **Membrane I**. The outer leaflet of the neural membrane is



**Aquaporin 4 embedded within Neural Membrane**  
**Lipid domains and motion patterns ( $\delta t = 900 - 1000$  ns)**

FIGURE 5.5: **Aquaporin 4 (AQP4) Membrane Protein Fingerprint.** PU lipids are mainly concentrated in outer leaflets ( $A_{III}$ ,  $B_{III}$ ) and show a great mobility in both leaflets ( $C_{III}$  and  $D_{III}$ ). FS lipids show opposite tendencies: 1) FS lipids are mainly concentrated in the inner leaflet as highlighted by density maps in  $A_{II}$  and  $B_{II}$ ; 2) show a low mobility in both leaflets as highlighted in  $C_{II}$ ,  $D_{II}$ . Instead, CHOL show great mobility in both leaflets ( $C_I$ ,  $D_I$ ) while is mainly concentrated in inner leaflet ( $A_I$  and  $B_I$ ).

negatively charged, due to the presence of phosphates and glycolipids, while fibril is globally neutral, because of the alternate of positively charged side chains of lysine and negatively charged side chains of aspartic acid. The spatial orientation of the fibril favoured its approach to **Membrane I**, thanks to the establishment of long-range electrostatic interactions between atomic groups charged in the opposite way. After 750 ns, the distance between fibril and **Membrane I** was less than 15 nm and fibril was oriented with **side face** pointing to neural membrane (fig. 5.6B). This conformation favoured long-range interactions among lipid and hydrophobic side chains of SAPs fibril, then the fibril kept moving in the same direction. At time of 1200 ns, the fibril reached the closest position next to the neural membrane (fig 5.6C). Then, the fibril began to move away from **Membrane I** after 1370 ns and subsequently reached the stationary distance of 11.4 nm, with **top-bottom face** pointing to **Membrane I** (fig. 5.6D).

A further diffusion of the fibril towards the **Membrane I** has been hampered by unfavourable long-range interactions among lipids and  $(LDLK)_3$  fibril. Indeed, in the range from 1200 ns to 1370 ns, lipids densities and motions were affected by the progressive approach of the fibril (fig. 5.7). More in details, CHOL concentration increased in the outer leaflet while decreased in the inner leaflet of **Membrane I**(fig. 5.7A<sub>I</sub>, B<sub>I</sub>). CHOL densities variation were associated with an high degree of mobility, as shown in fig. 5.7 C<sub>I</sub> and D<sub>I</sub>. Instead the patterns of FS and PU lipids resembled those observed in fig. 5.5. This probably means that such lipid patterns hamper the association between neural membrane and SAPs fibril.

### Short-range Interactions between SAPs Fibril and Neural Membrane

The starting configuration of **System II** is shown in fig. 5.2. As previously stated, this CG-MD simulation has been performed in order to elucidate the lipid dynamics when neural membrane directly interacts with the  $(LDLK)_3$  fibril.

As shown in fig. 5.8A<sub>I</sub>, at the time 0 ns the fibril was oriented with the **top-bottom face** anchored on the outer leaflet of **Membrane I**. The **top-bottom face** is highly hydrophilic due to the exposition of charge side chains of lysine and aspartic acid. Such orientation favors the electrostatic interactions among side chains of positively charge lysine side-chains and negative charge phosphate groups of lipids. This setup allowed to identify the most favorable orientation respect to the neural membrane, overcoming the main limitation of docking simulations, which don't allow to monitor the inter-dependent dynamics of lipids domains.

Progressively, the orientation of the fibril changed, bringing the **side face** into contact with the outer layer of **Membrane I**( See fig. 5.8A<sub>I</sub>).

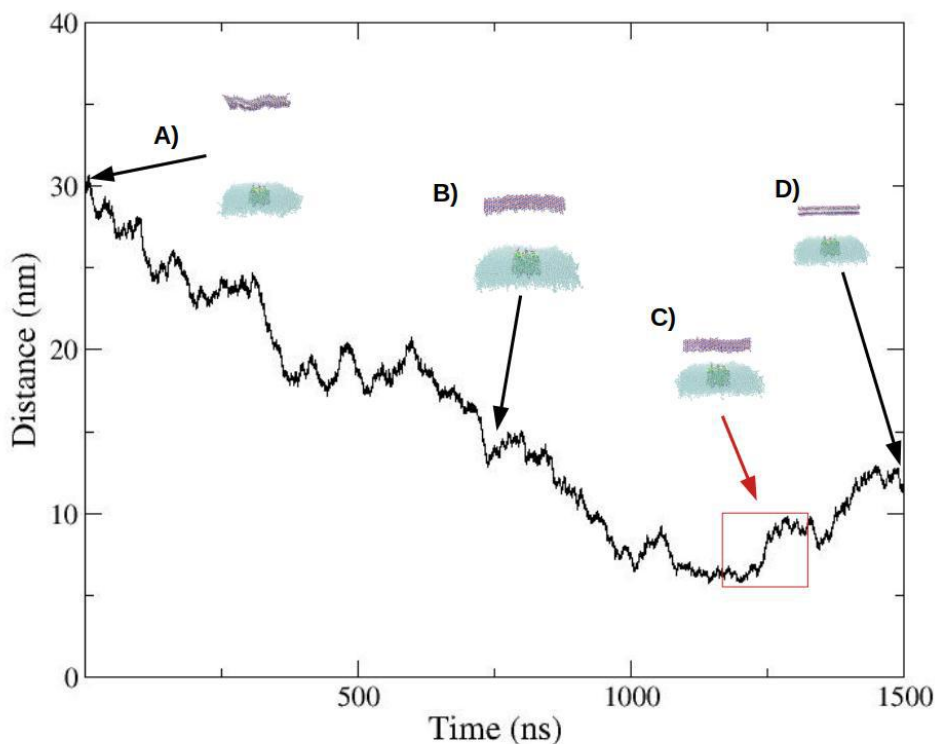


FIGURE 5.6:  $(LDLK)_3$  SAPs fibril interacts with neural membrane.  $(LDLK)_3$  moved towards the neural membrane (**Membrane I**) in the first 1200 ns of CG-MD simulation. In the last 300 ns,  $(LDLK)_3$  fibril reached the average distance of  $\approx 11$  nm.

This change also heavily influenced the localization of glycolipids in the outer leaflet, as shown in fig. 5.8 $A_{II}$ . The progressive colocalization of glycolipids and FS lipids with  $(LDLK)_3$  fibril was more evident in the last 100 ns of CG-MD simulation (See fig. 5.8 $B_I$ ,  $B_{II}$  and fig. 5.9,  $A_{II}$  and  $C_{II}$ ). Indeed, FS lipids densities increased in the outer leaflet while decreased in the inner leaflet (fig. 5.9 $B_{II}$ ). These variations were mainly ascribable to the movement of FS lipids towards the fibril, as shown in fig. 5.9  $C_{II}$  and  $D_{II}$ . Furthermore, the movement of FS lipids have also influenced the localization of CHOL, which moved around the FS molecules, in the outer leaflet (fig. 5.9 $C_I$ ). Despite, the densities fluctuations of PU lipids in both layer are similar to those observed in free membrane (See fig.5.5 $A_{III}$ ,  $B_{III}$  and

fig. 5.9  $A_{III}$ ,  $B_{III}$  for comparison) their movements in outer leaflets have been hampered, probably due to the increasing concentration of FS lipids (fig. 5.9  $C_{III}$ ,  $D_{III}$ ).

In summary, when  $(LDLK)_3$  fibril interacts with neural membrane the lipids domains and pattern motions are affected as follows: 1) FS lipids concentration increase in outer leaflet, while decrease in inner leaflet; 2) FS lipids, especially glycolipids, co-localize with  $(LDLK)_3$  fibrils; 3) CHOL and PU lipids concentrations show opposite tendencies to that of FS lipids. Such changes are ascribable to the establishment of electrostatic interactions, among glycolipids and charged side chains of lysine and aspartic acids, and are also stabilized by the hydrophobic interactions among "leucine zipper" and membrane lipids.

#### 5.4 CONCLUSIONS

In the present study, a CG-MD approach has been used to investigate interactions among SAPs fibril and neural membrane. The evidence from CG-MD simulations pointed out that  $(LDLK)_3$  fibril interacts with the neural membrane, only when "leucine zipper" is in contact with lipids of the outer leaflet (See fig. 5.8). Other systems conformations doesn't allow the docking process of the SAPs fibril on the neural membrane (See fig. 5.6). Such conformations heavily affect the lipid domains and their motion patterns (See fig. 5.7 and fig. 5.9). In particular, FS lipids are mainly involved in the establishment of favourable interactions among fibril "leucine zipper" and neural membrane lipids. This pattern is mainly ascribable to the co-localization of glycolipids with  $(LDLK)_3$  fibril (See fig. 5.8). Indeed, glyco-lipids motion patterns is affected by the presence of  $(LDLK)_3$  fibril, when it is anchored on the neural membrane (See fig. 5.10 A and B). These tendencies have been also confirmed from a simulation investigating the interactions among  $(LDLK)_3$  monomers and neural membranes (See fig. 11.2). In this simulation, despite  $(LDLK)_3$  SAPs aggregation is promoted in extra-cellular environment, some monomers interact with neural membranes promoting the migration of glycolipids. In addition, all the CG-simulations revealed that  $(LDLK)_3$  SAPs are not able to penetrate the neural membrane then preventing potentially cytotoxic effects, ascribable to SAPs internalization. This tendency is ascribable to the charge distribution along  $(LDLK)_3$  backbone. Indeed, differently from commonly internalized SAPs, which are positively charged,  $(LDLK)_3$  SAPs are globally neutral charged.[20] These evidences shed a new light on the *in-silico* investigation of mechanisms ruling biocompatibility of innovative materials for tissue engineering applications.



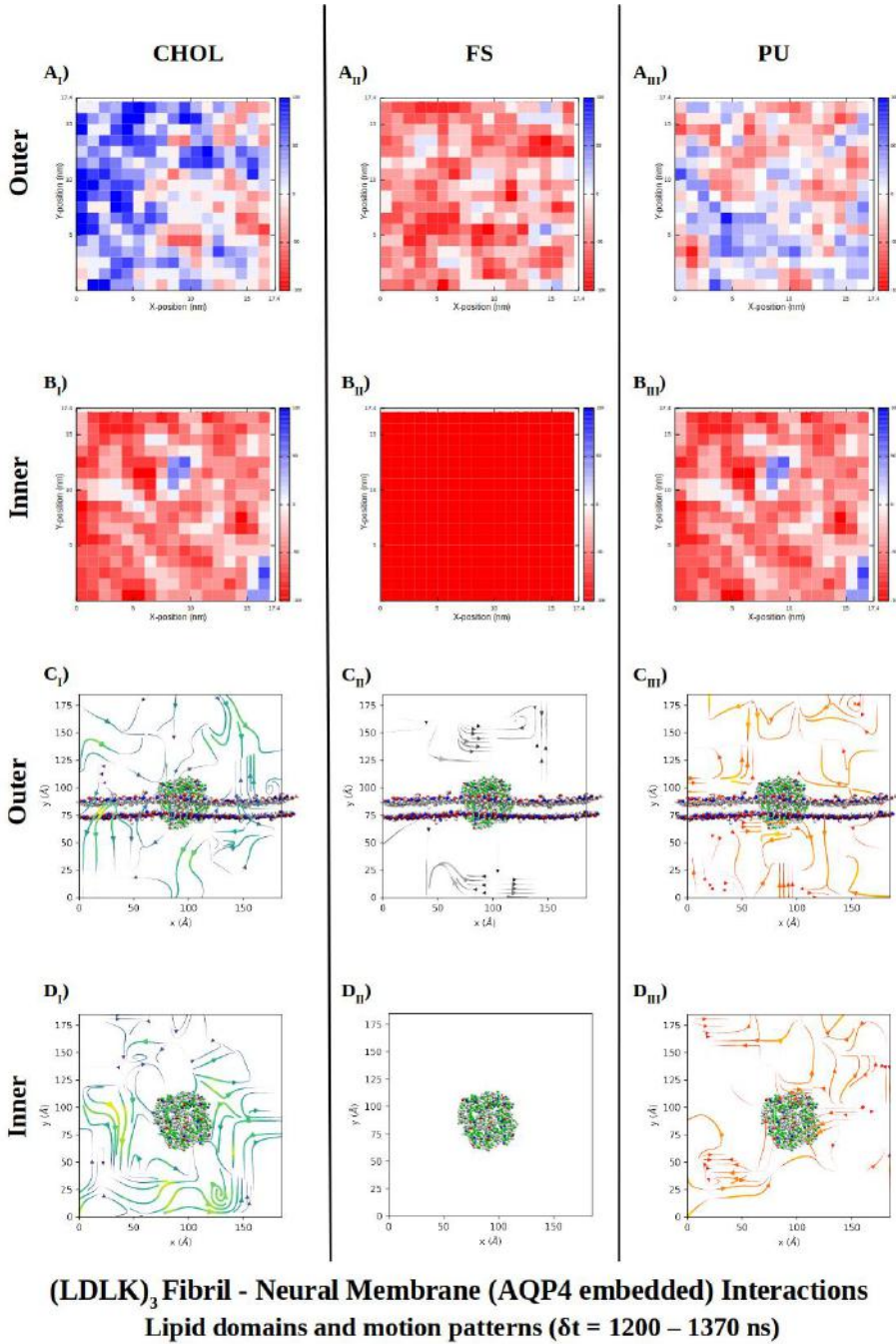


FIGURE 5.7: **Effect of  $(LDLK)_3$  Fibril progressive approaching on lipids densities and motions.** The presence of  $(LDLK)_3$  doesn't alter FS and PU lipids densities and motions ( $A_{II,III}$ ,  $B_{II,III}$ ,  $C_{II,III}$ ,  $D_{II,III}$ ). Instead, CHOL is highly mobile in both leaflets ( $C_I, D_I$ ) and its density increases in the outer leaflet ( $C_I, D_I$ ).

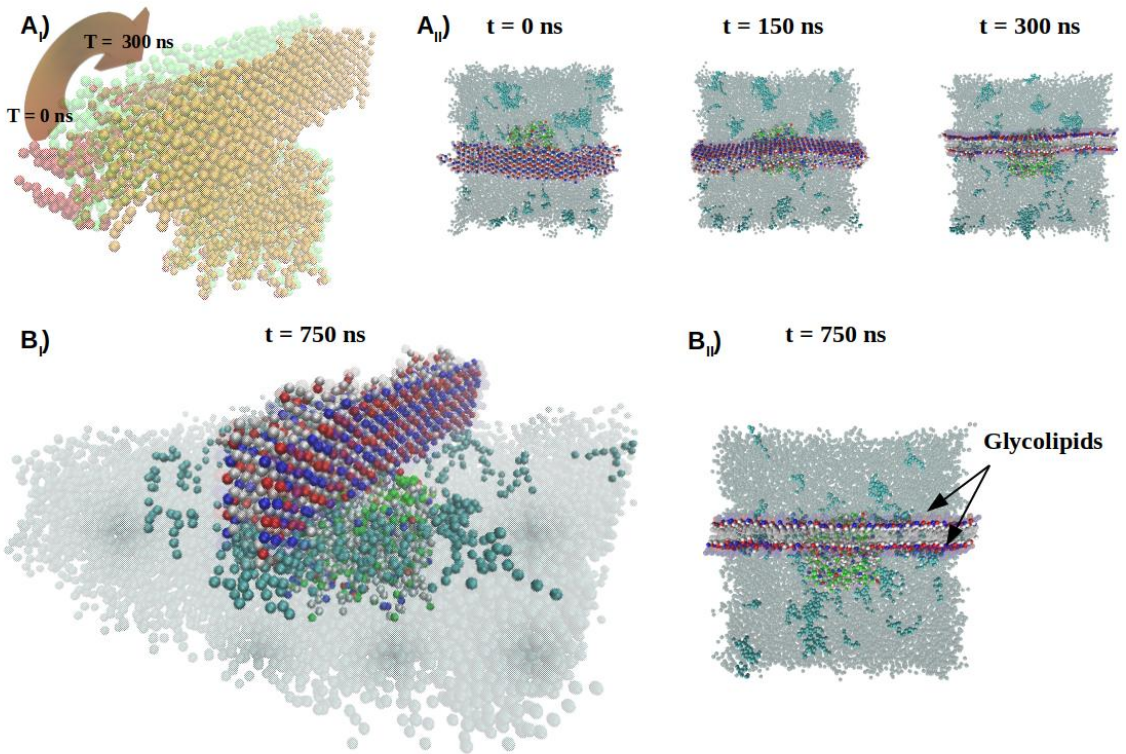
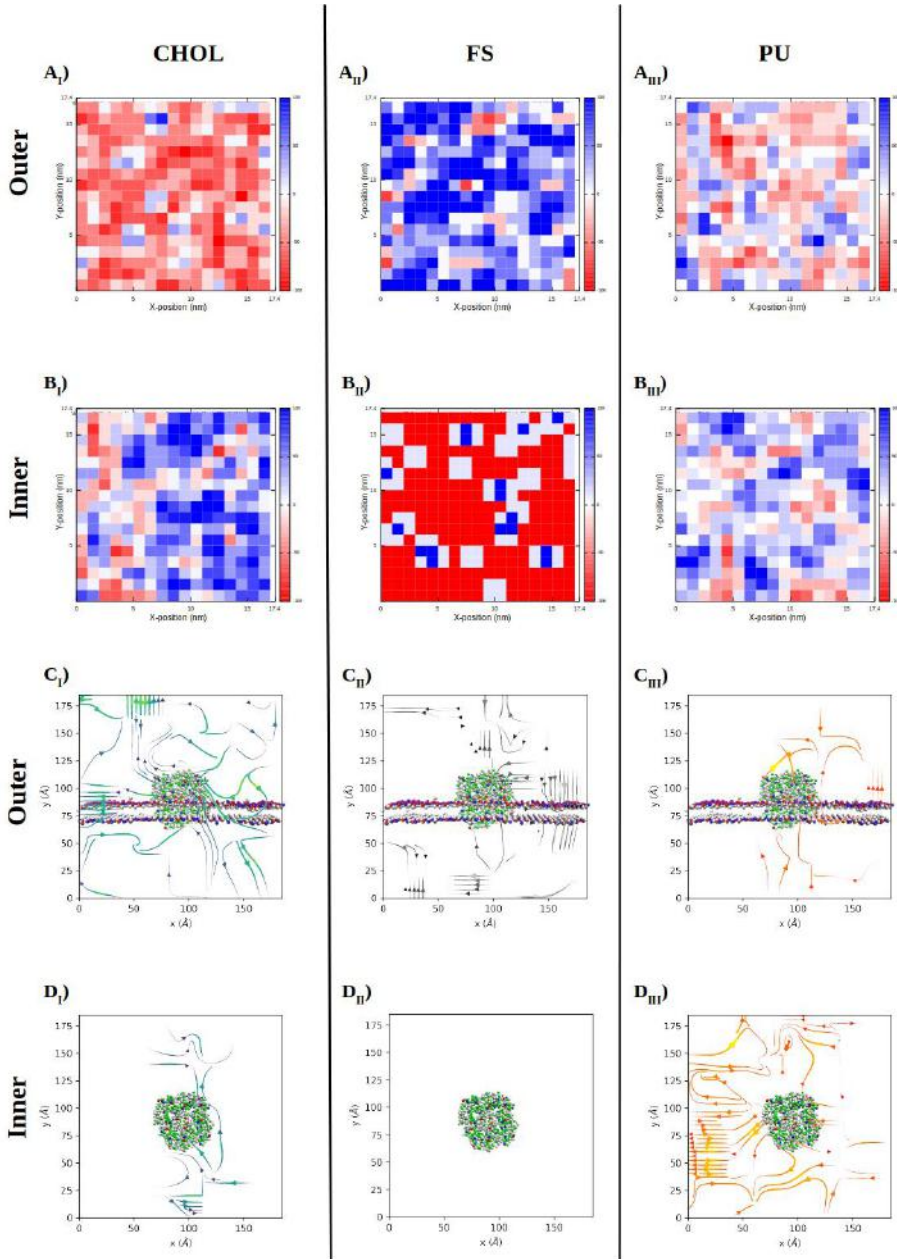


FIGURE 5.8: **SAPs fibril affects (glyco)lipids distribution in neural membrane.** At the beginning of CG-MD simulation, the **side face** of  $(LDLK)_3$  directly interacts with outer leaflet of **Membrane I** ( $A_I$ , highlighted in red). The progressive motion of  $(LDLK)_3$  brings the **lateral face** in contact with the outer leaflet of **Membrane I** ( $A_I$ , time-frames 150 ns and 300 ns are highlighted in green and orange, respectively). This movement affects the localization of glycolipids as shown in  $A_{II}$  (highlighted in cyan). Indeed, at 750 ns glycolipids directly interact with SAPs fibrils ( $B_I, B_{II}$ ).





**(LDLK)<sub>3</sub> Fibril - Neural Membrane (AQP4 embedded) Interactions**  
**Lipid domains and motion patterns ( $\delta t = 650 - 750$  ns)**

FIGURE 5.9: Lipids domains and motion patterns when  $(LDLK)_3$  fibril is anchored on Neural Membrane.  $(LDLK)_3$  fibril heavily affect FS and CHOL lipids densities and motion patterns in both leaflets ( $A_{I,II}$ ,  $B_{I,II}$ ,  $C_{I,II}$ ,  $D_{I,II}$ ). Instead, PU lipids motion pattern in outer leaflet is hampered, probably to the increasing densities of CHOL and FS lipids ( $C_{III}$ ,  $D_{III}$ ).

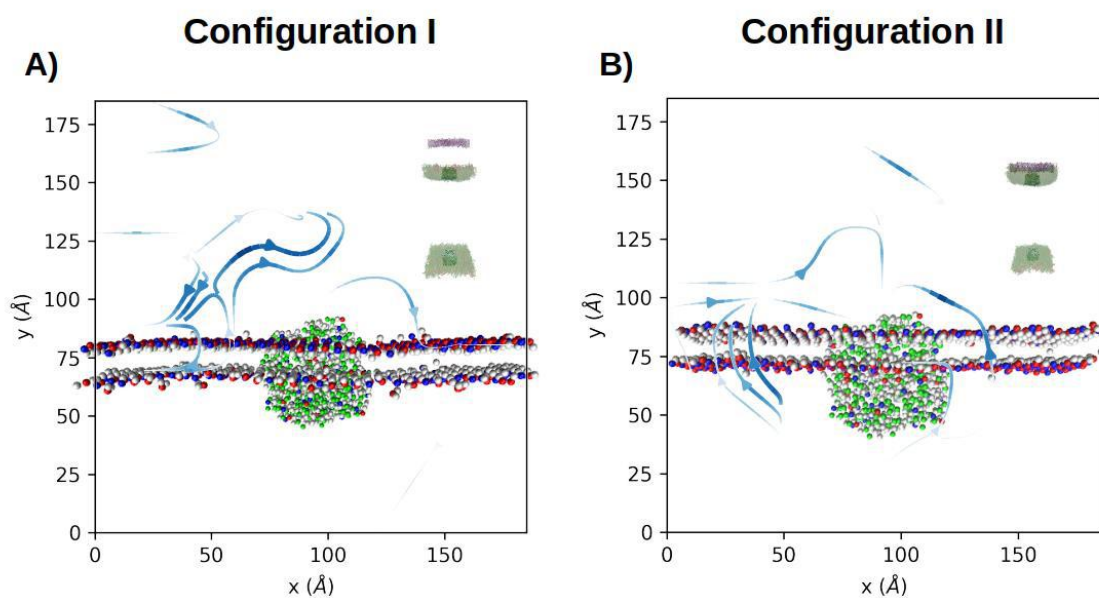


FIGURE 5.10: **Glyco-lipids motion patterns.** Glyco-lipids motion patterns depends on the position of interacting  $(LDLK)_3$  fibrils. Such patterns emerge as consequence of electrostatic interactions among glyco-lipids and charged side chains of lysine.



## Chapter 6

# CG Modeling of Glycosylated SAPs

## 6.1 INTRODUCTION

Extra-cellular matrix (ECM) is a complex network of intertwined nano-bio-structures which guides all aspects of cell physiology by providing physical signals and engaging cell surface receptors. Proteomics and glycomics have contributed to the elucidation of ECM composition, allowing large-scale determination of proteins expression levels and their post-translation modifications (PTMs). Among PTMs, glycosylation plays a pivotal role in protein folding, stability, cellular localization and immune reactions.[213]

Tissue engineering approaches aim to reproduce the nano- and micro-architecture of native ECM, in order to provide the appropriate stimuli to guide cell behaviour and promote regeneration of damaged tissues. During the last years, several synthetic scaffolds, mimicking different cell microenvironments, have been designed. Both peptides and glycans have been incorporated in synthetic scaffold, in order to provide specific biological signals and control cell adhesion and differentiation. In addition, peptides, as self-assembling peptides (SAPs), have been largely employed as building blocks for hydrogel scaffolds.[2][17][18][189]

The development of new SAPs hydrogel scaffolds requires the elucidation of SAPs hierarchical organization in order to minimize kinetically trapped structures. Synthetic peptides tend to assemble into nanofibers that subsequently arrange into random entangled networks because non-specific attractive forces overcome repulsive forces. Several chemical-physical methods can be used in order to promote alignment among synthetic nanofibers. An alternative strategy is represented by tailoring amino-acid sequences in order to promote specific alignments. Such approach relies on specific electrostatic and aromatic interactions. Inspired and motivated by Nature, the glycosylation of SAPs represents an intriguing strategy for improving control over SAPs hierarchical order. In addition, SAPs glycosylation offers also a new way to orchestrate cell-biomaterials interactions.[31][78][214]

In this work, starting from the well-known bone-marrow homing peptide I (BMHP1) SAPs, a series of glycosylated SAPs have been modeled.[19][91][128] More in details, the self-assembling propensity of O-maltosylated BMHP1 have been evaluated through MARTINI CG approach. Then, self-assembling propensity of differently O-glycosylated BMHP1 functionalized (*LDLK*)<sub>3</sub> SAPs has been evaluated via CG-MD simulations.

## 6.2 MATERIAL AND METHODS

### 6.2.1 CG-MD simulations of BMHP1

All-trans configuration of BMHP1 peptides were generated by Pymol (<https://pymol.org>) and mapped with *martinize.py* tool according to the MARTINI v2.2.[58] The C- and N-terminal of peptide monomers were acetylated and amidate respectively. As shown in Table 6.1, BMHP1 peptides consists of 7 residues comprising also Lysine. At the neutral pH, lysine because of it weak basic nature, can be considered fully protonated. Peptides have been randomly distributed in explicit cubic water boxes built by using PACKMOL in order to have the correct spatial distribution, with monomers placed at minimum distance of 10 Å far from each other.[108]

The MARTINI secondary structures parameters have been assigned as random coil because of experimental evidences. MD simulations were performed using the version 4.5.5 of GRO-MACS package. Prior to the production phase, the systems underwent to a minimization phase (1000 steps) and to a short equilibration phase of 100 ps, with a time-step of 2 fs. The production phase of 1000 ns was conducted in the NPT ensemble. Solutes and solvent were coupled independently to an external bath ( $T = 300$  K) with a coupling constant ( $\tau_T$ ) of 1 ps using v-rescale thermostat.[173] Periodic boundary conditions were imposed, and pressure was maintained at 1 bar using the Berendsen coupling.[174] The isothermal compressibility was set at  $3 \cdot 10^{-4}$  bar<sup>-1</sup> and the coupling constant ( $\tau_P$ ) was 1 ps. The constraints on lengths and angles of the bonds were applied with the LINCS algorithm.

### 6.2.2 CG-MD simulations of O-Maltosylated BMHP1

The all-trans configuration of BMHP1 peptides were generated and mapped as reported in 6.2.1. The corresponding glycosylated sequence (See Table 6.1) was built using the on-line tool **glycoprotein builder** of GLYCAM server (<http://glycam.org>). BMHP1 sequence and O-glycosylation were mapped separately, according to the available MARTINI model, and then merged.[61] CG-MD simulations have been performed following the same protocol reported in 6.2.1, according to the condition reported in Table 6.2.

### 6.2.3 CG-MD simulations of(*LDLK*)<sub>3</sub>-BMHP1 SAPs

The sequence of (*LDLK*)<sub>3</sub>-BMHP1, indicated as **6bis** in Table 6.1, was generated by Pymol (<https://pymol.org>) and mapped according to the MARTINI model. The C- and N- terminal of peptide monomers were acetylated and amidate respectively. At neutral pH, arginine, lysine and aspartic acid side chains, because of their weak basic and acidic nature, can be

ID	Sequence	O-glycosylation
BMHP1	Ac-PFSSTKT-NH <sub>2</sub>	Maltose
BMHP1-MAL	Ac-PFSSTKT-NH <sub>2</sub>	Maltose
6bis	Ac- <i>LDLK</i> <sub>3</sub> -PFSSTKT-NH <sub>2</sub>	
6bis-GLUC	Ac- <i>LDLK</i> <sub>3</sub> -PFSSTKT-NH <sub>2</sub>	Glucose
6bis-GLAC	Ac- <i>LDLK</i> <sub>3</sub> -PFSSTKT-NH <sub>2</sub>	$\beta$ -D-Glucose-pentaacetate

TABLE 6.1: **Glycosylated SAPs.** The glycosylated residues in each sequence are highlighted in bold, while the type of glycosylation are listed in column **O-glycosylation**.

considered fully protonated and deprotonated respectively. Peptides have been randomly distributed in explicit water cubic boxes built by using PACKMOL in order to have the correct spatial distribution of the monomers.[108] Atoms belonging to different peptides were placed at minimum distance of 10 Å far from each other (see Table 6.2 for details). In MARTINI coarse-grained molecular dynamics (CG-MD) simulations it is necessary to define peptide secondary structures, and the above mentioned parameters, to which individual amino acid residue must evolve.[50] The secondary structures have been assigned as fully extended to (*LDLK*)<sub>3</sub> moiety while were been assigned as coil to BMHP1 moiety, according to the evidences obtained from previous experimental analyses [21] and from ssNMR spectra as shown in Fig. 4.1. (See Section 4.3.1 for ssNMR experiment details) MD simulations were performed using the version 4.5.5 of GROMACS package. Prior to the production phase, the systems underwent to an equilibration phase (a 1000-steps minimization using steepest descents method) in order to eliminate high-energy interactions. The production phase of 1000 ns was conducted in the NPT ensemble. Solutes and solvent were coupled independently to an external bath ( $T = 300$  K) with a coupling constant ( $\tau_T$ ) of 1 ps using v-rescale thermostat.[173] Periodic boundary conditions were imposed, and pressure was maintained at 1 bar using the Berendsen coupling.[174] The isothermal compressibility was set at  $3 * 10^{-4}$  bar<sup>-1</sup> and the coupling constant ( $\tau_P$ ) was 1 ps. The constraints on lengths and angles of the bonds were applied with the LINCS algorithm.

#### 6.2.4 GLYcosylation of (*LDLK*)<sub>3</sub>-BMHP1 SAPs

As shown in Table 6.1, starting from 6bis, two differently glycosylated sequences have been obtained (See 6.2.2 for details). The simulation conditions were the same reported in 6.2.3 and simulations details are shown in Table 6.2.

ID	Concentration (w/v)	Box size (nm)	Sim x Time (ns)
BMHP1	1(%)	10.3	3 x 1000
	3(%)	7.1	3 x 1000
	5(%)	6	3 x 1000
BMHP1-MAL	1(%)	19.5	3 x 1000
	3(%)	13.5	3 x 1000
	5(%)	11.9	3 x 1000
6bis	1(%)	17.3	3 x 1000
	3(%)	17.6	3 x 1000
6bis-GLUC	1(%)	17.3	3 x 1000
	3(%)	17.7	3 x 1000
6bis-GLAC	1(%)	17.3	3 x 1000
	3(%)	17.7	3 x 1000

TABLE 6.2: CG-MD simulations setup of Glycosylated SAPs.

### 6.2.5 Analysis

Nematic order parameters analysis and aggregation analysis were performed by using Wordom Package and *g\_cluster* tool of GROMACS software package.[116]

More complex analysis were performed using the innovative python module, dubbed Morphoscanner (see Chapter 2 for development and technical details). The following parameters have been analyzed in each systems: 1) Dimension of coacervates, designated as *Number of Macroaggregates*; 2)  $\beta$ -sheet Organizational Index; 3) Percentage of peptides involved in  $\beta$ -sheets formation; 4) The mutual alignment of  $\beta$ -strands within  $\beta$ -sheets, represented using an innovative graphical aid, dubbed "Shift Profile".[189].



## 6.3 RESULTS

### 6.3.1 Self-Assembling of BMHP1 and Maltosylated BMHP1 SAPs

The self-assembling propensity of **BMHP1** and maltosylated BMHP1 (whose acronym is **BMHP1-MAL**) SAPs were investigated using MARTINI CG-MD simulations (See Table 6.2 for details).

As shown in fig. 6.1  $A_I$ , BMHP1 aggregation propensity is not affected by the concentration, despite a little variation in kinetic speed was observed at the concentration of 1%(w/v). The emerging coacervates are characterized by a low order degree, as highlighted in fig. 6.1  $A_{II}$ . Indeed, the nematic order parameter was generally less than 0.4, indicating a weak parallel alignment among peptides. Such features are reflected in  $\beta$ -sheets organization, as highlighted in figures 12.2 and 12.1:  $\beta$ -strands were transitory aligned in parallel and less than 20 % of peptides contributed to the formation of  $\beta$ -structured aggregates.

The O-maltosylation of C-terminal threonine in BMHP1 SAPs (See Table 6.1 for details), doesn't alter the formation of coacervates. Indeed, BMHP1-MAL coacervates share similar features to those of BMHP1 (fig. 6.1  $A_{II}$  and  $B_{II}$ ). More in details, the O-Maltysolation didn't promote the formation of ordered aggregates (fig. 6.1  $B_{II}$ ) and lead a slower aggregation kinetics, due the hydrophilic nature of maltose (fig. 6.1).

The alignment of  $\beta$ -strands was partially affected by the interactions among maltosylated serine, bringing to the formation of transitory antiparallel  $\beta$ -sheets (fig. 12.3).

### 6.3.2 Self-Assembling of differently glycosylated (*LDLK*)<sub>3</sub>-BMHP1 SAPs

BMHP1 has been chosen as functional motif of the well-known (*LDLK*)<sub>3</sub> SAPs, due to his proven biocompatibility features and due to the poor aggregation and  $\beta$ -structuring propensities of BMHP1, even if glycosylated (See section 6.3.1).[19][18][21][189].

As shown in Table 6.1, the sequence 6bis has been built by using (*LDLK*)<sub>3</sub> motif as self-assembling motif while BMHP1 has been used as C-terminal functional motif. The sequence 6bis-GLUC and 6bis-GLAC were designed starting from 6bis and modifying C-terminal threonine with  $\beta$ -glucose and  $\beta$ -D-glucose pentaacetate O-glycosylation, respectively.

The C-terminal functionalization of (*LDLK*)<sub>3</sub> SAPs bring to the formation of small and disordered aggregates, as highlighted in fig. 6.2  $A_I$  and  $A_{II}$ . Indeed, independently from the concentration, the nematic order parameters is always less than 0.5, indicating a weak parallel alignment. This is ascribable to the interference of functional motif in self-assembly pathways, as already observed in CG-MD simulations of FAQ-(*LDLK*)<sub>3</sub> SAPs (See fig. 4.3b and fig. 10.13). These tendencies were confirmed by analysis of  $\beta$ -sheet organizations. Indeed, less than 60% of SAPs backbone participate to the formation of stable  $\beta$ -sheet

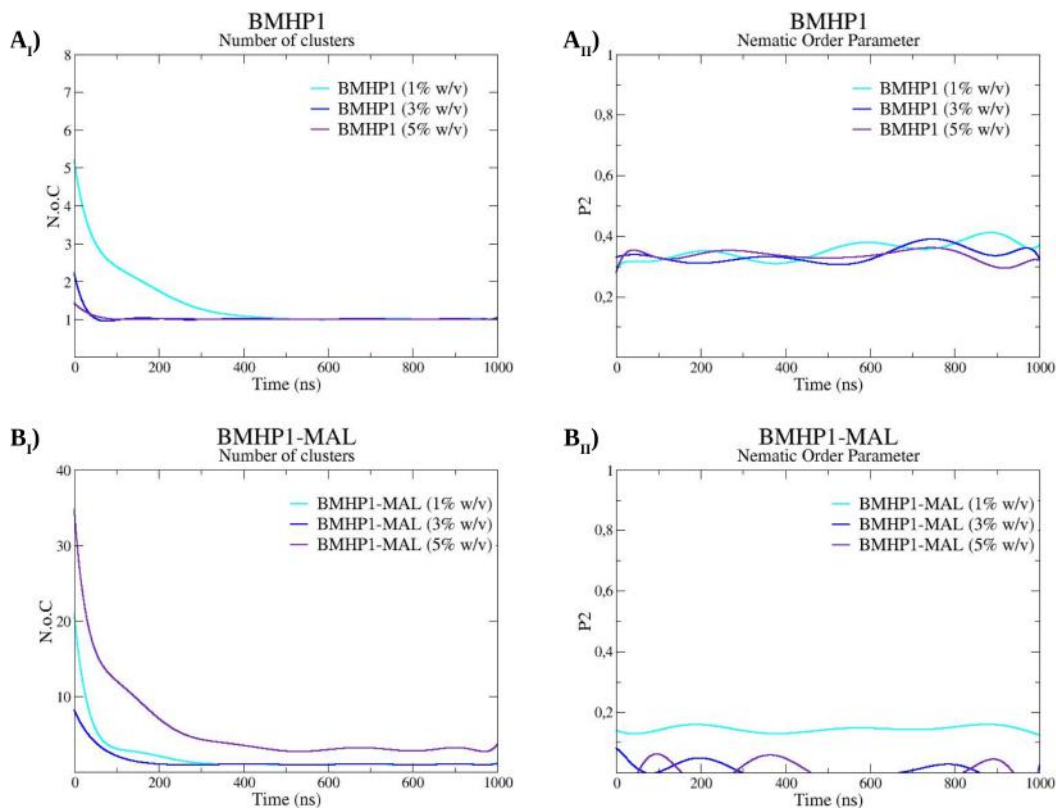


FIGURE 6.1: **Clustering and nematic order parameters of BMHP1 and Maltosylated BMHP1.** Clustering and order analyses didn't reveal any appreciable difference among CG-MD simulations of BMHP1 at different concentrations ( $A_I, A_{II}$ ). The glycosylation of C-terminal Threonine leads to more ordered aggregates if the concentration decreases ( $B_I, B_{II}$ ).

structures (fig. 12.4). Differently from  $(LDLK)_3$  SAP,  $(LDLK)_3$ -BMHP1 SAPs backbone are organized both in parallel than in anti-parallel  $\beta$ -sheets (See figure 4.3a; See also figures 6.3 and 6.4  $A_I, A_{II}$  and  $A_{III}$ ), while functional motif didn't participate to the formation of stable  $\beta$ -structures (See figure 12.5 and figures 12.6 and 12.7  $A_I, A_{II}, A_{III}$ ).

The O-glycosylation of C-terminal threonine with glucose leads to the formation of more ordered structures at the concentration of 1% (w/v) than at the concentration of 3% (w/v) (fig. 6.2  $B_I, B_{II}$ ). The detrimental effect of concentration over  $\beta$ -structuring propensity is ascribable to a better alignment of functional motif, that tend to self-assemble into parallel

$\beta$ -sheets structures (fig. 12.5  $A_{II}$ ,  $B_{II}$ ,  $C_{II}$  and fig. 12.7  $B_I$ ,  $B_{II}$  and  $B_{III}$ ). Such tendencies can be seen as consequence of aggregation propensity of glucose due to the favourable interactions among MARTINI polar beads.

Indeed, the O-glycosylation with  $\beta$ -D-glucose-pentaacetate leads to the formation of aggregates with similar features to those emerged from self-assembly of 6bis (fig. 6.2  $C_I$  and  $C_{II}$ ). These features are also reflected in  $\beta$ -sheets organization with less than 60% of SAPs backbone participate to the formation of stable  $\beta$ -sheet structures (fig. 12.4). In addition, such glycosylation leads to the formation of parallel  $\beta$ -sheet among backbone moieties (fig. 6.3  $C_I$ ,  $C_{II}$ ,  $C_{III}$ ) also stabilized by the formation of transitory parallel  $\beta$ -sheet among functional motifs (fig. 12.6  $C_I$ ,  $C_{II}$ ,  $C_{III}$ ). However, such feature is heavily affected by concentration, which led to the formation of parallel  $\beta$ -sheet structures (fig. 6.3  $C_I$ ,  $C_{II}$ ,  $C_{III}$ ), while functional didn't participated to the stabilization of such structures (fig. 12.7  $C_I$ ,  $C_{II}$ ,  $C_{III}$ ).

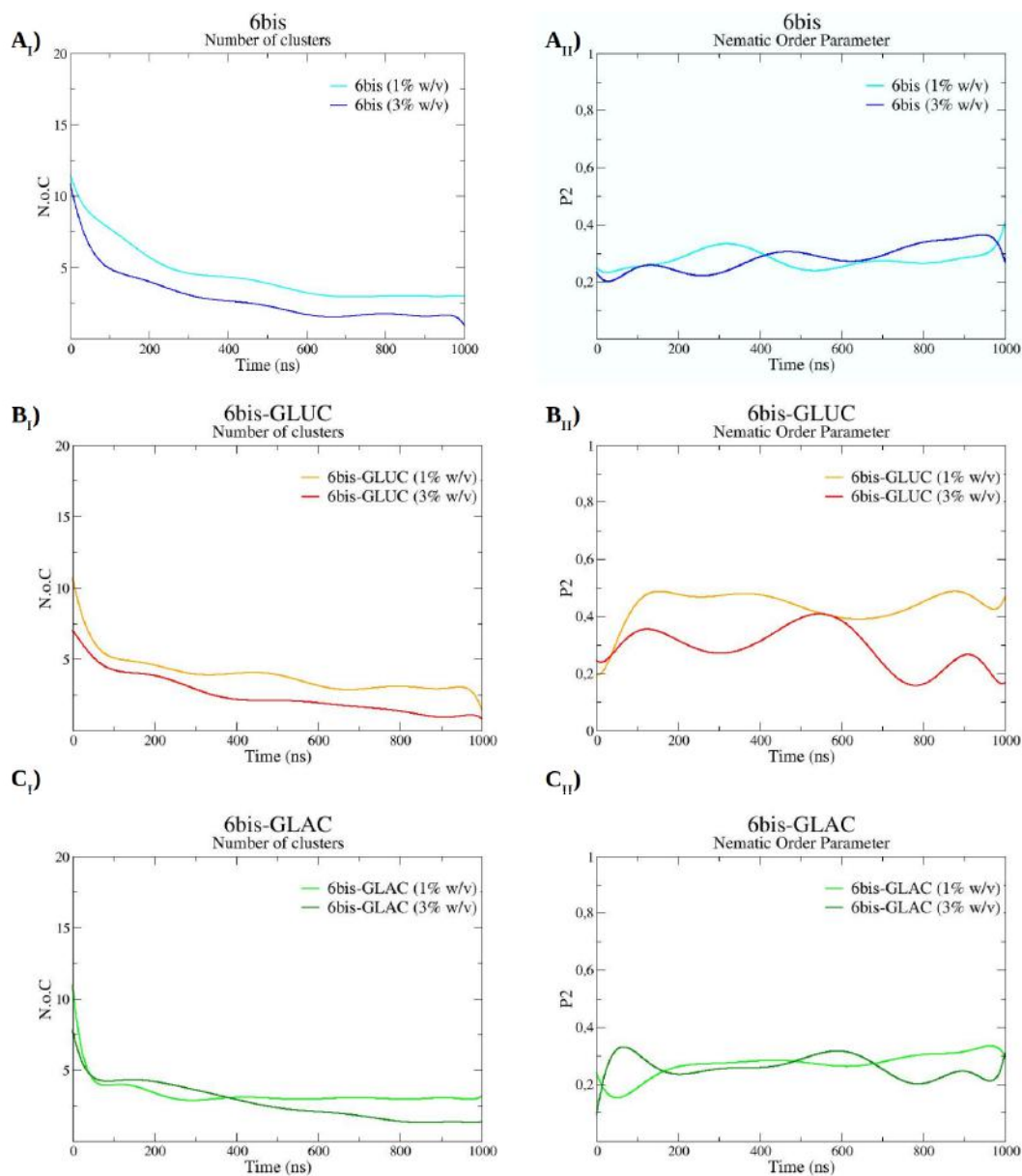


FIGURE 6.2: **Clustering and nematic order parameter of differently glycosylated  $(LDLK)_3$ -BMHP1 SAPs.** Despite, the different glycosylations didn't affect aggregation kinetics ( $A_I$ ,  $B_I$ ,  $C_I$ ), they led to important consequences on aggregates order also depending on the concentration ( $A_{II}$ ,  $B_{II}$ ,  $C_{II}$ ). More in details, the O-glycosylation of C-terminal Thr with Glucose led to the formation of more ordered aggregates at the concentration of 1% (w/v), while the ordering of aggregates was hampered at the concentration of 3% (w/v). Instead,  $\beta$ -D-Glucose-pentaacetate didn't alter the ordering of SAPs systems.

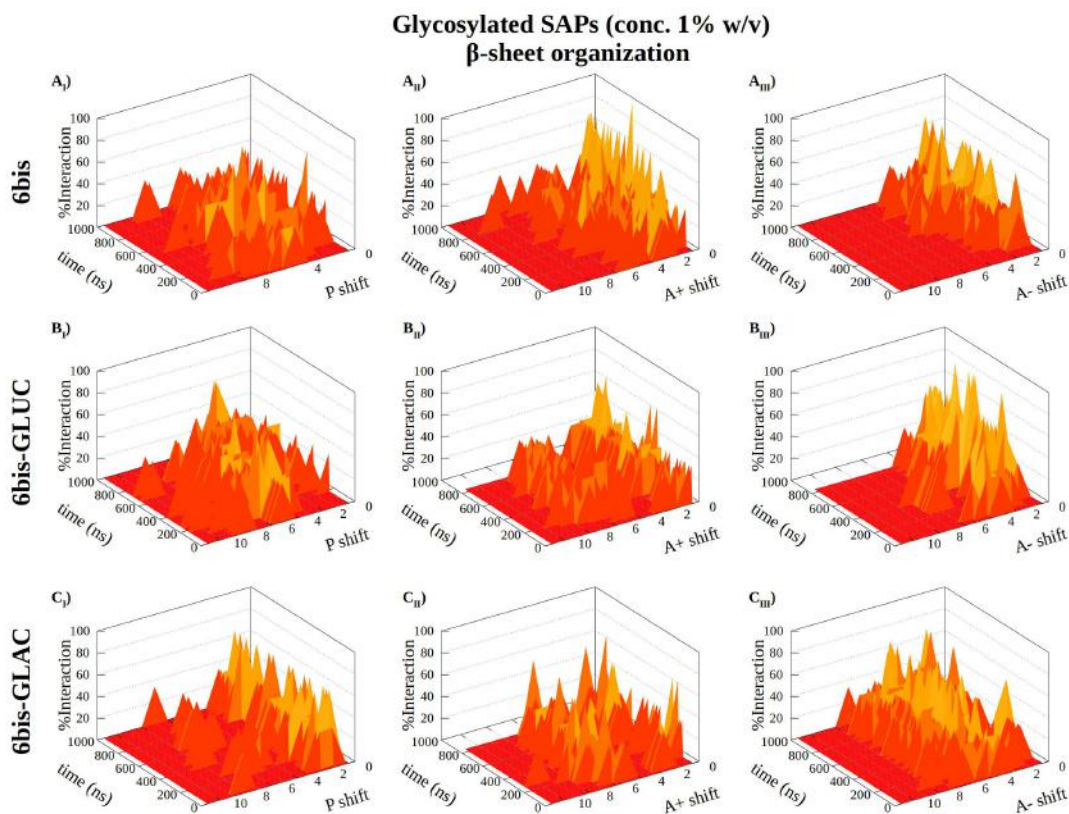


FIGURE 6.3:  $\beta$ -strands mutual alignment of backbone moiety of different glycosylated SAPs at the concentration of 1% (w/v). The shift profiles inherent  $\beta$ -strands mutual alignment of backbone moieties of different glycosylated SAPs revealed that glycosylation has a little effect on  $\beta$ -structuring propensities. Indeed, 6bis backbone  $\beta$ -strands are mainly mutually aligned in anti-parallel out-of-register by 2 residues. Instead, glycosylated SAPs show also a parallel alignment out-of-register by 2 or 4 residues.

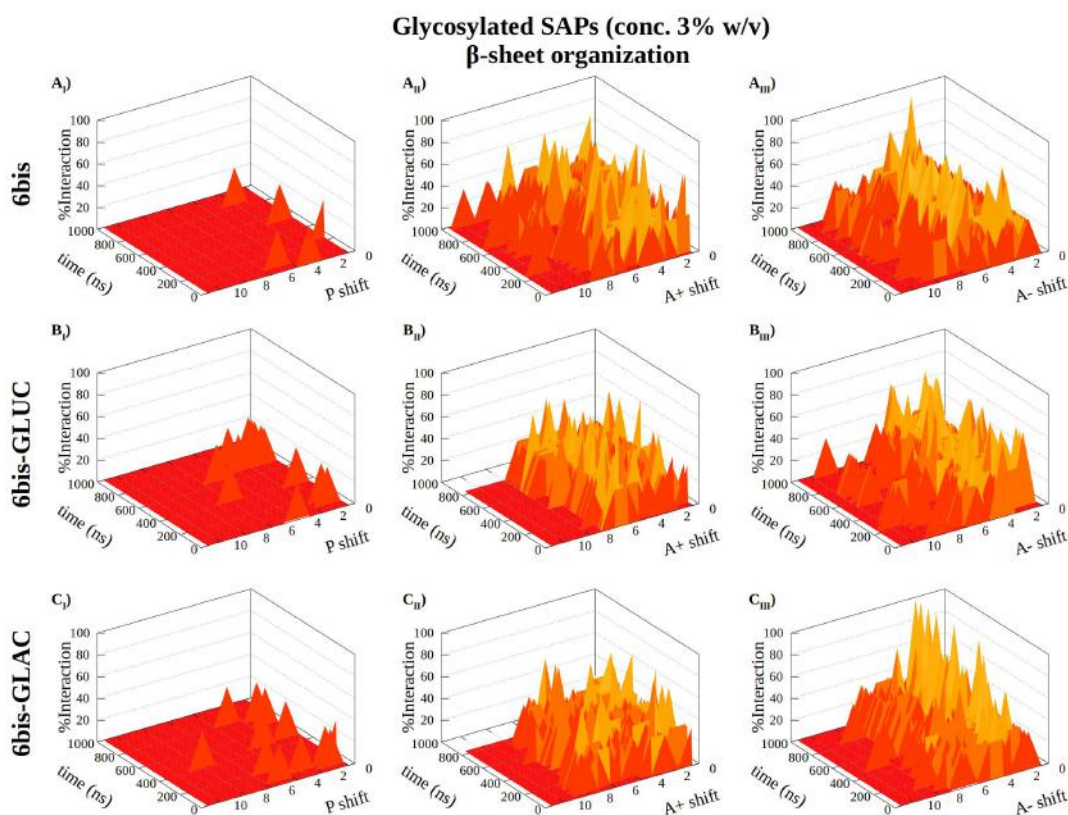


FIGURE 6.4:  $\beta$ -strands mutual alignment of backbone moiety of different glycosylated SAPs at the concentration of 3% (w/v). The increased concentration had a detrimental effect on ordered  $\beta$ -structuring. Indeed, backbone moieties of glycosylated SAPs were only aligned in anti-parallel out-of-register by 2 or 6 residues.

## 6.4 CONCLUSIONS

Glycosylation represents one of the most common PTMs and play a pivotal role also in protein folding, stability and cellular communication. Then, glycosylated is a successful strategy for building new self-assembling bio-materials by conferring them additional properties such as better supra-molecular organization or chemotaxis.

In this work, CG-MD simulations have been used to assess supra-molecular organization of differently glycosylated SAPs. As shown in figures 6.2  $B_{II}$  and 6.1  $B_{II}$ , glycosylation with standard carbohydrates allow to obtain more ordered supra-molecular aggregates at lower concentration, without improving  $\beta$ -structuring propensities (See Figures 6.3, 6.4, 12.2, 12.3).

Instead, the glycosylation with acetylated carbohydrates lead to the formation of more stable  $\beta$ -structures 12.4, by promoting stable interactions between functional motifs.

Given the obtained results, glycosilation is a doable approach to further improve the biomimetic properties of SAPs. But it comes with a price: i.e. different glycosilations may alter the self-assembling propensity of SAPs and, as such, they have to be weighted and carefully tested in silico first.

## Chapter 7

# Conclusions and future perspectives



In recent years, SAPs applications in tissue engineering and regenerative medicine have known increasing popularity.

In the field of bone tissue engineering, SAPs have been used to improve the bioactivity of demineralized bone matrix (DBM). The DBM found large applications in clinic and nowadays is the "gold standard" for bone grafting, despite its lacking of osteoinductive properties. Such drawback can be overcome thanks to the production of composite scaffolds made of SAPs hydrogels and DBM. The use of tissue-derived extracellular matrix scaffolds for myocardial repair is mainly hampered by potential immune-mediated rejection, as demonstrated in several *in vivo* studies. An interesting alternative is represented by SAPs scaffold, which could embed and mediate controlled release of specific growth factors. For neural tissue engineering purposes, the use of SAPs is motivated by the difficulties to obtain a fully bio-compatible decellularized ECM. Indeed, the use of decellularized brain ECM is still far from clinical applications and is mainly limited to *in-vitro* applications, differently from SAPs scaffolds which have been already tested in *in-vivo* experiments.

Despite such promising achievements, the clinical applications of SAPs are mainly limited by the weak control of their supra-molecular features and consequently hydrogels mechanical-structural features.

The recent progresses in the field of structural biochemistry could help to overcome the intrinsic limitation to the usage of SAPs hydrogels in several clinical applications. In particular, the development of reliable multiscale modelling strategies will allow to predict structural, mechanical and subsequently biochemical features of SAPs hydrogels.

In recent years, the advances in NMR spectroscopy allowed to investigate organization of biomolecular complexes, such as SAPs hydrogels, at atomic resolution. More in details, solution-state NMR, which was initially employed for the characterization of small molecules, have also found applications in the elucidation of surface properties of SAPs and collagen scaffolds.[78][77][214] However, such advances didn't allow to elucidated the bulk structural features of SAPs hydrogels, which instead play a pivotal role in the definition of biocompatibility of these materials.

The application of ssNMR spectroscopy to SAPs hydrogels have allowed to depict their bulk structural features, even without synthetic isotope enrichment. Indeed, ssNMR spectroscopy at the natural abundance has been successfully applied to highlight molecular rigidity of biotinylated BMHP1-derived hydrogels, a promising class of SAPs for neural tissue engineering applications.[19][57] Then, ssNMR evidences addressed atomistic restrained MD simulations of these SAPs to understand the role of chemical moieties, such as biotin, in their self-assembly pathways.[57] More specifically, the evidence of ssNMR demonstrated that biotin plays a critical role in the formation of rigid SAP hydrogels, packing into the hydrophobic core of the coacervates.[57]

The wide applications of such approach, for the *in-silico* characterization of SAPs hydrogels, is mainly hampered by the availability of large computational resources, in addition to the availability of advanced NMR spectrometers.

To cope with limited computational resources and even scaling the size of the simulated systems, MARTINI CG-MD simulations represent a valid alternative. Indeed, the MARTINI CG-MD simulations allow to explore larger systems on longer times, without losing details about amino-acid side chains conformations.[59][58] However, MARTINI CG-MD simulations don't permit to track hydrogen bonding formation and other relevant details for self-assembly mechanisms, due to the MARTINI mapping strategy.

Then, as shown in Chapter 2, an innovative software suite for the analysis of protein systems, easily extendable to other molecular classes, has been developed. Such software suite, dubbed Morphoscanner, have been used for the elucidation of three SAPs hydrogels self-assembly. In particular, the analysis of CG-MD simulations of CAPs and self-complementary (*LDLK*)<sub>3</sub> SAPs revealed that these SAPs formed patches of  $\beta$ -rich aggregates evolving toward cross- $\beta$  packing, yielding to highly ordered systems compatible with empirical observations.[17][24] On the other hand, the Morphoscanner analyses of CG-MD simulations of BMHP1-derived SAPs highlighted a thermodynamically stable alignment that however may prevent any subsequent evolution toward well-structured nanofibers detected in previous experimental works.[215][57] More in details, BMHP1-derived SAPs preferentially aligned into parallel arrangement, bringing to the formation of short and stable  $\beta$ -sheets, which can't further organize into larger supra-molecular aggregates. These  $\beta$ -structures are characterized by a number of contacts higher than those identified in  $\beta$ -structures made of CAPs and self-complementary (*LDLK*)<sub>3</sub> SAPs (See Chapter 2 for details). Such conditions imply thermodynamics stability of BMHP1-derived SAPs coacervates. The results in Chapter 2, under the light of the evidences from ssNMR and atomistic restrained MD of SAPs systems[57], define a reliable multiscale approach for the characterization of bulk structural features of SAPs hydrogels.

As shown in chapter 3, MARTINI CG-MD simulations, combined with Morphoscanner analyses, have been also used to highlight structural features of the innovative SAPs hydrogels made by mixture of branched and linear (*LDLK*)<sub>3</sub> SAPs, even functionalized with BMHP1 functional motif.[19][215] The branched SAPs represent promising tools for improving the mechanical properties of self-assembling scaffolds without chemical or enzymatic cross-linking, alternative strategies that may lead toxic side-effects. Indeed, branched SAPs may be added to both standard and previously functionalized SAPs to match the desired mechanical strength and to add multiple heterogeneous functional motifs or tags.[109] Such molecular features contributed to improve mechanical features of SAPs hydrogels. Besides, the correct exposure of BMHP1 functional motifs well-correlates with the improved adhesion

and proliferation of NSCs on SAPs hydrogel scaffolds.[109]

The structure-properties relationship for  $(LDLK)_3$  SAPs has been deeply investigated in chapter 4, through a multiscale modeling approach. More in details, atomistic SMD and GoMARTINI CG-SMD simulations have been used to derive the elastic and shear moduli of  $(LDLK)_3$  and FAQ- $(LDLK)_3$  fibrils. The comparison of the results of the above mentioned SMD approaches suggested that GoMARTINI-SMD simulations provide comparable results to atomistic SMD simulations. In addition, the evidence from both SMD simulations approaches pointed out that the shear modulus of fibrils is higher in  $(LDLK)_3$  than in FAQ- $(LDLK)_3$ , indicating a clear correlation with experimental characterization of  $(LDLK)_3$  and FAQ- $(LDLK)_3$  hydrogels.[20][109]

As demonstrated by several studies  $(LDLK)_3$  SAP hydrogels induce NSCs adhesion and proliferation.[109][200][20] In chapter 5, MARTINI CG-MD simulations have been used to investigate the interactions among SAPs fibril and neural membranes. These simulations revealed that the aspecific interactions among  $(LDLK)_3$  fibrils and neural membranes mainly involve glycolipids. In particular, the fibril "leucine zipper" drives the adhesion to the neural membrane, through establishment of hydrophobic interactions with membrane lipids. Then, charge side chains on  $(LDLK)_3$  fibrils establish interactions with glycolipids, stabilizing the conformation of the cell-fibril systems. In addition, such simulations demonstrated that  $(LDLK)_3$  SAPs are not internalized in NSCs, preventing then potentially cytotoxic effects. These results demonstrated that CG-MD simulations are also suitable for evaluating the biocompatibility of SAPs hydrogels through *in-silico* approaches.

Because glycosylation is the most common PTMs in the ECM environment, and taking into account the evidences of the previous chapters, in chapter 6 a series of differently glycosylated BMHP1 functionalized  $(LDLK)_3$  have been simulated through MARTINI CG-MD simulations, and then analyzed through Morphoscanner. Such simulations allowed to elucidate the supra-molecular organization of these SAPs, highlighting the effects of different glycosylations. Indeed, glycosylation with standard carbohydrates allow to obtain more ordered supra-molecular aggregates at lower concentration, while the glycosylation with acetylated carbohydrates lead to the formation of more stable  $\beta$ -sheets. These results will guide the development of other glycosylated SAPs, which will be following tested *in-silico* and then synthesized.

In conclusion, this thesis lay the foundation of an innovative and reliable CG-MD approach for the development of innovative SAPs hydrogels for tissue engineering applications. Indeed, MARTINI CG-MD simulations can be used to predict structural and mechanical properties of SAPs fibril (See Chapters 2, 3, 4 and 6) integrating structural insights from several experimental techniques.[57] Also, CG-MD simulations allow the elucidation or prediction of the interactions among hydrogels and cells at the nano-scale and micro-scale (See Chapter

5).

Soon, the results from SMD simulations of SAPs nano-fibrils could be used for the definition of the parameters for continuum models, which will allow the direct comparison among hydrogels mechanical characterization and simulation predictions. This step will complete the multiscale approach for SAPs hydrogels *in-silico* characterization, opening new opportunities in the field of tissue engineering.



Part I  
Appendices



## Chapter 8

# Morphoscanner: Additional Tables and Figures



## 8.1 COARSENING OF BIOTIN: FROM GROMOS53A6 TO MARTINI

The biotinyl termination of biotinylated BMHP1-derived SAPs was mapped and parametrized in accordance with the MARTINI approach. We adopted the coarsening approach proposed by Marrink et al.[50] At first we mapped the chemical structure of biotinyl for a CG representation. As shown in Fig. 8.1, biotinyl termination was divided in five atom groups, or grains. This mapping was necessary to assign the appropriate CG particle type to each grain.[50][58] The second step was the selection of the appropriate bonded interactions: lastly we optimized the model by comparing it to the corresponding UA (Gromos53a6 ff) simulations. We compared the UA and CG simulations of BMHP1-derived SAPs 8-mers. After many rounds of model optimization, the value of the bond lengths and angles measure, was chosen as shown in Figure 8.2, 8.3, 8.4.

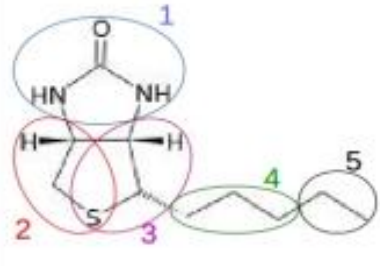
Biotinyl atom groups	Grain number	Interaction site	Type	Atom
	1	B61	P3	N2,C2,OB,N1
	2	B62	SC5	S,CF,CG
	3	B63	SC5	S,CE,CH
	4	B64	SC3	CO,CC,CB
	5	B65	Na	CA,C,O

FIGURE 8.1: **Biotinyl Coarse-grained mapping.** The biotinyl group has been divided in five groups of atoms. In accordance with MARTINI mapping each group consists of 3 or 4 heavy atoms (C,N,O,S). In order to preserve cyclical geometry of ureido and thiophene ring, they were mapped respectively as a single interaction site (B61) and two different interaction sites (B62,B63). The valeryl chain was mapped with two interaction sites (B64, B65). The B65 interaction sites represent the amide group connecting valeryl chain to the first residue of BMHP1-derived SAPs.

Bond id	Bond Type	Bond length (Å)	Force constant (kJ mol <sup>-1</sup> nm <sup>-2</sup> )
b1 (1-2)	P3-SC5	0.32	constraint
b2 (2-3)	SC5-SC5	0.09	constraint
b3 (1-3)	P3-SC5	0.319	constraint
b4 (3-4)	SC5-SC3	0.4	2500
b5 (4-5)	SC3-Na	0.29	1250

FIGURE 8.2: **Calculated bond lengths (Å) in biotinyl groups.** Sidechain bonds of the grains representing the biotin rings were introduced (b1,b2,b3) to preserve the cyclical geometry of biotinyl group. The lengths of these bonds are similar to those of Trp.

Angle id	Angle Type	Angle (Degree)	Force constant (kJ mol <sup>-1</sup> )
a1 (1-2-3)	P3-SC5-SC5	81.91	constraint
a2 (2-1-3)	SC5-P3-SC5	16.16	constraint
a3 (1-3-4)	P3-SC5-SC3	105.84	25.0
a4 (2-3-4)	SC5-SC5-SC3	154.371	25.0
a5 (3-4-5)	SC5-C3-Na	102.734	25.0

FIGURE 8.3: **Calculated bead angles in biotin structure.** In the CG model bead angles were introduced to mimic the atomic structure of biotin.

Dihedral id	Dihedral Type	Angle(Degree)
d1 (1-2-3-4)	P3-SC5-SC5-SC3	-0.61
d2 (3-1-2-4)	SC5-P3-SC5-SC3	-0.11
d3 (1-3-4-5)	P3-SC5-SC3-Na	-1.64
d4 (2-3-4-5)	SC5-SC5-SC3-Na	3.687

FIGURE 8.4: **Calculated dihedral angles in biotin structure.** Dihedral angles d1, d2, d3 and d4 were chosen to preserve the relative orientation among ureido and thiophene rings, as well as their planar geometry.

## 8.2 BIOTIN PARTITIONING COEFFICIENT

Following the MARTINI protocol for the parametrization of new molecules, we calculated the biotin octanol/water partition coefficient POW.[50][58] To obtain  $P_{OW}$ , the free energy of solvation of biotin was calculated in both aqueous and organic phase. The difference between the solvation free energy in the aqueous ( $\Delta G^W$ ) and organic phase ( $\Delta G^O$ ) is the partitioning free energy ( $\Delta\Delta G^{OW}$ ) of biotin between water-saturated octanol solution and water:

$$\Delta\Delta G^{OW} = -2.3RT \log P_{OW} \quad (8.1)$$

$R$  is the molar constant of Boltzmann,  $T$  is the temperature (set to 300 K),  $\Delta G^W$  and  $\Delta G^O$  are calculated as the free energy  $\Delta F$  of the solute in vacuum (state A) and in the condensed phase (state B) using the thermodynamic integration (TI) approach.

$$\Delta F = F_A - F_B = \int_{\lambda_A}^{\lambda_B} d\lambda \left\langle \frac{\delta U_{uv}(\lambda)}{\delta \lambda} \right\rangle_{\lambda} \quad (8.2)$$

$U_{uv}(\lambda)$  denotes the potential energy function describing the total solute-solvent interaction: the average  $\left\langle \frac{\delta U_{uv}(\lambda)}{\delta \lambda} \right\rangle$  is calculated over the MD trajectory.  $U_{uv}$  is a function of  $\lambda$  (the coupling parameter) and varies linearly from 0 to 1.

Calculations were performed at 20 intermediates  $\lambda$  values. Biotin atom types used for thermodynamic integration are reported in Fig. 8.1: however, atom type 5 had to be changed from Na to P3 (protonated carboxyl group). Indeed, in order to reproduce experimental conditions for partition coefficient calculation, biotin was assumed to be fully protonated (pKa = 4.4, pH = 4 in distilled water). The thermodynamic integration simulation setup and the calculated solvation free energies ( $\Delta G^W, \Delta G^O$ ) are reported in Fig. 8.5. As shown in Fig. 8.5 biotin CG model is satisfactorily parametrized as it reproduces biotin thermodynamic properties.

<b>Biotin</b>	<b>Water</b>	<b>Octanol</b>	<b>Time(ns)</b>	<b>T(K)</b>	<b><math>\Delta G_{\text{SOLV}}</math> (kJ/mol*K)</b>	
1	399	0	20 x 6	300	82.51	$\Delta G^{\text{W}}$
1	0	181	20 x 6	300	84.87	$\Delta G^{\text{O}}$
					2.36	$\Delta G^{\text{OW}}$
<b><math>\log P_{\text{OW}}(\text{CG})</math></b>					<b><math>\log P_{\text{OW}}(\text{exp})</math></b>	
-0.411					-0.462	

FIGURE 8.5: **Summary of the simulation performed for TI and related results.** The difference between the calculated ( $\log P_{\text{OW}}(\text{CG})$ ) and the experimental ( $\log P_{\text{OW}}(\text{exp})$ ) partition coefficients suggests a good reproduction of the thermodynamic properties of biotin with the MARTINI coarsened model we developed.

## 8.3 SECONDARY STRUCTURE PARAMETERS FROM CONFORMATIONAL SAMPLING OF UA-MD SIMULATIONS

Cluster	Cluster Size	SS parameters
1	4	CCSSCCCCC
2	2	CCCCCCCCC
3	1	CCSCCTTCC
4	1	CCSSCCSSCC

TABLE 8.1: **SAM Secondary structure parameters from conformational sampling of B24.** Secondary structure parameters were identified through the analysis of monomer UA-MD simulations. The secondary structure of the corresponding monomer has been monitored by means of DSSP algorithm of Kabsch and Sander.

Cluster	Cluster Size	SS parameters
1	3	CETTECCCCC
2	2	CEETTTEECCC
3	1	CCSSCCCSCCC
4	1	CCCSCCCCCC
5	1	CCSSCCSSS

TABLE 8.2: **SAM Secondary structure parameters from conformational sampling of 30.** The secondary structure parameters of 30 were identified following the same workflow adopted for B24. The 30 monomer starting conformations in octameric systems were more polymorphic compared to B24.

Cluster	Cluster Size	SS parameters
1	2	CCSSSCCCCC
2	2	CCCSSCCCCC
3	1	CCSSSSCCCC
4	1	CCSSSCSSS
5	1	CCSSCCSSS
6	1	CCCCCSSS

TABLE 8.3: **SAM Secondary structure parameters from conformational sampling of 31.** As reported in our previous work, secondary structure parameters were monitored, in monomer UA-MD simulations, by means of the DSSP algorithm. If compared to octameric systems of B24 and 30, the monomer starting conformations of 31 were more polymorphic.

## 8.4 CG-MD SIMULATIONS SETUP

Sequence ID	Sequence	Box size (nm)	CG ions beads (NA+/CL-)	CG Water beads	N° of peptides	N° sim x time (ns)
<b>2</b>	GGGPFSSTKT	17.56	50/150	43770	100	1 x 2000 2 x 500
<b>B3</b>	Btn-GGGPFSSTKT	18.6	60/160	52213	100	1 x 2000 2 x 500
<b>4</b>	WGGGPFSSTKT	18.61	60/160	52480	100	1 x 2000 2 x 500
<b>B24</b>	Btn-GGGAFAS TKT	18.35	58/158	50314	100	1 x 4500 2 x 500
<b>B26</b>	Btn-GGGPFAS TKT	18.52	59/159	51038	100	1 x 2000 2 x 500
<b>30</b>	WGGGAFAS TKT	18.4	58/158	50311	100	1 x 4500 2 x 500
<b>31</b>	WGGGAFSSTKT	18.42	58/158	50612	100	1 x 2000 2 x 500
<b>(LDLK)<sub>3</sub></b>	LDLKLDLKLDLK	28.8	0/0	200058	100	3 x 4500
<b>(LDDL)<sub>3</sub>+ (LKLK)<sub>3</sub></b>	LDDLDDLDDL+ LKLK LKLK LKLK	28.8	184/184	199649	50 + 50	3 x 4500

FIGURE 8.6: **CG-MD simulations setups** All BMHP1-derived SAPs (2, B3, 4, B24, B26, 30, 31) systems were simulated at 3% (w/v) to mimic the standard empirical conditions enabling nanostructured hydrogel formation.  $(LDLK)_3$  and CAP concentration was 1% (w/v). SS parameters of all residues were set to extend. Three CGMD simulations have been carried out for each system up to 500 ns: one simulation per each set was prolonged to 2000 ns. Lastly, simulations were further prolonged to 4500 ns for  $(LDLK)_3$ ,  $(LDDL)_3 + (LKLK)_3$ , B24 and 30

8.5 SHIFT VALUES OF BMHP1-DERIVED SAPS AND (LDLK)<sub>3</sub> SAPS

Shift Value (k)	Parallel arrangement (P)	Antiparallel arrangement with positive shift (A+)	Antiparallel arrangement with negative shift (A-)
0	NtGGGX <sub>1</sub> FX <sub>2</sub> STKT NtGGGX <sub>1</sub> FX <sub>2</sub> STKT	NtGGGX <sub>1</sub> FX <sub>2</sub> STKT TKTSX <sub>2</sub> FX <sub>1</sub> GGGN <sub>i</sub>	NtGGGX <sub>1</sub> FX <sub>2</sub> STKT TKTSX <sub>2</sub> FX <sub>1</sub> GGGN <sub>i</sub>
1	NtGGGX <sub>1</sub> FX <sub>2</sub> STKT NtGGGX <sub>1</sub> FX <sub>2</sub> STKT	NtGGGX <sub>1</sub> FX <sub>2</sub> STKT TKTSX <sub>2</sub> FX <sub>1</sub> GGGN <sub>i</sub>	NtGGGX <sub>1</sub> FX <sub>2</sub> STKT TKTSX <sub>2</sub> FX <sub>1</sub> GGGN <sub>i</sub>
2	NtGGGX <sub>1</sub> FX <sub>2</sub> STKT NtGGGX <sub>1</sub> FX <sub>2</sub> STKT	NtGGGX <sub>1</sub> FX <sub>2</sub> STKT TKTSX <sub>2</sub> FX <sub>1</sub> GGGN <sub>i</sub>	NtGGGX <sub>1</sub> FX <sub>2</sub> STKT TKTSX <sub>2</sub> FX <sub>1</sub> GGGN <sub>i</sub>
3	NtGGGX <sub>1</sub> FX <sub>2</sub> STKT NtGGGX <sub>1</sub> FX <sub>2</sub> STKT	NtGGGX <sub>1</sub> FX <sub>2</sub> STKT TKTSX <sub>2</sub> FX <sub>1</sub> GGGN <sub>i</sub>	NtGGGX <sub>1</sub> FX <sub>2</sub> STKT TKTSX <sub>2</sub> FX <sub>1</sub> GGGN <sub>i</sub>
4	NtGGGX <sub>1</sub> FX <sub>2</sub> STKT NtGGGX <sub>1</sub> FX <sub>2</sub> STKT	NtGGGX <sub>1</sub> FX <sub>2</sub> STKT TKTSX <sub>2</sub> FX <sub>1</sub> GGGN <sub>i</sub>	NtGGGX <sub>1</sub> FX <sub>2</sub> STKT TKTSX <sub>2</sub> FX <sub>1</sub> GGGN <sub>i</sub>
5	NtGGGX <sub>1</sub> FX <sub>2</sub> STKT NtGGGX <sub>1</sub> FX <sub>2</sub> STKT	NtGGGX <sub>1</sub> FX <sub>2</sub> STKT TKTSX <sub>2</sub> FX <sub>1</sub> GGGN <sub>i</sub>	NtGGGX <sub>1</sub> FX <sub>2</sub> STKT TKTSX <sub>2</sub> FX <sub>1</sub> GGGN <sub>i</sub>
6	NtGGGX <sub>1</sub> FX <sub>2</sub> STKT NtGGGX <sub>1</sub> FX <sub>2</sub> STKT	NtGGGX <sub>1</sub> FX <sub>2</sub> STKT TKTSX <sub>2</sub> FX <sub>1</sub> GGGN <sub>i</sub>	NtGGGX <sub>1</sub> FX <sub>2</sub> STKT TKTSX <sub>2</sub> FX <sub>1</sub> GGGN <sub>i</sub>
7	NtGGGX <sub>1</sub> FX <sub>2</sub> STKT NtGGGX <sub>1</sub> FX <sub>2</sub> STKT	NtGGGX <sub>1</sub> FX <sub>2</sub> STKT TKTSX <sub>2</sub> FX <sub>1</sub> GGGN <sub>i</sub>	NtGGGX <sub>1</sub> FX <sub>2</sub> STKT TKTSX <sub>2</sub> FX <sub>1</sub> GGGN <sub>i</sub>
8	NtGGGX <sub>1</sub> FX <sub>2</sub> STKT NtGGGX <sub>1</sub> FX <sub>2</sub> STKT	NtGGGX <sub>1</sub> FX <sub>2</sub> STKT TKTSX <sub>2</sub> FX <sub>1</sub> GGGN <sub>i</sub>	NtGGGX <sub>1</sub> FX <sub>2</sub> STKT TKTSX <sub>2</sub> FX <sub>1</sub> GGGN <sub>i</sub>
9	NtGGGX <sub>1</sub> FX <sub>2</sub> STKT NtGGGX <sub>1</sub> FX <sub>2</sub> STKT	NtGGGX <sub>1</sub> FX <sub>2</sub> STKT TKTSX <sub>2</sub> FX <sub>1</sub> GGGN <sub>i</sub>	NtGGGX <sub>1</sub> FX <sub>2</sub> STKT TKTSX <sub>2</sub> FX <sub>1</sub> GGGN <sub>i</sub>
10	NtGGGX <sub>1</sub> FX <sub>2</sub> STKT NtGGGX <sub>1</sub> FX <sub>2</sub> STKT	NtGGGX <sub>1</sub> FX <sub>2</sub> STKT TKTSX <sub>2</sub> FX <sub>1</sub> GGGN <sub>i</sub>	NtGGGX <sub>1</sub> FX <sub>2</sub> STKT TKTSX <sub>2</sub> FX <sub>1</sub> GGGN <sub>i</sub>

FIGURE 8.7: **Shift values of BMHP1-derived SAPs** Possible  $\beta$ -strands alignments within  $\beta$ -sheets of BMHP1-derived SAPs. Nt denotes N-terminal acetylation (Ac) or functionalization with Biotin(Btn) or the amino acid residue tryptophan (Ac-W).  $X_1$  denotes phenylalanine (P) or alanine (A).  $X_2$  stands for serine (S) or alanine (A). Only one type of parallel arrangement is represented as there are no differences among parallel arrangements with positive and negative shifts.



Shift Value (k)	Parallel arrangement	Antiparallel arrangement
0	LDLKLDLKLDLK LDLKLDLKLDLK	LDLKLDLKLDLK KLDLKLDLKLDL
1	LDLKLDLKLDLK LDLKLDLKLDLK	LDLKLDLKLDLK KLDLKLDLKLDL
2	LDLKLDLKLDLK LDLKLDLKLDLK	LDLKLDLKLDLK KLDLKLDLKLDL
3	LDLKLDLKLDLK LDLKLDLKLDLK	LDLKLDLKLDLK KLDLKLDLKLDL
4	LDLKLDLKLDLK LDLKLDLKLDLK	LDLKLDLKLDLK KLDLKLDLKLDL
5	LDLKLDLKLDLK LDLKLDLKLDLK	LDLKLDLKLDLK KLDLKLDLKLDL
6	LDLKLDLKLDLK LDLKLDLKLDLK	LDLKLDLKLDLK KLDLKLDLKLDL
7	LDLKLDLKLDLK LDLKLDLKLDLK	LDLKLDLKLDLK KLDLKLDLKLDL
8	LDLKLDLKLDLK LDLKLDLKLDLK	LDLKLDLKLDLK KLDLKLDLKLDL
9	LDLKLDLKLDLK LDLKLDLKLDLK	LDLKLDLKLDLK KLDLKLDLKLDL
10	LDLKLDLKLDLK LDLKLDLKLDLK	LDLKLDLKLDLK KLDLKLDLKLDL
11	LDLKLDLKLDLK LDLKLDLKLDLK	LDLKLDLKLDLK KLDLKLDLKLDL

FIGURE 8.8: **Shift values of LDLK-derived SAPs.** The mutual alignment among  $(LDLK)_3$  SAP or CAPs can be summarized in parallel or antiparallel alignments without distinction between positive and negative shifts.

## 8.6 UA-MD SIMULATIONS OF 8-MER SYSTEMS

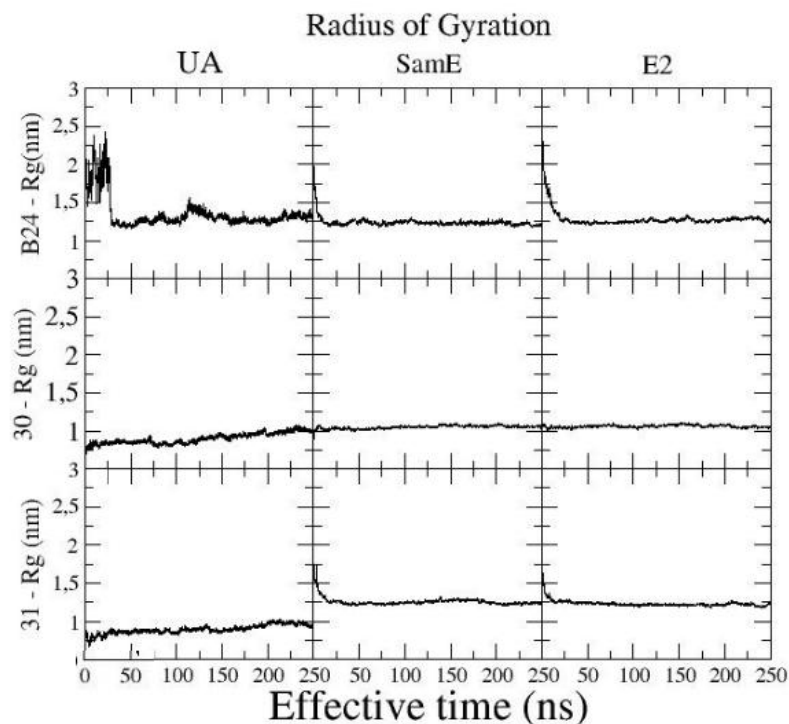


FIGURE 8.9: **Radius of gyration of octameric systems in UA-MD and CG-MD simulations.** As reported in our previous work, [91] the nucleation in UA-MD simulations occurred within 50 ns. The CG simulations of octameric systems with fully extended secondary structure parameters denoted a similar tendency in the nucleation feature of SAP systems. Indeed, the aggregate sizes of octameric systems were similar regardless of the chosen simulation model.

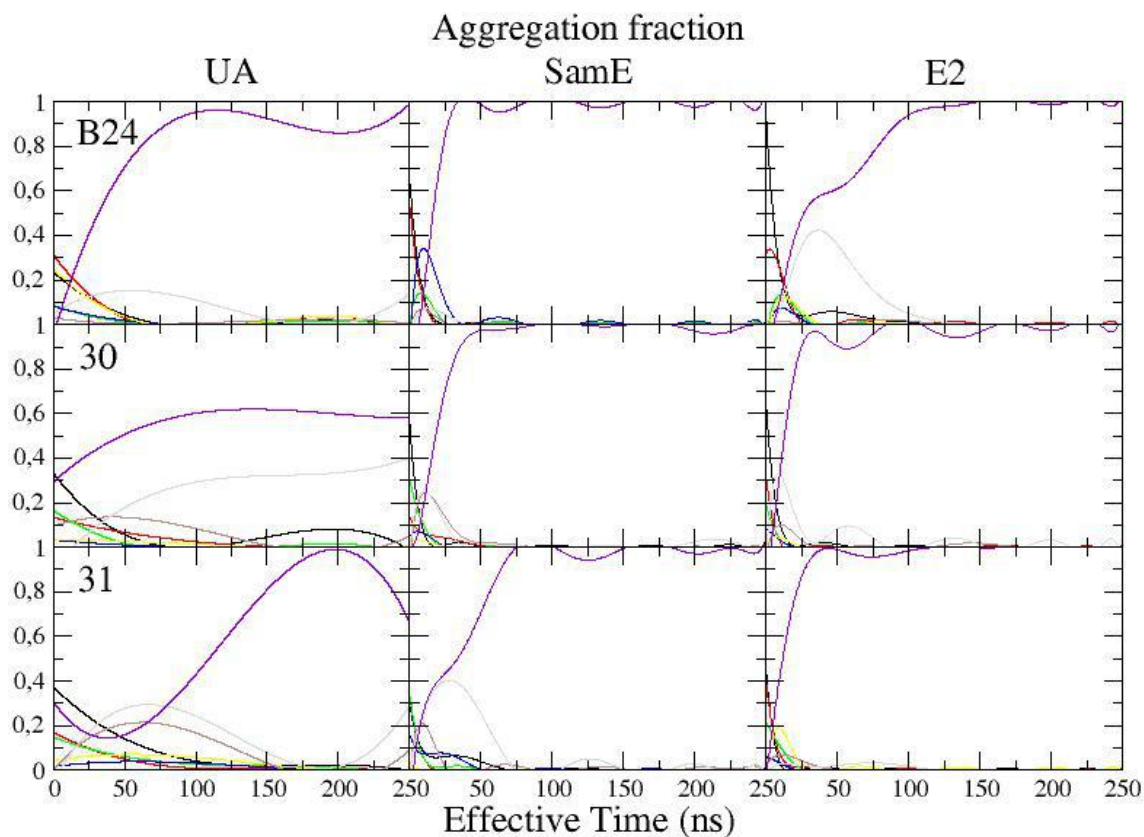


FIGURE 8.10: **Aggregation fraction of the multi-mers composing each system:** 8-mer in purple, 7-mer in silver, 6-mer in grey, 5-mer in blue, 4-mer in yellow, 3-mer in green, 2-mer in red, 1-mer in black. UA-MD and CG-MD simulations refer to octameric systems containing NaCl 0.015 M. The starting conformations of monomers were Sam (sampled from the UA-MD simulation of monomer) or E (fully extended). In CG-MD simulations with E secondary structure parameters oligomerization mechanism proceeded through similar intermediate steps unrelated to the initial monomeric conformation. These tendencies were similar to those observed in UA-MD simulations.

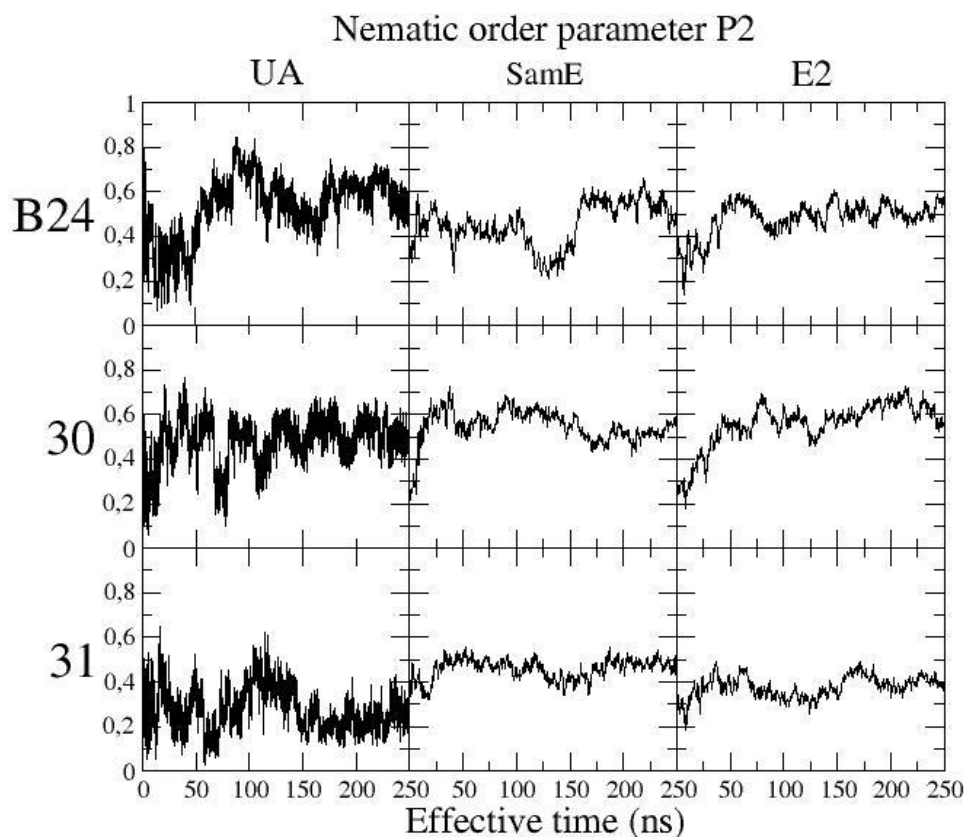


FIGURE 8.11: **Nematic order parameter  $P_2$  of octamers of B24,30,31.** In CG-MD simulations (SS parameters=E) the nematic order parameter  $P_2$  reached similar values observed in UA-MD simulations regardless of the initial monomeric conformations.



# Morphoscanner: the python module

This section shows some python functions of the Morphoscanner module. As shown in section 2.3.5, the recognition of  $\beta$ -sheets relies on the definition of  $\beta$ -contacts. The python module allow to reconstruct the distance map from CG beads coordinates, as shown below.

LISTING 8.1: Python function for the calculation of euclidean distance among two CG beads

```
import numpy as np

import tqdm

def get_euclidean_distance(point_1, point_2):

    euclidean_distance = np.sqrt(np.sum([((point_1[0] - point_2[0])**2),
    ((point_1[1] - point_2[1])**2), ((point_1[2] - point_2[2])**2)]))

    return euclidean_distance
```

The contact map is derived from the distance map.

LISTING 8.2: Python function for the calculation of the contact map

```
def contact_map_helix_torch(distance_map):

    contact_map = distance_map.clone()
    contact_map[contact_map <= 4.4] = 0
    contact_map[(contact_map > 4.4) & (contact_map <=5.1)] = 1
    contact_map[(contact_map > 5.1) & (contact_map <=6.5)] = 2
    contact_map[contact_map > 6.5] = 3

    return contact_map
```

The description of the interactions between two strands or peptides is provided by the Strand Backbone Contact matrix: a square matrix whose dimensions correspond to the number of strand/peptide backbone grains.

A set of matrices, named shift matrices, was developed to be used as references for the identification of the mutual arrangements described by the strand backbone contact matrix. Shift matrices describe the different arrangements between pairs of peptides. In detail, parallel and antiparallel shift arrangements are calculated through the following python functions:

LISTING 8.3: Python function for the calculation of shift matrices

```

import torch
import numpy as np
import pandas as pd
import tqdm

def shift_library_maker_torch(contact_map_to_analyze, device = 'cpu'):

    row = contact_map_to_analyze.shape[0]
    col = contact_map_to_analyze.shape[1]

    kron_dict = {}
    kron_list_parallel = []
    kron_list_antiparallel = []

    for e in range(-row+1, col):
        array = np.eye(row, col, e)
        kron_list_parallel.append(array)
        kron_list_antiparallel.append(np.fliplr(array))

    kron_dict['parallel'] =
    torch.from_numpy(np.asarray(kron_list_parallel)).to(device)
    kron_dict['antiparallel'] =
    torch.from_numpy(np.asarray(kron_list_antiparallel)).to(device)
    return kron_dict

```

To calculate the maximum similarity of shift matrices with peptide backbone matrix, the normalized cross-correlation function (NCC) was used, as shown below.

LISTING 8.4: Python function for the calculation of normalized cross-correlation

```
def normalized_cross_correlation_function_torch_v1(contact_map,
minimum_contact=2, device='cpu'):

    contact_map = contact_map.double()
    shift_matrix_library = shift_library_maker_torch(contact_map,
device=device)

    cross_correlation_values = []
    max_val = []
    sum_contact_map = torch.sum(contact_map)
    shift_matrix_center_index = ((contact_map.shape[0] +
contact_map.shape[1]) - 1)//2

if sum_contact_map < minimum_contact:
    pass

else:

    for sense in shift_matrix_library:

        signal_full = contact_map * shift_matrix_library[sense]
        signal_tens = torch.sum(signal_full, dim=(1,2))
        norm = torch.sqrt(sum_contact_map) *
        torch.sqrt(torch.sum(shift_matrix_library[sense],
dim=(1,2)))
        ncc = signal_tens/norm
        ncc_index = torch.argmax(ncc)
        ncc_val = ncc[ncc_index]

        denoised = signal_full[ncc_index]
        cross_correlation_values.append([ncc_val, ncc_index,
sum_contact_map, sense, denoised])

    max_val = max(cross_correlation_values)
    sum_denoised = torch.sum(max_val[4])
```



```
if sum_denoised >= minimum_contact:  
  
    shift = shift_matrix_center_index - max_val[1]  
    max_val[2] = sum_denoised  
    max_val.append(shift)  
  
    return max_val  
  
else :  
    pass
```

$\beta$ -sheet structures are detected by Morphoscanner by using the backbone contact and the strand interaction matrices, obtained from the functions above mentioned.

The Morphoscanner module is available at the following link:  
<https://github.com/lillux/morphoscanner.git>

# Analysis of CG-MD simulations with Morphoscanner: additional figures

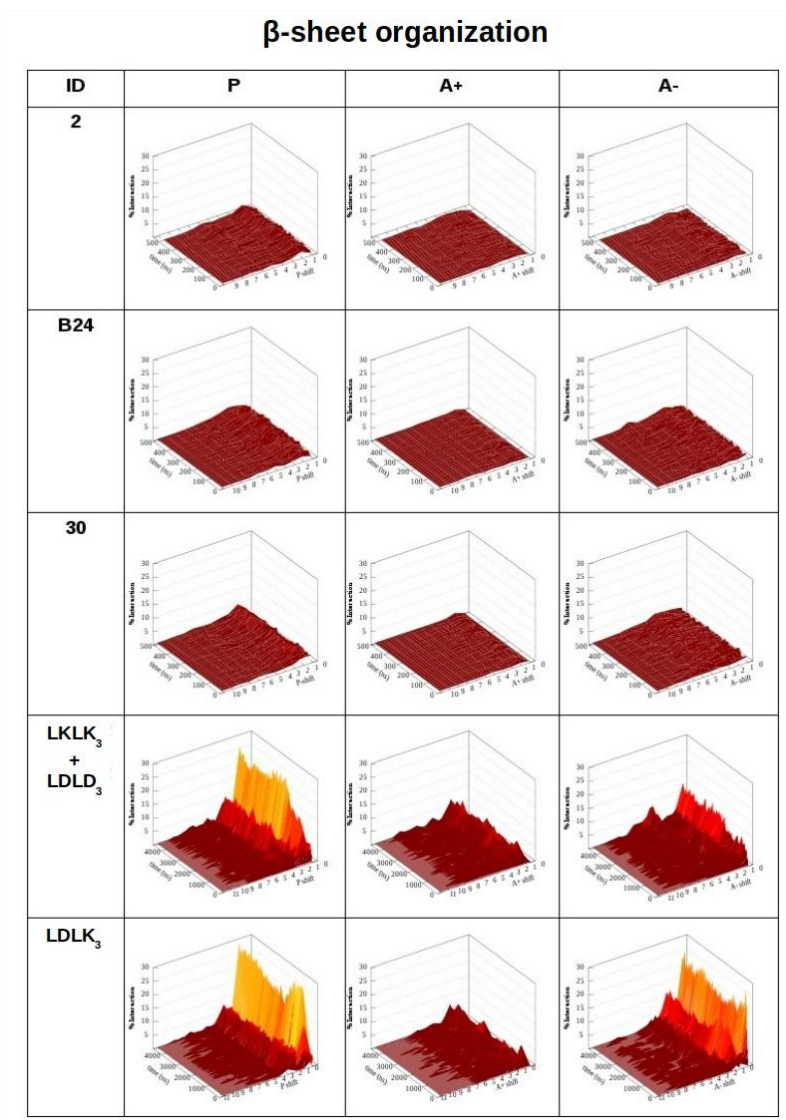


FIGURE 8.12: CAPs and  $(LDLK)_3$  assembled in stable  $\beta$ -sheet structures. Instead, BMHP1-derived SAPs did not show relevant formation of  $\beta$ -sheets. SAP 2, B24 and 30 were simulated with fully extended secondary structure parameters (see 8.6).

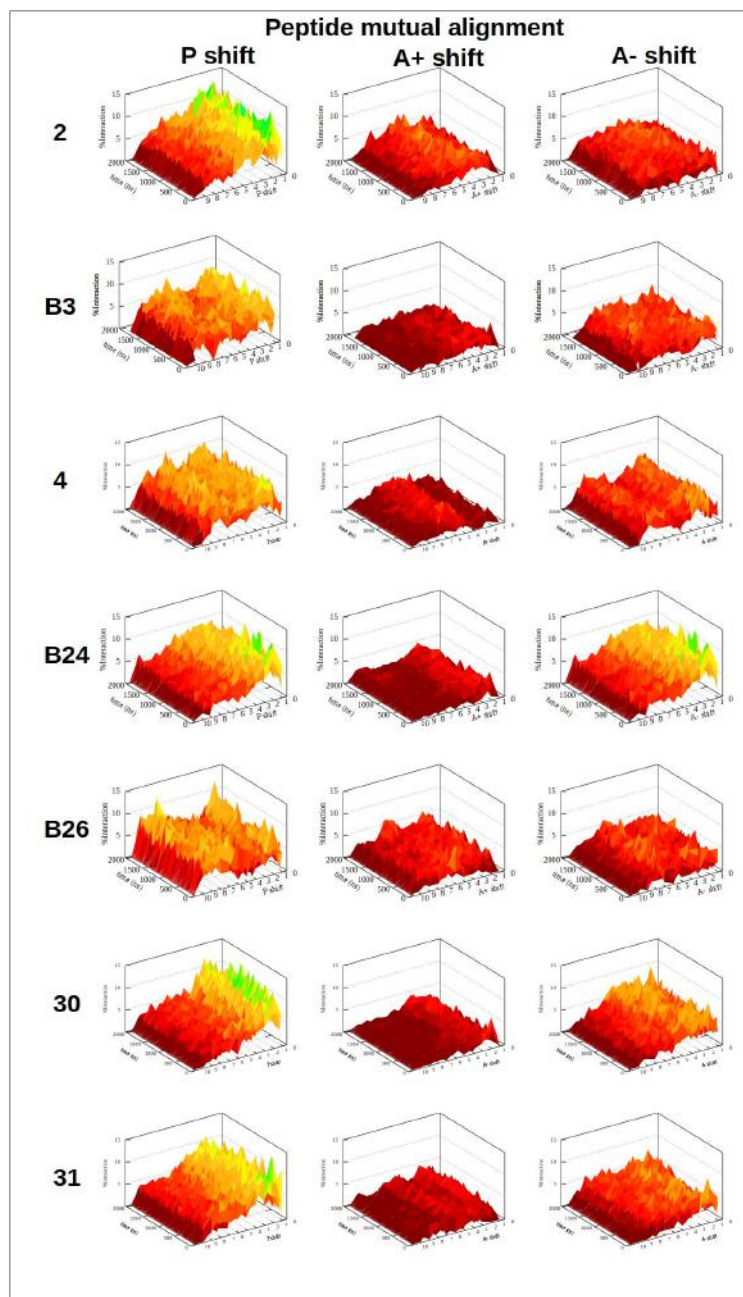


FIGURE 8.13: **Analysis of CG-MD simulations with full extended MARTINI SS parameters.** BMHP1-derived SAPs were preferentially aligned at one-residue shift in parallel arrangements. Notably, shift profiles of SAPs with Pro privileged parallel shift out-of-register by one-residue (2, B3, 4, B26), while mutation with Ala coaxed the onset of A- shift (B24, 30, 31).

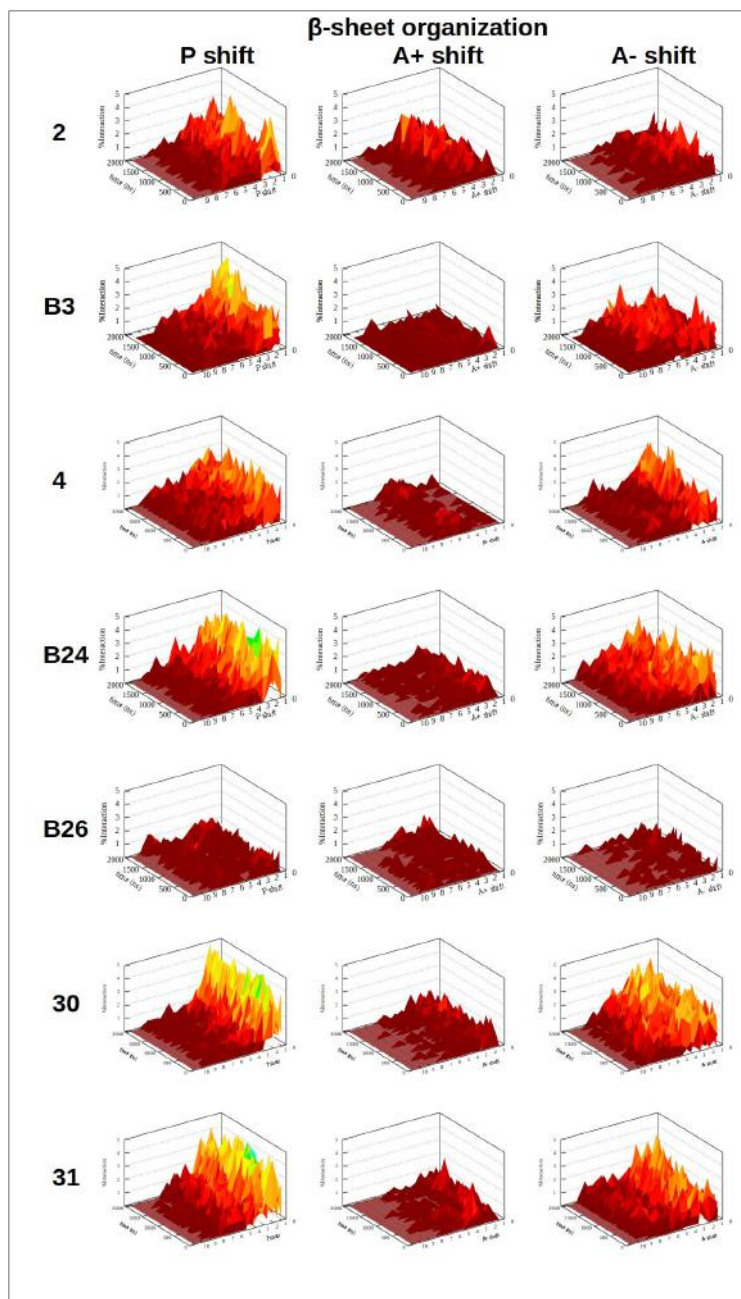


FIGURE 8.14:  $\beta$ -sheet organization of BMHP1-derived SAPs. BMHP1-derived SAPs preferentially aligned at one-residue shift in parallel arrangements within  $\beta$ -sheets. B26 showed the poorest propensity to  $\beta$ -sheet organization.

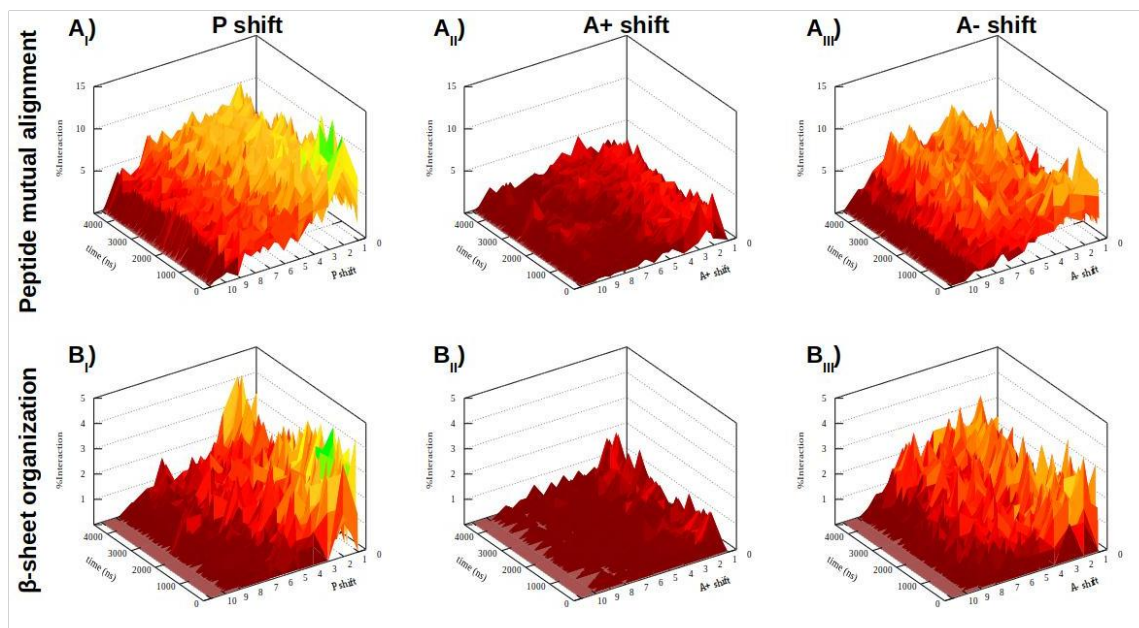


FIGURE 8.15: **Shift profiles of B24 (SS parameters=E).** The analysis of peptide mutual alignment and  $\beta$ -sheet organization were extended till 4500 ns for B24. Shift profiles showed that B24 preferentially aligned in parallel out-of-register but were not centered around any particular value, therefore B24 oligomers were characterized by a heterogeneous alignment. Shift profiles of  $\beta$ -sheet organization showed that  $\beta$ -strands were mutually aligned in parallel out-of-register.

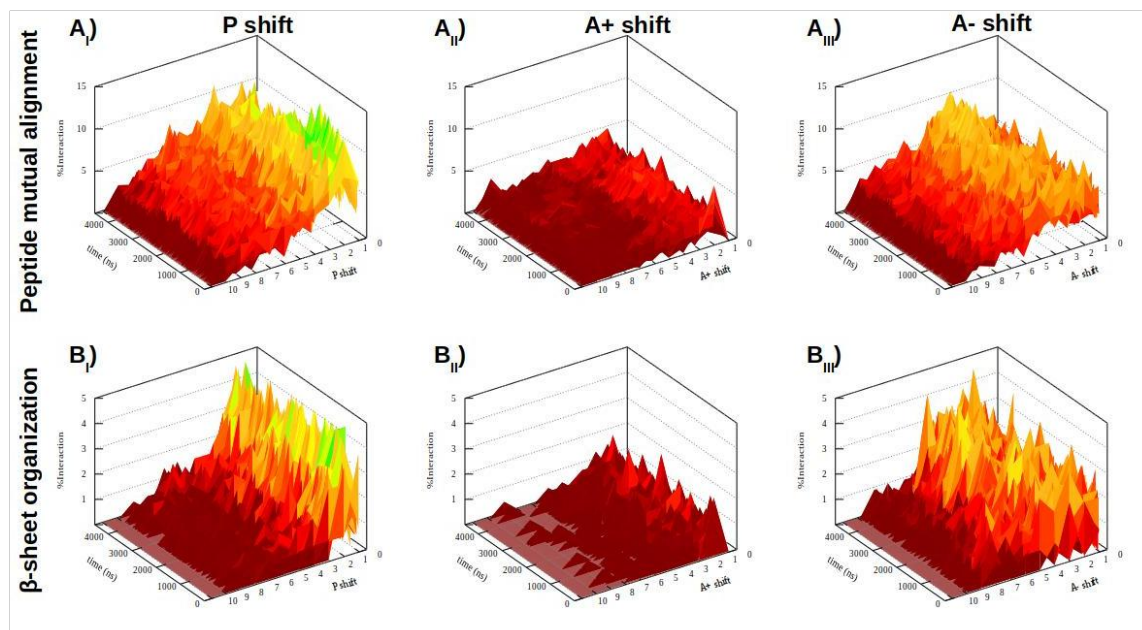


FIGURE 8.16: **Shift profiles of SAP 30 (SS parameters=E).** Shift profiles of CG-MD simulations of peptide 30 for up to 4500 ns. In  $A_{I,II,III}$  peptides were preferentially aligned in parallel out-of-register by one-residue. Same situation could be appreciated in  $B_{I,II,III}$  for  $\beta$ -sheet organization. 30 showed a lower tendency to  $\beta$ -structuring if compared to B24. This feature is likely given by the presence of Trp at the N-terminal.

## Chapter 9

# Branched SAPs: Additional Tables and Figures

Acronym	Box Size(nm)	Number of Molecules
$(LDLK)_3$	28.87	100
BMHP1-bis $(LDLK)_3$	27.93	33
tris $(LDLK)_3$	28.2	33
epta $(LDLK)_3$	29.5	14
$(LDLK)_3$ /BMHP1-bis $(LDLK)_3$	32.06	BMHP1-bis $(LDLK)_3$ + 131 $(LDLK)_3$
$(LDLK)_3$ /tris $(LDLK)_3$	33.72	tris $(LDLK)_3$ + 157 $(LDLK)_3$
$(LDLK)_3$ /epta $(LDLK)_3$	33.68	epta $(LDLK)_3$ + 150 $(LDLK)_3$

TABLE 9.1: **CG-MD simulation details:** box dimension (nm) and number of peptide molecules introduced in the simulation boxes.



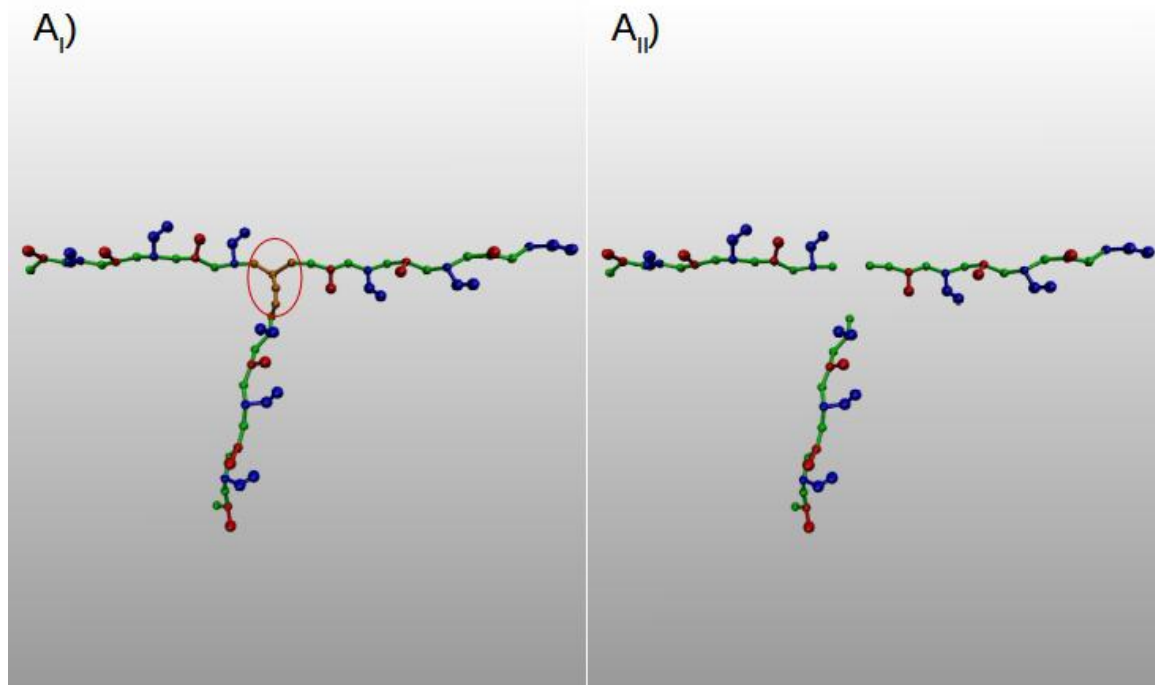


FIGURE 9.1: **Peptide branched as independent linear peptides.** *A<sub>I</sub>*) Branched peptides are made of tree-like branches linked with previously double-capped lysine knots (highlighted in orange). *A<sub>II</sub>*) Peptide branches can be considered as independent linear peptides for peptide alignment and  $\beta$ -sheet formation analyses. Peptides are represented with ball-and-stick model with Lysine, Aspartic acid, Leucine in blue, red and green respectively

## Chapter 10

# Nano-Mechanics of SAPs structures: Additional Tables and Figures

10.1 GoMARTINI MAPPING OF  $(LDLK)_3$  AND FAQ- $(LDLK)_3$  SAPs

Residue	BB atom type	SC atom type	Charge
LEU-1	P5	C1	0
ASP-2	P5	Qa	-1
LEU-3	P5	C1	0
LYS-4	P5	C3,Qd	+1
LEU-5	P5	C1	0
ASP-6	P5	Qa	-1
LEU-7	P5	C1	0
LYS-8	P5	C3,Qd	+1
LEU-9	P5	C1	0
ASP-10	P5	Qa	-1
LEU-11	P5	C1	0
LYS-12	P5	C3,Qd	+1

FIGURE 10.1: **GoMARTINI mapping of  $(LDLK)_3$  peptides.** Residue refers to amino-acid residue. BB atom type refers to the MARTINI grain type corresponding to the backbone atoms of a specific residue. SC atom type refers to the MARTINI grain type corresponding to the sidechain atoms of a specific residue. The UA backmapped fibril seed structures were analyzed with DSSP and then the SS parameters have been assigned.

Residue	BB atom type	SC atom type	Charge
LEU-1	Nda	C1	0
ASP-2	Nda	Qa	-1
LEU-3	Nda	C1	0
LYS-4	Nda	C3,Qd	+1
LEU-5	Nda	C1	0
ASP-6	Nda	Qa	-1
LEU-7	Nda	C1	0
LYS-8	Nda	C3,Qd	+1
LEU-9	Nda	C1	0
ASP-10	Nda	Qa	-1
LEU-11	Nda	C1	0
LYS-12	Nda	C3,Qd	+1

FIGURE 10.2: **GoMARTINI mapping of  $(LDLK)_3$  peptides with full extended SS parameters.** Residue refers to amino-acid residue. BB atom type refers to the MARTINI grain type associated with the backbone atoms of a specific residue. SC atom type refers to the MARTINI grain type associated with the sidechain atoms of a specific residue. The SS parameters have been assigned as fully extended.

Residue	BB atom type	SC atom type	Charge
PHE-1	P5	SC5,SC5,SC5	0
ALA-2	P4		0
GLN-3	P5	P4	0
ARG-4	P5	N0,Qd	+1
VAL-5	P5	C2	0
PRO-6	P4	C3	0
PRO-7	P4	C3	0
GLY-8	P5		0
GLY-9	P5		0
GLY-10	P5		0
LEU-11	Nda	C1	0
ASP-12	Nda	Qa	-1
LEU-13	Nda	SC1	0
LYS-14	Nda	C3,Qd	+1
LEU-15	Nda	C1	0
ASP-16	Nda	Qa	-1
LEU-17	Nda	C1	0
LYS-18	Nda	C3,Qd	+1
LEU-19	Nda	C1	0
ASP-20	Nda	Qa	-1
LEU-21	Nda	C1	0
LYS-22	Nda	C3,Qd	+1

FIGURE 10.3: **GoMARTINI mapping of FAQ-(LDLK)<sub>3</sub> peptides.** Residue refers to amino-acid residue. BB atom type refers to the MARTINI grain type corresponding to the backbone atoms of a specific residue. SC atom type refers to the MARTINI grains type corresponding to sidechain atoms of a specific residue. The UA backmapped fibril seed structures were analyzed with STRIDE and then the secondary structures were assigned.

## 10.2 FAILURE CLASSIFICATION OF SAPS SEEDS AND FIBRILS

Seed/Fibril ID	Young's Modulus (E) [MPa]	Shear Modulus (G) [MPa]	Shear Contribution Ratio $s(L)$
A	500	381	2.19
A (CG - dssp)	1279	840	2.41
A (CG-Ext)	1029	532	3.06
B	781	524	1.88
B (CG-dssp)	1167	821	1.39
B (CG-Ext)	820	313	2.56
C	664	566	1.31
C (CG-dssp)	1626	907	1.47
C (CG-Ext)	737	532	1.14
Fibrils	2003	612	0.06
Fibril (CG-dssp)	6252	787	0.14
Fibrils (CG-Ext)	5110	770	0.04

FIGURE 10.4: **Failure classification of  $(LDLK)_3$  seeds and fibrils.** Young's (or elastic) and shear moduli were derived considering the stress-strain curves by means of ratio between the maximum stress and the corresponding strain. The shear contribution ratio was calculated as shown in section 4.3.6. The shear contribution ratio,  $s(L)$ , provides information about strain distribution during bending failure; if  $s(L) > 1$ , non-covalent interactions are being sheared, otherwise are stretched along their direction. In  $(LDLK)_3$  SAPs supramolecular structures, shear contribution ratio points out that the bending failure mechanism are mainly affected by the geometrical features of the aggregates. Indeed, the bending failure mechanism of fibril seeds is mainly ruled by shear stress, whereas the bending failure mechanism of fibrils is mainly ruled by tensional stretching of non-covalent interactions

Seed/Fibril ID	Young's Modulus (E) [MPa]	Shear Modulus (G) [MPa]	Shear Contribution Ratio s(L)
A	701	350	2.38
A (CG - dssp)	837	331	2.45
B	823	339	0.43
B(CG-dssp)	878	539	0.29
C	706	393	2.01
C (CG-dssp)	654	299	2.12
Fibrils	3823	366	0.04
Fibril (CG-dssp)	4975	503	0.03

FIGURE 10.5: **Failure classification of FAQ-(LDLK)<sub>3</sub> seeds and fibrils.** Young's and shear moduli were derived as described in Table S8, meanwhile shear contribution ratio was calculated as shown in section 4.3.6. In FAQ-(LDLK)<sub>3</sub> SAPs supramolecular structures, the shear contribution ratio points out that the bending failure mechanisms are mainly affected by the geometrical features of the aggregates. Indeed, the bending failure mechanism of fibril seeds is mainly ruled by shear stress, whereas the bending failure mechanism of fibrils is mainly ruled by tensional stretching of non-covalent interactions.

## 10.3 COMPUTATIONAL PERFORMANCE ON GPU GEFORCE GTX 1080

Seed/Fibril ID	Number of Atoms/Grains	Simulated Time (ns/day)	Simulation Setup
A	62970	14.66	Traction
A(CG)	16045	368.43	Traction
A	62970	14.65	Bending
A(CG)	16045	409.79	Bending
B	62846	14.76	Traction
B(CG)	16038	144.88	Traction
B	62846	15.22	Bending
B(CG)	16038	133.39	Bending
C	62758	12.87	Traction
C(CG)	16035	159.75	Traction
C	62758	14.73	Bending
C(CG)	16035	162.82	Bending
Fibrils	152733	6.6	Traction
Fibrils(CG)	38469	75	Traction
Fibrils	225907	4.36	Bending
Fibrils(CG)	55853	33.8	Bending

FIGURE 10.6: **Details of  $(LDLK)_3$  SAPs SMD simulations.** Simulated Time refers to the output provided from the mdrun program of the GROMACS software suite.



<b>Seed/Fibril ID</b>	<b>Number of Atoms/Grains</b>	<b>Simulated Time (ns/day)</b>	<b>Simulation Setup</b>
A	43098	21.34	Traction
A(CG)	11013	168.47	Traction
A	43179	21.75	Bending
A(CG)	11025	181.39	Bending
B	43118	19.73	Traction
B(CG)	11013	195.87	Traction
B	43199	22.01	Bending
B(CG)	11016	112.88	Bending
C	43118	20.90	Traction
C(CG)	11021	225.22	Traction
C	43199	19.11	Bending
C(CG)	11019	163.69	Bending
Fibrils	248294	3.70	Traction
Fibrils(CG)	58759	55.68	Traction
Fibrils	544025	1.5	Bending
Fibrils(CG)	136218	25.27	Bending

FIGURE 10.7: **Details of FAQ-(LDLK)<sub>3</sub> SAPs SMD simulations.** Simulated Time refers to the output provided from the mdrun program of the GROMACS software suite.

# Nanomechanics of SAPs structure: Morphoscanner Analysis

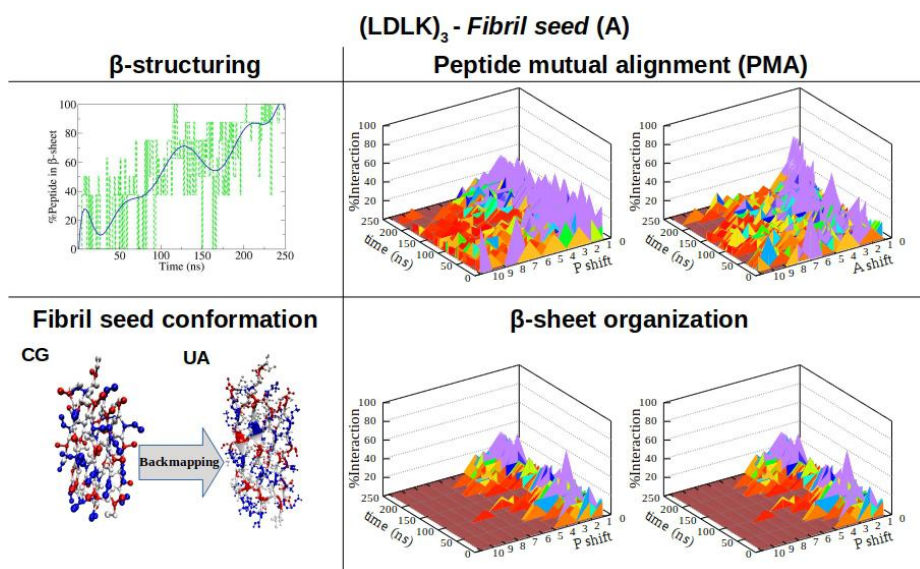


FIGURE 10.8: **Shift profiles and  $\beta$ -structuring propensity of  $(LDLK)_3$  SAPs.** P refers to the parallel alignment, A refers to the antiparallel alignment. Differently from the data shown in Fig.4.3,  $(LDLK)_3$  SAPs assembled in a less ordered double layered  $\beta$ -sheet structure. Indeed,  $(LDLK)_3$  were preferentially antiparallel aligned, whereas  $\beta$ -strands didn't show any preferential alignment.

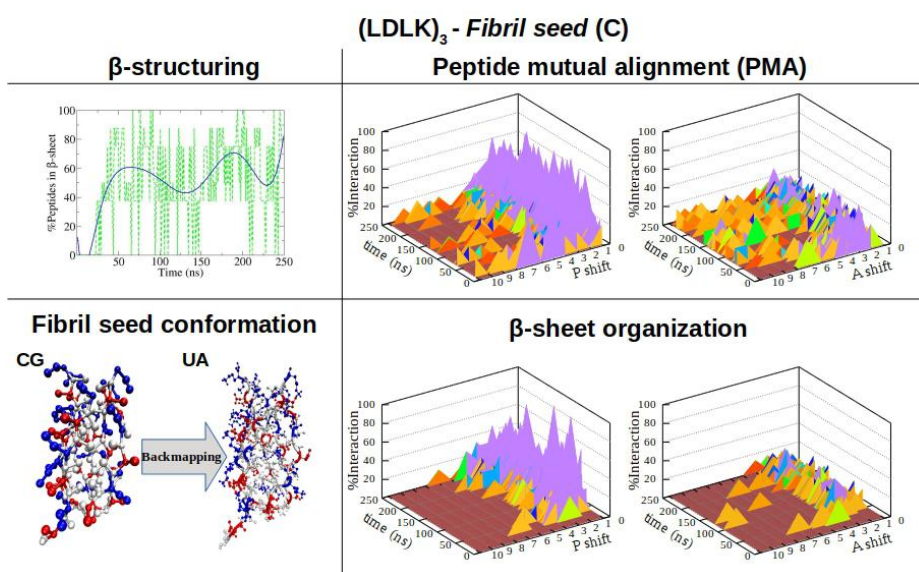


FIGURE 10.9: Shift profiles and  $\beta$ -structuring propensity of (LDLK)<sub>3</sub> SAPs. P refers to parallel alignment, A refers to antiparallel alignment. Differently from the data shown in Fig.4.3, (LDLK)<sub>3</sub> SAPs assembled in a less ordered double layered  $\beta$ -sheet structure. Indeed, (LDLK)<sub>3</sub> peptides were preferentially parallel aligned, such as  $\beta$ -strands.

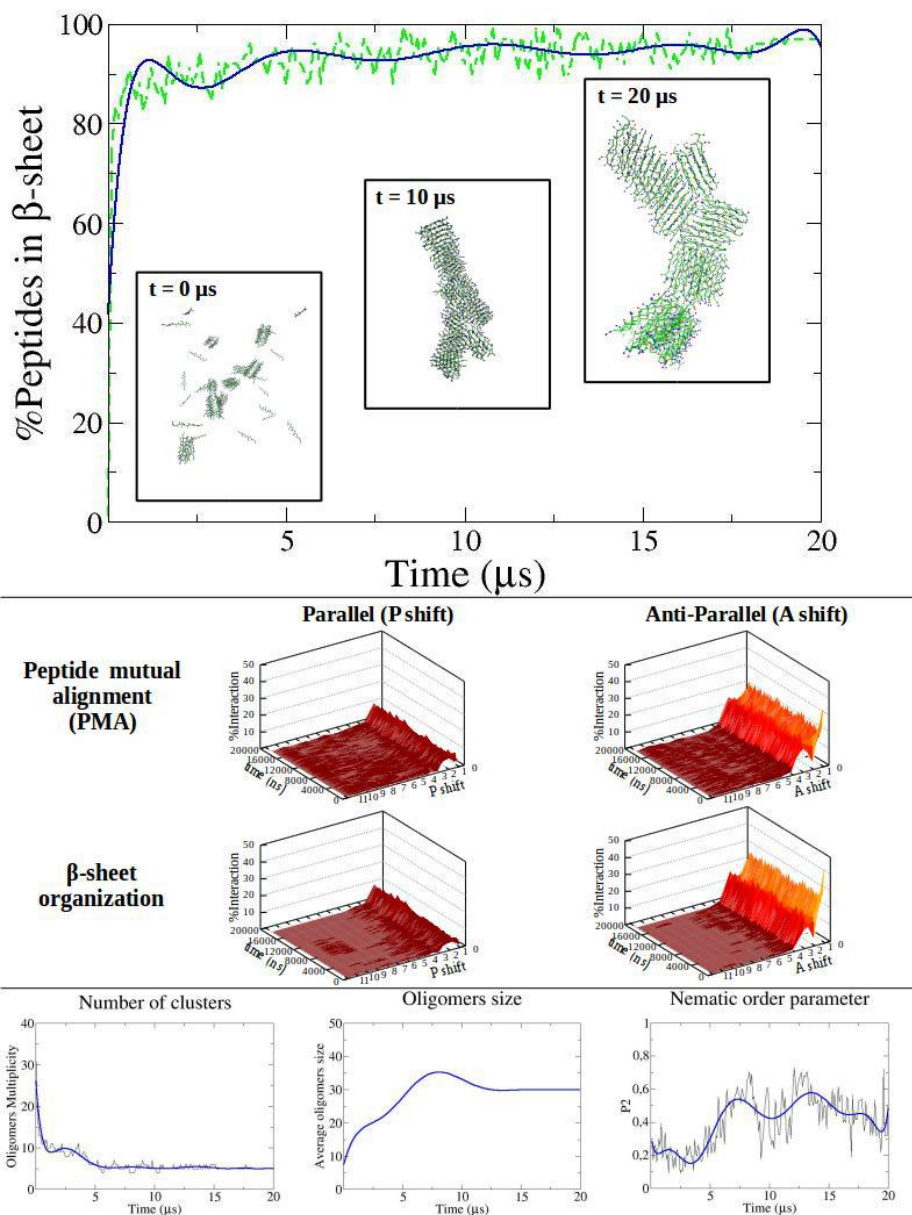


FIGURE 10.10: **ONE-POT CG-MD of  $(LDLK)_3$  SAPs.** ONE-POT CG-MD simulations have been prepared according to the data reported in Fig. 4.2. The fibril seed conformation corresponded to the final structure of CG-MD simulation reported in Fig. 4.3a. The  $(LDLK)_3$  SAPs, such as  $\beta$ -strands were mutually antiparallel aligned. This tendency was also reflected by nematic order parameter, which reached value equal to 0.5 within 5  $\mu\text{s}$ .

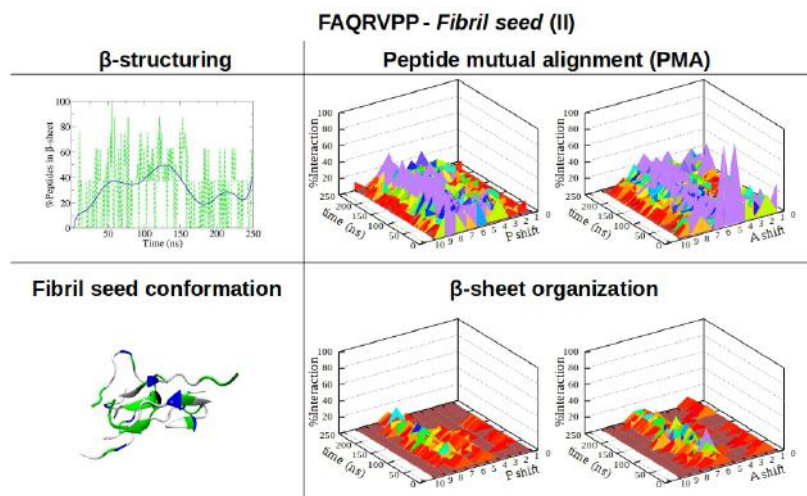


FIGURE 10.11: Shift profiles and  $\beta$ -structuring propensity of FAQ SAPs, 2nd replica. As shown in Fig. 4.5, FAQ peptides didn't show any preferential mutual alignment. However,  $\beta$ -strands were weakly aligned according to antiparallel and parallel arrangement.

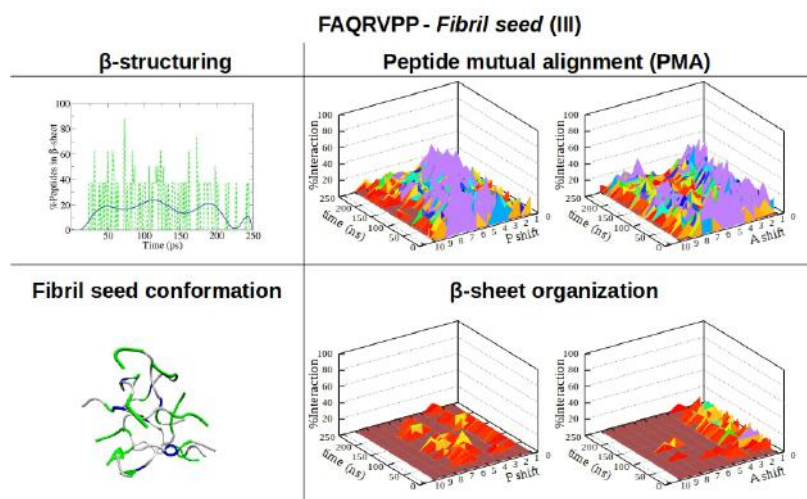
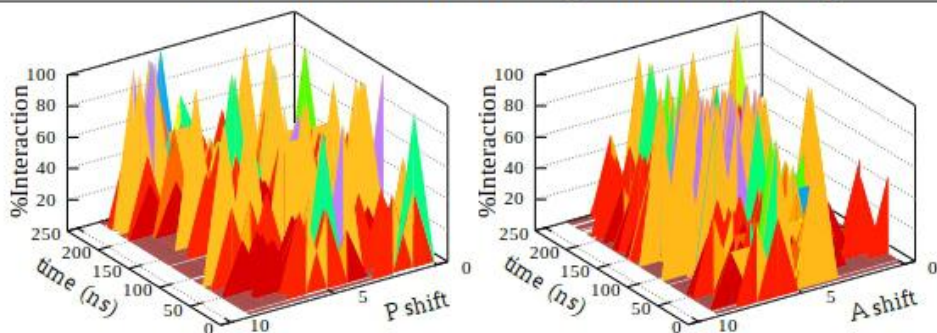


FIGURE 10.12: Shift profiles and  $\beta$ -structuring propensity of FAQ SAPs, 3rd replica. As shown in Fig. 4.5, the FAQ peptides didn't show any preferential mutual alignment and any  $\beta$ -strands alignment.



**FAQ-(LDLK)<sub>3</sub> - Fibril seed (C)**  
**Functional motif alignment (FMA)**



**$\beta$ -sheet organization**

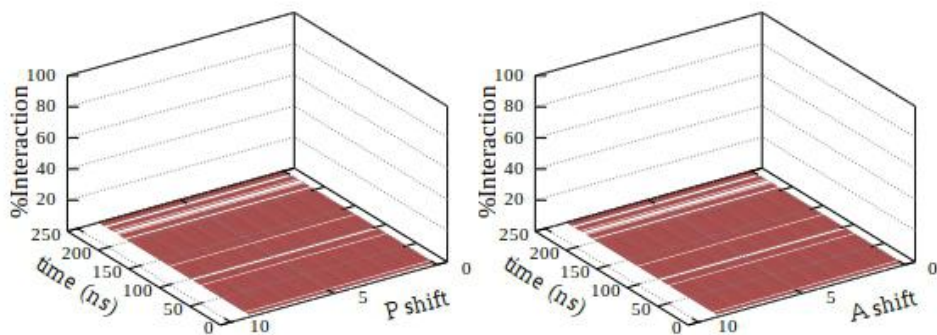


FIGURE 10.13: **Shift profiles and  $\beta$ -structuring propensity of functional motif FAQ-(LDLK)<sub>3</sub> SAPs.** According to the data shown in Fig. 4.5, Fig. 10.11 and Fig. 10.12, FAQ functional motif didn't assemble into ordered aggregates. This hampered the formation of  $\beta$ -sheet structures. Such features didn't alter the  $\beta$ -structuring propensity of backbone moieties, as shown in Fig. 4.3

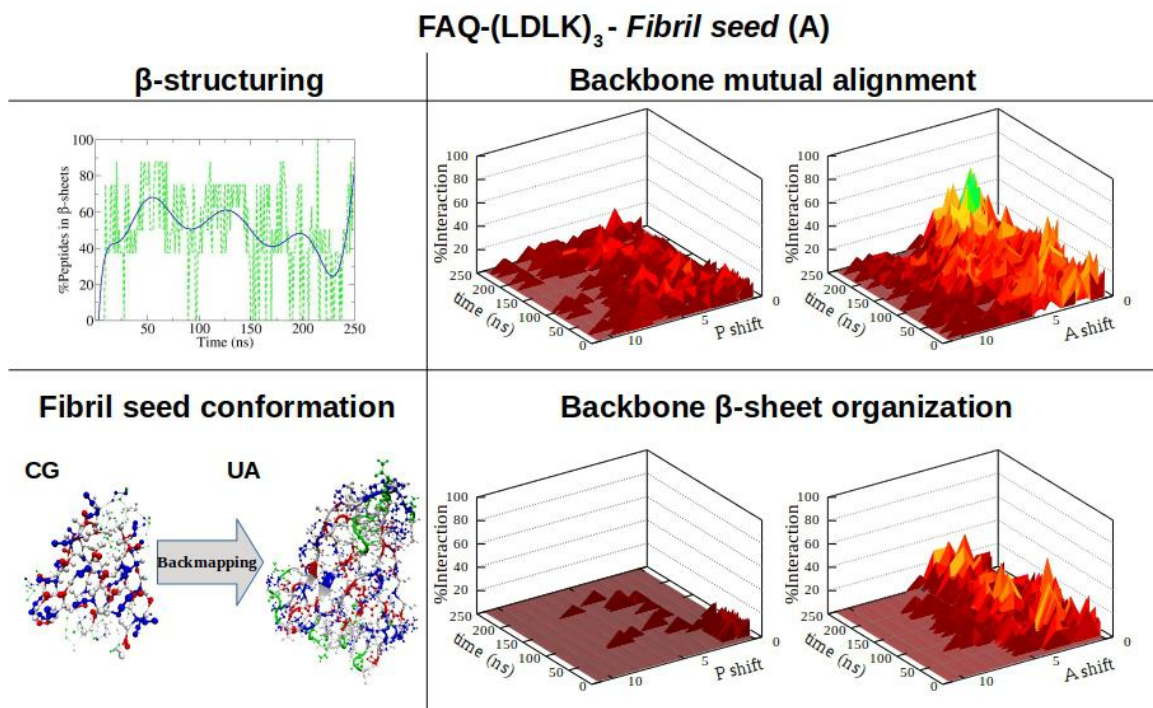
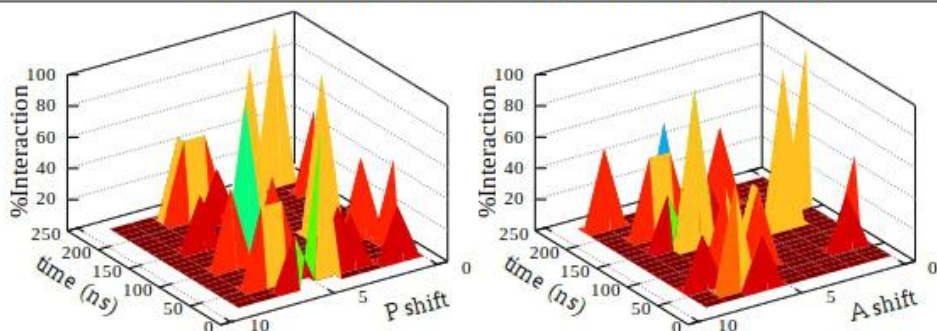


FIGURE 10.14: Shift profiles and  $\beta$ -structuring propensity of backbone moieties FAQ-(LDLK)<sub>3</sub> SAPs. As shown in Fig. 4.3b, FAQ-(LDLK)<sub>3</sub> backbone moieties PMA and  $\beta$ -sheet organization reflected those of (LDLK)<sub>3</sub> SAPs. Due to the presence of FAQ functional motif, FAQ-(LDLK)<sub>3</sub> peptides assembled into disordered aggregates.



**FAQ-(LDLK)<sub>3</sub> - Fibril seed (A)**  
**Functional motif alignment (FMA)**



**$\beta$ -sheet organization**

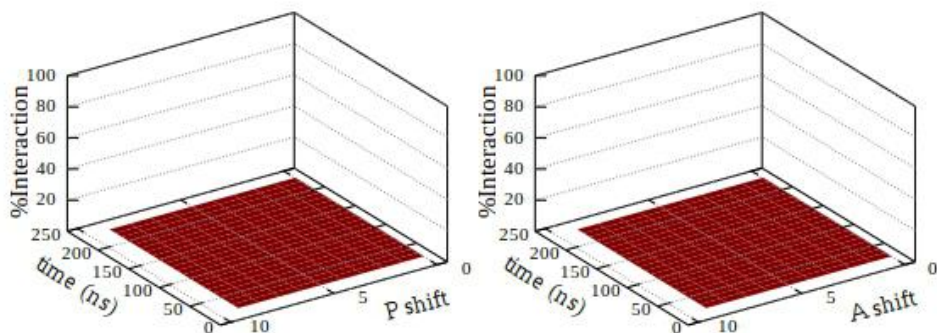


FIGURE 10.15: **Shift profiles and  $\beta$ -structuring propensity of functional motif FAQ-(LDLK)<sub>3</sub> SAPs.** According to the data shown in Fig. 4.5, Fig. 10.11 and Fig. 10.12, FAQ functional motifs didn't assemble into ordered aggregates. This hampered the formation of  $\beta$ -sheet structures. Such features didn't alter the  $\beta$ -structuring propensity of backbone moieties, as shown in Fig. 10.14

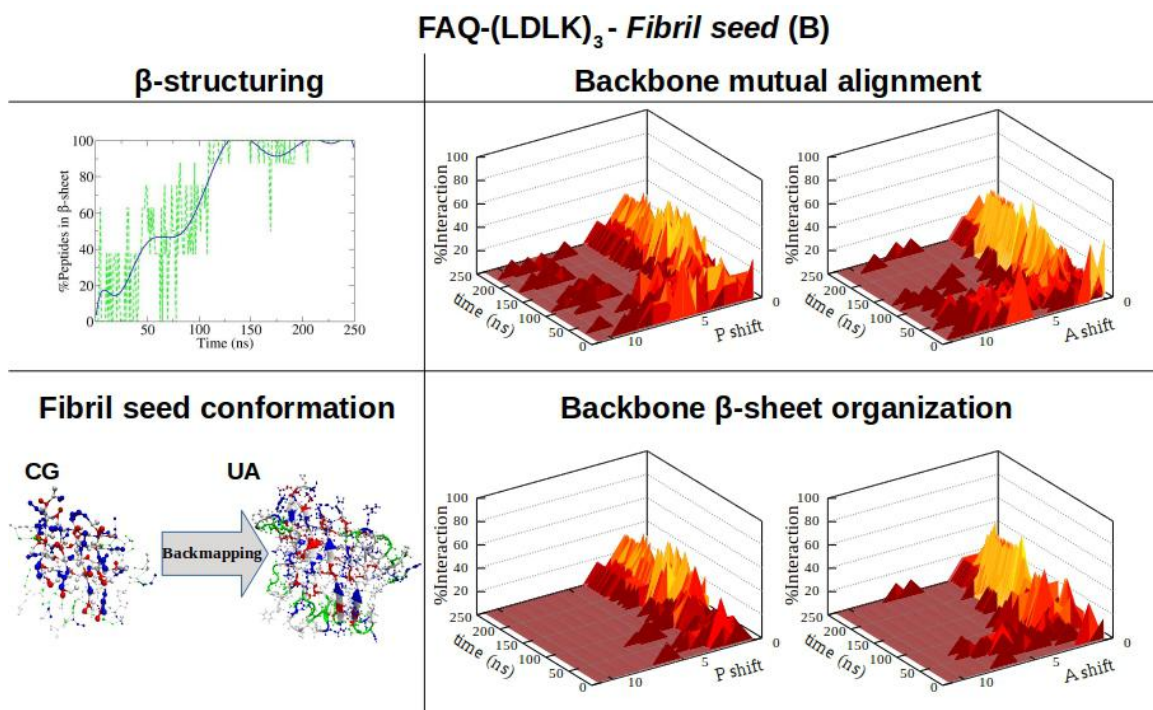


FIGURE 10.16: Shift profiles and  $\beta$ -structuring propensity of backbone moieties FAQ-(LDLK)<sub>3</sub> SAPs. Differently from the results shown in Fig. 4.3B and Fig. 10.14, FAQ-(LDLK)<sub>3</sub> assembled into two orthogonally oriented  $\beta$ -sheets. However, the  $\beta$ -strands organization reflected the backbone moieties mutual alignment. Indeed, peptides are mutually alignment both in A and P.

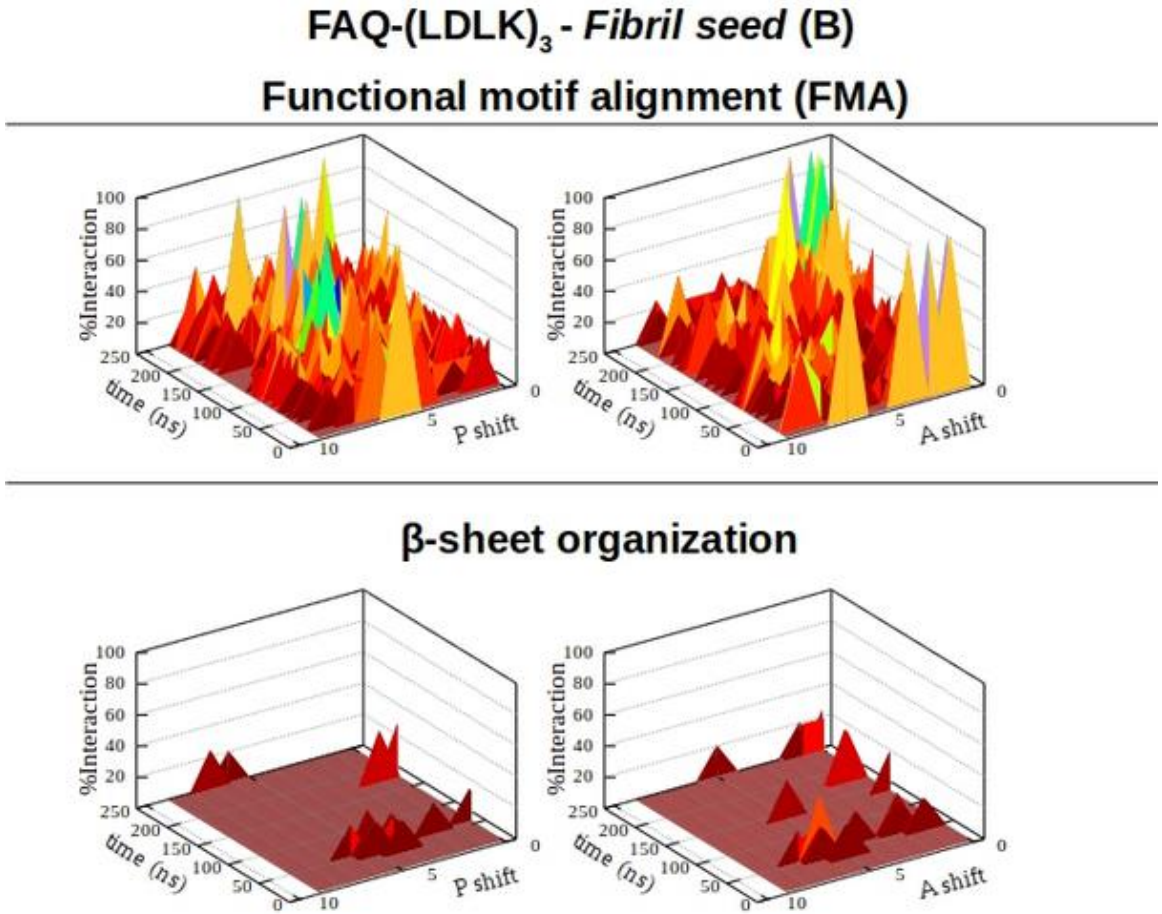


FIGURE 10.17: **Shift profiles and  $\beta$ -structuring propensity of functional motif FAQ-(LDLK)<sub>3</sub> SAPs.** According to the data shown in Fig.4.5, Fig. 10.11 and Fig. 10.12, FAQ functional motif didn't assemble into ordered aggregates. However, FAQ functional motifs assembled into disordered  $\beta$ -sheet structures. Such features heavily altered the  $\beta$ -structuring propensity and mutual alignment of backbone moieties, as shown in Fig. 10.16

## Chapter 11

# SAPs-Neural Membrane Interactions: Additional Tables and Figures

Lipids	Inner leaflet Count	Outer Leaflet Count
<b>Phosphatidylcholine (PC)</b>		
<b>DPPC</b> (di-C16:0-C18:0 PC)	35	20
<b>DOPC</b> (di-C16:1-C18:1 PC)	58	33
<b>POPC</b> (C16:0/18:1 PC)	35	8
<b>PFPC</b> (C16:0/18:1 PC)	4	2
<b>PAPC</b> (C16:0/20:4 PC)	31	17
<b>PUPC</b> (C16:0/22:6 PC)	11	6
<b>OIPC</b> (C18:1/18:2 PC)	4	2
<b>OUPC</b> (C18:1/22:6 PC)	2	1
<b>Phosphatidylethanolamine (PE)</b>		
<b>POPE</b> (C16:0/18:1 PE)	8	16
<b>PAPE</b> (C16:0/20:4 PE)	20	41
<b>PUPE</b> (C16:0/22:6 PE)	43	85
<b>Sphingomyelin (SM)</b>		
<b>DPSM</b> (c(d18:0/18:0) SM)	60	15
<b>Glycolipid (GM1)</b>		
<b>DPG1</b> (c(d18:1/18:0) GM1)	7	
<b>PNG1</b> (c(d18:1/24:1) GM1)	2	
<b>Glycolipid (GM3)</b>		
<b>DPG3</b> (c(d18:1/18:0) GM3)	7	
<b>PNG3</b> (c(d18:1/24:1) GM3)	2	
<b>Phosphatidylinositol (PI)</b>		
<b>POPI</b> (C16:0/18:1 PI)		8
<b>PAPI</b> (C16:0/20:4 PI)		8
<b>PIPI</b> (C16:0/18:2 PI)		3
<b>PUPI</b> (C16:0/22:6 PI)		13
<b>Phosphatidylinositol Phosphates (PIPs)</b>		
<b>POP1</b> (C16:0/18:1 PIP)		6
<b>POP2</b> (C16:0/18:1 PIP2)		3
<b>POP3</b> (C16:0/18:1 PIP3)		3
<b>Phosphatidylserine (PS)</b>		
<b>POPS</b> (C16:0/18:1 PS)		66
<b>Cerebrosides</b>		
<b>DPGS</b> (C(d16:1/16:0) GS)	50	
<b>Ceramide</b>		
<b>DPCE</b> (C(d18:1/18:0) CER)	4	4
<b>Cholesterol (CHOL)</b>	306	307

TABLE 11.1: **Neural Membrane Composition.** The neural membrane consist of 1335 lipids molecules, divided into 10 main classes: Phosphatidylcholine (PS), Phosphatidylethanolamine (PE), Sphingomyelin (SM), Glycolipids (GM1,GM3),Phosphatidylinositol (PI), Phosphatidylinositol Phosphates (PIPs), Phosphatidylserine (PS), Cerebrosides, Ceramide and CHOL.

Ions	Intracellular concentrations	Extracellular concentrations	Inner/Outer ratio
$Na^+$	15	150	0.1
$K^+$	140	5	28
$CL^-$	13	150	0.09

TABLE 11.2: Ions Concentrations

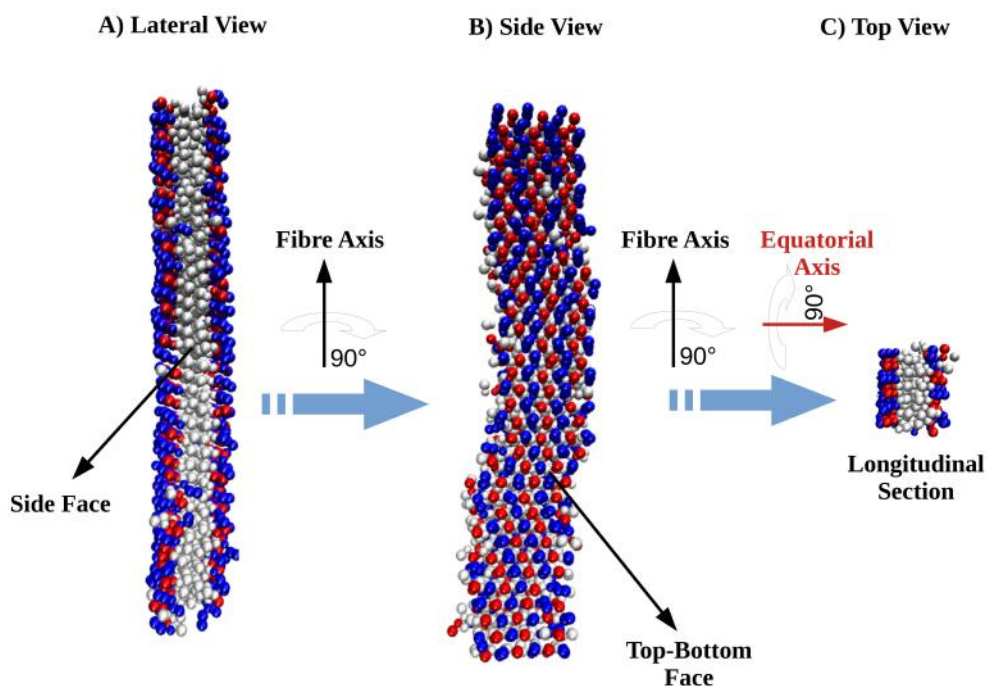


FIGURE 11.1: **Scheme of  $(LDLK)_3$  Fibril.** The geometry of  $(LDLK)_3$  allow to define three faces, depending on the view. The faces are also different in terms of chemical properties. Indeed, the **side face** exposes the "leucine zipper" to the solvent, then it is more hydrophobic than the other faces. Instead, the **top-bottom face** consists of Lysine and Aspartic acid side chains, then side face is hydrophilic. The third face is usually not exposed to the solvent and it is only identifiable through rotation around both axis of the fibril.

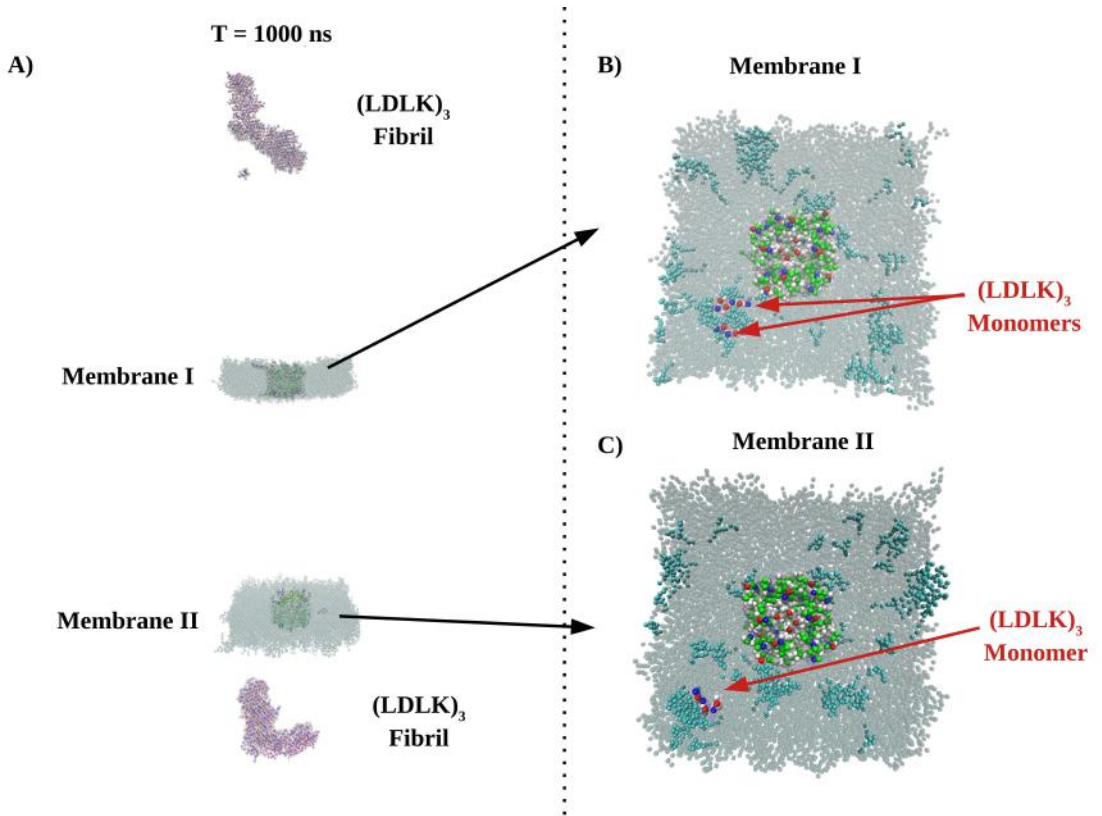


FIGURE 11.2: Last frame CG-MD simulations of interactions among  $(LDLK)_3$  monomers and neural membranes.

## Chapter 12

# CG Modeling of Glycosylated SAPs: Additional Tables and Figures



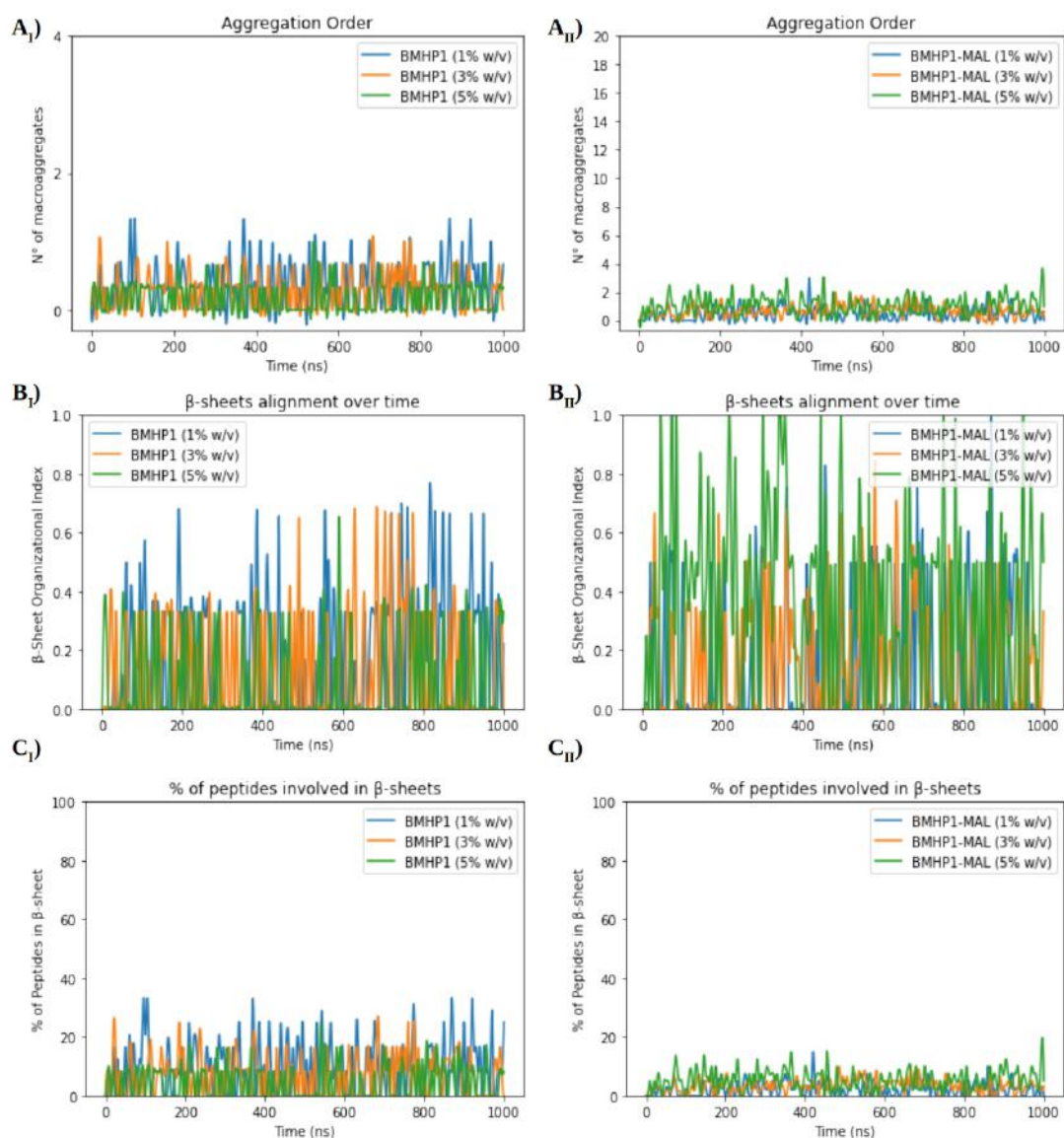


FIGURE 12.1: **Analysis of CG-MD simulations: BMHP1 and Maltosylated BMHP1.** *Aggregation Order* plots refer to the number of  $\beta$ -structured aggregates.  *$\beta$ -sheet Organizational Index* is the quantification of antiparallel strands over parallel strands. Increasing the concentration didn't alter the aggregation order and  $\beta$ -sheet organization. Instead, the maltosylation of C-terminal threonine heavily affected the stability of  $\beta$ -sheet structures.

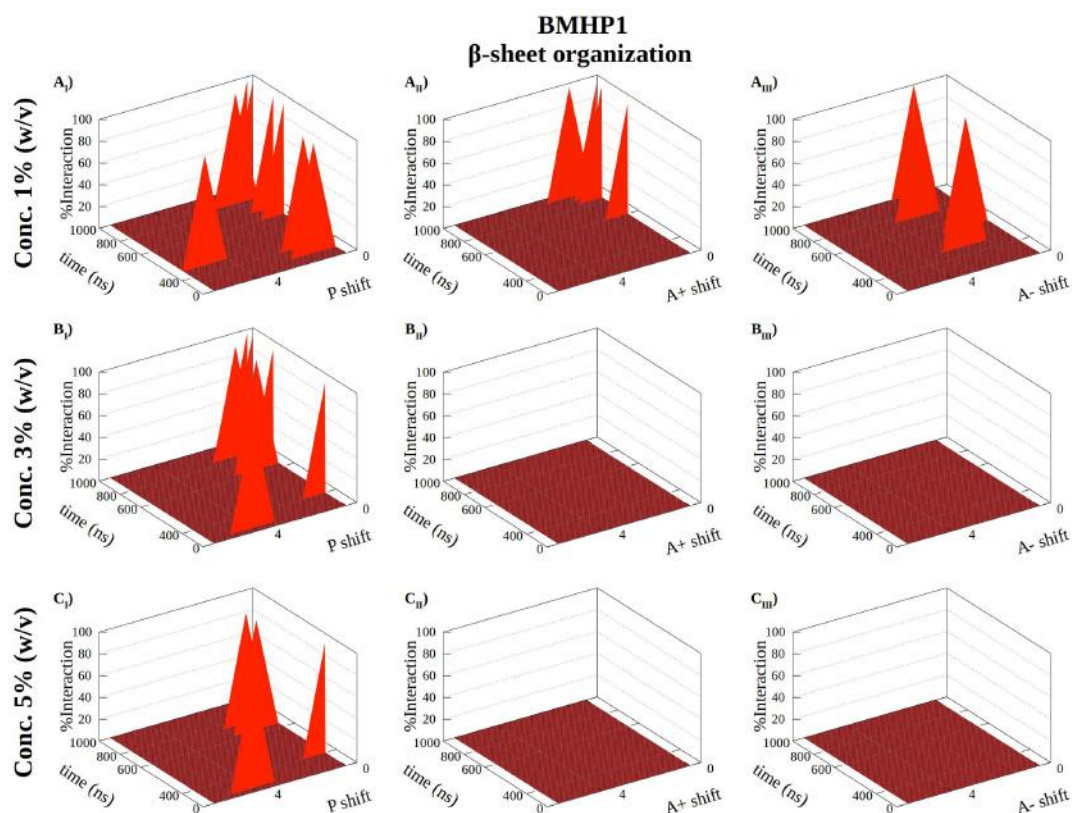


FIGURE 12.2:  $\beta$ -sheet shift profiles of BMHP1. Despite the low  $\beta$ -structuring propensity, BMHP1  $\beta$ -strands, independently from the concentration are preferentially aligned in parallel out-of-register by one-residue.

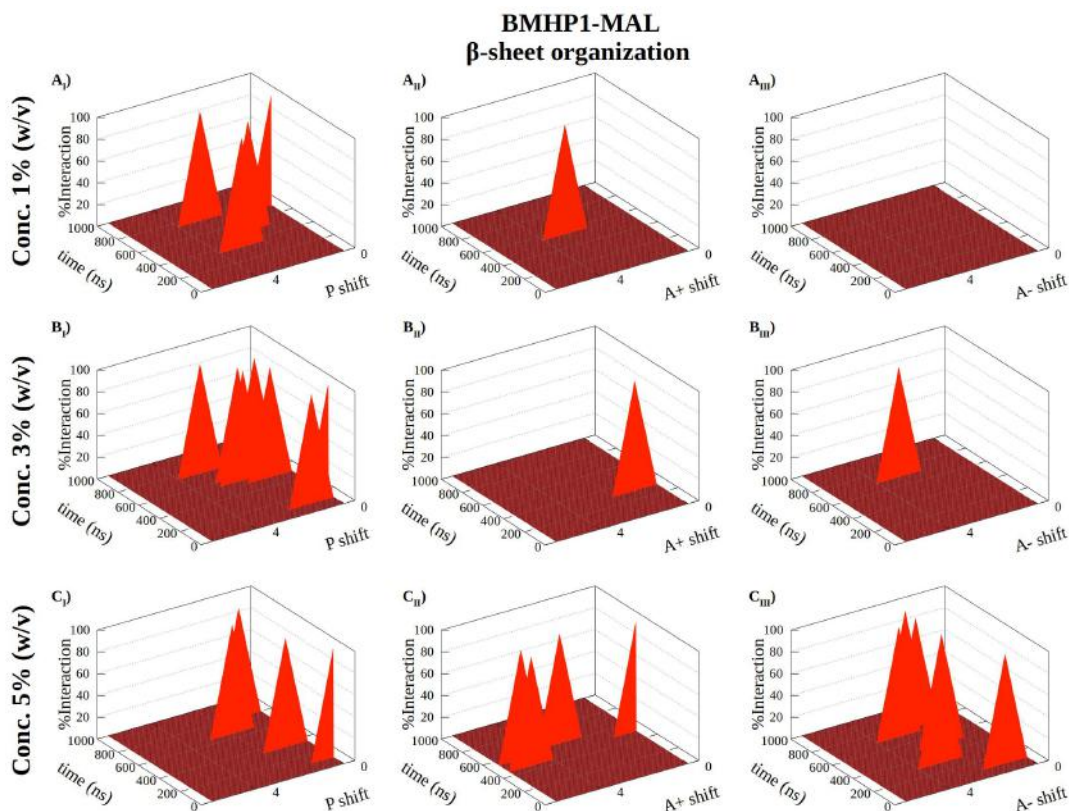


FIGURE 12.3:  $\beta$ -sheet shift profiles of BMHP1-MAL. As already highlighted in fig. 12.1, the C-terminal maltosylation heavily affected  $\beta$ -strands aligned. Indeed, BMHP1-MAL  $\beta$ -strands are also antiparallel aligned.

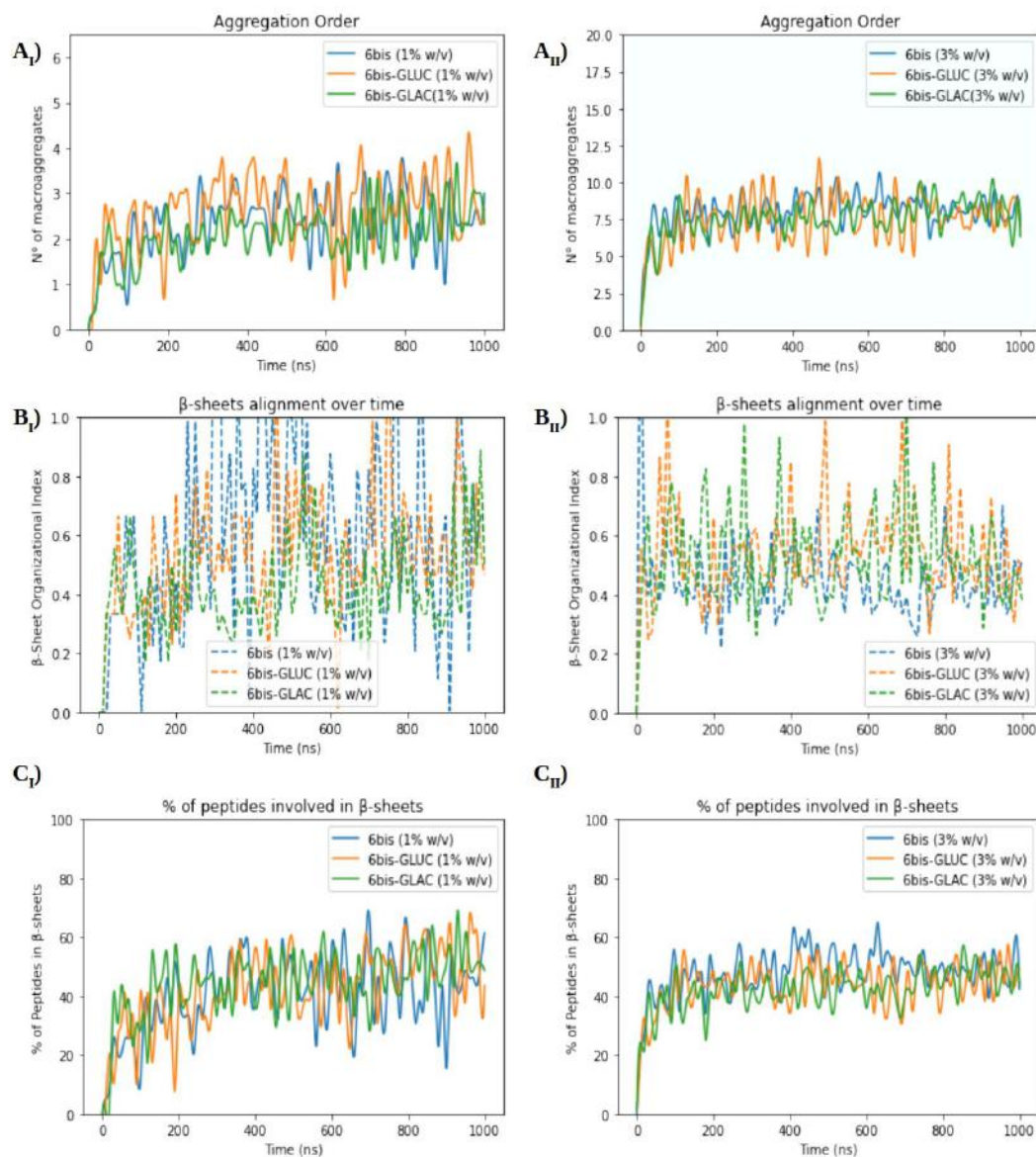


FIGURE 12.4: **Analysis of differently glycosylated  $(LDLK)_3$ -BMHP1 SAPs.** (**Backbone Moieties**) *Aggregation Order* plots refer to the number of  $\beta$ -structured aggregates.  *$\beta$ -sheet Organizational Index* is the quantification of antiparallel strands over parallel strands. The different glycoylation types didn't affect  $\beta$ -structuring propensity of backbone moieties of SAPs, while was lightly influenced by the variation of concentration.

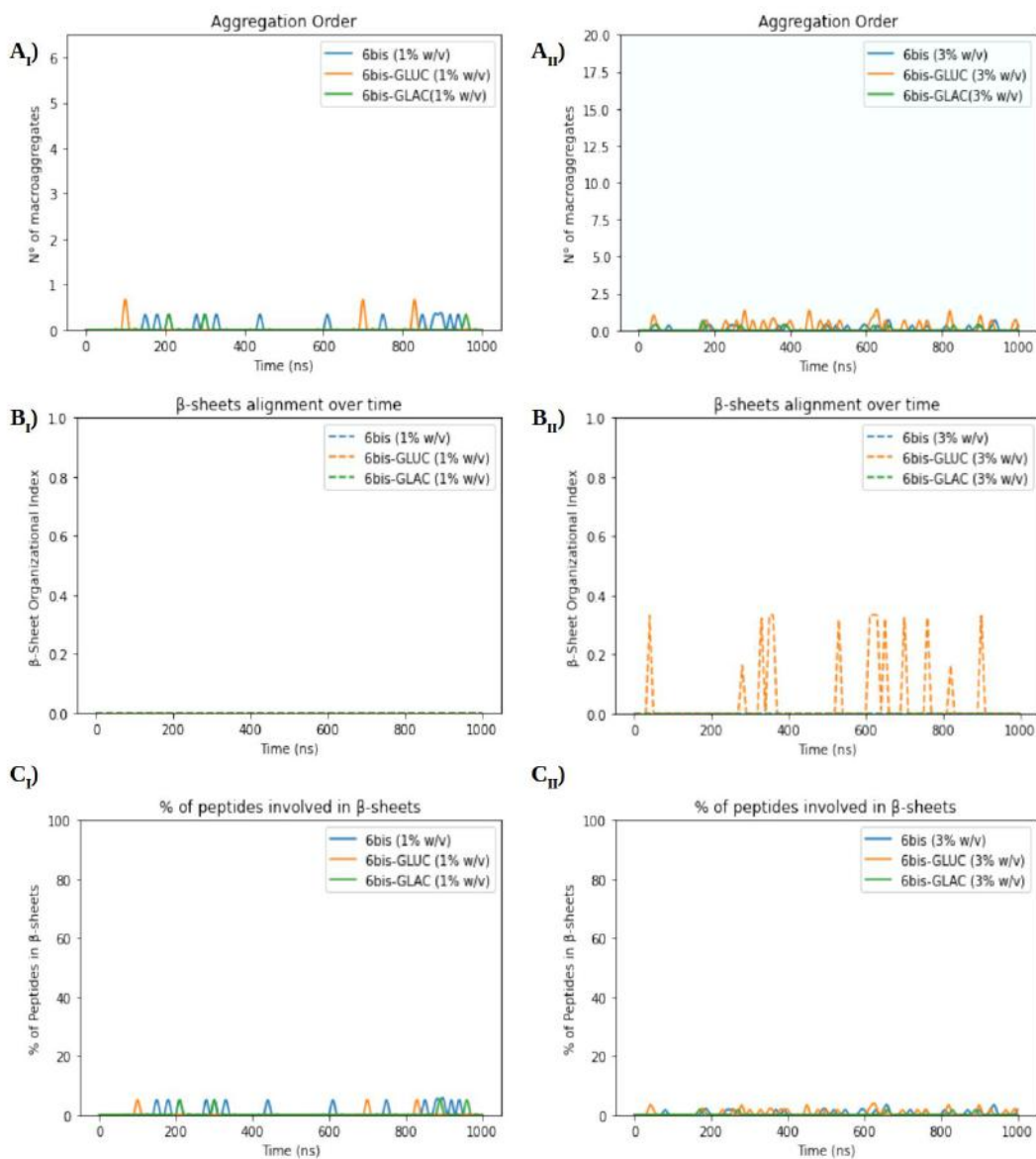


FIGURE 12.5: **Analysis of differently glycosylated  $(LDLK)_3$ -BMHP1 SAPs.** In general, glycosylated functional motifs had a low  $\beta$ -structuring propensity.



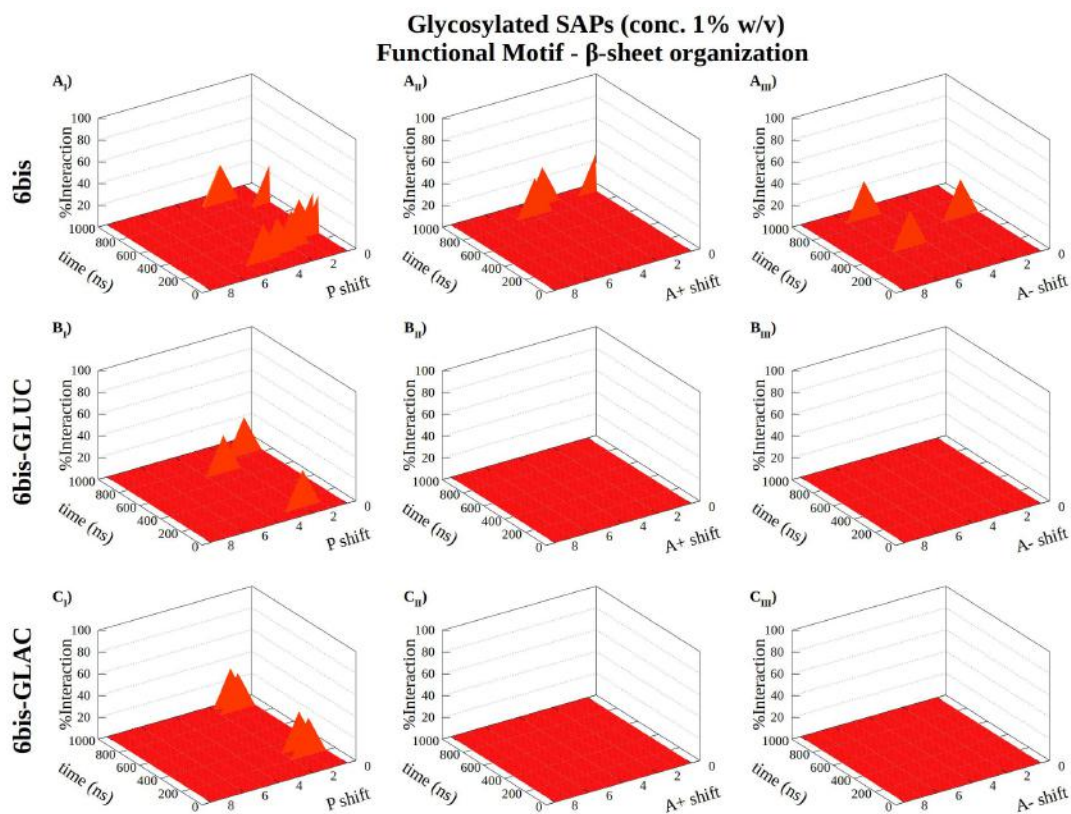


FIGURE 12.6:  $\beta$ -sheet shift profiles of Functional Motif of different glycosylated 6bis at the concentration of 1% (w/v).

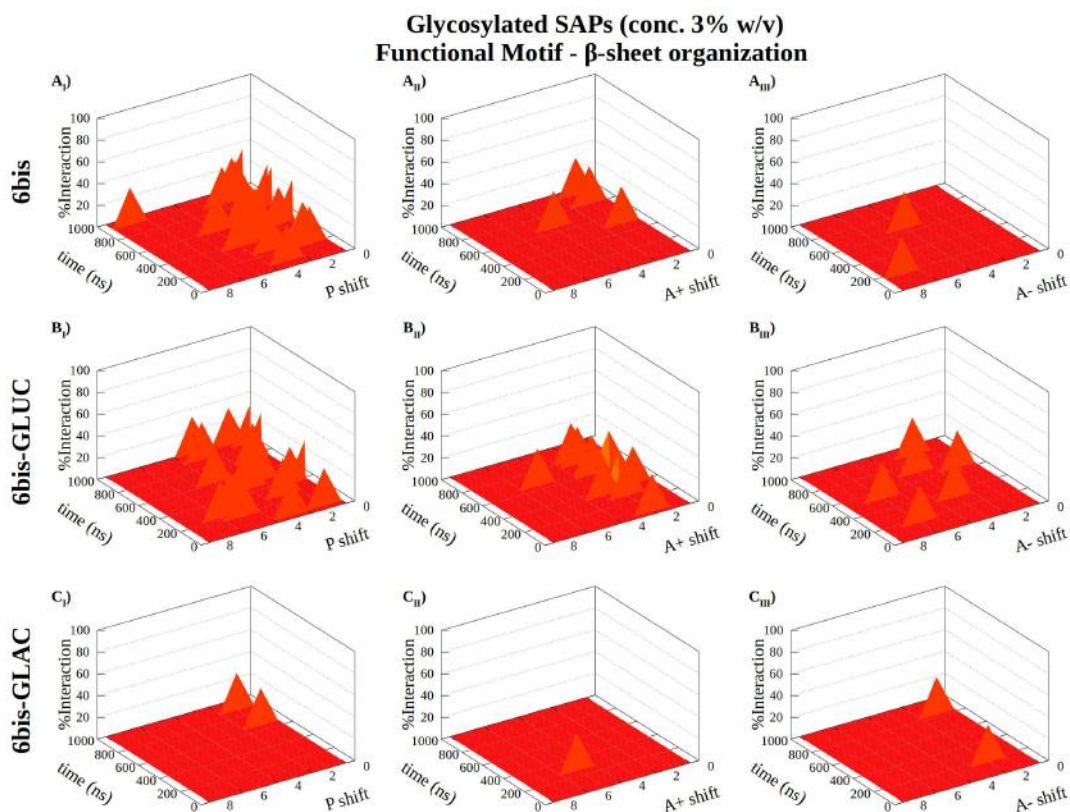


FIGURE 12.7:  $\beta$ -sheet shift profiles of Functional Motif of different glycosylated 6bis at the concentration of 3% (w/v).

# Bibliography

- [1] G. M. Whitesides. “Self-Assembly at All Scales”. In: *Science* 295 (5564 Mar. 2002), pp. 2418–2421. ISSN: 00368075. DOI: [10.1126/science.1070821](https://doi.org/10.1126/science.1070821). URL: <https://www.sciencemag.org/lookup/doi/10.1126/science.1070821>.
- [2] S. Zhang. “Fabrication of novel biomaterials through molecular self-assembly”. In: *Nature Biotechnology* 21 (10 Oct. 2003), pp. 1171–1178. ISSN: 1087-0156. DOI: [10.1038/nbt874](https://doi.org/10.1038/nbt874). URL: <http://www.nature.com/articles/nbt874>.
- [3] S. Kyle; A. Aggeli; E. Ingham; M. J. McPherson. “Production of self-assembling biomaterials for tissue engineering”. In: *Trends in Biotechnology* 27 (7 July 2009), pp. 423–433. ISSN: 01677799. DOI: [10.1016/j.tibtech.2009.04.002](https://doi.org/10.1016/j.tibtech.2009.04.002). URL: <https://linkinghub.elsevier.com/retrieve/pii/S0167779909000936>.
- [4] K. Subramani; W. Ahmed. “Self-assembly of proteins and peptides and their applications in bionanotechnology and dentistry”. In: *Emerging Nanotechnologies in Dentistry* (2018), pp. 231–249. DOI: [10.1016/B978-0-12-812291-4.00012-1](https://doi.org/10.1016/B978-0-12-812291-4.00012-1). URL: <https://linkinghub.elsevier.com/retrieve/pii/B9780128122914000121>.
- [5] J. V. I. Timonen; M. Latikka; L. Leibler; R. H. A. Ras; O. Ikkala. “Switchable Static and Dynamic Self-Assembly of Magnetic Droplets on Superhydrophobic Surfaces”. In: *Science* 341 (6143 July 2013), pp. 253–257. ISSN: 0036-8075. DOI: [10.1126/science.1233775](https://doi.org/10.1126/science.1233775). URL: <https://www.sciencemag.org/lookup/doi/10.1126/science.1233775>.
- [6] O. G. Mouritsen. “Self-assembly and organization of lipid-protein membranes”. In: *Current Opinion in Colloid Interface Science* 3 (1 Feb. 1998), pp. 78–87. ISSN: 13590294. DOI: [10.1016/S1359-0294\(98\)80045-9](https://doi.org/10.1016/S1359-0294(98)80045-9). URL: <https://linkinghub.elsevier.com/retrieve/pii/S1359029498800459>.
- [7] M. F. Serag; A. Aikeremu; R. Tsukamoto; H. Piwoński; M. Abadi; N. Kaji; J. R. Dwyer; Y. Baba; S. Habuchi. “Geometry-Based Self-Assembly of Histone–DNA Nanostructures at Single-Nucleotide Resolution”. In: *ACS Nano* 13 (7 July 2019), pp. 8155–8168. ISSN: 1936-0851. DOI: [10.1021/acsnano.9b03259](https://doi.org/10.1021/acsnano.9b03259). URL: <https://pubs.acs.org/doi/10.1021/acsnano.9b03259>.



- [8] S. A. Woodson. “RNA Folding Pathways and the Self-Assembly of Ribosomes”. In: *Accounts of Chemical Research* 44 (12 Dec. 2011), pp. 1312–1319. ISSN: 0001-4842. DOI: [10.1021/ar2000474](https://pubs.acs.org/doi/10.1021/ar2000474). URL: <https://pubs.acs.org/doi/10.1021/ar2000474>.
- [9] H. Otsuka; Y. Nagasaki; K. Kataoka. *Self-assembly of block copolymers*. 2001.
- [10] G. Foffano; N. Levernier; M. Lenz. “The dynamics of filament assembly define cytoskeletal network morphology”. In: *Nature Communications* 7 (Dec. 2016). ISSN: 20411723. DOI: [10.1038/ncomms13827](https://doi.org/10.1038/ncomms13827).
- [11] M. Tassieri; R. M.L. Evans; L. Barbu-Tudoran; J. Trinick; T. A. Waigh. “The self-assembly, elasticity, and dynamics of cardiac thin filaments”. In: *Biophysical Journal* 94 (6 Mar. 2008), pp. 2170–2178. ISSN: 15420086. DOI: [10.1529/biophysj.107.116087](https://doi.org/10.1529/biophysj.107.116087).
- [12] E. Busseron; Y. Ruff; E. Moulin; N. Giuseppone. “Supramolecular self-assemblies as functional nanomaterials”. In: *Nanoscale* 5 (16 2013), p. 7098. ISSN: 2040-3364. DOI: [10.1039/c3nr02176a](https://doi.org/10.1039/c3nr02176a). URL: <http://xlink.rsc.org/?DOI=c3nr02176a>.
- [13] B. He; X. Yuan; D. Jiang. “Molecular self-assembly guides the fabrication of peptide nanofiber scaffolds for nerve repair”. In: *RSC Adv.* 4 (45 2014), pp. 23610–23621. ISSN: 2046-2069. DOI: [10.1039/C4RA01826E](https://doi.org/10.1039/C4RA01826E). URL: <http://xlink.rsc.org/?DOI=C4RA01826E>.
- [14] R. Krishnamurthy. “Giving Rise to Life: Transition from Prebiotic Chemistry to Protobiology”. In: *Accounts of Chemical Research* 50 (3 Mar. 2017), pp. 455–459. ISSN: 0001-4842. DOI: [10.1021/acs.accounts.6b00470](https://doi.org/10.1021/acs.accounts.6b00470). URL: <https://pubs.acs.org/doi/10.1021/acs.accounts.6b00470>.
- [15] C. Mathis; S. Ramprasad; S. Walker; N. Lehman. “Prebiotic RNA Network Formation: A Taxonomy of Molecular Cooperation”. In: *Life* 7 (4 Oct. 2017), p. 38. ISSN: 2075-1729. DOI: [10.3390/life7040038](https://doi.org/10.3390/life7040038). URL: <http://www.mdpi.com/2075-1729/7/4/38>.
- [16] P. G. Higgs. “Chemical Evolution and the Evolutionary Definition of Life”. In: *Journal of Molecular Evolution* 84 (5-6 June 2017), pp. 225–235. ISSN: 0022-2844. DOI: [10.1007/s00239-017-9799-3](https://doi.org/10.1007/s00239-017-9799-3). URL: <http://link.springer.com/10.1007/s00239-017-9799-3>.
- [17] F. Gelain; D. Bottai; A. Vescovi; S. Zhang. “Designer Self-Assembling Peptide Nanofiber Scaffolds for Adult Mouse Neural Stem Cell 3-Dimensional Cultures”. In: *PLoS ONE* 1 (1 Dec. 2006), e119. ISSN: 1932-6203. DOI: [10.1371/journal.pone.0000119](https://doi.org/10.1371/journal.pone.0000119). URL: <https://dx.plos.org/10.1371/journal.pone.0000119>.

- [18] F. Gelain; L. D. Unsworth; S. Zhang. “Slow and sustained release of active cytokines from self-assembling peptide scaffolds”. In: *Journal of Controlled Release* 145 (3 Aug. 2010), pp. 231–239. ISSN: 01683659. DOI: [10.1016/j.jconrel.2010.04.026](https://doi.org/10.1016/j.jconrel.2010.04.026). URL: <https://linkinghub.elsevier.com/retrieve/pii/S0168365910003019>.
- [19] F. Gelain; D. Silva; A. Caprini; F. Taraballi; A. Natalello; O. Villa; K. T. Nam; R. N. Zuckermann; S. M. Doglia; A. Vescovi. “BMHP1-Derived Self-Assembling Peptides: Hierarchically Assembled Structures with Self-Healing Propensity and Potential for Tissue Engineering Applications”. In: *ACS Nano* 5 (3 Mar. 2011), pp. 1845–1859. ISSN: 1936-0851. DOI: [10.1021/nn102663a](https://doi.org/10.1021/nn102663a). URL: <https://pubs.acs.org/doi/10.1021/nn102663a>.
- [20] F. Gelain; D. Cigognini; A. Caprini; D. Silva; B. Colleoni; M. Donegá; S. Antonini; B. E. Cohen; A. Vescovi. “New bioactive motifs and their use in functionalized self-assembling peptides for NSC differentiation and neural tissue engineering”. In: *Nanoscale* 4 (9 2012), p. 2946. ISSN: 2040-3364. DOI: [10.1039/c2nr30220a](https://doi.org/10.1039/c2nr30220a). URL: <http://xlink.rsc.org/?DOI=c2nr30220a>.
- [21] R. Pugliese; F. Gelain. “Peptidic Biomaterials: From Self-Assembling to Regenerative Medicine”. In: *Trends in Biotechnology* 35 (2 Feb. 2017), pp. 145–158. ISSN: 01677799. DOI: [10.1016/j.tibtech.2016.09.004](https://doi.org/10.1016/j.tibtech.2016.09.004). URL: <https://linkinghub.elsevier.com/retrieve/pii/S0167779916301536>.
- [22] E. L. Baker; R. T. Bonnecaze; M. H. Zaman. “Extracellular matrix stiffness and architecture govern intracellular rheology in cancer”. In: *Biophysical Journal* 97 (4 Aug. 2009), pp. 1013–1021. ISSN: 15420086. DOI: [10.1016/j.bpj.2009.05.054](https://doi.org/10.1016/j.bpj.2009.05.054).
- [23] A. Byron; J. D. Humphries; M. J. Humphries. “Defining the extracellular matrix using proteomics”. In: *International Journal of Experimental Pathology* 94 (2 Apr. 2013), pp. 75–92. ISSN: 09599673. DOI: [10.1111/iep.12011](https://doi.org/10.1111/iep.12011).
- [24] A. Raspa; G. A. A. Saracino; R. Pugliese; D. Silva; D. Cigognini; A. Vescovi; F. Gelain. “Complementary Co-assembling Peptides: From In Silico Studies to In Vivo Application”. In: *Advanced Functional Materials* 24 (40 Oct. 2014), pp. 6317–6328. ISSN: 1616301X. DOI: [10.1002/adfm.201400956](https://doi.org/10.1002/adfm.201400956). URL: <http://doi.wiley.com/10.1002/adfm.201400956>.
- [25] H. Cui; M. J. Webber; Samuel I. Stupp. “Self-assembly of peptide amphiphiles: From molecules to nanostructures to biomaterials”. In: *Biopolymers* 94 (1 Jan. 2010), pp. 1–18. ISSN: 00063525. DOI: [10.1002/bip.21328](https://doi.org/10.1002/bip.21328). URL: <http://doi.wiley.com/10.1002/bip.21328>.

- [26] S. Zhang; C. Lockshin; A. Herbert; E. Winter; A. Rich. “Zuotin, a putative Z-DNA binding protein in *Saccharomyces cerevisiae*.” In: *The EMBO Journal* 11 (10 Oct. 1992), pp. 3787–3796. ISSN: 02614189. DOI: [10.1002/j.1460-2075.1992.tb05464.x](https://doi.org/10.1002/j.1460-2075.1992.tb05464.x). URL: <http://doi.wiley.com/10.1002/j.1460-2075.1992.tb05464.x>.
- [27] E. Kokkoli; A. Mardilovich; A. Wedekind; E. L. Rexeisen; A. Garg; J. A. Craig. “Self-assembly and applications of biomimetic and bioactive peptide-amphiphiles”. In: *Soft Matter* 2 (12 2006), p. 1015. ISSN: 1744-683X. DOI: [10.1039/b608929a](https://doi.org/10.1039/b608929a). URL: <http://xlink.rsc.org/?DOI=b608929a>.
- [28] A. Mahler; M. Reches; M. Rechter; S. Cohen; E. Gazit. “Rigid, Self-Assembled Hydrogel Composed of a Modified Aromatic Dipeptide”. In: *Advanced Materials* 18 (11 June 2006), pp. 1365–1370. ISSN: 0935-9648. DOI: [10.1002/adma.200501765](https://doi.org/10.1002/adma.200501765). URL: <http://doi.wiley.com/10.1002/adma.200501765>.
- [29] T. D. Clark; L. K. Buehler; M. Reza Ghadiri. “Self-Assembling Cyclic  $\beta^3$ -Peptide Nanotubes as Artificial Transmembrane Ion Channels”. In: *Journal of the American Chemical Society* 120 (4 Feb. 1998), pp. 651–656. ISSN: 0002-7863. DOI: [10.1021/ja972786f](https://doi.org/10.1021/ja972786f). URL: <https://pubs.acs.org/doi/10.1021/ja972786f>.
- [30] N. Rodriguez-Vazquez; H. Ozores; A. Guerra; E. Gonzalez-Freire; A. Fuertes; M. Panciera; J. Priegue; J. Outeiral; J. Montenegro; R. Garcia-Fandino; M. Amorin; J. Granja. “Membrane-Targeted Self-Assembling Cyclic Peptide Nanotubes”. In: *Current Topics in Medicinal Chemistry* 14 (23 Jan. 2015), pp. 2647–2661. ISSN: 15680266. DOI: [10.2174/1568026614666141215143431](https://doi.org/10.2174/1568026614666141215143431). URL: <http://www.eurekaselect.com/openurl/content.php?genre=article&issn=1568-0266&volume=14&issue=23&spage=2647>.
- [31] A. Restuccia; D. T. Seroski; K. L. Kelley; C. S. O’Bryan; J. J. Kurian; K. R. Knox; S. A. Farhadi; T. E. Angelini; G. A. Hudalla. “Hierarchical self-assembly and emergent function of densely glycosylated peptide nanofibers”. In: *Communications Chemistry* 2 (1 Dec. 2019), p. 53. ISSN: 2399-3669. DOI: [10.1038/s42004-019-0154-z](https://doi.org/10.1038/s42004-019-0154-z). URL: <http://www.nature.com/articles/s42004-019-0154-z>.
- [32] D. Datta; O. Tiwari; M. K. Gupta. “Self-Assembly of Diphenylalanine–Peptide Nucleic Acid Conjugates”. In: *ACS Omega* 4 (6 June 2019), pp. 10715–10728. ISSN: 2470-1343. DOI: [10.1021/acsomega.9b00047](https://doi.org/10.1021/acsomega.9b00047). URL: <https://pubs.acs.org/doi/10.1021/acsomega.9b00047>.
- [33] T. Macculloch; A. Buchberger; N. Stephanopoulos. “Emerging applications of peptide-oligonucleotide conjugates: Bioactive scaffolds, self-assembling systems, and

- hybrid nanomaterials”. In: *Organic and Biomolecular Chemistry* 17 (7 2019), pp. 1668–1682. ISSN: 14770520. DOI: [10.1039/c8ob02436g](https://doi.org/10.1039/c8ob02436g).
- [34] R. Freeman; M. Han; Z. Álvarez; J. A. Lewis; J. R. Wester; N. Stephanopoulos; M. T. McClendon; C. Lynsky; J. M. Godbe; H. Sangji; E. Luijten; S. I. Stupp. “Reversible self-assembly of superstructured networks”. In: *Science* 362 (6416 Nov. 2018), pp. 808–813. ISSN: 0036-8075. DOI: [10.1126/science.aat6141](https://doi.org/10.1126/science.aat6141). URL: <https://www.sciencemag.org/lookup/doi/10.1126/science.aat6141>.
- [35] R. Pugliese; M. Maleki; R. N. Zuckermann; F. Gelain. “Self-assembling peptides cross-linked with genipin: resilient hydrogels and self-standing electrospun scaffolds for tissue engineering applications”. In: *Biomaterials Science* 7 (1 2019), pp. 76–91. ISSN: 2047-4830. DOI: [10.1039/C8BM00825F](https://doi.org/10.1039/C8BM00825F). URL: <http://xlink.rsc.org/?DOI=C8BM00825F>.
- [36] L. Ma. “Collagen/chitosan porous scaffolds with improved biostability for skin tissue engineering”. In: *Biomaterials* 24 (26 Nov. 2003), pp. 4833–4841. ISSN: 01429612. DOI: [10.1016/S0142-9612\(03\)00374-0](https://doi.org/10.1016/S0142-9612(03)00374-0). URL: <https://linkinghub.elsevier.com/retrieve/pii/S0142961203003740>.
- [37] R. Pugliese; A. Marchini; G. A. A. Saracino; R. N. Zuckermann; F. Gelain. “Cross-linked self-assembling peptide scaffolds”. In: *Nano Research* 11 (1 Jan. 2018), pp. 586–602. ISSN: 1998-0124. DOI: [10.1007/s12274-017-1834-6](https://doi.org/10.1007/s12274-017-1834-6). URL: <http://link.springer.com/10.1007/s12274-017-1834-6>.
- [38] P. Jurečka; J. Šponer; J. Černý; P. Hobza. “Benchmark database of accurate (MP2 and CCSD(T) complete basis set limit) interaction energies of small model complexes, DNA base pairs, and amino acid pairs”. In: *Phys. Chem. Chem. Phys.* 8 (17 2006), pp. 1985–1993. ISSN: 1463-9076. DOI: [10.1039/B600027D](https://doi.org/10.1039/B600027D). URL: <http://xlink.rsc.org/?DOI=B600027D>.
- [39] Zhaoyang Lou et al. “First-principles study of the adsorption of lysine on hydroxyapatite (100) surface”. In: *Applied Surface Science* 258 (11 Mar. 2012). ISSN: 01694332. DOI: [10.1016/j.apsusc.2012.01.116](https://doi.org/10.1016/j.apsusc.2012.01.116).
- [40] Wu Qin et al. “Density functional theory calculations and molecular dynamics simulations of the adsorption of biomolecules on graphene surfaces”. In: *Biomaterials* 31 (5 Feb. 2010). ISSN: 01429612. DOI: [10.1016/j.biomaterials.2009.10.013](https://doi.org/10.1016/j.biomaterials.2009.10.013).
- [41] P. A. Garrain; D. Costa; P. Marcus. “BiomaterialBiomolecule Interaction: DFT-D Study of Glycine Adsorption on Cr<sub>2</sub>O<sub>3</sub>”. In: *The Journal of Physical Chemistry C* 115 (3 Jan. 2011), pp. 719–727. ISSN: 1932-7447. DOI: [10.1021/jp109704b](https://doi.org/10.1021/jp109704b). URL: <https://pubs.acs.org/doi/10.1021/jp109704b>.

- [42] M. Corno; A. Rimola; V. Bolis; P. Ugliengo. “Hydroxyapatite as a key biomaterial: quantum-mechanical simulation of its surfaces in interaction with biomolecules”. In: *Physical Chemistry Chemical Physics* 12 (24 2010), p. 6309. ISSN: 1463-9076. DOI: [10.1039/c002146f](https://doi.org/10.1039/c002146f). URL: <http://xlink.rsc.org/?DOI=c002146f>.
- [43] Maedeh Kamel et al. “Theoretical elucidation of the amino acid interaction with graphene and functionalized graphene nanosheets: insights from DFT calculation and MD simulation”. In: *Amino Acids* 52 (10 Oct. 2020). ISSN: 0939-4451. DOI: [10.1007/s00726-020-02905-5](https://doi.org/10.1007/s00726-020-02905-5).
- [44] C. Gustafsson; M. Linares; P. Norman. “Quantum Mechanics/Molecular Mechanics Density Functional Theory Simulations of the Optical Properties Fingerprinting the Ligand-Binding of Pentameric Formyl Thiophene Acetic Acid in Amyloid- $\beta$ (1–42)”. In: *The Journal of Physical Chemistry A* 124 (5 Feb. 2020), pp. 875–888. ISSN: 1089-5639. DOI: [10.1021/acs.jpca.9b09779](https://doi.org/10.1021/acs.jpca.9b09779). URL: <https://pubs.acs.org/doi/abs/10.1021/acs.jpca.9b09779>.
- [45] N. Arul Murugan, Robert Zalesny, and Hans Ågren. “Unusual binding-site-specific photophysical properties of a benzothiazole-based optical probe in amyloid beta fibrils”. In: *Physical Chemistry Chemical Physics* 20 (31 2018). ISSN: 1463-9076. DOI: [10.1039/C8CP03274B](https://doi.org/10.1039/C8CP03274B).
- [46] James A. Platts. “Quantum chemical molecular dynamics and metadynamics simulation of aluminium binding to amyloid- and related peptides”. In: *Royal Society Open Science* 7 (2 Feb. 2020). ISSN: 2054-5703. DOI: [10.1098/rsos.191562](https://doi.org/10.1098/rsos.191562).
- [47] Alba Espargaró et al. “On the Binding of Congo Red to Amyloid Fibrils”. In: *Angewandte Chemie* 132 (21 May 2020). ISSN: 0044-8249. DOI: [10.1002/ange.201916630](https://doi.org/10.1002/ange.201916630).
- [48] V. S. Bystrov; P. S. Zelenovskiy; A. S. Nuraeva; S. Kopyl; O. A. Zhulyabina; V. A. Tverdislov. “Molecular modeling and computational study of the chiral-dependent structures and properties of self-assembling diphenylalanine peptide nanotubes”. In: *Journal of Molecular Modeling* 25 (7 July 2019), p. 199. ISSN: 1610-2940. DOI: [10.1007/s00894-019-4080-x](https://doi.org/10.1007/s00894-019-4080-x). URL: <http://link.springer.com/10.1007/s00894-019-4080-x>.
- [49] S. Fleming; P. W. J. M. Frederix; I. R. Sasselli; N. T. Hunt; R. V. Ulijn; T. Tuttle. “Assessing the Utility of Infrared Spectroscopy as a Structural Diagnostic Tool for -Sheets in Self-Assembling Aromatic Peptide Amphiphiles”. In: *Langmuir* 29 (30 July 2013), pp. 9510–9515. ISSN: 0743-7463. DOI: [10.1021/la400994v](https://doi.org/10.1021/la400994v). URL: <https://pubs.acs.org/doi/10.1021/la400994v>.

- [50] S. J. Marrink; H. J. Risselada; S. Yefimov; D. P. Tieleman; A. H. de Vries. “The MARTINI Force Field: Coarse Grained Model for Biomolecular Simulations”. In: *The Journal of Physical Chemistry B* 111 (27 July 2007), pp. 7812–7824. ISSN: 1520-6106. DOI: [10.1021/jp071097f](https://pubs.acs.org/doi/10.1021/jp071097f). URL: <https://pubs.acs.org/doi/10.1021/jp071097f>.
- [51] P. S. Georgoulia; N. M. Glykos. “On the Foldability of Tryptophan-Containing Tetra- and Pentapeptides: An Exhaustive Molecular Dynamics Study”. In: *The Journal of Physical Chemistry B* 117 (18 May 2013), pp. 5522–5532. ISSN: 1520-6106. DOI: [10.1021/jp401239v](https://pubs.acs.org/doi/10.1021/jp401239v). URL: <https://pubs.acs.org/doi/10.1021/jp401239v>.
- [52] C. D. Kroenke; D. Ziemnicka-Kotula; J. Xu; L. Kotula; A. G. Palmer. “Solution Conformations of a Peptide Containing the Cytoplasmic Domain Sequence of the  $\beta$ -Amyloid Precursor Protein”. In: *Biochemistry* 36 (26 July 1997), pp. 8145–8152. ISSN: 0006-2960. DOI: [10.1021/bi9705669](https://pubs.acs.org/doi/10.1021/bi9705669). URL: <https://pubs.acs.org/doi/10.1021/bi9705669>.
- [53] R. Rosal; M. R. Pincus; P. W. Brandt-Rauf; R. L. Fine; J. Michl; H. Wang. “NMR Solution Structure of a Peptide from the mdm-2 Binding Domain of the p53 Protein that Is Selectively Cytotoxic to Cancer Cells <sup>†</sup> <sup>,</sup> <sup>,</sup> <sup>‡</sup>”. In: *Biochemistry* 43 (7 Feb. 2004), pp. 1854–1861. ISSN: 0006-2960. DOI: [10.1021/bi035718g](https://pubs.acs.org/doi/10.1021/bi035718g). URL: <https://pubs.acs.org/doi/10.1021/bi035718g>.
- [54] T. Wymore; T. C. Wong. “Molecular Dynamics Study of Substance P Peptides in a Biphasic Membrane Mimic”. In: *Biophysical Journal* 76 (3 Mar. 1999), pp. 1199–1212. ISSN: 00063495. DOI: [10.1016/S0006-3495\(99\)77284-X](https://linkinghub.elsevier.com/retrieve/pii/S000634959977284X). URL: <https://linkinghub.elsevier.com/retrieve/pii/S000634959977284X>.
- [55] L. Zhao; Z. Cao; Y. Bian; G. Hu; J. Wang; Y. Zhou. “Molecular Dynamics Simulations of Human Antimicrobial Peptide LL-37 in Model POPC and POPG Lipid Bilayers”. In: *International Journal of Molecular Sciences* 19 (4 Apr. 2018), p. 1186. ISSN: 1422-0067. DOI: [10.3390/ijms19041186](http://www.mdpi.com/1422-0067/19/4/1186). URL: <http://www.mdpi.com/1422-0067/19/4/1186>.
- [56] M. Rad-Malekshahi; K. M. Visscher; J. P. G. L. M. Rodrigues; R. de Vries; W. E. Hennink; M. Baldus; A. M. J. J. Bonvin; E. Mastrobattista; M. Weingarth. “The Supramolecular Organization of a Peptide-Based Nanocarrier at High Molecular Detail”. In: *Journal of the American Chemical Society* 137 (24 June 2015), pp. 7775–7784. ISSN: 0002-7863. DOI: [10.1021/jacs.5b02919](https://pubs.acs.org/doi/10.1021/jacs.5b02919). URL: <https://pubs.acs.org/doi/10.1021/jacs.5b02919>.

- [57] S. Jekhmane; M. Prachar; R. Pugliese, J. M. Silva **Federico Fontana**, and F. Gelain; M. Weingarth. “Design Parameters of Tissue-Engineering Scaffolds at the Atomic Scale”. In: *Angewandte Chemie International Edition* 58 (47 Nov. 2019), pp. 16943–16951. ISSN: 1433-7851. DOI: [10.1002/anie.201907880](https://doi.org/10.1002/anie.201907880). URL: <https://onlinelibrary.wiley.com/doi/abs/10.1002/anie.201907880>.
- [58] S. J. Marrink; D. P. Tieleman. “Perspective on the Martini model”. In: *Chemical Society Reviews* 42 (16 2013), p. 6801. ISSN: 0306-0012. DOI: [10.1039/c3cs60093a](https://doi.org/10.1039/c3cs60093a). URL: <http://xlink.rsc.org/?DOI=c3cs60093a>.
- [59] L. Monticelli; S. K. Kandasamy; X. Periole; R. G. Larson; D. Peter Tieleman; S. J. Marrink. “The MARTINI Coarse-Grained Force Field: Extension to Proteins”. In: *Journal of Chemical Theory and Computation* 4 (5 May 2008), pp. 819–834. ISSN: 1549-9618. DOI: [10.1021/ct700324x](https://doi.org/10.1021/ct700324x). URL: <https://pubs.acs.org/doi/10.1021/ct700324x>.
- [60] J. J. Uusitalo; H. I. Ingólfsson; P. Akhshi; D. P. Tieleman; S. J. Marrink. “Martini Coarse-Grained Force Field: Extension to DNA”. In: *Journal of Chemical Theory and Computation* 11 (8 Aug. 2015), pp. 3932–3945. ISSN: 1549-9618. DOI: [10.1021/acs.jctc.5b00286](https://doi.org/10.1021/acs.jctc.5b00286). URL: <https://pubs.acs.org/doi/10.1021/acs.jctc.5b00286>.
- [61] C. A. López; A. J. Rzepiela; A. H. de Vries; L. Dijkhuizen; P. H. Hünenberger; S. J. Marrink. “Martini Coarse-Grained Force Field: Extension to Carbohydrates”. In: *Journal of Chemical Theory and Computation* 5 (12 Dec. 2009), pp. 3195–3210. ISSN: 1549-9618. DOI: [10.1021/ct900313w](https://doi.org/10.1021/ct900313w). URL: <https://pubs.acs.org/doi/10.1021/ct900313w>.
- [62] XiaoCong He et al. “Molecular analysis of interactions between a PAMAM dendrimer–paclitaxel conjugate and a biomembrane”. In: *Physical Chemistry Chemical Physics* 17 (44 2015). ISSN: 1463-9076. DOI: [10.1039/C5CP02242H](https://doi.org/10.1039/C5CP02242H).
- [63] A. Zaghmi et al. “Mechanisms of activity loss for a multi-PEGylated protein by experiment and simulation”. In: *Materials Today Chemistry* 12 (June 2019). ISSN: 24685194. DOI: [10.1016/j.mtchem.2018.12.007](https://doi.org/10.1016/j.mtchem.2018.12.007).
- [64] P. Vidossich; A. Magistrato. “QM/MM Molecular Dynamics Studies of Metal Binding Proteins”. In: *Biomolecules* 4 (3 July 2014), pp. 616–645. ISSN: 2218-273X. DOI: [10.3390/biom4030616](https://doi.org/10.3390/biom4030616). URL: <http://www.mdpi.com/2218-273X/4/3/616>.
- [65] J. Garrec; C. Patel; U. Rothlisberger; E. Dumont. “Insights into Intrastrand Cross-Link Lesions of DNA from QM/MM Molecular Dynamics Simulations”. In: *Journal of the American Chemical Society* 134 (4 Feb. 2012), pp. 2111–2119. ISSN: 0002-7863. DOI: [10.1021/ja2084042](https://doi.org/10.1021/ja2084042). URL: <https://pubs.acs.org/doi/10.1021/ja2084042>.



- [66] P. Sokkar; E. Boulanger; W. Thiel; E. Sanchez-Garcia. “Hybrid Quantum Mechanics/Molecular Mechanics/Coarse Grained Modeling: A Triple-Resolution Approach for Biomolecular Systems”. In: *Journal of Chemical Theory and Computation* 11 (4 Apr. 2015), pp. 1809–1818. ISSN: 1549-9618. DOI: [10.1021/ct500956u](https://pubs.acs.org/doi/10.1021/ct500956u). URL: <https://pubs.acs.org/doi/10.1021/ct500956u>.
- [67] T. Dannenhoffer-Lafage; G. A. Voth. “Reactive Coarse-Grained Molecular Dynamics”. In: *Journal of Chemical Theory and Computation* 16 (4 Apr. 2020), pp. 2541–2549. ISSN: 1549-9618. DOI: [10.1021/acs.jctc.9b01140](https://pubs.acs.org/doi/10.1021/acs.jctc.9b01140). URL: <https://pubs.acs.org/doi/10.1021/acs.jctc.9b01140>.
- [68] Z. Xu; R. Paparcone; Markus J. Buehler. “Alzheimer’s A(1-40) Amyloid Fibrils Feature Size-Dependent Mechanical Properties”. In: *Biophysical Journal* 98 (10 May 2010), pp. 2053–2062. ISSN: 00063495. DOI: [10.1016/j.bpj.2009.12.4317](https://linkinghub.elsevier.com/retrieve/pii/S0006349510000858). URL: <https://linkinghub.elsevier.com/retrieve/pii/S0006349510000858>.
- [69] S. Keten; Z. Xu; B. Ihle; Markus J. Buehler. “Nanoconfinement controls stiffness, strength and mechanical toughness of -sheet crystals in silk”. In: *Nature Materials* 9 (4 Apr. 2010), pp. 359–367. ISSN: 1476-1122. DOI: [10.1038/nmat2704](http://www.nature.com/articles/nmat2704). URL: <http://www.nature.com/articles/nmat2704>.
- [70] S. Sivaramakrishnan; B. J. Spink; A. Y. L. Sim; S. Doniach; J. A. Spudich. “Dynamic charge interactions create surprising rigidity in the ER/K -helical protein motif”. In: *Proceedings of the National Academy of Sciences* 105 (36 Sept. 2008), pp. 13356–13361. ISSN: 0027-8424. DOI: [10.1073/pnas.0806256105](http://www.pnas.org/cgi/doi/10.1073/pnas.0806256105). URL: <http://www.pnas.org/cgi/doi/10.1073/pnas.0806256105>.
- [71] M. Goktas; C. Luo; R. M. A. Sullan; A. E. Bergues-Pupo; R. Lipowsky; A. Vila Verde; K. G. Blank. “Molecular mechanics of coiled coils loaded in the shear geometry”. In: *Chemical Science* 9 (20 2018), pp. 4610–4621. ISSN: 2041-6520. DOI: [10.1039/C8SC01037D](http://xlink.rsc.org/?DOI=C8SC01037D). URL: <http://xlink.rsc.org/?DOI=C8SC01037D>.
- [72] C. Y. J. Lau; **Federico Fontana**; L. D. B. Mandemaker; D. Wezendonk; B. Vermeer; A. M.J.J. Bonvin; R. de Vries; H. Zhang; K. Remaut; J. van den Dikkenberg; J. Medeiros-Silva; A. Hassan; B. Perrone; R. Kuemmerle; F. Gelain; W. E. Hennink; M. Weingarth; E. Mastrobattista. “Control over the fibrillization yield by varying the oligomeric nucleation propensities of self-assembling peptides”. In: *Nature Communications Chemistry* (accepted).
- [73] T. Yu; O. S. Lee; G. C. Schatz. “Steered Molecular Dynamics Studies of the Potential of Mean Force for Peptide Amphiphile Self-Assembly into Cylindrical Nanofibers”. In: *The Journal of Physical Chemistry A* 117 (32 Aug. 2013), pp. 7453–7460. ISSN:



- 1089-5639. DOI: [10.1021/jp401508w](https://doi.org/10.1021/jp401508w). URL: <https://pubs.acs.org/doi/10.1021/jp401508w>.
- [74] P. C. T. Souza; S. Thallmair; P. Conflitti; C. Ramírez-Palacios; R. Alessandri; S. Raniolo; V. Limongelli; S. J. Marrink. “Protein–ligand binding with the coarse-grained Martini model”. In: *Nature Communications* 11 (1 Dec. 2020), p. 3714. ISSN: 2041-1723. DOI: [10.1038/s41467-020-17437-5](https://doi.org/10.1038/s41467-020-17437-5). URL: <http://www.nature.com/articles/s41467-020-17437-5>.
- [75] A. B. Poma; M. Cieplak; P. E. Theodorakis. “Combining the MARTINI and Structure-Based Coarse-Grained Approaches for the Molecular Dynamics Studies of Conformational Transitions in Proteins”. In: *Journal of Chemical Theory and Computation* 13 (3 Mar. 2017), pp. 1366–1374. ISSN: 1549-9618. DOI: [10.1021/acs.jctc.6b00986](https://doi.org/10.1021/acs.jctc.6b00986). URL: <https://pubs.acs.org/doi/10.1021/acs.jctc.6b00986>.
- [76] B. Arshava; I. Taran; H. Xie; J. M. Becker; F. Naider. “High resolution NMR analysis of the seven transmembrane domains of a heptahelical receptor in organic-aqueous medium”. In: *Biopolymers* 64 (3 July 2002), pp. 161–176. ISSN: 0006-3525. DOI: [10.1002/bip.10157](https://doi.org/10.1002/bip.10157). URL: <http://doi.wiley.com/10.1002/bip.10157>.
- [77] M. Wallace; J. A. Iggo; D. J. Adams. “Probing the surface chemistry of self-assembled peptide hydrogels using solution-state NMR spectroscopy”. In: *Soft Matter* 13 (8 2017), pp. 1716–1727. ISSN: 1744-683X. DOI: [10.1039/C6SM02404A](https://doi.org/10.1039/C6SM02404A). URL: <http://xlink.rsc.org/?DOI=C6SM02404A>.
- [78] L. Russo; A. Sgambato; M. Lecchi; V. Pastori; M. Raspanti; A. Natalello; S. M. Doglia; F. Nicotra; L. Cipolla. “Neoglycosylated Collagen Matrices Drive Neuronal Cells to Differentiate”. In: *ACS Chemical Neuroscience* 5 (4 Apr. 2014), pp. 261–265. ISSN: 1948-7193. DOI: [10.1021/cn400222s](https://doi.org/10.1021/cn400222s). URL: <https://pubs.acs.org/doi/10.1021/cn400222s>.
- [79] A. Kijac; A. Y. Shih; A. J. Nieuwkoop; K. Schulten; S. G. Sligar; C. M. Rienstra. “LipidProtein Correlations in Nanoscale Phospholipid Bilayers Determined by Solid-State Nuclear Magnetic Resonance”. In: *Biochemistry* 49 (43 Nov. 2010), pp. 9190–9198. ISSN: 0006-2960. DOI: [10.1021/bi1013722](https://doi.org/10.1021/bi1013722). URL: <https://pubs.acs.org/doi/10.1021/bi1013722>.
- [80] S. Xiang; U. B. lePaige; V. Horn; K. Houben; M. Baldus; H. van Ingen. “Site-Specific Studies of Nucleosome Interactions by Solid-State NMR Spectroscopy”. In: *Angewandte Chemie International Edition* 57 (17 Apr. 2018), pp. 4571–4575. ISSN: 14337851. DOI: [10.1002/anie.201713158](https://doi.org/10.1002/anie.201713158). URL: <http://doi.wiley.com/10.1002/anie.201713158>.

- [81] A. Gautieri; A. Russo; S. Vesentini; A. Redaelli; M. J. Buehler. “Coarse-Grained Model of Collagen Molecules Using an Extended MARTINI Force Field”. In: *Journal of Chemical Theory and Computation* 6 (4 Apr. 2010), pp. 1210–1218. ISSN: 1549-9618. DOI: [10.1021/ct100015v](https://doi.org/10.1021/ct100015v). URL: <https://pubs.acs.org/doi/10.1021/ct100015v>.
- [82] D. L. Barreiro; J. Yeo; A. Tarakanova; F. J. Martín-Martínez; M. J. Buehler. “Multi-scale Modeling of Silk and Silk-Based Biomaterials—A Review”. In: *Macromolecular Bioscience* 19 (3 Mar. 2019), p. 1800253. ISSN: 1616-5187. DOI: [10.1002/mabi.201800253](https://doi.org/10.1002/mabi.201800253). URL: <https://onlinelibrary.wiley.com/doi/abs/10.1002/mabi.201800253>.
- [83] J. Yeo; G. Jung; A. Tarakanova; F. J. Martín-Martínez; Z. Qin; Y. Cheng; Y. W. Zhang; M. J. Buehler. “Multiscale modeling of keratin, collagen, elastin and related human diseases: Perspectives from atomistic to coarse-grained molecular dynamics simulations”. In: *Extreme Mechanics Letters* 20 (Apr. 2018), pp. 112–124. ISSN: 23524316. DOI: [10.1016/j.eml.2018.01.009](https://doi.org/10.1016/j.eml.2018.01.009). URL: <https://linkinghub.elsevier.com/retrieve/pii/S2352431617301682>.
- [84] M. J. Webber; E. A. Appel; E. W. Meijer; R. Langer. “Supramolecular biomaterials”. In: *Nature Materials* 15 (1 Jan. 2016), pp. 13–26. ISSN: 1476-1122. DOI: [10.1038/nmat4474](https://doi.org/10.1038/nmat4474). URL: <http://www.nature.com/articles/nmat4474>.
- [85] K. Rajagopal; J. P. Schneider. “Self-assembling peptides and proteins for nanotechnological applications”. In: *Current Opinion in Structural Biology* 14 (4 Aug. 2004), pp. 480–486. ISSN: 0959440X. DOI: [10.1016/j.sbi.2004.06.006](https://doi.org/10.1016/j.sbi.2004.06.006). URL: <https://linkinghub.elsevier.com/retrieve/pii/S0959440X04001046>.
- [86] C. E. Schmidt; J. B. Leach. “Neural Tissue Engineering: Strategies for Repair and Regeneration”. In: *Annual Review of Biomedical Engineering* 5 (1 Aug. 2003), pp. 293–347. ISSN: 1523-9829. DOI: [10.1146/annurev.bioeng.5.011303.120731](https://doi.org/10.1146/annurev.bioeng.5.011303.120731). URL: <http://www.annualreviews.org/doi/10.1146/annurev.bioeng.5.011303.120731>.
- [87] V. P. Singh; K. K. Vimal; G. S. Kapur; S. Sharma; V. Choudhary. “High-density polyethylene/halloysite nanocomposites: morphology and rheological behaviour under extensional and shear flow”. In: *Journal of Polymer Research* 23 (3 Mar. 2016), p. 43. ISSN: 1022-9760. DOI: [10.1007/s10965-016-0937-1](https://doi.org/10.1007/s10965-016-0937-1). URL: <http://link.springer.com/10.1007/s10965-016-0937-1>.
- [88] N. Singh; M. Tena-Solsona; J. F. Miravet; B. Escuder. “Towards Supramolecular Catalysis with Small Self-assembled Peptides”. In: *Israel Journal of Chemistry* 55

- (6-7 June 2015), pp. 711–723. ISSN: 00212148. DOI: [10.1002/ijch.201400185](https://doi.org/10.1002/ijch.201400185). URL: <http://doi.wiley.com/10.1002/ijch.201400185>.
- [89] X. Zhao; S. Zhang. “Molecular designer self-assembling peptides”. In: *Chemical Society Reviews* 35 (11 2006), p. 1105. ISSN: 0306-0012. DOI: [10.1039/b511336a](https://doi.org/10.1039/b511336a). URL: <http://xlink.rsc.org/?DOI=b511336a>.
- [90] F. Taraballi. “Glycine-spacers influence functional motifs exposure and self-assembling propensity of functionalized substrates tailored for neural stem cell cultures”. In: *Frontiers in Neuroengineering* 3 (2010). ISSN: 16626443. DOI: [10.3389/neuro.16.001.2010](https://doi.org/10.3389/neuro.16.001.2010). URL: <http://journal.frontiersin.org/article/10.3389/neuro.16.001.2010/abstract>.
- [91] G. A. A. Saracino; F. Gelain. “Modelling and analysis of early aggregation events of BMHP1-derived self-assembling peptides”. In: *Journal of Biomolecular Structure and Dynamics* 32 (5 May 2014), pp. 759–775. ISSN: 0739-1102. DOI: [10.1080/07391102.2013.790848](https://doi.org/10.1080/07391102.2013.790848). URL: <http://www.tandfonline.com/doi/abs/10.1080/07391102.2013.790848>.
- [92] J. E. Smith; C. Liang; M. Tseng; N. Li; S. Li; A. K. Mowles; A. K. Mehta; D. G. Lynn. “Defining the Dynamic Conformational Networks of Cross- $\beta$  Peptide Assembly”. In: *Israel Journal of Chemistry* 55 (6-7 June 2015), pp. 763–769. ISSN: 00212148. DOI: [10.1002/ijch.201500012](https://doi.org/10.1002/ijch.201500012). URL: <http://doi.wiley.com/10.1002/ijch.201500012>.
- [93] Y. Liang; D. G. Lynn; K. M. Berland. “Direct Observation of Nucleation and Growth in Amyloid Self-Assembly”. In: *Journal of the American Chemical Society* 132 (18 May 2010), pp. 6306–6308. ISSN: 0002-7863. DOI: [10.1021/ja910964c](https://doi.org/10.1021/ja910964c). URL: <https://pubs.acs.org/doi/10.1021/ja910964c>.
- [94] L. Breydo; V. N. Uversky. “Structural, morphological, and functional diversity of amyloid oligomers”. In: *FEBS Letters* 589 (19PartA Sept. 2015), pp. 2640–2648. ISSN: 00145793. DOI: [10.1016/j.febslet.2015.07.013](https://doi.org/10.1016/j.febslet.2015.07.013). URL: <http://doi.wiley.com/10.1016/j.febslet.2015.07.013>.
- [95] T. R. Serio. “Nucleated Conformational Conversion and the Replication of Conformational Information by a Prion Determinant”. In: *Science* 289 (5483 Aug. 2000), pp. 1317–1321. ISSN: 00368075. DOI: [10.1126/science.289.5483.1317](https://doi.org/10.1126/science.289.5483.1317). URL: <https://www.sciencemag.org/lookup/doi/10.1126/science.289.5483.1317>.
- [96] S. Auer; F. Meersman; C. M. Dobson; M. Vendruscolo. “A Generic Mechanism of Emergence of Amyloid Protofilaments from Disordered Oligomeric Aggregates”. In: *PLoS Computational Biology* 4 (11 Nov. 2008), e1000222. ISSN: 1553-7358. DOI: [10.1371/journal.pcbi.1000222](https://doi.org/10.1371/journal.pcbi.1000222).

- 1371/journal.pcbi.1000222. URL: <https://dx.plos.org/10.1371/journal.pcbi.1000222>.
- [97] I. W. Fu; C. B. Markegard; H. D. Nguyen. “Solvent Effects on Kinetic Mechanisms of Self-Assembly by Peptide Amphiphiles via Molecular Dynamics Simulations”. In: *Langmuir* 31 (1 Jan. 2015), pp. 315–324. ISSN: 0743-7463. DOI: [10.1021/la503399x](https://doi.org/10.1021/la503399x). URL: <https://pubs.acs.org/doi/10.1021/la503399x>.
- [98] L. Xu; Y. Chen; X. Wang. “Assembly of Amyloid Peptides in the Presence of Fibril Seeds: One-Pot Coarse-Grained Molecular Dynamics Simulations”. In: *The Journal of Physical Chemistry B* 118 (31 Aug. 2014), pp. 9238–9246. ISSN: 1520-6106. DOI: [10.1021/jp505551m](https://doi.org/10.1021/jp505551m). URL: <https://pubs.acs.org/doi/10.1021/jp505551m>.
- [99] M. Chiricotto; T. T. Tran; P. H. Nguyen; S. Melchionna; F. Sterpone; P. Derreumaux. “Coarse-grained and All-atom Simulations towards the Early and Late Steps of Amyloid Fibril Formation”. In: *Israel Journal of Chemistry* 57 (7-8 July 2017), pp. 564–573. ISSN: 00212148. DOI: [10.1002/ijch.201600048](https://doi.org/10.1002/ijch.201600048). URL: <http://doi.wiley.com/10.1002/ijch.201600048>.
- [100] L. Dorosh; M. Stepanova. “Probing oligomerization of amyloid beta peptide in silico”. In: *Molecular BioSystems* 13 (1 2017), pp. 165–182. ISSN: 1742-206X. DOI: [10.1039/C6MB00441E](https://doi.org/10.1039/C6MB00441E). URL: <http://xlink.rsc.org/?DOI=C6MB00441E>.
- [101] M. C. Hsieh; D. G. Lynn; M. A. Grover. “Kinetic Model for Two-Step Nucleation of Peptide Assembly”. In: *The Journal of Physical Chemistry B* 121 (31 Aug. 2017), pp. 7401–7411. ISSN: 1520-6106. DOI: [10.1021/acs.jpcc.7b03085](https://doi.org/10.1021/acs.jpcc.7b03085). URL: <https://pubs.acs.org/doi/10.1021/acs.jpcc.7b03085>.
- [102] O. Lee; V. Cho; G. C. Schatz. “Modeling the Self-Assembly of Peptide Amphiphiles into Fibers Using Coarse-Grained Molecular Dynamics”. In: *Nano Letters* 12 (9 Sept. 2012), pp. 4907–4913. ISSN: 1530-6984. DOI: [10.1021/nl302487m](https://doi.org/10.1021/nl302487m). URL: <https://pubs.acs.org/doi/10.1021/nl302487m>.
- [103] A. Iscen; G. C. Schatz. “Peptide amphiphile self-assembly”. In: *EPL (Europhysics Letters)* 119 (3 Aug. 2017), p. 38002. ISSN: 0295-5075. DOI: [10.1209/0295-5075/119/38002](https://doi.org/10.1209/0295-5075/119/38002). URL: <https://iopscience.iop.org/article/10.1209/0295-5075/119/38002>.
- [104] P. W. J. M. Frederix; I. Patmanidis; S. J. Marrink. “Molecular simulations of self-assembling bio-inspired supramolecular systems and their connection to experiments”. In: *Chemical Society Reviews* 47 (10 2018), pp. 3470–3489. ISSN: 0306-0012. DOI: [10.1039/C8CS00040A](https://doi.org/10.1039/C8CS00040A). URL: <http://xlink.rsc.org/?DOI=C8CS00040A>.

- [105] P. W. J. M. Frederix; R. V. Ulijn; N. T. Hunt; T. Tuttle. “Virtual Screening for Dipeptide Aggregation: Toward Predictive Tools for Peptide Self-Assembly”. In: *The Journal of Physical Chemistry Letters* 2 (19 Oct. 2011), pp. 2380–2384. ISSN: 1948-7185. DOI: [10.1021/jz2010573](https://doi.org/10.1021/jz2010573). URL: <https://pubs.acs.org/doi/10.1021/jz2010573>.
- [106] V. Knecht; G. Reiter; H. Schlaad; R. Reiter. “Structure Formation in Langmuir Peptide Films As Revealed from Coarse-Grained Molecular Dynamics Simulations”. In: *Langmuir* 33 (26 July 2017), pp. 6492–6502. ISSN: 0743-7463. DOI: [10.1021/acs.langmuir.7b01455](https://doi.org/10.1021/acs.langmuir.7b01455). URL: <https://pubs.acs.org/doi/10.1021/acs.langmuir.7b01455>.
- [107] P. W. J. M. Frederix; G. G. Scott; Y. M. Abul-Haija; D. Kalafatovic; C. G. Pappas; N. Javid; N. T. Hunt; R. V. Ulijn; T. Tuttle. “Exploring the sequence space for (tri-)peptide self-assembly to design and discover new hydrogels”. In: *Nature Chemistry* 7 (1 Jan. 2015), pp. 30–37. ISSN: 1755-4330. DOI: [10.1038/nchem.2122](https://doi.org/10.1038/nchem.2122). URL: <http://www.nature.com/articles/nchem.2122>.
- [108] L. Martínez; R. Andrade; E. G. Birgin; J. M. Martínez. “PACKMOL: A package for building initial configurations for molecular dynamics simulations”. In: *Journal of Computational Chemistry* 30 (13 Oct. 2009), pp. 2157–2164. ISSN: 01928651. DOI: [10.1002/jcc.21224](https://doi.org/10.1002/jcc.21224). URL: <http://doi.wiley.com/10.1002/jcc.21224>.
- [109] R. Pugliese; **Federico Fontana**; A. Marchini; F. Gelain. “Branched peptides integrate into self-assembled nanostructures and enhance biomechanics of peptidic hydrogels”. In: *Acta Biomaterialia* 66 (Jan. 2018), pp. 258–271. ISSN: 17427061. DOI: [10.1016/j.actbio.2017.11.026](https://doi.org/10.1016/j.actbio.2017.11.026). URL: <https://linkinghub.elsevier.com/retrieve/pii/S1742706117307109>.
- [110] T.F. Chan; L.A. Vese. “Active contours without edges”. In: *IEEE Transactions on Image Processing* 10 (2 2001), pp. 266–277. ISSN: 10577149. DOI: [10.1109/83.902291](https://doi.org/10.1109/83.902291). URL: <http://ieeexplore.ieee.org/document/902291/>.
- [111] R. Karchin; M. Cline; K. Karplus. “Evaluation of local structure alphabets based on residue burial”. In: *Proteins: Structure, Function, and Bioinformatics* 55 (3 Mar. 2004), pp. 508–518. ISSN: 08873585. DOI: [10.1002/prot.20008](https://doi.org/10.1002/prot.20008). URL: <http://doi.wiley.com/10.1002/prot.20008>.
- [112] J. Cheng; P. Baldi. “Improved residue contact prediction using support vector machines and a large feature set”. In: *BMC Bioinformatics* 8 (1 Dec. 2007), p. 113. ISSN: 1471-2105. DOI: [10.1186/1471-2105-8-113](https://doi.org/10.1186/1471-2105-8-113). URL: <https://bmcbioinformatics.biomedcentral.com/articles/10.1186/1471-2105-8-113>.

- [113] Y. Shao; C. Bystroff. “Predicting interresidue contacts using templates and pathways”. In: *Proteins: Structure, Function, and Genetics* 53 (S6 2003), pp. 497–502. ISSN: 0887-3585. DOI: [10.1002/prot.10539](https://doi.org/10.1002/prot.10539). URL: <http://doi.wiley.com/10.1002/prot.10539>.
- [114] F. Emmert-Streib; A. Mushegian. “A topological algorithm for identification of structural domains of proteins”. In: *BMC Bioinformatics* 8 (1 Dec. 2007), p. 237. ISSN: 1471-2105. DOI: [10.1186/1471-2105-8-237](https://doi.org/10.1186/1471-2105-8-237). URL: <https://bmcbioinformatics.biomedcentral.com/articles/10.1186/1471-2105-8-237>.
- [115] N. Michaud-Agrawal; E. J. Denning; T. B. Woolf; O. Beckstein. “MDAnalysis: A toolkit for the analysis of molecular dynamics simulations”. In: *Journal of Computational Chemistry* 32 (10 July 2011), pp. 2319–2327. ISSN: 01928651. DOI: [10.1002/jcc.21787](https://doi.org/10.1002/jcc.21787). URL: <http://doi.wiley.com/10.1002/jcc.21787>.
- [116] M. Seeber; M. Cecchini; F. Rao; G. Settanni; A. Caffisch. “Wordom: a program for efficient analysis of molecular dynamics simulations”. In: *Bioinformatics* 23 (19 Oct. 2007), pp. 2625–2627. ISSN: 1367-4803. DOI: [10.1093/bioinformatics/btm378](https://doi.org/10.1093/bioinformatics/btm378). URL: <https://academic.oup.com/bioinformatics/article-lookup/doi/10.1093/bioinformatics/btm378>.
- [117] A. V. McDonnell; M. Menke; N. Palmer; J. King; L. Cowen; Bonnie Berger. “Fold recognition and accurate sequence-structure alignment of sequences directing  $\beta$ -sheet proteins”. In: *Proteins: Structure, Function, and Bioinformatics* 63 (4 Mar. 2006), pp. 976–985. ISSN: 08873585. DOI: [10.1002/prot.20942](https://doi.org/10.1002/prot.20942). URL: <http://doi.wiley.com/10.1002/prot.20942>.
- [118] D. Eisenberg. “The discovery of the  $\alpha$ -helix and  $\beta$ -sheet, the principal structural features of proteins”. In: *Proceedings of the National Academy of Sciences* 100 (20 Sept. 2003), pp. 11207–11210. ISSN: 0027-8424. DOI: [10.1073/pnas.2034522100](https://doi.org/10.1073/pnas.2034522100). URL: <http://www.pnas.org/cgi/doi/10.1073/pnas.2034522100>.
- [119] L. C. Serpell. “Alzheimer’s amyloid fibrils: structure and assembly”. In: *Biochimica et Biophysica Acta (BBA) - Molecular Basis of Disease* 1502 (1 July 2000), pp. 16–30. ISSN: 09254439. DOI: [10.1016/S0925-4439\(00\)00029-6](https://doi.org/10.1016/S0925-4439(00)00029-6). URL: <https://linkinghub.elsevier.com/retrieve/pii/S0925443900000296>.
- [120] A. Gorkovskiy; K. R. Thurber; R. Tycko; R. B. Wickner. “Locating folds of the in-register parallel  $\beta$ -sheet of the Sup35p prion domain infectious amyloid”. In: *Proceedings of the National Academy of Sciences* 111 (43 Oct. 2014), E4615–E4622. ISSN: 0027-8424. DOI: [10.1073/pnas.1417974111](https://doi.org/10.1073/pnas.1417974111). URL: <http://www.pnas.org/cgi/doi/10.1073/pnas.1417974111>.

- [121] K. Briechle; U. D. Hanebeck. “Template matching using fast normalized cross correlation” in: Mar. 2001, pp. 95–102. DOI: [10.1117/12.421129](https://doi.org/10.1117/12.421129). URL: <http://proceedings.spiedigitallibrary.org/proceeding.aspx?articleid=914530>.
- [122] S. Boccaletti; G. Bianconi; R. Criado; C.I. del Genio; J. Gómez-Gardeñes; M. Romance; I. Sendiña-Nadal; Z. Wang; M. Zanin. “The structure and dynamics of multilayer networks”. In: *Physics Reports* 544 (1 Nov. 2014), pp. 1–122. ISSN: 03701573. DOI: [10.1016/j.physrep.2014.07.001](https://doi.org/10.1016/j.physrep.2014.07.001). URL: <https://linkinghub.elsevier.com/retrieve/pii/S0370157314002105>.
- [123] Y. Xiao; B. Ma; D. McElheny; S. Parthasarathy; F. Long; M. Hoshi; R. Nussinov; Y. Ishii. “ $A\beta(1-42)$  fibril structure illuminates self-recognition and replication of amyloid in Alzheimer’s disease”. In: *Nature Structural Molecular Biology* 22 (6 June 2015), pp. 499–505. ISSN: 1545-9993. DOI: [10.1038/nsmb.2991](https://doi.org/10.1038/nsmb.2991). URL: <http://www.nature.com/articles/nsmb.2991>.
- [124] K. Makabe; D. McElheny; V. Tereshko; A. Hilyard; G. Gawlak; S. Yan; A. Koide; S. Koide. “Atomic structures of peptide self-assembly mimics”. In: *Proceedings of the National Academy of Sciences* 103 (47 Nov. 2006), pp. 17753–17758. ISSN: 0027-8424. DOI: [10.1073/pnas.0606690103](https://doi.org/10.1073/pnas.0606690103). URL: <http://www.pnas.org/cgi/doi/10.1073/pnas.0606690103>.
- [125] I. Grishkovskaya; G. V. Avvakumov; G. Sklenar; D. Dales; G. L. Hammond; Y. A. Muller. “Crystal structure of human sex hormone-binding globulin: steroid transport by a laminin G-like domain”. In: *The EMBO Journal* 19 (4 Feb. 2000), pp. 504–512. ISSN: 0261-4189. DOI: [10.1093/emboj/19.4.504](https://doi.org/10.1093/emboj/19.4.504). URL: <http://emboj.embopress.org/cgi/doi/10.1093/emboj/19.4.504>.
- [126] R. E. Georgescu; S. S. Kim; O. Yurieva; J. Kuriyan; X. P. Kong; M. O’Donnell. “Structure of a Sliding Clamp on DNA”. In: *Cell* 132 (1 Jan. 2008), pp. 43–54. ISSN: 00928674. DOI: [10.1016/j.cell.2007.11.045](https://doi.org/10.1016/j.cell.2007.11.045). URL: <https://linkinghub.elsevier.com/retrieve/pii/S009286740701608X>.
- [127] T. C. Holmes; S. de Lacalle; X. Su; G. Liu; A. Rich; S. Zhang. “Extensive neurite outgrowth and active synapse formation on self-assembling peptide scaffolds”. In: *Proceedings of the National Academy of Sciences* 97 (12 June 2000), pp. 6728–6733. ISSN: 0027-8424. DOI: [10.1073/pnas.97.12.6728](https://doi.org/10.1073/pnas.97.12.6728). URL: <http://www.pnas.org/cgi/doi/10.1073/pnas.97.12.6728>.



- [128] D. Silva; A. Natalello; B. Sani; R. Vasita; G. Saracino; R. N. Zuckermann and S. M. Doglia; F. Gelain. “Synthesis and characterization of designed BMHP1-derived self-assembling peptides for tissue engineering applications”. In: *Nanoscale* 5 (2 2013), pp. 704–718. ISSN: 2040-3364. DOI: [10.1039/C2NR32656F](https://doi.org/10.1039/C2NR32656F). URL: <http://xlink.rsc.org/?DOI=C2NR32656F>.
- [129] T. C. Broussard; S. Pakhomova; D. B. Neau; R. Bonnot; G. L. Waldrop. “Structural Analysis of Substrate, Reaction Intermediate, and Product Binding in *Haemophilus influenzae* Biotin Carboxylase”. In: *Biochemistry* 54 (24 June 2015), pp. 3860–3870. ISSN: 0006-2960. DOI: [10.1021/acs.biochem.5b00340](https://doi.org/10.1021/acs.biochem.5b00340). URL: <https://pubs.acs.org/doi/10.1021/acs.biochem.5b00340>.
- [130] K. P. Wilson; L. M. Shewchuk; R. G. Brennan; A. J. Otsuka; B. W. Matthews. “Escherichia coli biotin holoenzyme synthetase/bio repressor crystal structure delineates the biotin- and DNA-binding domains.” In: *Proceedings of the National Academy of Sciences* 89 (19 Oct. 1992), pp. 9257–9261. ISSN: 0027-8424. DOI: [10.1073/pnas.89.19.9257](https://doi.org/10.1073/pnas.89.19.9257). URL: <http://www.pnas.org/cgi/doi/10.1073/pnas.89.19.9257>.
- [131] A. W. P. Fitzpatrick; G. T. Debelouchina; M. J. Bayro; D. K. Clare; M. A. Caporini; V. S. Bajaj; C. P. Jaroniec; L. Wang; V. Ladizhansky; S. A. Muller; C. E. MacPhee; C. A. Waudby; H. R. Mott; A. De Simone; T. P. J. Knowles; H. R. Saibil; M. Vendruscolo; E. V. Orlova; R. G. Griffin; C. M. Dobson. “Atomic structure and hierarchical assembly of a cross-amyloid fibril”. In: *Proceedings of the National Academy of Sciences* 110 (14 Apr. 2013), pp. 5468–5473. ISSN: 0027-8424. DOI: [10.1073/pnas.1219476110](https://doi.org/10.1073/pnas.1219476110). URL: <http://www.pnas.org/cgi/doi/10.1073/pnas.1219476110>.
- [132] R. N. Rambaran; L. C. Serpell. “Amyloid fibrils”. In: *Prion* 2 (3 July 2008), pp. 112–117. ISSN: 1933-6896. DOI: [10.4161/pri.2.3.7488](https://doi.org/10.4161/pri.2.3.7488). URL: <http://www.tandfonline.com/doi/abs/10.4161/pri.2.3.7488>.
- [133] J. W. Essam; M. E. Fisher. “Some Basic Definitions in Graph Theory”. In: *Reviews of Modern Physics* 42 (2 Apr. 1970), pp. 272–288. ISSN: 0034-6861. DOI: [10.1103/RevModPhys.42.272](https://doi.org/10.1103/RevModPhys.42.272). URL: <https://link.aps.org/doi/10.1103/RevModPhys.42.272>.
- [134] S. Vishveshwara; K. V. Brinda; N. Kannan. “PROTEIN STRUCTURE: INSIGHTS FROM GRAPH THEORY”. In: *Journal of Theoretical and Computational Chemistry* 01 (01 July 2002), pp. 187–211. ISSN: 0219-6336. DOI: [10.1142/S0219633602000117](https://doi.org/10.1142/S0219633602000117). URL: <https://www.worldscientific.com/doi/abs/10.1142/S0219633602000117>.



- [135] I. Faustino; S. J. Marrink. “cgHeliParm: analysis of dsDNA helical parameters for coarse-grained MARTINI molecular dynamics simulations”. In: *Bioinformatics* 33 (23 Dec. 2017), pp. 3813–3815. ISSN: 1367-4803. DOI: [10.1093/bioinformatics/btx444](https://doi.org/10.1093/bioinformatics/btx444). URL: <https://academic.oup.com/bioinformatics/article/33/23/3813/3964380>.
- [136] S. Ranganathan; S. K. Maji; R. Padinhateeri. “Defining a Physical Basis for Diversity in Protein Self-Assemblies Using a Minimal Model”. In: *Journal of the American Chemical Society* 138 (42 Oct. 2016), pp. 13911–13922. ISSN: 0002-7863. DOI: [10.1021/jacs.6b06433](https://doi.org/10.1021/jacs.6b06433). URL: <https://pubs.acs.org/doi/10.1021/jacs.6b06433>.
- [137] C. Qi; X. Yan; C. Huang; A. Melerzanov; Y. Du. “Biomaterials as carrier, barrier and reactor for cell-based regenerative medicine”. In: *Protein Cell* 6 (9 Sept. 2015), pp. 638–653. ISSN: 1674-800X. DOI: [10.1007/s13238-015-0179-8](https://doi.org/10.1007/s13238-015-0179-8). URL: <http://link.springer.com/10.1007/s13238-015-0179-8>.
- [138] E. J. Lee; F. K. Kasper; A. G. Mikos. “Biomaterials for Tissue Engineering”. In: *Annals of Biomedical Engineering* 42 (2 Feb. 2014), pp. 323–337. ISSN: 0090-6964. DOI: [10.1007/s10439-013-0859-6](https://doi.org/10.1007/s10439-013-0859-6). URL: <http://link.springer.com/10.1007/s10439-013-0859-6>.
- [139] T. Garg; O. Singh; S. Arora; R. S. R. Murthy. “Scaffold: A Novel Carrier for Cell and Drug Delivery”. In: *Critical Reviews in Therapeutic Drug Carrier Systems* 29 (1 2012), pp. 1–63. ISSN: 0743-4863. DOI: [10.1615/CritRevTherDrugCarrierSyst.v29.i1.10](https://doi.org/10.1615/CritRevTherDrugCarrierSyst.v29.i1.10). URL: <http://www.dl.begellhouse.com/journals/3667c4ae6e8fd136,2ccd8f8553046ba4,54eb9b5a0d45ccd7.html>.
- [140] T. Garg; A. K. Goyal. “Biomaterial-based scaffolds – current status and future directions”. In: *Expert Opinion on Drug Delivery* 11 (5 May 2014), pp. 767–789. ISSN: 1742-5247. DOI: [10.1517/17425247.2014.891014](https://doi.org/10.1517/17425247.2014.891014). URL: <http://www.tandfonline.com/doi/full/10.1517/17425247.2014.891014>.
- [141] A. J. Engler; S. Sen; H. L. Sweeney; D. E. Discher. “Matrix Elasticity Directs Stem Cell Lineage Specification”. In: *Cell* 126 (4 Aug. 2006), pp. 677–689. ISSN: 00928674. DOI: [10.1016/j.cell.2006.06.044](https://doi.org/10.1016/j.cell.2006.06.044). URL: <https://linkinghub.elsevier.com/retrieve/pii/S0092867406009615>.
- [142] H. Han; H. Ning; S. Liu; Q. Lu; Z. Fan; H. Lu; G. Lu; D. L. Kaplan. “Silk Biomaterials with Vascularization Capacity”. In: *Advanced Functional Materials* 26 (3 Jan. 2016), pp. 421–432. ISSN: 1616301X. DOI: [10.1002/adfm.201504160](https://doi.org/10.1002/adfm.201504160). URL: <http://doi.wiley.com/10.1002/adfm.201504160>.

- [143] B. J. Lawrence; S. V. Madihally. “Cell colonization in degradable 3D porous matrices”. In: *Cell Adhesion Migration* 2 (1 Jan. 2008), pp. 9–16. ISSN: 1933-6918. DOI: [10.4161/cam.2.1.5884](https://doi.org/10.4161/cam.2.1.5884). URL: <http://www.tandfonline.com/doi/abs/10.4161/cam.2.1.5884>.
- [144] R. D. Bartlett; D. Choi; J. B. Phillips. “Biomechanical properties of the spinal cord: implications for tissue engineering and clinical translation”. In: *Regenerative Medicine* 11 (7 Oct. 2016), pp. 659–673. ISSN: 1746-0751. DOI: [10.2217/rme-2016-0065](https://doi.org/10.2217/rme-2016-0065). URL: <https://www.futuremedicine.com/doi/10.2217/rme-2016-0065>.
- [145] L. A. Flanagan; Y. E. Ju; B. Marg; M. Osterfield; P. A. Janmey. “Neurite branching on deformable substrates”. In: *NeuroReport* 13 (18 Dec. 2002), pp. 2411–2415. ISSN: 0959-4965. DOI: [10.1097/00001756-200212200-00007](https://doi.org/10.1097/00001756-200212200-00007). URL: <http://journals.lww.com/00001756-200212200-00007>.
- [146] A. Caprini; D. Silva; I. Zanoni; C. Cunha; C. Volontè; A. Vescovi; F. Gelain. “A novel bioactive peptide: assessing its activity over murine neural stem cells and its potential for neural tissue engineering”. In: *New Biotechnology* 30 (5 June 2013), pp. 552–562. ISSN: 18716784. DOI: [10.1016/j.nbt.2013.03.005](https://doi.org/10.1016/j.nbt.2013.03.005). URL: <https://linkinghub.elsevier.com/retrieve/pii/S1871678413000381>.
- [147] C. E. Morgan; A. W. Dombrowski; C. M. R. Pérez; E. S.M. Bahnson; N. D. Tshilis; W. Jiang; Q. Jiang; J. M. Vercammen; V. S. Prakash; T. A. Pritts; S. I. Stupp; M. R. Kibbe. “Tissue-Factor Targeted Peptide Amphiphile Nanofibers as an Injectable Therapy To Control Hemorrhage”. In: *ACS Nano* 10 (1 Jan. 2016), pp. 899–909. ISSN: 1936-0851. DOI: [10.1021/acsnano.5b06025](https://doi.org/10.1021/acsnano.5b06025). URL: <https://pubs.acs.org/doi/10.1021/acsnano.5b06025>.
- [148] M. Ozeki; S. Kuroda; K. Kon; S. Kasugai. “Differentiation of Bone Marrow Stromal Cells into Osteoblasts in a Self-assembling Peptide Hydrogel: *In Vitro* and *In Vivo* Studies”. In: *Journal of Biomaterials Applications* 25 (7 Mar. 2011), pp. 663–684. ISSN: 0885-3282. DOI: [10.1177/0885328209356328](https://doi.org/10.1177/0885328209356328). URL: <http://journals.sagepub.com/doi/10.1177/0885328209356328>.
- [149] A. Schneider; J. A. Garlick; C. Egles. “Self-Assembling Peptide Nanofiber Scaffolds Accelerate Wound Healing”. In: *PLoS ONE* 3 (1 Jan. 2008), e1410. ISSN: 1932-6203. DOI: [10.1371/journal.pone.0001410](https://doi.org/10.1371/journal.pone.0001410). URL: <https://dx.plos.org/10.1371/journal.pone.0001410>.
- [150] Y. Loo; Y. C. Wong; E. Z. Cai; C. H. Ang; A. Raju; A. Lakshmanan; A. G. Koh; H. J. Zhou; T. C. Lim; S. M. Moochhala; C. A. E. Hauser. “Ultrashort peptide nanofibrous hydrogels for the acceleration of healing of burn wounds”. In: *Biomaterials* 35 (17 June

- 2014), pp. 4805–4814. ISSN: 01429612. DOI: [10.1016/j.biomaterials.2014.02.047](https://doi.org/10.1016/j.biomaterials.2014.02.047). URL: <https://linkinghub.elsevier.com/retrieve/pii/S0142961214002038>.
- [151] P. D. Tatman; W. Gerull; S. Sweeney-Easter; J. I. Davis; A. O. Gee; D. Kim. “Multi-scale Biofabrication of Articular Cartilage: Bioinspired and Biomimetic Approaches”. In: *Tissue Engineering Part B: Reviews* 21 (6 Dec. 2015), pp. 543–559. ISSN: 1937-3368. DOI: [10.1089/ten.teb.2015.0142](https://doi.org/10.1089/ten.teb.2015.0142). URL: <https://www.liebertpub.com/doi/10.1089/ten.teb.2015.0142>.
- [152] P. A. Brunton; R. P. W. Davies; J. L. Burke; A. Smith; A. Aggeli; S. J. Brookes; J. Kirkham. “Treatment of early caries lesions using biomimetic self-assembling peptides – a clinical safety trial”. In: *British Dental Journal* 215 (4 Aug. 2013), E6–E6. ISSN: 0007-0610. DOI: [10.1038/sj.bdj.2013.741](https://doi.org/10.1038/sj.bdj.2013.741). URL: <http://www.nature.com/articles/sj.bdj.2013.741>.
- [153] L. Y. Sang; Y. Liang; Y. Li; W. Wong; D. K. Tay; K. So; R. G. Ellis-Behnke; W. Wu; R. T. Cheung. “A self-assembling nanomaterial reduces acute brain injury and enhances functional recovery in a rat model of intracerebral hemorrhage”. In: *Nanomedicine: Nanotechnology, Biology and Medicine* 11 (3 Apr. 2015), pp. 611–620. ISSN: 15499634. DOI: [10.1016/j.nano.2014.05.012](https://doi.org/10.1016/j.nano.2014.05.012). URL: <https://linkinghub.elsevier.com/retrieve/pii/S1549963414002251>.
- [154] J. Guo; K. K. G. Leung; H. Su; Q. Yuan; L. Wang; T. Chu; W. Zhang; J. K. S. Pu; G. K. Po Ng; W. M. Wong; X. Dai; W. Wu. “Self-assembling peptide nanofiber scaffold promotes the reconstruction of acutely injured brain”. In: *Nanomedicine: Nanotechnology, Biology and Medicine* 5 (3 Sept. 2009), pp. 345–351. ISSN: 15499634. DOI: [10.1016/j.nano.2008.12.001](https://doi.org/10.1016/j.nano.2008.12.001). URL: <https://linkinghub.elsevier.com/retrieve/pii/S1549963408001901>.
- [155] D. Cigognini; A. Satta; B. Colleoni; D. Silva; M. Donegà; S. Antonini; F. Gelain. “Evaluation of Early and Late Effects into the Acute Spinal Cord Injury of an Injectable Functionalized Self-Assembling Scaffold”. In: *PLoS ONE* 6 (5 May 2011), e19782. ISSN: 1932-6203. DOI: [10.1371/journal.pone.0019782](https://doi.org/10.1371/journal.pone.0019782). URL: <https://dx.plos.org/10.1371/journal.pone.0019782>.
- [156] D. Cigognini; D. Silva; S. Paloppi; F. Gelain. “Evaluation of Mechanical Properties and Therapeutic Effect of Injectable Self-Assembling Hydrogels for Spinal Cord Injury”. In: *Journal of Biomedical Nanotechnology* 10 (2 Feb. 2014), pp. 309–323. ISSN: 1550-7033. DOI: [10.1166/jbn.2014.1759](https://doi.org/10.1166/jbn.2014.1759). URL: <http://www.ingentaconnect.com/content/10.1166/jbn.2014.1759>.

- [157] N. L. Angeloni; C. W. Bond; Y. Tang; D. A. Harrington; S. Zhang; S. I. Stupp and K. E. McKenna; C. A. Podlasek. “Regeneration of the cavernous nerve by Sonic hedgehog using aligned peptide amphiphile nanofibers”. In: *Biomaterials* 32 (4 Feb. 2011), pp. 1091–1101. ISSN: 01429612. DOI: [10.1016/j.biomaterials.2010.10.003](https://doi.org/10.1016/j.biomaterials.2010.10.003). URL: <https://linkinghub.elsevier.com/retrieve/pii/S0142961210012883>.
- [158] M. T. McClendon; Samuel I. Stupp. “Tubular hydrogels of circumferentially aligned nanofibers to encapsulate and orient vascular cells”. In: *Biomaterials* 33 (23 Aug. 2012), pp. 5713–5722. ISSN: 01429612. DOI: [10.1016/j.biomaterials.2012.04.040](https://doi.org/10.1016/j.biomaterials.2012.04.040). URL: <https://linkinghub.elsevier.com/retrieve/pii/S0142961212004620>.
- [159] E. L. Bakota; O. Sensoy; B. Ozgur; M. Sayar; J. D. Hartgerink. “Self-Assembling Multidomain Peptide Fibers with Aromatic Cores”. In: *Biomacromolecules* 14 (5 May 2013), pp. 1370–1378. ISSN: 1525-7797. DOI: [10.1021/bm4000019](https://doi.org/10.1021/bm4000019). URL: <https://pubs.acs.org/doi/10.1021/bm4000019>.
- [160] N. C. Wickremasinghe; V. A. Kumar; S. Shi; J. D. Hartgerink. “Controlled Angiogenesis in Peptide Nanofiber Composite Hydrogels”. In: *ACS Biomaterials Science Engineering* 1 (9 Sept. 2015), pp. 845–854. ISSN: 2373-9878. DOI: [10.1021/acsbiomaterials.5b00210](https://doi.org/10.1021/acsbiomaterials.5b00210). URL: <https://pubs.acs.org/doi/10.1021/acsbiomaterials.5b00210>.
- [161] V. A. Kumar; Q. Liu; N. C. Wickremasinghe; S. Shi; T. T. Cornwright; Y. Deng; A. Azares; A. N. Moore; A. M. Acevedo-Jake; N. R. Agudo; S. Pan; D. G. Woodside; P. Vanderslice; J. T. Willerson; R. A. Dixon; J. D. Hartgerink. “Treatment of hind limb ischemia using angiogenic peptide nanofibers”. In: *Biomaterials* 98 (Aug. 2016), pp. 113–119. ISSN: 01429612. DOI: [10.1016/j.biomaterials.2016.04.032](https://doi.org/10.1016/j.biomaterials.2016.04.032). URL: <https://linkinghub.elsevier.com/retrieve/pii/S0142961216301430>.
- [162] V. A. Kumar; N. L. Taylor; S. Shi; N. C. Wickremasinghe; R. N. D’Souza; J. D. Hartgerink. “Self-assembling multidomain peptides tailor biological responses through biphasic release”. In: *Biomaterials* 52 (June 2015), pp. 71–78. ISSN: 01429612. DOI: [10.1016/j.biomaterials.2015.01.079](https://doi.org/10.1016/j.biomaterials.2015.01.079). URL: <https://linkinghub.elsevier.com/retrieve/pii/S0142961215001027>.
- [163] N. C. Wickremasinghe; V. A. Kumar; J. D. Hartgerink. “Two-Step Self-Assembly of Liposome-Multidomain Peptide Nanofiber Hydrogel for Time-Controlled Release”. In: *Biomacromolecules* 15 (10 Oct. 2014), pp. 3587–3595. ISSN: 1525-7797. DOI: [10.1021/bm500856c](https://doi.org/10.1021/bm500856c). URL: <https://pubs.acs.org/doi/10.1021/bm500856c>.

- [164] S. Budday; G. Sommer; J. Haybaeck; P. Steinmann; G.A. Holzapfel; E. Kuhl. “Rheological characterization of human brain tissue”. In: *Acta Biomaterialia* 60 (Sept. 2017), pp. 315–329. ISSN: 17427061. DOI: [10.1016/j.actbio.2017.06.024](https://doi.org/10.1016/j.actbio.2017.06.024). URL: <https://linkinghub.elsevier.com/retrieve/pii/S1742706117303884>.
- [165] F. H. Silver; J. W. Freeman; D. DeVore. “Viscoelastic properties of human skin and processed dermis”. In: *Skin Research and Technology* 7 (1 Feb. 2001), pp. 18–23. ISSN: 0909752X. DOI: [10.1034/j.1600-0846.2001.007001018.x](https://doi.org/10.1034/j.1600-0846.2001.007001018.x). URL: <http://doi.wiley.com/10.1034/j.1600-0846.2001.007001018.x>.
- [166] X. L. Lu; V. C. Mow. “Biomechanics of Articular Cartilage and Determination of Material Properties”. In: *Medicine Science in Sports Exercise* 40 (2 Feb. 2008), pp. 193–199. ISSN: 0195-9131. DOI: [10.1249/mss.0b013e31815cb1fc](https://doi.org/10.1249/mss.0b013e31815cb1fc). URL: <http://journals.lww.com/00005768-200802000-00002>.
- [167] J. Kisiday; M. Jin; B. Kurz; H. Hung; C. Semino; S. Zhang; A. J. Grodzinsky. “Self-assembling peptide hydrogel fosters chondrocyte extracellular matrix production and cell division: Implications for cartilage tissue repair”. In: *Proceedings of the National Academy of Sciences* 99 (15 July 2002), pp. 9996–10001. ISSN: 0027-8424. DOI: [10.1073/pnas.142309999](https://doi.org/10.1073/pnas.142309999). URL: <http://www.pnas.org/cgi/doi/10.1073/pnas.142309999>.
- [168] J. Sun; Q. Zheng; Y. Wu; Y. Liu; X. Guo; W. Wu. “Biocompatibility of KLD-12 peptide hydrogel as a scaffold in tissue engineering of intervertebral discs in rabbits”. In: *Journal of Huazhong University of Science and Technology [Medical Sciences]* 30 (2 Apr. 2010), pp. 173–177. ISSN: 1672-0733. DOI: [10.1007/s11596-010-0208-z](https://doi.org/10.1007/s11596-010-0208-z). URL: <http://link.springer.com/10.1007/s11596-010-0208-z>.
- [169] J. Sun; Q. Zheng. “Experimental study on self-assembly of KLD-12 peptide hydrogel and 3-D culture of MSC encapsulated within hydrogel in vitro”. In: *Journal of Huazhong University of Science and Technology [Medical Sciences]* 29 (4 Aug. 2009), pp. 512–516. ISSN: 1672-0733. DOI: [10.1007/s11596-009-0424-6](https://doi.org/10.1007/s11596-009-0424-6). URL: <http://link.springer.com/10.1007/s11596-009-0424-6>.
- [170] J. K. Tripathi; S. Pal; B. Awasthi; A. Kumar; A. Tandon; K. Mitra; N. Chattopadhyay; J. K. Ghosh. “Variants of self-assembling peptide, KLD-12 that show both rapid fracture healing and antimicrobial properties”. In: *Biomaterials* 56 (July 2015), pp. 92–103. ISSN: 01429612. DOI: [10.1016/j.biomaterials.2015.03.046](https://doi.org/10.1016/j.biomaterials.2015.03.046). URL: <https://linkinghub.elsevier.com/retrieve/pii/S0142961215003245>.

- [171] A. Rahimi; S. Amjad-Iranagh; H. Modarress. “Molecular dynamics simulation of coarse-grained poly(L-lysine) dendrimers”. In: *Journal of Molecular Modeling* 22 (3 Mar. 2016), p. 59. ISSN: 1610-2940. DOI: [10.1007/s00894-016-2925-0](https://doi.org/10.1007/s00894-016-2925-0). URL: <http://link.springer.com/10.1007/s00894-016-2925-0>.
- [172] S. Pronk; S. Páll; R. Schulz; P. Larsson; P. Bjelkmar; R. Apostolov; M. R. Shirts; J. C. Smith; P. M. Kasson; D. van der Spoel; B. Hess; E. Lindahl. “GROMACS 4.5: a high-throughput and highly parallel open source molecular simulation toolkit”. In: *Bioinformatics* 29 (7 Apr. 2013), pp. 845–854. ISSN: 1460-2059. DOI: [10.1093/bioinformatics/btt055](https://doi.org/10.1093/bioinformatics/btt055). URL: <https://academic.oup.com/bioinformatics/article-lookup/doi/10.1093/bioinformatics/btt055>.
- [173] G. Bussi; D. Donadio; M. Parrinello. “Canonical sampling through velocity rescaling”. In: *The Journal of Chemical Physics* 126 (1 Jan. 2007), p. 014101. ISSN: 0021-9606. DOI: [10.1063/1.2408420](https://doi.org/10.1063/1.2408420). URL: <http://aip.scitation.org/doi/10.1063/1.2408420>.
- [174] H. J. C. Berendsen; J. P. M. Postma; W. F. van Gunsteren; A. DiNola; J. R. Haak. “Molecular dynamics with coupling to an external bath”. In: *The Journal of Chemical Physics* 81 (8 Oct. 1984), pp. 3684–3690. ISSN: 0021-9606. DOI: [10.1063/1.448118](https://doi.org/10.1063/1.448118). URL: <http://aip.scitation.org/doi/10.1063/1.448118>.
- [175] B. Hess. “P-LINCS: A Parallel Linear Constraint Solver for Molecular Simulation”. In: *Journal of Chemical Theory and Computation* 4 (1 Jan. 2008), pp. 116–122. ISSN: 1549-9618. DOI: [10.1021/ct700200b](https://doi.org/10.1021/ct700200b). URL: <https://pubs.acs.org/doi/10.1021/ct700200b>.
- [176] G. Reddy; J. E. Straub; D. Thirumalai. “Influence of Preformed Asp23Lys28 Salt Bridge on the Conformational Fluctuations of Monomers and Dimers of A $\beta$  Peptides with Implications for Rates of Fibril Formation”. In: *The Journal of Physical Chemistry B* 113 (4 Jan. 2009), pp. 1162–1172. ISSN: 1520-6106. DOI: [10.1021/jp808914c](https://doi.org/10.1021/jp808914c). URL: <https://pubs.acs.org/doi/10.1021/jp808914c>.
- [177] B. Ma; R. Nussinov. “Stabilities and conformations of Alzheimer’s  $\beta$ -amyloid peptide oligomers (A $\beta$ 16-22, A $\beta$ 16-35, and A $\beta$ 10-35): Sequence effects”. In: *Proceedings of the National Academy of Sciences* 99 (22 Oct. 2002), pp. 14126–14131. ISSN: 0027-8424. DOI: [10.1073/pnas.212206899](https://doi.org/10.1073/pnas.212206899). URL: <http://www.pnas.org/cgi/doi/10.1073/pnas.212206899>.
- [178] L. Serpell. “Amyloid structure”. In: *Essays in Biochemistry* 56 (Aug. 2014), pp. 1–10. ISSN: 0071-1365. DOI: [10.1042/bse0560001](https://doi.org/10.1042/bse0560001). URL: <https://portlandpress.com/essaysbiochem/article/doi/10.1042/bse0560001/78373/Amyloid-structure>.

- [179] J. F. Smith; T. P. J. Knowles; C. M. Dobson; C. E. MacPhee; M. E. Welland. “Characterization of the nanoscale properties of individual amyloid fibrils”. In: *Proceedings of the National Academy of Sciences* 103 (43 Oct. 2006), pp. 15806–15811. ISSN: 0027-8424. DOI: [10.1073/pnas.0604035103](https://doi.org/10.1073/pnas.0604035103). URL: <http://www.pnas.org/cgi/doi/10.1073/pnas.0604035103>.
- [180] Bumjoon Choi et al. “Nanomechanical Characterization of Amyloid Fibrils Using Single-Molecule Experiments and Computational Simulations”. In: *Journal of Nanomaterials* 2016 (2016), pp. 1–16. ISSN: 1687-4110. DOI: [10.1155/2016/5873695](https://doi.org/10.1155/2016/5873695). URL: <http://www.hindawi.com/journals/jnm/2016/5873695/>.
- [181] G. Lamour; R. Nassar; P. H.W. Chan; G. Bozkurt; J. Li; J. M. Bui; C. K. Yip; T. Mayor; H. Li; H. Wu; J. A. Gsponer. “Mapping the Broad Structural and Mechanical Properties of Amyloid Fibrils”. In: *Biophysical Journal* 112 (4 Feb. 2017), pp. 584–594. ISSN: 00063495. DOI: [10.1016/j.bpj.2016.12.036](https://doi.org/10.1016/j.bpj.2016.12.036). URL: <https://linkinghub.elsevier.com/retrieve/pii/S0006349516343429>.
- [182] J. Crowet; M. Nasir; N. Dony; A. Deschamps; V. Stroobant; P. Morsomme; M. Deleu and P. Soumillion; Laurence Lins. “Insight into the Self-Assembling Properties of Peptergents: A Molecular Dynamics Simulation Study”. In: *International Journal of Molecular Sciences* 19 (9 Sept. 2018), p. 2772. ISSN: 1422-0067. DOI: [10.3390/ijms19092772](https://doi.org/10.3390/ijms19092772). URL: <http://www.mdpi.com/1422-0067/19/9/2772>.
- [183] J. W. Bourne; P. A. Torzilli. “Molecular simulations predict novel collagen conformations during cross-link loading”. In: *Matrix Biology* 30 (5-6 June 2011), pp. 356–360. ISSN: 0945053X. DOI: [10.1016/j.matbio.2011.03.010](https://doi.org/10.1016/j.matbio.2011.03.010). URL: <https://linkinghub.elsevier.com/retrieve/pii/S0945053X1100031X>.
- [184] H. Ghodsi; K. Darvish. “Investigation of mechanisms of viscoelastic behavior of collagen molecule”. In: *Journal of the Mechanical Behavior of Biomedical Materials* 51 (Nov. 2015), pp. 194–204. ISSN: 17516161. DOI: [10.1016/j.jmbbm.2015.07.015](https://doi.org/10.1016/j.jmbbm.2015.07.015). URL: <https://linkinghub.elsevier.com/retrieve/pii/S1751616115002568>.
- [185] M. Sotomayor; K. Schulten. “Single-Molecule Experiments in Vitro and in Silico”. In: *Science* 316 (5828 May 2007), pp. 1144–1148. ISSN: 0036-8075. DOI: [10.1126/science.1137591](https://doi.org/10.1126/science.1137591). URL: <https://www.sciencemag.org/lookup/doi/10.1126/science.1137591>.
- [186] Y. Lien; D. R. Mahato; F. Hoppe-Seyler; W. B. Fischer. “Membrane partitioning of peptide aggregates: coarse-grained molecular dynamics simulations”. In: *Journal of Biomolecular Structure and Dynamics* 38 (2 Jan. 2020), pp. 524–532. ISSN: 0739-1102.



- DOI: [10.1080/07391102.2019.1581660](https://doi.org/10.1080/07391102.2019.1581660). URL: <https://www.tandfonline.com/doi/full/10.1080/07391102.2019.1581660>.
- [187] N. Thota; Z. Luo; Z. Hu; J. Jiang. “Self-Assembly of Amphiphilic Peptide (AF)<sub>6</sub>H<sub>5</sub>K<sub>15</sub>: Coarse-Grained Molecular Dynamics Simulation”. In: *The Journal of Physical Chemistry B* 117 (33 Aug. 2013), pp. 9690–9698. ISSN: 1520-6106. DOI: [10.1021/jp4059752](https://doi.org/10.1021/jp4059752). URL: <https://pubs.acs.org/doi/10.1021/jp4059752>.
- [188] J. In Kim; J. Kwon; I. Baek; S. Na. “Steered molecular dynamics analysis of the role of cofilin in increasing the flexibility of actin filaments”. In: *Biophysical Chemistry* 218 (Nov. 2016), pp. 27–35. ISSN: 03014622. DOI: [10.1016/j.bpc.2016.08.002](https://doi.org/10.1016/j.bpc.2016.08.002). URL: <https://linkinghub.elsevier.com/retrieve/pii/S0301462216302666>.
- [189] G. A. A. Saracino; **Federico Fontana**; S. Jekhmene; J. M. Silva; M. Weingarth; F. Gelain. “Elucidating Self-Assembling Peptide Aggregation via Morphoscanner: A New Tool for Protein-Peptide Structural Characterization”. In: *Advanced Science* 5 (8 Aug. 2018), p. 1800471. ISSN: 21983844. DOI: [10.1002/advs.201800471](https://doi.org/10.1002/advs.201800471). URL: <http://doi.wiley.com/10.1002/advs.201800471>.
- [190] Xavier Daura et al. “Peptide Folding: When Simulation Meets Experiment”. In: *Angew. Chem. Int. Ed. Engl* 31 (1998), pp. 1387–1404.
- [191] T. A. Wassenaar; K. Pluhackova; R. A. Böckmann; S. J. Marrink; D. P. Tieleman. “Going Backward: A Flexible Geometric Approach to Reverse Transformation from Coarse Grained to Atomistic Models”. In: *Journal of Chemical Theory and Computation* 10 (2 Feb. 2014), pp. 676–690. ISSN: 1549-9618. DOI: [10.1021/ct400617g](https://doi.org/10.1021/ct400617g). URL: <https://pubs.acs.org/doi/10.1021/ct400617g>.
- [192] C. Oostenbrink; T. A. Soares; N. F. A. van der Vegt; W. F. van Gunsteren. “Validation of the 53A6 GROMOS force field”. In: *European Biophysics Journal* 34 (4 June 2005), pp. 273–284. ISSN: 0175-7571. DOI: [10.1007/s00249-004-0448-6](https://doi.org/10.1007/s00249-004-0448-6). URL: <http://link.springer.com/10.1007/s00249-004-0448-6>.
- [193] T. P. Knowles; A. W. Fitzpatrick; S. Meehan; H. R. Mott; M. Vendruscolo; C. M. Dobson; M. E. Welland. “Role of Intermolecular Forces in Defining Material Properties of Protein Nanofibrils”. In: *Science* 318 (5858 Dec. 2007), pp. 1900–1903. ISSN: 0036-8075. DOI: [10.1126/science.1150057](https://doi.org/10.1126/science.1150057). URL: <https://www.sciencemag.org/lookup/doi/10.1126/science.1150057>.
- [194] T. Biagini; F. Petrizzelli; M. Truglio; R. Cespa; A. Barbieri; D. Capocéfalo; S. Castellana; M. F. Tevy; M. Carella; T. Mazza. “Are Gaming-Enabled Graphic Processing Unit Cards Convenient for Molecular Dynamics Simulation?” In: *Evolutionary Bioinformatics* 15 (Jan. 2019), p. 117693431985014. ISSN: 1176-9343. DOI: [10.117693431985014](https://doi.org/10.117693431985014).



- 1177/1176934319850144. URL: <http://journals.sagepub.com/doi/10.1177/1176934319850144>.
- [195] M. Kyoung; A. Srivastava; Y. Zhang; J. Diao; M. Vrljic; P. Grob; E. Nogales; S. Chu; A. T. Brunger. “In vitro system capable of differentiating fast Ca<sup>2+</sup>-triggered content mixing from lipid exchange for mechanistic studies of neurotransmitter release”. In: *Proceedings of the National Academy of Sciences* 108 (29 July 2011), E304–E313. ISSN: 0027-8424. DOI: [10.1073/pnas.1107900108](https://doi.org/10.1073/pnas.1107900108). URL: <http://www.pnas.org/cgi/doi/10.1073/pnas.1107900108>.
- [196] V. Corradi; E. Mendez-Villuendas; H. I. Ingólfsson; R. X. Gu; I. Siuda; M. N. Melo; A. Moussatova; L. J. DeGagné; B. I. Sejdiu; G. Singh; T. A. Wassenaar; K. Delgado Magnero; S. J. Marrink; D. P. Tieleman. “Lipid–Protein Interactions Are Unique Fingerprints for Membrane Proteins”. In: *ACS Central Science* 4 (6 June 2018), pp. 709–717. ISSN: 2374-7943. DOI: [10.1021/acscentsci.8b00143](https://doi.org/10.1021/acscentsci.8b00143). URL: <https://pubs.acs.org/doi/10.1021/acscentsci.8b00143>.
- [197] L. Lim; M. R. Wenk. “Neuronal Membrane Lipids – Their Role in the Synaptic Vesicle Cycle”. In: *Handbook of Neurochemistry and Molecular Neurobiology* (2009), pp. 223–238. DOI: [10.1007/978-0-387-30378-9\\_9](https://doi.org/10.1007/978-0-387-30378-9_9). URL: [http://link.springer.com/10.1007/978-0-387-30378-9\\_9](http://link.springer.com/10.1007/978-0-387-30378-9_9).
- [198] I. Levitan; Y. Fang; A. Rosenhouse-Dantsker; V. Romanenko. “Cholesterol and Ion Channels”. In: (2010), pp. 509–549. DOI: [10.1007/978-90-481-8622-8\\_19](https://doi.org/10.1007/978-90-481-8622-8_19). URL: [http://link.springer.com/10.1007/978-90-481-8622-8\\_19](http://link.springer.com/10.1007/978-90-481-8622-8_19).
- [199] C. Dart. “SYMPOSIUM REVIEW: Lipid microdomains and the regulation of ion channel function”. In: *The Journal of Physiology* 588 (17 Sept. 2010), pp. 3169–3178. ISSN: 00223751. DOI: [10.1113/jphysiol.2010.191585](https://doi.org/10.1113/jphysiol.2010.191585). URL: <http://doi.wiley.com/10.1113/jphysiol.2010.191585>.
- [200] A. Marchini; A. Raspa; R. Pugliese; M. Abd El Malek; V. Pastori; M. Lecchi and A. L. Vescovi; F. Gelain. “Multifunctionalized hydrogels foster hNSC maturation in 3D cultures and neural regeneration in spinal cord injuries”. In: *Proceedings of the National Academy of Sciences* 116 (15 Apr. 2019), pp. 7483–7492. ISSN: 0027-8424. DOI: [10.1073/pnas.1818392116](https://doi.org/10.1073/pnas.1818392116). URL: <http://www.pnas.org/lookup/doi/10.1073/pnas.1818392116>.
- [201] A. Marchini; C. Favoino; F. Gelain. “Multi-Functionalized Self-Assembling Peptides as Reproducible 3D Cell Culture Systems Enabling Differentiation and Survival of Various Human Neural Stem Cell Lines”. In: *Frontiers in Neuroscience* 14 (May

- 2020). ISSN: 1662-453X. DOI: [10.3389/fnins.2020.00413](https://doi.org/10.3389/fnins.2020.00413). URL: <https://www.frontiersin.org/article/10.3389/fnins.2020.00413/full>.
- [202] H. I. Ingólfsson; M. N. Melo; F. J. van Eerden; C. Arnarez; C. A. Lopez; T. A. Wassenaar; X. Periole; A. H. de Vries; D. P. Tieleman; S. J. Marrink. “Lipid Organization of the Plasma Membrane”. In: *Journal of the American Chemical Society* 136 (41 Oct. 2014), pp. 14554–14559. ISSN: 0002-7863. DOI: [10.1021/ja507832e](https://doi.org/10.1021/ja507832e). URL: <https://pubs.acs.org/doi/10.1021/ja507832e>.
- [203] W. Pezeshkian; M. König; T. A. Wassenaar; S. J. Marrink. “Backmapping triangulated surfaces to coarse-grained membrane models”. In: *Nature Communications* 11 (1 Dec. 2020), p. 2296. ISSN: 2041-1723. DOI: [10.1038/s41467-020-16094-y](https://doi.org/10.1038/s41467-020-16094-y). URL: <http://www.nature.com/articles/s41467-020-16094-y>.
- [204] V. Corradi; B. I. Sejdiu; H. Mesa-Galoso; H. Abdizadeh; S. Y. Noskov; S. J. Marrink; D. Peter Tieleman. “Emerging Diversity in Lipid–Protein Interactions”. In: *Chemical Reviews* 119 (9 May 2019), pp. 5775–5848. ISSN: 0009-2665. DOI: [10.1021/acs.chemrev.8b00451](https://doi.org/10.1021/acs.chemrev.8b00451). URL: <https://pubs.acs.org/doi/10.1021/acs.chemrev.8b00451>.
- [205] C. Zhou; K. Liu. “Molecular dynamics simulation of reversible electroporation with Martini force field”. In: *BioMedical Engineering OnLine* 18 (1 Dec. 2019), p. 123. ISSN: 1475-925X. DOI: [10.1186/s12938-019-0743-1](https://doi.org/10.1186/s12938-019-0743-1). URL: <https://biomedical-engineering-online.biomedcentral.com/articles/10.1186/s12938-019-0743-1>.
- [206] H. I. Ingólfsson; T. S. Carpenter; H. Bhatia; P. T. Bremer; S. J. Marrink; F. C. Lightstone. “Computational Lipidomics of the Neuronal Plasma Membrane”. In: *Biophysical Journal* 113 (10 Nov. 2017), pp. 2271–2280. ISSN: 00063495. DOI: [10.1016/j.bpj.2017.10.017](https://doi.org/10.1016/j.bpj.2017.10.017). URL: <https://linkinghub.elsevier.com/retrieve/pii/S0006349517311323>.
- [207] R. A. Vaishnav; R. Liu; J. Chapman; A. M. Roberts; H. Ye; J. D. Rebolledo-Mendez; T. Tabira; A. H. Fitzpatrick; A. Achiron; M. P. Running; R. P. Friedland. “Aquaporin 4 molecular mimicry and implications for neuromyelitis optica”. In: *Journal of Neuroimmunology* 260 (1-2 July 2013), pp. 92–98. ISSN: 01655728. DOI: [10.1016/j.jneuroim.2013.04.015](https://doi.org/10.1016/j.jneuroim.2013.04.015). URL: <https://linkinghub.elsevier.com/retrieve/pii/S0165572813000994>.
- [208] C. Nicaise; M. S. Soyfoo; M. Authelet; R. De Decker; D. Bataveljic; C. Delporte; R. Pochet. “Aquaporin-4 Overexpression in Rat ALS Model”. In: *The Anatomical Record: Advances in Integrative Anatomy and Evolutionary Biology* 292 (2 Feb. 2009),

- pp. 207–213. ISSN: 19328486. DOI: [10.1002/ar.20838](https://doi.org/10.1002/ar.20838). URL: <http://doi.wiley.com/10.1002/ar.20838>.
- [209] B. Yang; Z. Zador; A. S. Verkman. “Glial Cell Aquaporin-4 Overexpression in Transgenic Mice Accelerates Cytotoxic Brain Swelling”. In: *Journal of Biological Chemistry* 283 (22 May 2008), pp. 15280–15286. ISSN: 0021-9258. DOI: [10.1074/jbc.M801425200](https://doi.org/10.1074/jbc.M801425200). URL: <http://www.jbc.org/lookup/doi/10.1074/jbc.M801425200>.
- [210] T. A. Wassenaar; H. I. Ingólfsson; R. A. Böckmann; D. P. Tieleman; S. J. Marrink. “Computational Lipidomics with *insane* : A Versatile Tool for Generating Custom Membranes for Molecular Simulations”. In: *Journal of Chemical Theory and Computation* 11 (5 May 2015), pp. 2144–2155. ISSN: 1549-9618. DOI: [10.1021/acs.jctc.5b00209](https://doi.org/10.1021/acs.jctc.5b00209). URL: <https://pubs.acs.org/doi/10.1021/acs.jctc.5b00209>.
- [211] M. I. Mahmood; H. Noguchi; K. Okazaki. “Curvature induction and sensing of the F-BAR protein Pacsin1 on lipid membranes via molecular dynamics simulations”. In: *Scientific Reports* 9 (1 Dec. 2019), p. 14557. ISSN: 2045-2322. DOI: [10.1038/s41598-019-51202-z](https://doi.org/10.1038/s41598-019-51202-z). URL: <http://www.nature.com/articles/s41598-019-51202-z>.
- [212] X. Periole; M. Cavalli; S. J. Marrink; M. A. Ceruso. “Combining an Elastic Network With a Coarse-Grained Molecular Force Field: Structure, Dynamics, and Intermolecular Recognition”. In: *Journal of Chemical Theory and Computation* 5 (9 Sept. 2009), pp. 2531–2543. ISSN: 1549-9618. DOI: [10.1021/ct9002114](https://doi.org/10.1021/ct9002114). URL: <https://pubs.acs.org/doi/10.1021/ct9002114>.
- [213] M. S. Buckeridge. “The evolution of the Glycomic Codes of extracellular matrices”. In: *Biosystems* 164 (Feb. 2018), pp. 112–120. ISSN: 03032647. DOI: [10.1016/j.biosystems.2017.10.003](https://doi.org/10.1016/j.biosystems.2017.10.003). URL: <https://linkinghub.elsevier.com/retrieve/pii/S0303264717302721>.
- [214] I. Figueredo; A. Paiotta; R. Dal Magro; F. Tinelli; R. Corti; F. Re; V. Cassina; E. Caneva; F. Nicotra; L. Russo. “A New Approach for Glyco-Functionalization of Collagen-Based Biomaterials”. In: *International Journal of Molecular Sciences* 20 (7 Apr. 2019), p. 1747. ISSN: 1422-0067. DOI: [10.3390/ijms20071747](https://doi.org/10.3390/ijms20071747). URL: <https://www.mdpi.com/1422-0067/20/7/1747>.
- [215] G. A. A. Saracino; D. Cigognini; D. Silva; A. Caprini; F. Gelain. “Nanomaterials design and tests for neural tissue engineering”. In: *Chem. Soc. Rev.* 42 (1 2013), pp. 225–262. ISSN: 0306-0012. DOI: [10.1039/C2CS35065C](https://doi.org/10.1039/C2CS35065C). URL: <http://xlink.rsc.org/?DOI=C2CS35065C>.

# List of Publications

The author of this thesis contribute to the following articles:

**2018.** *Branched peptides integrate into self-assembled nanostructures and enhance biomechanics of peptidic hydrogels.* DOI:10.1016/j.actbio.2017.11.026. pp.258-271. In *Acta Biomaterialia* - ISSN:1742-7061 vol. 66, Pugliese, R; **Fontana, F**; Marchini, A; Gelain, F.

**2018.** *Elucidating Self-Assembling Peptide Aggregation via Morphoscanner: A New Tool for Protein-Peptide Structural Characterization.* DOI:10.1002/adv.201800471. In *Advanced Science* - ISSN:2198-3844 vol. 5 (8), Saracino, G\*; **Fontana, F\***; Jekhmane, S; Silva, J; Weingarth, M; Gelain, F

**2019.** *Design Parameters of Tissue-Engineering Scaffolds at the Atomic Scale.* DOI:10.1002/anie.201907880. pp.16943-16951. In *Angewandte Chemie. International Edition* - ISSN:1433-7851 vol. 58 (47), Jekhmane, S; Prachar, M; Pugliese, R; **Fontana, F**; Medeiros-Silva, J; Gelain, F; Weingarth, M

**2020.** *Probing mechanical properties and failure mechanisms of fibrils of self-assembling peptides.* DOI:10.1039/C9NA00621D. pp.190-198. In *Nanoscale Advances* - ISSN:2516-0230 vol. 2 (1) **Fontana, F**; Gelain, F

**2020.** *Control over the fibrillization yield by varying the oligomeric nucleation propensities of self-assembling peptides.* DOI: 10.1038/s42004-020-00417-7. In *Nature Communications Chemistry* - ISSN: 2399-3669 vol. 3, C. Y. J. Lau; **F. Fontana** ; L. D. B. Mandemaker; D. Wezendonk; B. Vermeer; A. M.J.J. Bonvin; R. de Vries; H. Zhang; K. Remaut; J. van den Dikkenberg; J. Medeiros-Silva; A. Hassan; B. Perrone; R. Kuemmerle; F. Gelain; W. E. Hennink; M. Weingarth; E. Mastrobattista

**2020.** *Controlled release of active Chondroitinase ABC reduces level of inhibitory CSPGs chains over time.* DOI: 10.1016/j.jconrel.2020.11.027. In *Journal of Controlled Release*

- ISSN: 0168-3659. A. Raspa; L. Carminati; R. Pugliese; **F. Fontana**; F. Gelain. (**In press**)

**2021.** *HyperBeta: characterizing the structural dynamics of proteins and self-assembling peptides* M. S. Nobile\*; **Federico Fontana\***; L. Manzoni; P. Cazzaniga; G. Mauri; G. A. A. Saracino; D. Besozzi; F. Gelain. In: *Scientific Reports* (**Under Revision**)

*\*The authors contributed equally to the manuscript*

# Curriculum Vitae

Federico Fontana was born June 17, 1992 in Piacenza, Italy. In 2014, he obtained a bachelor degree in Biomedical Engineering at the Polytechnic of Milan, Milano, Italy. In 2017, he obtained a Master of Science in Industrial Biotechnology at the University of Milano-Bicocca, Milano, Italy. Then, he joined the research group of Dott. Fabrizio Gelain at Grande Ospedale Metropolitano Niguarda, Milano, Italy. In November 2017, he was abilitated as Biologist at the University of Milan. From 2018, he is a member of National Order of Biologists. From November 2017, he was also enrolled as PhD candidate at the department of Biotechnology and Biosciences of University of Milano-Bicocca. From June to September 2019, he was visiting student at the ssNMR group of Prof. Markus Weingarth at the Bijvoet Center for Biomolecular Research, Utrecht University, Utrecht, the Netherlands. The work of his PhD is described in this thesis.



# Acknowledgements

First of all, I would like to express my gratitude to my supervisor, Dr Fabrizio Gelain for offering me the opportunity to join his group at the Niguarda Hospital to do my PhD work and work on the challenging research projects, also for his enthusiasm in science and the work discussions I was involved in the past three years of my PhD, and in which I will still be involved soon.

Besides, I would like to thank Prof Francesco Nicotra and Dr Laura Russo for offering me the opportunity to join the Department of Biotechnology and Bioscience at the University of Milano-Bicocca as PhD student and having all the supports that I needed to complete my PhD project.

I would like to thank my colleagues at the Niguarda Hospital, who are biologists and materials scientists. Thanks to their suggestions and constant comparisons, I was able to cross the border and bring computational chemistry closer to biology. Thank you so much, Andrea, Amanda and Raffaele.

I would like to thank Prof Markus Weingarth and all his colleagues for having me as guest PhD student at the Utrecht University. Thanks also for your suggestions and scientific discussions.

During the last year (better known as the year of the pandemic) I supervised three brilliant master students from the department of biotechnology and bioscience of University of Milano-Bicocca. This experience has allowed me to grow a lot from a professional but above all personal point of view. Thanks Alice, Cristian and Calogero.

I would also thank my master thesis supervisor Dr Gloria Saracino, which has lead my first steps in the field of computational chemistry.

Last but not the least, I would express my unlimited gratitude to my family. Thank you for



your help and always supporting me unconditionally, encouraging me with your best wishes during my PhD time.